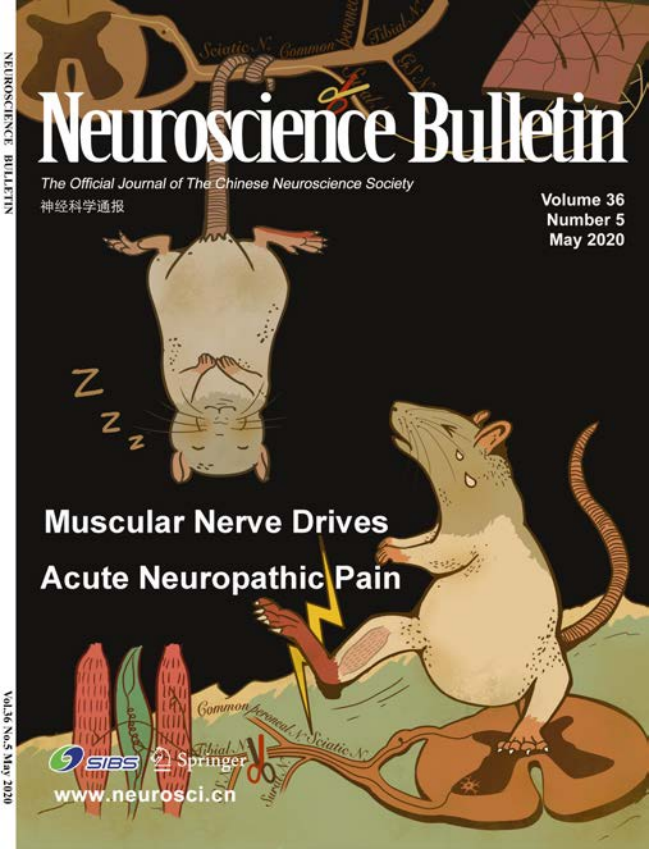


Neuroscience Bulletin

The Official Journal of The Chinese Neuroscience Society

神经科学通报

Volume 36
Number 5
May 2020



Muscular Nerve Drives Acute Neuropathic Pain

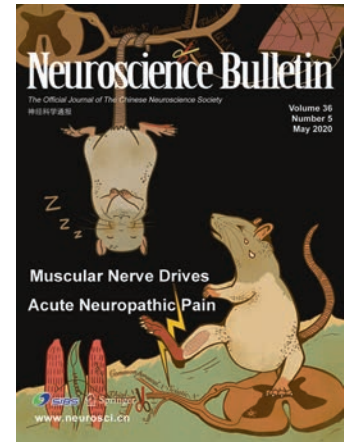
SIBS Springer

www.neurosci.cn

About the Cover

Acute neuropathic pain is a common complication following trauma or injury of a peripheral nerve but the underlying mechanism is obscure. In this issue, Zhu *et al.* established a rat model of acute nerve injury and applied *in vivo* electrophysiology to demonstrate that mechanical hypersensitivity and nociceptive neuronal hyperexcitabilities can be induced immediately after transection of a muscular but not cutaneous nerve. In the cover image, a model rat (below) demonstrated pain (hindpaw lifting) when the tibial nerve (including muscular afferents) was transected. The lightning indicated pain and hyperexcitabilities of nociceptive sensory neurons. However, no obvious pain was observed in another rat (top) with the sural nerve (cutaneous only) transected. See pages 453–462. (Cover image provided by Prof. Chao Ma).

Volume 36 Number 5
May 2020



Original Articles

453 Injury of Muscular but not Cutaneous Nerve Drives Acute Neuropathic Pain in Rats

Jie Zhu · Zhiyong Chen · Yehong Fang · Wanru Duan · Yikuan Xie · Chao Ma

463 Angiotensin Type 1 Receptors and Superoxide Anion Production in Hypothalamic Paraventricular Nucleus Contribute to Capsaicin-Induced Excitatory Renal Reflex and Sympathetic Activation

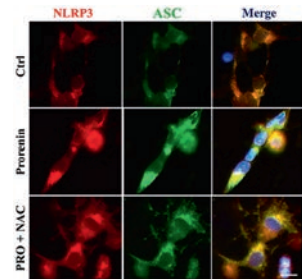
Yun Qiu · Fen Zheng · Chao Ye · Ai-Dong Chen · Jue-Jin Wang · Qi Chen · Yue-Hua Li · Yu-Ming Kang · Guo-Qing Zhu

475 Microglia-Derived NLRP3 Activation Mediates the Pressor Effect of Prorenin in the Rostral Ventrolateral Medulla of Stress-Induced Hypertensive Rats

Li Hu · Shutian Zhang · Kokwin Ooi · Xuehai Wu · Jiayang Wu · Jian Cai · Yinggang Sun · Jijiang Wang · Danian Zhu · Fuxue Chen · Chunmei Xia

493 A Whole-brain Map of Long-range Inputs to GABAergic Interneurons in the Mouse Caudal Forelimb Area

Zhuonan Duan · Anan Li · Hui Gong · Xiangning Li



p 488

506 Test–Retest Reliability of Functional Magnetic Resonance Imaging Activation for a Vergence Eye Movement Task

Cristian Morales · Suril Gohel · Xiaobo Li · Mitchell Scheiman · Bharat B. Biswal · Elio M. Santos · Chang Yaramothu · Tara L. Alvarez

519 Role of T-type Calcium Channels in Generating Hyperexcitatory Behaviors during Emergence from Sevoflurane Anesthesia in Neonatal Rats

Feng-Yan Shen · Byung-Gun Lim · Wen Wen · Yu Zhang · Bo Cao · Yue-Guang Si · Li-Qing Ma · Meng Deng · Yang In Kim · Young-Beom Kim · Ying-Wei Wang

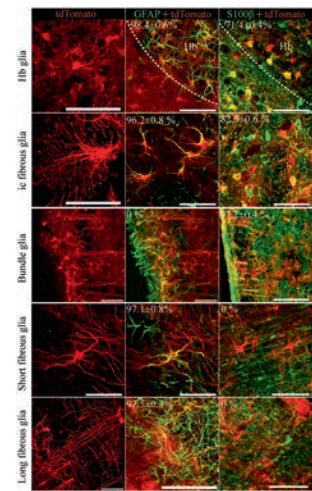
Methods

530 Expression Patterns of Inducible Cre Recombinase Driven by Differential Astrocyte-Specific Promoters in Transgenic Mouse Lines

Neng-Yuan Hu · Ya-Ting Chen · Qian Wang · Wei Jie · Yi-Si Liu · Qiang-Long You · Ze-Lin Li · Xiao-Wen Li · Sophie Reibel · Frank W. Pfrieger · Jian-Ming Yang · Tian-Ming Gao

545 *In Vivo* Two-photon Calcium Imaging in Dendrites of Rabies Virus-labeled V1 Corticothalamic Neurons

Yajie Tang · Liang Li · Leqiang Sun · Jinsong Yu · Zhe Hu · Kaiqi Lian · Gang Cao · Jinxia Dai



p 536

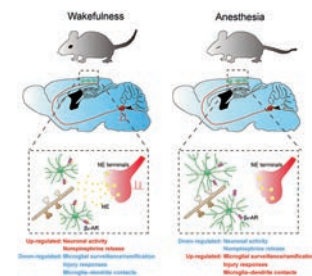
Research Highlights

554 Norepinephrine from the Locus Coeruleus Regulates Microglia Dynamics During Wakefulness

Yaling Hu · Peng Shi · Zhihua Gao

557 Meningeal Lymphatic Vessels: A Drain of the Brain Involved in Neurodegeneration?

Yuan Cheng · Yan-Jiang Wang



p 555

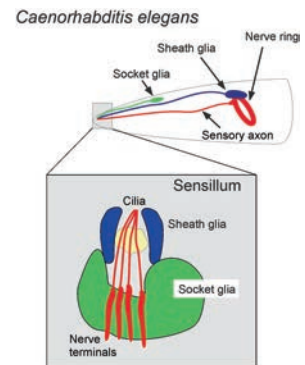
561 Glial-neuronal Sensory Organs: Evolutionary Journey from *Caenorhabditis elegans* to Mammals

Yong Tang · Peter Illes · Alexei Verkhratsky

Correction

565 Correction to: Regional Metabolic Patterns of Abnormal Postoperative Behavioral Performance in Aged Mice Assessed by ¹H-NMR Dynamic Mapping Method

Taotao Liu · Zhengqian Li · Jindan He · Ning Yang · Dengyang Han · Yue Li · Xuebi Tian · Huili Liu · Anne Manyande · Hongbing Xiang · Fuqiang Xu · Jie Wang · Xiangyang Guo



p 562



Injury of Muscular but not Cutaneous Nerve Drives Acute Neuropathic Pain in Rats

Jie Zhu^{1,2} · Zhiyong Chen^{1,3,4} · Yehong Fang^{1,3} · Wanru Duan⁵ · Yikuan Xie¹ · Chao Ma^{1,3} 

Received: 31 July 2019 / Accepted: 27 September 2019 / Published online: 13 January 2020
© Shanghai Institutes for Biological Sciences, CAS 2020

Abstract Acute pain is a common complication after injury of a peripheral nerve but the underlying mechanism is obscure. We established a model of acute neuropathic pain *via* pulling a pre-implanted suture loop to transect a peripheral nerve in awake rats. The tibial (both muscular and cutaneous), gastrocnemius–soleus (muscular only), and sural nerves (cutaneous only) were each transected. Transection of the tibial and gastrocnemius–soleus nerves, but not the sural nerve immediately evoked spontaneous pain and mechanical allodynia in the skin territories innervated by the adjacent intact nerves. Evans blue extravasation and cutaneous temperature of the intact skin territory were also significantly increased. *In vivo* electrophysiological recordings revealed that injury of a muscular

nerve induced mechanical hypersensitivity and spontaneous activity in the nociceptive C-neurons in adjacent intact nerves. Our results indicate that injury of a muscular nerve, but not a cutaneous nerve, drives acute neuropathic pain.

Keywords Muscular nerve · Cutaneous nerve · Acute neuropathic pain

Introduction

Acute neuropathic pain is a common complaint in clinical practice, but it is often underappreciated and undertreated in patients who experience trauma, surgery, and illness. In about one-half of patients, acute neuropathic pain develops into chronic neuropathic pain lasting for years, which greatly damages physical and mental health [1].

Growing evidence in animal models has demonstrated that it is injury of the muscular nerve, not the cutaneous nerve that matters in chronic neuropathic pain [2–4]. A significant proportion of patients who recover from poliovirus infection, which mainly targets muscular nerves and leads to progressive muscle weakness, suffer from chronic neuropathic pain, indicating that pathology of muscular nerves contributes to chronic pain [5, 6]. Besides, the sural nerve, a cutaneous branch of the sciatic nerve, is widely harvested in nerve repair surgery and most patients report no chronic pain after grafting [7].

However, it remains unclear whether muscular nerves also play a significant role in the generation of acute neuropathic pain. Some limitations have restricted the research on acute pain in animal models. To ensure that animals are awake and avoid the influence of anesthetics, pain-related behaviors are usually observed at least hours

Jie Zhu, Zhiyong Chen, and Yehong Fang have contributed equally to this work.

✉ Chao Ma
machao@ibms.cas.cn

¹ Department of Human Anatomy, Histology and Embryology, Institute of Basic Medical Sciences, Neuroscience Center, Chinese Academy of Medical Sciences, School of Basic Medicine, Peking Union Medical College, Beijing 100005, China

² Department of Radiation Oncology, Sichuan Cancer Hospital and Institute, Sichuan Cancer Center, School of Medicine, University of Electronic Science and Technology of China, Chengdu 610054, China

³ Joint Laboratory of Anesthesia and Pain, Peking Union Medical College, Beijing 100730, China

⁴ Department of Anesthesiology and Critical Care Medicine, Johns Hopkins University, School of Medicine, Baltimore, MD 21205, USA

⁵ Department of Neurosurgery, Xuanwu Hospital, Capital Medical University, Beijing 100053, China

or days after surgery, leaving the acute neuropathic pain that occurs immediately after nerve injury rarely investigated. Previous studies have demonstrated that chronic neuropathic pain is associated with the release of inflammatory cytokines and the overexpression of sodium channels [8–15]. In fact, it usually takes hours or even days for significant neurophysiological changes to develop, implying that different mechanisms drive acute neuropathic pain. In a previous study, we applied a novel method to transect the L5 spinal nerve in awake rats to study acute neuropathic pain. Using this novel method, we observed the rapid onset of spontaneous pain and evoked pain hypersensitivity. The outburst of pain-related behavior was synchronous with the spontaneous activity and hyperexcitability of nociceptive neurons in the adjacent intact L4 dorsal root ganglion (DRG) [16].

In this study, we continued to apply this modified surgical method to transect peripheral nerves in awake rats to investigate the role of muscular nerves in acute neuropathic pain. The tibial (both muscular and cutaneous), gastrocnemius–soleus (GS) (muscular only), and sural (cutaneous only) nerves were each transected in awake rats by quickly pulling a pre-implanted suture loop surrounding the nerve. Then we measured the paw withdrawal threshold (PWT) to mechanical stimuli and the duration of spontaneous foot lifting, investigated the hypersensitivity of nociceptive C-neurons by *in vivo* electrophysiological recording, and evaluated neurogenic inflammation by Evans blue extravasation. This study was designed to help unravel the mechanisms underlying acute neuropathic pain.

Materials and Methods

Animals

Adult female Sprague-Dawley rats (180 g–200 g) provided by the National Institutes for Food and Drug Control, China, were housed under a 12-h light/12-h dark cycle at room temperature ($23\text{ }^{\circ}\text{C} \pm 2\text{ }^{\circ}\text{C}$). All rats had free access to rodent chow and water. All experiments were performed in Peking Union Medical College, Beijing, China and were approved by the Institutional Animal Care and Use Committees of the Chinese Academy of Medical Sciences and the Institute of Basic Medical Sciences (Project #211-2014). A total of 137 rats were used: 33 for PWT measurement, 36 for spontaneous foot lifting measurement, 32 for *in vivo* electrophysiological recording, 21 for Evans blue extravasation, and 15 for cutaneous temperature measurement.

Surgery

The day of acute nerve transection was defined as day 0. On day -2 (2 days before transection), after the behavioral test, rats were anesthetized with pentobarbital sodium (50 mg/kg intraperitoneally; Sigma-Aldrich Corp., St. Louis, MO). Under sterile conditions, a longitudinal incision was made in the lateral skin of the right thigh, then the biceps femoris muscle was bluntly separated to expose and isolate the sciatic nerve with its three branches: tibial, common peroneal, and sural. The GS is a branch of the tibial nerve that innervates the gastrocnemius and soleus muscles. A suture loop was placed around the target branch with its two ends running through a 2 mm-long sterilized transparent tube. A knot in the distal end of the tube was made to prevent the tube from slipping out. The tube was embedded under the skin and then the incision was closed in layers. To assess the influence of the surgery itself, the behavioral test was repeated 1 day before transection (day -1). On day 0, the target nerve was transected in awake rats by quickly pulling the pre-implanted suture loop while holding the transparent tube steady (Fig. 1A). When the target nerve was completely transected by the suture loop, the intact loop was pulled out. After all experiments, we checked the target nerve to confirm it was completely transected.

Behavioral Test

Paw Withdrawal Threshold

Before all tests, rats were placed in an acrylic glass box to habituate to the environment and observed for 1 h/day for 3 days. Before each test, habituation was allowed for 10 min.

The plantar surface of the rat hind paw can be divided into three territories: medial (saphenous nerve receptive field), middle (tibial nerve receptive field), and lateral (sural nerve receptive field), with overlaps between adjacent territories [17]. A calibrated electronic von Frey filament (Electronic von Frey 2390-5 Anesthesiometer; IITC Life Science, Woodland Hills, CA) was applied perpendicular to each of the sites 1, 2, and 3 on the plantar surface, and held for ~ 3 s (Fig. 1B). The PWTs of sites 1, 2, and 3 represented those of the lateral, middle, and medial territories, respectively. Sharp paw withdrawal with licking or shaking was regarded as a positive response. The average of three repeated measurements was taken as the final PWT. The average PWTs for days -4 , -3 , and -2 were defined as the baseline.

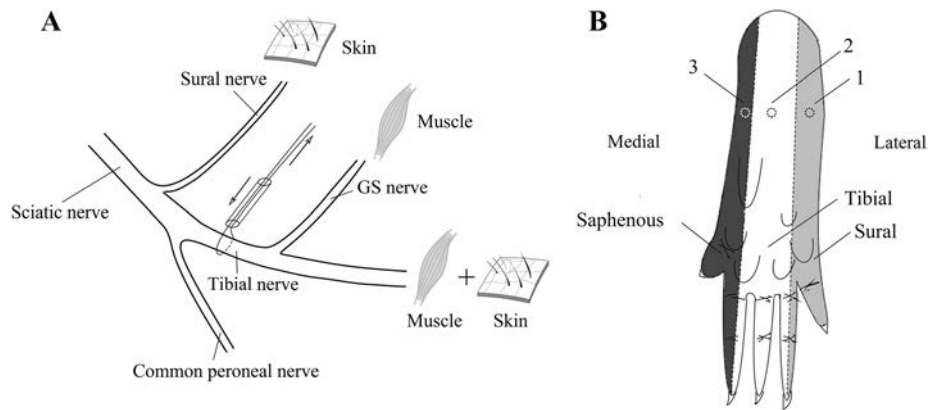


Fig. 1 Nerve branches and plantar territories. **A** Diagram of the sciatic nerve and its branches: tibial (both muscular and cutaneous), gastrocnemius-soleus (GS; muscular only) and sural (cutaneous only). In nerve transection, the transparent tube was held steady and the suture loop was pulled rapidly. **B** The plantar hind paw is divided into

three territories: lateral, middle, and medial, innervated by the sural, tibial, and saphenous nerves, respectively. Paw withdrawal thresholds were measured at sites 1, 2, and 3 (dashed circles) in the corresponding territories.

Spontaneous Pain Duration

The habituation process in spontaneous pain assessment was the same as for the PWT test. Behaviors such as spontaneous foot lifting, biting, and licking were regarded as indicators of spontaneous pain [18]. To observe the behaviors clearly, a mirror was placed below the glass box at an angle of 45° to the experimental platform. A high-definition camera was placed in front of the box to capture direct images and indirect inverted images in the mirror. The cumulative duration (in seconds) of spontaneous foot lifting, biting, and licking the right hind paw per 30 min was recorded as the quantitative assessment of spontaneous pain. The average of spontaneous pain duration on days – 3 and – 2 (before implanting the loop) was defined as the baseline.

Electrophysiological Recording

L4 Dorsal Root Ganglion Exposure

L4 DRG exposure and *in vivo* electrophysiological recording were as previously reported [19]. Briefly, rats were anesthetized with pentobarbital sodium (initial dose of 50 mg/kg intraperitoneally followed by supplementary doses of 20 mg/kg as needed), the L5 transverse process was removed, and a laminectomy was made from L1 to L6. Oxygenated artificial cerebrospinal fluid at 35 °C was dripped onto the surface of the L4 DRG during surgery and recording. Under a dissecting microscope, the perineurium and epineurium of the L4 DRG were carefully removed, then the rat was transferred to the recording platform. A pool was made by attaching the skin to a metal ring.

Identification of C-neurons and Their Receptive Fields

The receptive field of a neuron was identified by applying peripheral stimuli. Axonal conduction velocity was determined by dividing the distance between the receptive field and the cell body by the latency of the action potential. A C-neuron was identified by a velocity < 2 m/s, then mechanical (50 mN von Frey filament for 3 s), warm (51 °C fine tube for 5 s), and cold stimuli (0 °C ice-water for 10 s) were applied to identify the subtype of the C-neuron.

Mechanical stimuli were applied to the C-neuron receptive field using a Q-tip, light brush, and von Frey filaments in ascending order (5 mN, 10 mN, 30 mN, and 50 mN). *In vivo* recording started 20 min before nerve transection and lasted for 2 h. If action potentials were recorded in C-neurons when mechanical stimuli were delivered, the stimuli were labeled as positive.

Criteria for Defining a Spontaneously Active C-neuron

For an identified C-neuron, a continuous recording started 5 min before transection and lasted for 4 h without any external stimulation. If an identified C-neuron discharged continuously during this period, it was classified as spontaneously active. Any discharge associated with electrode insertion and lasting < 30 s was classified as “injury discharge” and terminated as a failure.

Compensatory A-fiber Input

After identifying a spontaneously active C-neuron, stimulation mimicking A-fiber strength (10 Hz, 0.5 mA for

3 min) was delivered to the proximal segment of the transected nerve through a pair of silver hook electrodes.

Evans Blue Extravasation

Evans blue (1%, 2 mL in saline, intravenously; Sigma-Aldrich, St. Louis, MO) was injected into the caudal vein 2 min before nerve transection. Transcardial perfusion with 0.1 mol/L phosphate-buffered saline was carried out 30 min after transection. After perfusion, photographs of the dorsal paws were taken, and then the dorsal skin of the ipsilateral and contralateral paws was removed. Extravasated dye was measured using a previously reported method [20]. Briefly, the removed skin was incubated overnight with N, N-dimethylformamide at 55 °C to completely dissolve the Evans blue into the solvent. Then, the Evans blue absorbance value was measured by a microplate spectrophotometer at 630 nm. The concentration of Evans blue was normalized to a reference sample (0 µg/mL–9.6 µg/mL).

Cutaneous Temperature Measurement

Rats were placed prone with an electrical temperature sensor in the rectum to measure the rectal temperature. Another two electrical temperature sensors were closely attached to the skin surface on different plantar territories of the hind paw with adhesive tape. The nerves were exposed as described above and were transected using fine scissors. Temperature recording started 5 min before transection and ended 30 min later.

Statistical Analysis

All data are presented as the mean \pm SEM. Differences of PWT at different time points were analyzed using one-way analysis of variance (ANOVA) followed by the Bonferroni *post hoc* test. Student's *t* test was applied to compare the mechanical threshold of C-neuron discharge and Evans blue extravasation between different groups. The χ^2 test was applied to compare the incidence of spontaneous discharge between different groups. Two-way (time and group) ANOVA with the Bonferroni *post hoc* test was applied to compare repeated measurements of cutaneous temperature at different time points among different groups. A statistically significant difference was defined as a two-sided *P* value < 0.05 . IBM SPSS Statistics for Windows (version 21.0, Armonk, NY) was used for analysis.

Results

Animal Behavior

When rats were awake on the day after implanting the tube (day -1), they behaved almost normally, except for occasionally licking at the wound. On day 0, after acute transection of the tibial nerve and GS nerve, the rats immediately became restless, walked around clumsily and limped on the injured right hind paw with licking and biting. Hours later, there was a tendency to recover with a decreased licking and biting frequency. In contrast, rats behaved normally after sural nerve transection and sham transection.

Mechanical Allodynia of the Lateral Plantar Paw (Sural Nerve Receptive Field)

Compared with baseline, the PWTs of the lateral territory showed no significant changes on day -1 in the four groups ($P > 0.05$). After tibial nerve transection, the PWT of the lateral territory decreased dramatically, from baseline (13.6 g \pm 0.4 g) to the range of 1.2 g \pm 0.3 g to 2.4 g \pm 0.9 g ($P < 0.05$, $n = 9$). After GS nerve transection, a moderate decline in the PWT of the lateral territory occurred, from baseline (14.1 g \pm 0.2 g) to the range of 4.5 g \pm 0.8 g to 6.8 g \pm 0.7 g ($P < 0.01$, $n = 10$). After sural nerve transection, only the PWTs at 5 h, 3 days, and 7 days slightly but significantly decreased ($P < 0.05$, $n = 8$). In the sham group, the PWTs in the lateral territory were between 12.9 g \pm 0.5 g and 14.3 g \pm 0.8 g with significant differences at 5 h and 7 days ($P < 0.05$, $n = 6$) (Fig. 2A).

Mechanical Allodynia of the Medial Plantar Paw (Saphenous Nerve Receptive Field)

Compared with baseline, the PWTs of the medial territory on day -1 showed no significant differences in the four groups. After tibial nerve transection, the PWT of the medial territory was significantly lower than baseline at 5 h post-transection with a threshold of 8.6 g \pm 0.8 g ($P < 0.05$, $n = 9$). After GS nerve transection, the PWTs of the medial territory dropped from baseline (12.8 g \pm 0.3 g) to the range of 5.8 g \pm 0.6 g to 8.9 g \pm 0.5 g ($P < 0.01$, $n = 10$). After sural nerve transection, the PWTs at most time points were not significantly changed. Only the PWT on day 3 was significantly decreased to 10.2 g \pm 0.5 g ($P < 0.01$, $n = 8$). In the sham group, there were no significant changes in the PWTs of the medial territory ($P > 0.05$, $n = 6$) (Fig. 2B).

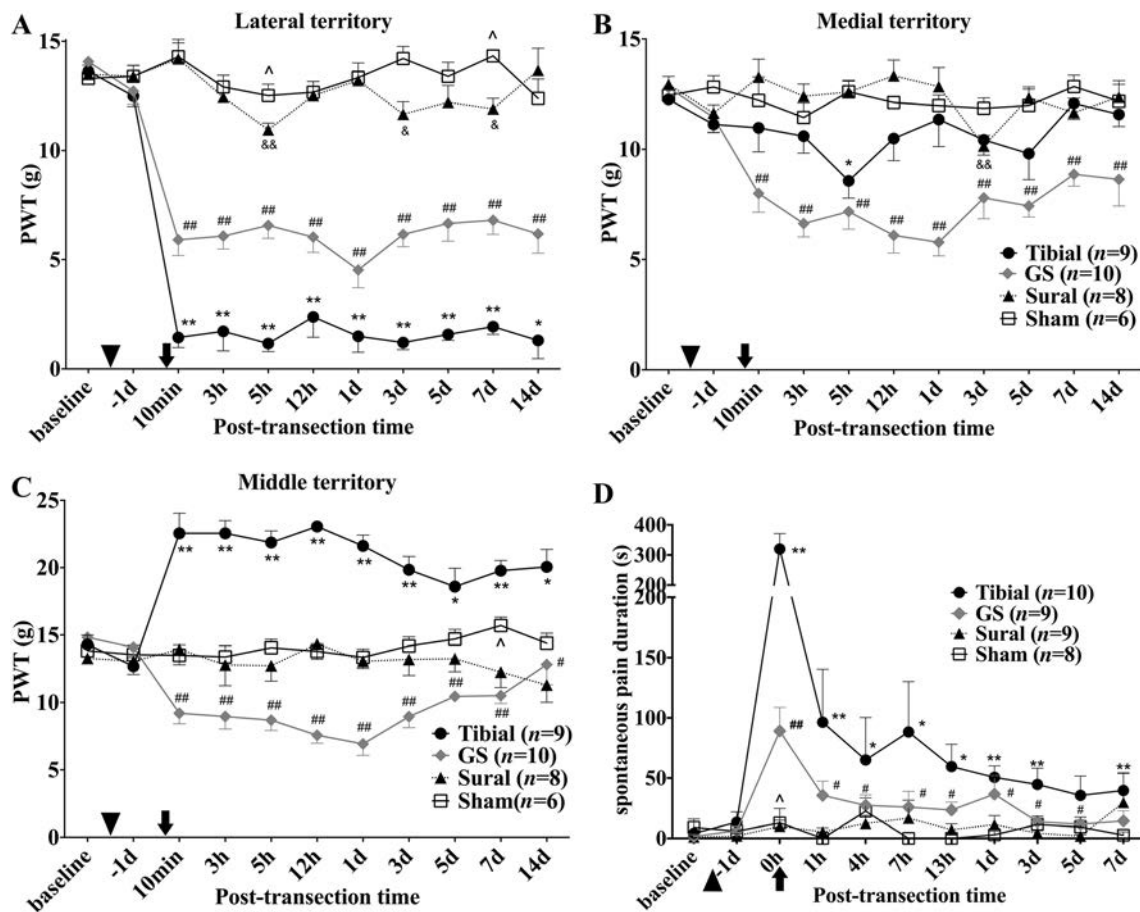


Fig. 2 Paw withdrawal thresholds (PWTs) in each territory and spontaneous pain duration. **A** PWTs of the lateral territory. In the tibial and GS transection groups, PWTs significantly decreased immediately after transection and lasted for 14 days. In the sural and sham groups, PWTs showed no significant change at most time points. **B** PWTs of the medial territory. PWTs decreased significantly after GS nerve transection. In the tibial, sural, and sham groups, the PWTs at most time points showed no significant change. **C** PWTs of the middle territory. PWTs increased significantly after tibial nerve transection and dropped after GS nerve transection with a potential

recovery tendency after 1 day. **D** Spontaneous pain duration. After tibial nerve transection and GS nerve transection, the spontaneous pain duration extended significantly, and a recovery tendency occurred over time. In the sural and sham groups, spontaneous pain duration did not significantly change at most time points [time points vs baseline, * $P < 0.05$, ** $P < 0.01$ (tibial group); # $P < 0.05$, ## $P < 0.01$ (GS group); & $P < 0.05$, && $P < 0.01$ (sural group); ^ $P < 0.05$, ^^ $P < 0.01$ (sham group); arrowheads, implantation of suture loop and tube without nerve transection on day - 2; arrows, nerve transection].

Mechanical Allodynia of the Middle Plantar Paw (Tibial Nerve Receptive Field)

Compared with baseline, the PWTs of the middle territory were not significantly changed on day - 1 in all groups. After tibial nerve transection, rats lost sensation to mechanical stimuli applied to the middle territory. Because of paralysis and numbness, the rats did not respond to mechanical stimuli even if the force of the von Frey filament was up to 20 g. Paws were elevated passively by the von Frey filament with PWTs between 18.6 g ± 1.4 g and 23.1 g ± 0.4 g ($P < 0.05$, $n = 9$). After GS transection, the PWTs of the middle territory declined significantly from baseline 14.8 g ± 0.3 g to the range of 6.9 g ± 0.9 g to 12.8 g ± 1.5 g ($P < 0.05$, $n = 10$). In

the sural group, the PWTs of the middle territory at different time points were not significantly changed ($P > 0.05$, $n = 8$). In the sham group, the PWTs of the middle territory remained between 13.4 g ± 0.8 g and 15.7 g ± 0.6 g with only that on post-transection day 7 higher than baseline ($P < 0.05$, $n = 6$) (Fig. 2C).

Extended Spontaneous Pain Duration After Muscular Nerve Transection

In all four groups, no spontaneous pain appeared on the day after implanting the tube (day - 1), and there was no significant difference in spontaneous pain duration between baseline and day - 1. Rats exhibited pain behaviors and high facilitation of spontaneous pain immediately after

tibial nerve transection ($P < 0.05$, except for $P = 0.05$ on day 5, $n = 10$). The most frequent spontaneous pain occurred immediately after tibial nerve transection, with an extremely long duration of $319.9 \text{ s} \pm 51.1 \text{ s}$ ($P < 0.01$). Then, rats tended to recover and spontaneous pain duration was attenuated to $39.6 \text{ s} \pm 14.4 \text{ s}$ on post-transection day 7. After GS nerve transection, spontaneous pain duration was moderately extended ($P < 0.05$, except for $P > 0.05$ on day 7, $n = 9$), and the longest duration ($89.1 \text{ s} \pm 19.6 \text{ s}$) occurred immediately after transection with a tendency to decline afterwards. Compared with baseline ($1.1 \text{ s} \pm 1.1 \text{ s}$), spontaneous pain duration slightly increased to $10.0 \text{ s} \pm 5.0 \text{ s}$ immediately after sural nerve transection ($P < 0.05$ at 0 h, $n = 9$), but no significant spontaneous pain behaviors were observed thereafter ($P > 0.05$). No spontaneous pain behaviors were observed in the sham group ($P > 0.05$, $n = 8$) (Fig. 2D).

Sensitization of Nociceptive C-neurons After Muscular Nerve Transection

We made *in vivo* extracellular recordings from C-neuron cell bodies in L4 DRGs after nerve transection, noting the conduction velocity and responses to mechanical, warm, and cold stimuli of 22 nociceptive C-neurons (Fig. 3A–G). The receptive fields of nociceptive C-neurons after tibial

nerve transection were mainly in the adjacent lateral (sural nerve receptive field) and medial (saphenous nerve receptive field) territories (Fig. 3F). The mechanical threshold to evoke C-neuron discharge significantly decreased within 5 min after tibial nerve transection (post-transection $5.6 \text{ mN} \pm 2.3 \text{ mN}$ vs pre-transection $31.4 \text{ mN} \pm 5.9 \text{ mN}$, $P < 0.01$, $n = 6$) and GS nerve transection (post-transection $11.6 \text{ mN} \pm 2.9 \text{ mN}$ vs pre-transection $32.7 \text{ mN} \pm 3.7 \text{ mN}$, $P < 0.01$, $n = 5$). The mechanical threshold did not significantly change after sural nerve transection (post-transection $28.5 \text{ mN} \pm 4.9 \text{ mN}$ vs pre-transection $30.8 \text{ mN} \pm 5.1 \text{ mN}$, $P > 0.05$, $n = 5$) (Fig. 3H).

Increased Spontaneous Activity of Nociceptive C-neurons After Muscular Nerve Transection

The spontaneous activity of L4 DRG C-neurons became evident $\sim 3 \text{ min}$ after tibial or GS nerve transection (Fig. 4A–C). The percentage of C-neurons with spontaneous activity was significantly higher after tibial (37%, 21/57, $P < 0.01$) and GS transection (18%, 7/38, $P < 0.01$) than in the sham group (3%, 1/38) (Fig. 4D). Spontaneous activity was rarely recorded in C-neurons after sural nerve transection (1%, 1/80, $P > 0.05$). Spontaneous activity was suppressed when continuous A-fiber-strength electrical

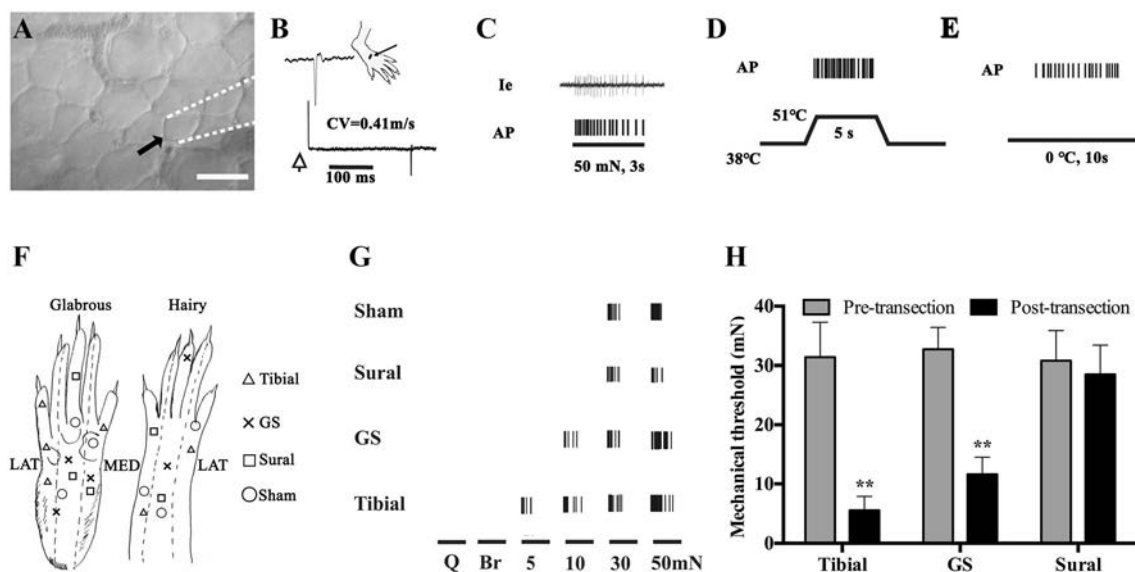


Fig. 3 *In vivo* responses of nociceptive C-neurons to mechanical stimuli in the tibial, GS, and sural nerve transection groups. **A** Bright-field image of the L4 DRG surface showing a neuron cell body (arrow) and an extracellular recording electrode (dashed lines) (scale bar, $50 \mu\text{m}$). **B** Conduction velocity (CV) was measured by electrically stimulating the peripheral receptive field on the dorsal surface of the paw (black dot) (bar, 100 ms). **C** Typical response of the C-neuron to 50 mN mechanical stimulation. Action potentials (APs) in the original recording trace (Ie) are presented as corresponding tic marks below. **D** Representative response of the C-neuron to

nociceptive thermal stimulation ($51 \text{ }^\circ\text{C}$ for 5 s). **E** Representative response of the C-neuron to cold stimulation ($0 \text{ }^\circ\text{C}$ for 10 s). **F** Receptive fields of nociceptive C-neurons after tibial (Δ), GS (\times), sural (\square), and sham (\circ) transection. **G** Action potentials (vertical lines) evoked by different mechanical stimuli—Q-tip (Q), light brush (Br), and von-Frey filaments with 5 mN , 10 mN , 30 mN , and 50 mN bending forces—immediately after nerve transection. **H** Mechanical thresholds to evoke the discharge of nociceptive C-neurons ($*P < 0.05$, $**P < 0.01$, post-transection vs pre-transection).

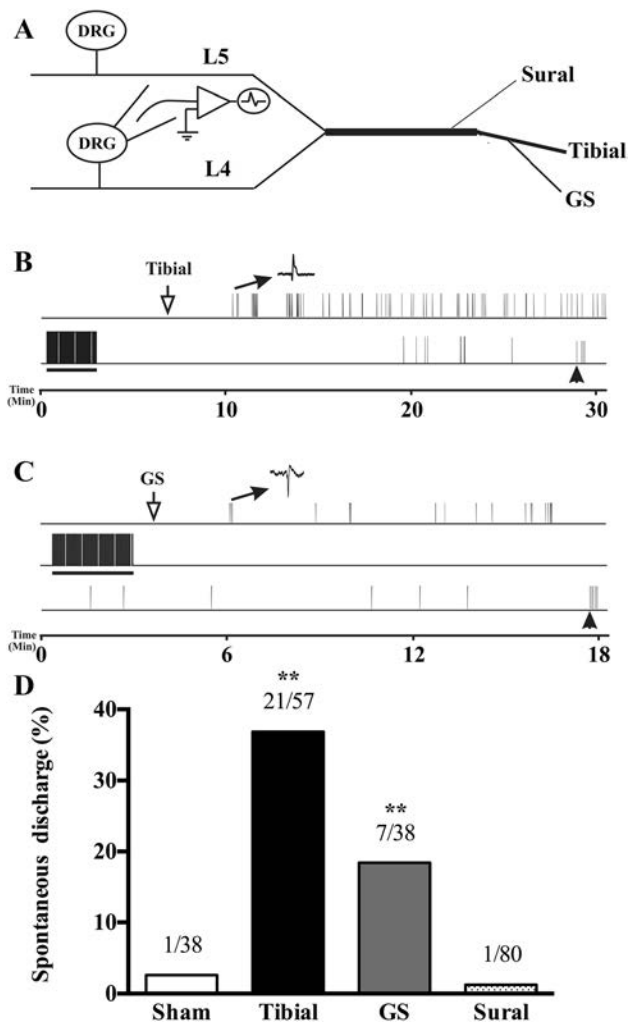


Fig. 4 Rapid-onset of spontaneous C-neuron discharges in the L4 DRG following muscular nerve transection. **A** Schematic of the recording setup. **B, C** An initially quiescent C-nociceptive neuron showed spontaneous activity within 3 min after tibial and GS nerve transections, with inhibitory modulation by A-fiber strength stimuli (horizontal bar, electrical stimulation at 10 Hz, 0.5 mA for 3 min; arrowheads, mechanical stimulation in the receptive field). **D** Percentage of C-neurons exhibiting spontaneous discharges after nerve transection. The number of neurons exhibiting spontaneous discharge/total neurons recorded is indicated above each column (* $P < 0.05$, ** $P < 0.01$, tibial, GS, and sural groups vs sham).

stimulation (10 Hz, 0.5 mA for 3 min) was applied to the proximal tibial or GS nerve (Fig. 4B, C).

Increased Evans Blue Extravasation After Muscular Nerve Transection

Evans blue extravasation was evident in the ipsilateral affected skin ~ 10 min after tibial (Fig. 5A) and GS (Fig. 5B) transection. Compared with $6.25 \mu\text{g/g} \pm 1.02 \mu\text{g/g}$ in the contralateral intact skin, the Evans blue concentration was significantly increased to $21.24 \mu\text{g/g}$

$\pm 3.26 \mu\text{g/g}$ in the ipsilateral affected skin after tibial nerve transection ($P < 0.01$, $n = 7$). After GS nerve transection, the Evans blue concentration in the ipsilateral affected skin was significantly higher than that the contralateral intact skin (ipsilateral $14.34 \mu\text{g/g} \pm 2.08 \mu\text{g/g}$ vs contralateral $6.12 \mu\text{g/g} \pm 1.35 \mu\text{g/g}$, $P < 0.01$, $n = 7$) (Fig. 5D). After sural nerve transection, there was no significant difference in Evans blue concentration between the ipsilateral affected and contralateral intact skin ($P > 0.05$, $n = 7$) (Fig. 5C, D).

Increased Cutaneous Temperature Following Muscular Nerve Transection

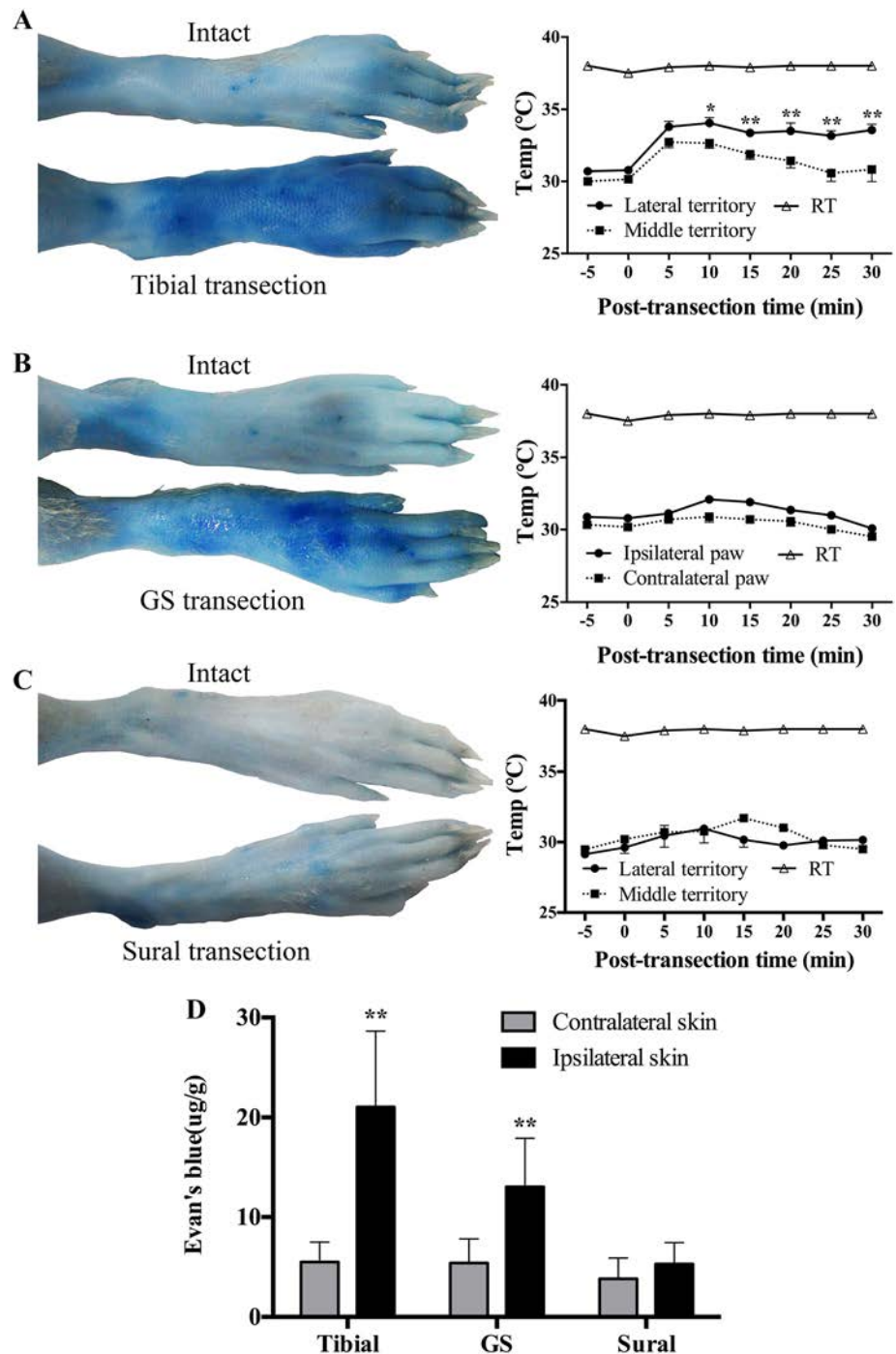
In the tibial and sural nerve transection groups, the cutaneous temperature of the lateral and middle territories of the ipsilateral plantar paw was simultaneously recorded. Ten minutes after tibial transection, the temperature of the lateral territory was significantly increased ($P < 0.05$, $n = 5$), with no significant change in the middle territory (Fig. 5A). The temperature of the lateral and middle territories was not significantly changed after sural nerve transection ($P > 0.05$, $n = 5$) (Fig. 5C).

In the GS transection group, the cutaneous temperature of the middle territory on the ipsilateral and contralateral paws was simultaneously measured. Transection of the GS nerve did not induce a significant temperature change ($P > 0.05$, $n = 5$) (Fig. 5B).

Discussion

In clinical practice, acute neuropathic pain frequently occurs after trauma and surgery, and may progress to chronic pain. A pathological muscular nerve is critical in the development of chronic neuropathic pain in rodent models and human subjects [2–7]. Due to the impact of anesthetics, it is difficult to study acute pain in rodent models and it remains unclear whether muscular nerves also play a significant role in acute neuropathic pain. In this study, we successfully applied a modified surgical method to investigate acute neuropathic pain by transecting the nerve with a pre-implanted suture loop, and found that the transection of a muscular nerve, but not a cutaneous nerve, led to the rapid onset of mechanical allodynia of the adjacent skin territory supplied by intact nerves. Spontaneous pain and mechanical allodynia were accompanied by spontaneous discharges and hypersensitivity of nociceptive C-neurons. These findings have important clinical implications. To relieve acute neuropathic pain and prevent chronic pain, muscular nerves should be carefully protected during surgery. Muscular nerves may be a potential target in the management of acute neuropathic pain.

Fig. 5 Evans blue extravasation and cutaneous temperature after nerve transection. **A** Evans blue clearly extravasated in the affected skin 30 min after tibial nerve transection (left), and the temperature of the lateral territory of the plantar hind paw increased significantly after the transection (right) ($*P < 0.05$, $**P < 0.01$, lateral vs middle territory). **B** Evans blue extravasated significantly after GS nerve transection (left), but with no significant change in the temperature of the ipsilateral paw (right) ($*P < 0.05$, $**P < 0.01$, ipsilateral middle vs contralateral middle territory). **C** No significant Evans blue extravasation (left) and cutaneous temperature change (right) were found following sural nerve transection ($*P < 0.05$, $**P < 0.01$, lateral vs middle territory). **D** Concentration of Evans blue dye in the dorsal skin after tibial, GS, and sural nerve transections ($*P < 0.05$, $**P < 0.01$, ipsilateral vs contralateral skin).



The inflammatory cytokine TNF- α is known to play a key role in the initiation of nerve injury-induced neuropathic pain, but this occurs at least several hours after the injury [13–15]. It also takes hours to days for the aberrant expression of voltage-gated sodium channels to dominate ectopic activity [8–10]. Evidently, previous evidence on inflammatory cytokines, ion channels, and Wallerian degeneration may not provide an appropriate explanation for this rapid onset of pain following muscular nerve

transection. Chronic neuropathic pain is common in patients with Guillain-Barré syndrome and diabetic neuropathy, diseases leading to peripheral demyelination in myelinated A-fibers [21, 22]. In a rat model of acute demyelination of the sciatic nerve by cobra venom, C-fibers discharge spontaneously several minutes after selectively blocking the A-fiber afferents [23]. These findings suggest that the loss of tonic A-fiber inputs may lead to the activation of nociceptive C-fibers and the

generation of neuropathic pain. Besides, electrical stimulation of deep tissue A β afferent fibers, but not cutaneous A β afferents, relieves the hyperalgesia evoked by knee joint inflammation in rats [24]. Deep acupuncture also has a better short-term anti-hyperalgesic effect than superficial acupuncture in patients with lateral epicondylalgia [25], suggesting that external stimulation of A-fiber muscular afferents may compensate for the loss of tonic A-fiber inputs and relieve neuropathic pain.

We hypothesize that the sensitization of adjacent intact sensory neurons occurs through a spinal mechanism involving gate-control and the dorsal root reflex, so that the absence of deep tissue A-fiber inputs following muscular nerve transection leads to acute neuropathic pain. According to gate-control theory, there is an interactive balance between myelinated large-diameter afferents and unmyelinated small-diameter afferents, and the large-diameter fibers inhibit small-diameter fibers in the inhibitory substantia gelatinosa [26]. Low-threshold mechanoreceptive primary afferent A-fibers indirectly inhibit neighboring nociceptive C-fibers *via* inhibitory gamma-aminobutyric acid (GABA)-ergic and glycinergic interneurons [27–29]. The inhibitory neurotransmitters GABA and glycine are released onto the central terminals of C-fibers, resulting in their hyperpolarization and the inhibition of C-fiber discharges. When the tonic discharges from deep tissue (muscular) A-fiber inputs are blocked, such as by transection or demyelination, the disinhibited C-fiber central terminals may depolarize and discharge antidromically to the peripheral terminals. The antidromic discharge of polymodal C-fibers in the intact nerves may therefore induce neurogenic inflammation by releasing substance P and calcitonin gene-related peptide from the nerve terminals [30]. Neurogenic inflammation, in reverse, may further sensitize peripheral terminals of the adjacent C-fibers and evoke orthodromic discharges, evoking spontaneous pain and cutaneous sensitivity. In this study, when the muscular nerve was transected, C-fibers in the nerve were also blocked. Only the C-fibers in the adjacent intact nerves could be activated and induce neurogenic inflammation in the receptive fields *via* the mechanisms proposed above, leading to spontaneous pain, mechanical allodynia, and a temperature increase in the hindpaw skin territories. This hypothesis can be further explored using spinal electrophysiological recordings. It is also possible that the neighboring nerve fibers might be sensitized by local inflammation from the transected nerve. However, since the spontaneous pain and mechanical allodynia were evoked almost immediately (within minutes) after nerve transection, it is unlikely that local inflammation plays a major role in this process.

In conclusion, injury of muscular nerves, but not cutaneous nerves, drives acute neuropathic pain. Neurons

innervating the muscle may be a potential target in the management of acute neuropathic pain.

Acknowledgements We thank Bo Yuan, B.S., Tao Wang, Ph.D. and Jin Tao, M.S. from the Institute of Basic Medical Sciences, Chinese Academy of Medical Sciences, Beijing, China, for technical assistance. This work was supported by grants from the National Natural Science Foundation of China (NSFC; 81271239 and 91632113 to CM, and NSFC for Young Scientists 81600956 to WD), and the Chinese Academy of Medical Sciences Innovation Fund for Medical Sciences (2017-I2M-3-008 to CM).

Conflict of interest The authors claim that there are no conflicts of interest.

References

- Hayes C, Browne S, Lantry G, Burstal R. Neuropathic pain in the acute pain service: a prospective survey. *Acute Pain* 2002, 4: 45–48.
- Obata K, Yamanaka H, Kobayashi K, Dai Y, Mizushima T, Katsura H, *et al.* The effect of site and type of nerve injury on the expression of brain-derived neurotrophic factor in the dorsal root ganglion and on neuropathic pain behavior. *Neuroscience* 2006, 137: 961–970.
- Luo ZD, Chaplan SR, Higuera ES, Sorkin LS, Stauderman KA, Williams ME, *et al.* Upregulation of dorsal root ganglion (alpha)2(delta) calcium channel subunit and its correlation with allodynia in spinal nerve-injured rats. *J Neurosci* 2001, 21: 1868–1875.
- Ramer LM, Borisoff JF, Ramer MS. Rho-kinase inhibition enhances axonal plasticity and attenuates cold hyperalgesia after dorsal rhizotomy. *J Neurosci* 2004, 24: 10796–10805.
- Stoelb BL, Carter GT, Abresch RT, Purekal S, McDonald CM, Jensen MP. Pain in persons with postpolio syndrome: frequency, intensity, and impact. *Arch Phys Med Rehabil* 2008, 89: 1933–1940.
- Ijpm FF, Nicolai JP, Meek MF. Sural nerve donor-site morbidity: thirty-four years of follow-up. *Ann Plast Surg* 2006, 57: 391–395.
- Miloro M, Stoner JA. Subjective outcomes following sural nerve harvest. *J Oral Maxillofac Surg* 2005, 63: 1150–1154.
- Waxman SG, Kocsis JD, Black JA. Type III sodium channel mRNA is expressed in embryonic but not adult spinal sensory neurons, and is reexpressed following axotomy. *J Neurophysiol* 1994, 72: 466–470.
- Dib-Hajj SD, Fjell J, Cummins TR, Zheng Z, Fried K, LaMotte R, *et al.* Plasticity of sodium channel expression in DRG neurons in the chronic constriction injury model of neuropathic pain. *Pain* 1999, 83: 591–600.
- Black JA, Cummins TR, Plumpton C, Chen YH, Hormuzdiar W, Clare JJ, *et al.* Upregulation of a silent sodium channel after peripheral, but not central, nerve injury in DRG neurons. *J Neurophysiol* 1999, 82: 2776–2785.
- Liefner M, Siebert H, Sachse T, Michel U, Kollias G, Brück W. The role of TNF-alpha during Wallerian degeneration. *J Neuroimmunol* 2000, 108: 147–152.
- Kim CH, Oh Y, Chung JM, Chung K. The changes in expression of three subtypes of TTX sensitive sodium channels in sensory neurons after spinal nerve ligation. *Mol Brain Res* 2001, 95: 153–161.
- Shamash S, Reichert F, Rotshenker S. The cytokine network of Wallerian degeneration: tumor necrosis factor-alpha, interleukin-1alpha, and interleukin-1beta. *J Neurosci* 2002, 22: 3052–3060.

14. Zelenka M, Schäfers M, Sommer C. Intraneural injection of interleukin-1 β and tumor necrosis factor-alpha into rat sciatic nerve at physiological doses induces signs of neuropathic pain. *Pain* 2005, 116: 257–263.
15. Cunha TM, Verri WJ, Silva JS, Poole S, Cunha FQ, Ferreira SH. A cascade of cytokines mediates mechanical inflammatory hypernociception in mice. *Proc Natl Acad Sci U S A* 2005, 102: 1755–1760.
16. Chen ZY, Wang T, Fang YH, Luo D, Anderson M, Huang Q, *et al.* Adjacent intact neurons drive the acute outburst of pain following peripheral axotomy. *Sci Rep* 2019, 9: 7651.
17. Decosterd I, Woolf CJ. Spared nerve injury: an animal model of persistent peripheral neuropathic pain. *Pain* 2000, 87: 149–158.
18. Bennett GJ, Xie YK. A peripheral mononeuropathy in rat that produces disorders of pain sensation like those seen in man. *Pain* 1988, 33: 87–107.
19. Ma C, LaMotte RH. Multiple sites for generation of ectopic spontaneous activity in neurons of the chronically compressed dorsal root ganglion. *J Neurosci* 2007, 27: 14059–14068.
20. Donelan J, Boucher W, Papadopoulou N, Lytinas M, Papaliadis D, Dobner P, *et al.* Corticotropin-releasing hormone induces skin vascular permeability through a neurotensin-dependent process. *Proc Natl Acad Sci U S A* 2006, 103: 7759–7764.
21. Kuwabara S, Yuki N. Axonal Guillain-Barré syndrome: concepts and controversies. *Lancet Neurol* 2013, 12: 1180–1188.
22. Tesfaye S, Boulton AJ, Dyck PJ, Freeman R, Horowitz M, Kempner P, *et al.* Diabetic neuropathies: update on definitions, diagnostic criteria, estimation of severity, and treatments. *Diabetes Care* 2010, 33: 2285–2293.
23. Zhu YL, Xie ZL, Wu YW, Duan WR, Xie YK. Early demyelination of primary A-fibers induces a rapid-onset of neuropathic pain in rat. *Neuroscience* 2012, 200: 186–198.
24. Radhakrishnan R, Sluka KA. Deep tissue afferents, but not cutaneous afferents, mediate transcutaneous electrical nerve stimulation-induced antihyperalgesia. *J Pain* 2005, 6: 673–680.
25. Haker E, Lundeberg T. Acupuncture treatment in epicondylalgia: a comparative study of two acupuncture techniques. *Clin J Pain* 1990, 6: 221–226.
26. Melzack R, Wall PD. Pain mechanisms: a new theory. *Science* 1965, 150: 971–979.
27. Powell JJ, Todd AJ. Light and electron microscope study of GABA-immunoreactive neurones in lamina III of rat spinal cord. *J Comp Neurol* 1992, 315: 125–136.
28. Sivilotti L, Woolf CJ. The contribution of GABAA and glycine receptors to central sensitization: disinhibition and touch-evoked allodynia in the spinal cord. *J Neurophysiol* 1994, 72: 169–179.
29. Takahashi A, Mashimo T, Uchida I. GABAergic tonic inhibition of substantia gelatinosa neurons in mouse spinal cord. *Neuroreport* 2006, 17: 1331–1335.
30. Willis WD. Dorsal root potentials and dorsal root reflexes: a double-edged sword. *Exp Brain Res* 1999, 124: 395–421.



Angiotensin Type 1 Receptors and Superoxide Anion Production in Hypothalamic Paraventricular Nucleus Contribute to Capsaicin-Induced Excitatory Renal Reflex and Sympathetic Activation

Yun Qiu¹ · Fen Zheng¹ · Chao Ye¹ · Ai-Dong Chen¹ · Jue-Jin Wang¹ · Qi Chen² · Yue-Hua Li² · Yu-Ming Kang³ · Guo-Qing Zhu^{1,2}

Received: 23 June 2019 / Accepted: 15 October 2019 / Published online: 27 January 2020
© Shanghai Institutes for Biological Sciences, CAS 2020

Abstract Chemical stimulation of the kidney increases sympathetic activity and blood pressure in rats. The hypothalamic paraventricular nucleus (PVN) is important in mediating the excitatory renal reflex (ERR). In this study, we examined the role of molecular signaling in the PVN in mediating the capsaicin-induced ERR and sympathetic activation. Bilateral PVN microinjections were performed in rats under anesthesia. The ERR was elicited by infusion of capsaicin into the cortico-medullary border of the right kidney. The reflex was evaluated as the capsaicin-induced changes in left renal sympathetic nerve activity and mean arterial pressure. Blockade of angiotensin type 1 receptors with losartan or inhibition of angiotensin-converting enzyme with captopril in the PVN abolished the capsaicin-induced ERR. Renal infusion of capsaicin significantly increased NAD(P)H oxidase activity and superoxide anion production in the PVN, which were prevented by ipsilateral renal denervation or microinjection of losartan into the PVN. Furthermore, either scavenging of superoxide anions or inhibition of NAD(P)H oxidase in the PVN abolished the capsaicin-induced ERR. We conclude that the ERR induced by renal infusion of capsaicin is

mediated by angiotensin type 1 receptor-related NAD(P)H oxidase activation and superoxide anion production within the PVN.

Keywords Renal reflex · Sympathetic activity · Blood pressure · Paraventricular nucleus · Angiotensin · Reactive oxygen species

Introduction

Sympathetic over-activity contributes to the development of chronic heart failure, hypertension, and chronic kidney disease [1–3], and the kidneys play important roles in the sympathetic activation in these diseases [4, 5]. It is well known that the renal nerve contains both afferents and efferents. Chemoreceptors in the kidney can be activated by capsaicin, bradykinin, adenosine, and hypertonic NaCl in the renal tissue and pelvis, while mechanoreceptors mainly respond to changes in pelvic pressure [6]. The renal afferent sensory signals contribute to the sympathetic activation in hypertension and chronic heart failure [7, 8]. Renal denervation has been used as an interventional approach to chronic kidney disease and some cardiovascular diseases [9, 10]. Recently, we showed that renal infusion of capsaicin, angiotensin II (Ang II), bradykinin, or adenosine activates renal afferents, and then causes increases in sympathetic activity and blood pressure, indicating that chemical stimulation of the kidney results in an excitatory renal reflex (ERR) in rats, resulting in sympathetic activation and pressor responses [11].

Afferent activity from the kidneys is closely associated with several brain sites involved in the modulation of cardiovascular and sympathetic activity, including the nucleus of the solitary tract, rostral ventrolateral medulla,

✉ Guo-Qing Zhu
gqzhucn@njmu.edu.cn

¹ Key Laboratory of Targeted Intervention of Cardiovascular Disease, Collaborative Innovation Center of Translational Medicine for Cardiovascular Disease, and Department of Physiology, Nanjing Medical University, Nanjing 211166, China

² Department of Pathophysiology, Nanjing Medical University, Nanjing 211166, China

³ Department of Physiology and Pathophysiology, Cardiovascular Research Center, Xi'an Jiaotong University School of Medicine, Xi'an 710061, China

paraventricular nucleus of the hypothalamus (PVN), pre-optic area, and subfornical organ [4]. The PVN receives inputs from various visceral receptors including arterial baroreceptors and pulmonary/cardiac vagal afferents [12], cardiac sympathetic afferents [13], adipose afferents [14], and renal afferents [11]. The PVN is critical in the integration and regulation of sympathetic and cardiovascular activity by sending its descending projections to the rostral ventrolateral medulla and spinal intermediolateral column [15, 16]. Renal afferent inputs increase sympathetic activity [7], and renal nerve stimulation excites some neurons in the PVN [17]. An imbalance of excitatory and inhibitory synaptic inputs in the PVN is the basis of the enhanced sympathetic activity in hypertension [7, 18]. We recently showed that chemical stimulation of the kidneys promotes c-Fos expression in the PVN, and lesioning PVN neurons with kainic acid abolishes the sympathetic activation and pressor responses to renal infusion of capsaicin, suggesting that the PVN is a crucial central nucleus in the ERR pathway [11]. Angiotensin type 1 receptors (AT₁Rs) are densely distributed in the PVN, and are involved in the control of sympathetic activity [19, 20]. We previously showed that AT₁Rs in the PVN mediate the cardiac sympathetic afferent reflex (CSAR), a sympatho-excitatory reflex induced by chemical stimulation of sympathetic afferent endings innervating the heart [13, 21]. Both N-methyl-D-aspartate receptors (NMDARs) and non-NMDARs in the PVN mediate the adipose afferent reflex (AAR), by which afferent activity from white adipose tissue increases sympathetic outflow and blood pressure [22]. However, the molecular signaling in the PVN that mediates the ERR was not known. The aim of this study was to determine the molecular signaling mechanism in the PVN that mediates the ERR.

Methods

Animals and General Procedures

Experiments were carried out on 196 male Sprague-Dawley rats weighing 280 g–320 g. The experimental procedures were approved by the Experimental Animal Care and Use Committee, and complied with the Guide for the Care and Use of Laboratory Animals. The animals were kept under a 12-h dark-light cycle with free access to tap water and chow. The experiments were performed on rats anaesthetized by intraperitoneal injection of α -chloralose (40 mg/kg) combined with urethane (800 mg/kg). Corneal and paw withdrawal reflexes were used to assess the depth of anesthesia [23]. The right carotid artery and trachea were exposed *via* a midline neck incision, the trachea was cannulated, and positive-pressure ventilation was applied

with a small animal ventilator (model 51600, Stoelting, Chicago, IL). The right carotid artery was cannulated to record pressure. The blood pressure, heart rate, and renal sympathetic nerve activity (RSNA) were simultaneously recorded with a data acquisition system (8SP, ADInstruments, Bella Vista, NSW, Australia). Following the surgery, the animal was allowed to stabilize for at least 30 min. At the end of each experiment, animals were euthanized by overdose with pentobarbital sodium (100 mg/kg, *i.v.*).

PVN Microinjection

Each rat was fixed prone in a stereotaxic frame (Stoelting, Chicago, IL). The coordinates for microinjections into the PVN were 1.8 mm caudal to bregma, 0.4 mm lateral to the midline, and 7.9 mm below the dorsal surface [21]. Glass micropipettes with tip size 50 μ m were used for bilateral PVN microinjections of 50 nL on each side completed in 1 min. After experiments, the same volume of Evans Blue was microinjected into the PVN for histological identification of the injection sites [24]. The visible spread of dye was < 300 μ m in diameter. Data were excluded for microinjection sites outside the PVN.

RSNA Recording

Recordings were made for the left RSNA as we reported previously [25]. Briefly, the left flank was incised to expose the renal artery and nerve. The nerve was carefully isolated and cut at its distal end to abolish afferent activity. The central end of the nerve was laid on silver electrodes immersed in mineral oil at 37°C and its activity was amplified with a band-pass filter at 100–3000 Hz using a differential amplifier (model DP-304, Warner Instruments, Hamden, CT). The signals were integrated at a 100-ms time constant using LabChart 8 (ADInstruments). After each experiment, the background noise was recorded after cutting the central end of the nerve. The RSNA value was calculated as the measured RSNA value minus the background noise value. The effects of chemicals on RSNA were calculated as a percentage change of the control value.

Renal Infusion of Capsaicin to Induce the ERR

As we previously reported, the ERR was elicited by renal infusion of capsaicin [11]. Briefly, the right flank was incised to expose the right kidney. A stainless-steel tube (0.31 mm OD) was horizontally inserted into the kidney from right to left for renal infusion. The insertion was stopped when the tube encountered a slight resistance, indicating that its tip had reached the cortico-

medullary border, about 2 mm below the renal surface. The outer end of the tube was connected to a programmable pressure injector (Model PM2000B, MDI Inc., Lakewood, NJ) through a PE50 polyethylene catheter. The ERR was elicited by infusion of capsaicin (1 nmol/ μ L) into the kidney at 1.0 μ L/min for 20 min. An equal amount of vehicle was infused as a control. The ERR was evaluated by the capsaicin-induced RSNA and mean arterial pressure (MAP) responses.

Measurement of Superoxide Anions and NAD(P)H Oxidase Activity

Coronal sections 450 μ m thick were cut at the PVN level on a cryostat microtome (Model CM1900, Leica, Wetzlar, Germany), and the bilateral PVN areas were punched out using a 15-gauge needle. The punched tissue was homogenized and centrifuged in lysis buffer. Total protein concentration was determined with the Bradford assay (BCA; Pierce, Santa Cruz, CA).

Superoxide anion content was assessed by the lucigenin-derived chemiluminescence method [26–28]; the photon emission was started by adding dark-adapted lucigenin (5 μ mol/L). NAD(P)H oxidase activity was determined by the same method [29–31]; the photon emission was started by adding both dark-adapted lucigenin and NAD(P)H (100 μ mol/L). Light emission was measured ten times in 10 min using a luminometer (Model 20/20n, Turner, CA). The values were expressed as relative mean light units/min per mg protein. Background chemiluminescence in the buffer containing lucigenin (5 μ mol/L) was also measured.

Detection of Superoxide Anions in the PVN

Superoxide anions in the PVN were detected with the specific fluorogenic probe dihydroethidium (DHE), as we reported previously [32, 33]. Experimental samples and corresponding control samples were processed in parallel. The settings of the detector and laser were kept constant during experiments. The DHE fluorescence was detected under a fluorescence microscope (DP70, Olympus Optical, Tokyo, Japan).

Chemicals

Capsaicin was from MedChem Express (Monmouth Junction, NJ). Ang II, losartan, captopril, tempol, apocynin, N-acetylcysteine (NAC), diethyldithiocarbamic acid (DETC), capsazepine, diphenyleiiodonium (DPI), and allopurinol were from Sigma (St. Louis, MO). AP5 and CNQX were from Apexbio (Houston, TX). Capsaicin, captopril, apocynin, or DPI was dissolved in PBS with 1% DMSO. The vehicle (Veh) was used as control. All other

chemicals were dissolved in PBS, and PBS served as control. The concentrations of losartan, captopril, and other compounds were selected according to their dose-effect relationships or our previous data [21, 24].

Statistics

RSNA and MAP changes were assessed by averaging the values for 1 min at the maximal chemically-induced responses. The statistical significance of differences between groups was evaluated by one-way analysis of variance (ANOVA) followed by the Bonferroni *post hoc* test. Data are expressed as the mean \pm SEM. A *P*-value < 0.05 was considered statistically significant.

Results

Effects of Ang II, Losartan, and Captopril on the ERR

Microinjection of PBS, Ang II (0.3 nmol), losartan (10 nmol), or captopril (10 nmol) into the PVN was carried out 10 min before renal infusion of vehicle or capsaicin (1 nmol/min, 20 min). The renal infusion site, rate, and duration as well as the dose of capsaicin were determined based on our previous study [11]. Representative recordings showed that renal infusion of capsaicin induced the ERR, as evidenced by increased RSNA and MAP (Fig. 1A), which were prevented by pretreatment of the PVN with losartan, an antagonist of AT₁Rs (Fig. 1B). Microinjection of Ang II into the PVN increased the baseline RSNA and MAP, but losartan or the angiotensin-converting enzyme inhibitor captopril had no significant effects on these baseline values (Fig. 2A). To compare the renal infusion-induced RSNA and MAP changes, they were calculated as the difference between the values before and after the renal infusion. Microinjection of Ang II into the PVN failed to have a greater effect on the capsaicin-induced RSNA and MAP changes than those caused by microinjection of PBS (RSNA: + 14.1% \pm 3.5% versus + 18.2% \pm 2.3%, *P* > 0.05; MAP: + 5.9 \pm 1.5 mmHg vs + 8.1 \pm 2.0 mmHg, *P* > 0.05; Fig. 2B). To compare the RSNA and MAP changes caused by PVN microinjection plus renal infusion, the total RSNA and MAP changes were calculated as the difference between the values before the PVN microinjection and those after the renal infusion. The total RSNA and MAP changes due to PVN microinjection of Ang II plus renal infusion of capsaicin were also not significantly greater than those caused by PVN microinjection of PBS plus renal infusion of capsaicin (RSNA: + 23.5% \pm 3.6% vs + 18.9% \pm 3.6%, *P* > 0.05; MAP: + 11.7 \pm 1.7 mmHg vs + 8.0 \pm 1.8 mmHg, *P* > 0.05). Importantly, the capsaicin-induced ERR was

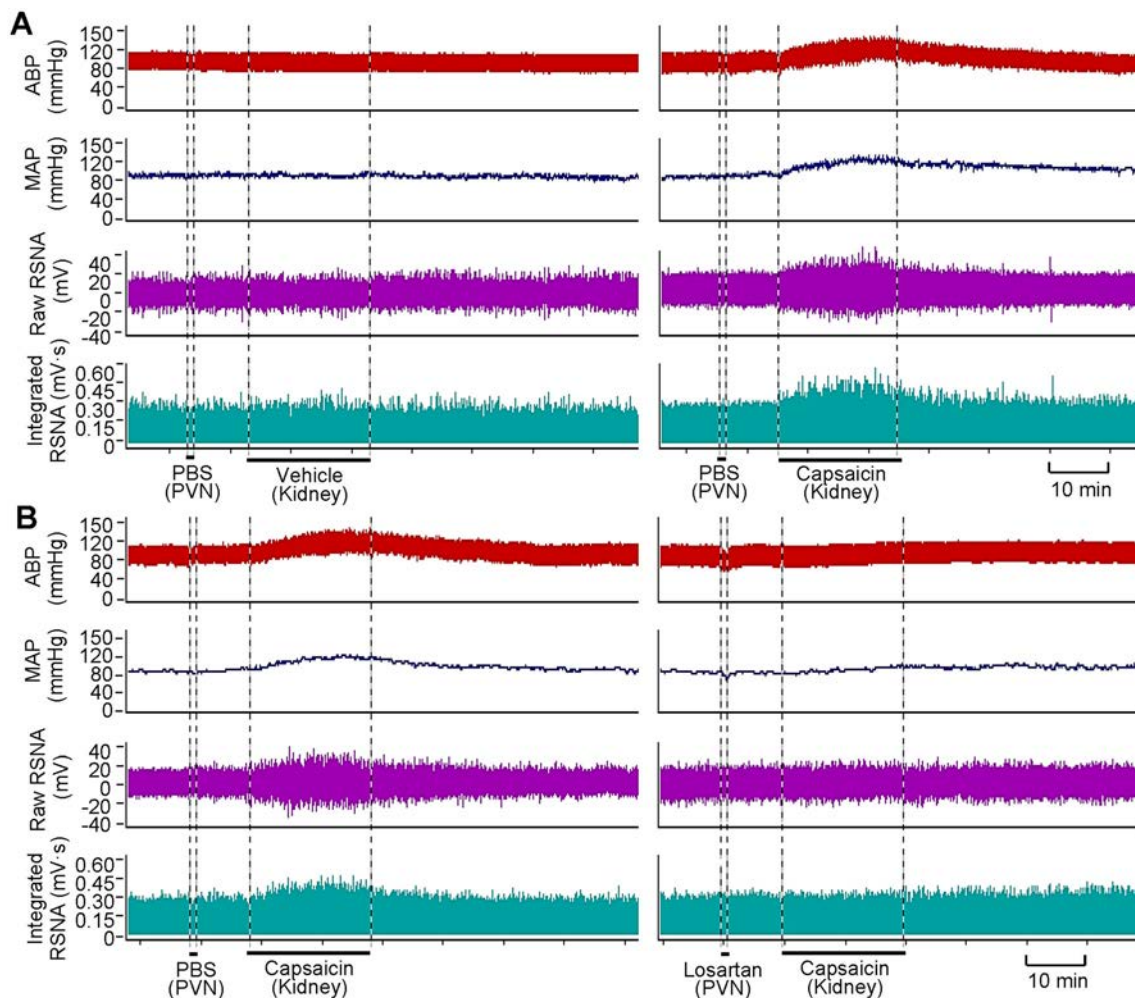


Fig. 1 Representative recordings showing the capsaicin-induced excitatory renal reflex. **A** Renal infusion of capsaicin at 1 nmol/min for 20 min causes reflex changes of arterial blood pressure (ABP), mean arterial pressure (MAP) and contralateral renal sympathetic

nerve activity (RSNA). **B** Effect of pretreatment with PVN microinjection of losartan (10 nmol) on the reflex. The pretreatment was carried out 10 min before renal infusion of vehicle (PBS) or capsaicin.

almost abolished by PVN pretreatment with losartan or captopril (Fig. 2B). These findings suggest that the capsaicin-induced ERR is mediated by Ang II and its AT₁Rs in the PVN. Microinjection of losartan into anterior hypothalamic areas close to the PVN failed to abolish the ERR, suggesting that the effect of losartan on the ERR is not due to diffusion.

Effects of Tempol, NAC, and DETC on the ERR

Our previous study has shown that reactive oxygen species (ROS) in the PVN mediate the effect of Ang II on the CSAR in hypertensive rats [24]. In this study, microinjection of PBS, tempol (20 nmol), NAC (40 nmol), or DETC (10 nmol) into the PVN was carried out 10 min before renal infusion of vehicle or capsaicin (1 nmol/min, 20 min). Microinjection of the ROS scavenger tempol or NAC into

the PVN reduced the baseline RSNA and MAP values, while DETC, a superoxide dismutase inhibitor, increased these values (Fig. 3A). The capsaicin-induced ERR was almost abolished by pretreatment with PVN microinjection of tempol or NAC. Microinjection of DETC into the PVN failed to have greater effects on the capsaicin-induced RSNA and MAP changes than those caused by microinjection of PBS (RSNA: $+12.7\% \pm 2.7\%$ vs $+17.9\% \pm 3.3\%$, $P > 0.05$; MAP: $+5.4 \pm 1.7$ mmHg vs $+8.0 \pm 1.7$ mmHg, $P > 0.05$; Fig. 3B). The total RSNA and MAP changes due to PVN microinjection of DETC plus renal infusion of capsaicin were significantly greater than those caused by PVN microinjection of PBS plus renal infusion of capsaicin (RSNA: $+29.6\% \pm 3.5\%$ vs $+19.4\% \pm 2.8\%$, $P < 0.05$; MAP: $+11.9 \pm 1.4$ mmHg vs $+7.1 \pm 1.4$ mmHg, $P < 0.05$). These results suggest that superoxide anions in the PVN mediate the capsaicin-induced ERR.

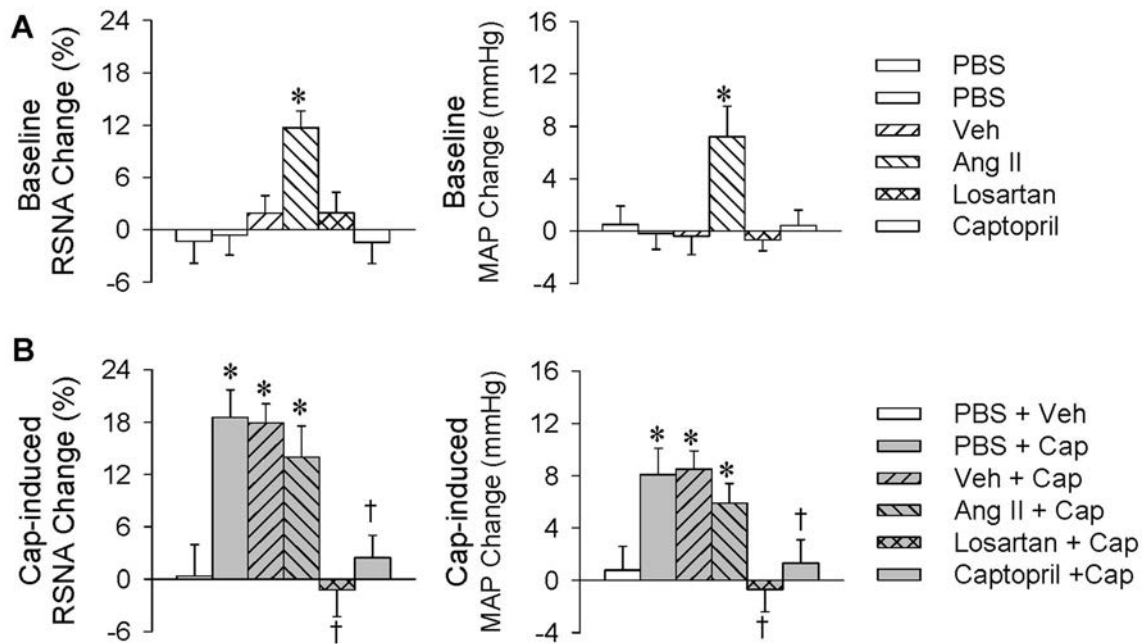


Fig. 2 Roles of Ang II in the PVN in the capsaicin-induced excitatory renal reflex. The reflex was induced by renal infusion of capsaicin (Cap) at 1 nmol/min for 20 min. The PVN microinjection was carried out 10 min before renal infusion. **A** Baseline RSNA and MAP changes caused by the PVN microinjection of Ang II (0.3

nmol), losartan (10 nmol), or captopril (10 nmol) ($*P < 0.05$ vs PBS or Veh). **B** Effects of PVN microinjection of Ang II, losartan, or captopril on the capsaicin-induced reflex ($*P < 0.05$ vs PBS + Veh; $†P < 0.05$ vs PBS + Cap or Veh + Cap). Values are the mean \pm SEM; $n = 6$ per group.

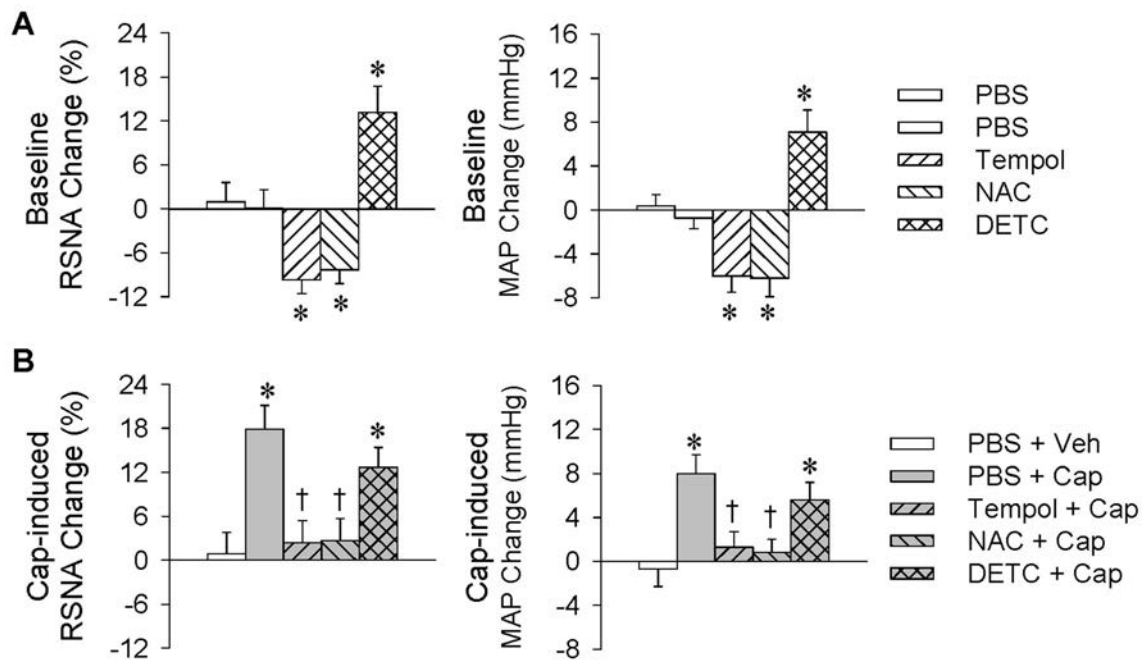


Fig. 3 Roles of reactive oxygen species in the PVN in the capsaicin-induced excitatory renal reflex. The reflex was induced by renal infusion of capsaicin (Cap) at 1 nmol/min for 20 min. The PVN microinjection was carried out 10 min before renal infusion. **A** Baseline RSNA and MAP changes caused by the PVN

microinjection of tempol (20 nmol), NAC (40 nmol), or DETC (10 nmol) ($*P < 0.05$ vs PBS). **B** Effects of PVN microinjection of tempol, NAC, or DETC on the reflex ($*P < 0.05$ vs PBS + Veh; $†P < 0.05$ vs PBS + Cap). Values are the mean \pm SEM; $n = 6$ per group.

Effects of Losartan and Renal Denervation on Superoxide Anion Production

Superoxide anion production in the PVN was determined in order to provide further evidence about their importance in mediating the capsaicin-induced ERR. The PVN microinjection of PBS or losartan (10 nmol) was carried out 10 min before renal infusion of capsaicin (1 nmol/min for 20 min), and tissue samples for measurements were prepared immediately after the infusion. Renal infusion of capsaicin promoted superoxide anion production in the bilateral PVN, and this was prevented by bilateral losartan pretreatment (Fig. 4A and B). Furthermore, right renal denervation (RD) was carried out 60 min before ipsilateral renal infusion of capsaicin, and tissue samples were prepared immediately afterwards. Ipsilateral RD abolished the increase in superoxide anions in the bilateral PVN elicited by renal infusion of capsaicin, indicating that this superoxide anion production mediates the effects of renal infusion of capsaicin *via* afferent signals from the kidney rather than changes in circulating hormones or other secondary effects (Fig. 4C).

Effects of Apocynin, DPI, and Allopurinol

Inhibitors of NAD(P)H oxidase and xanthine oxidase were each used to determine the origin of superoxide anions in the PVN. Microinjection of PBS, vehicle, apocynin (1 nmol), DPI (1.5 nmol), or allopurinol (10 nmol) into the PVN was carried out 10 min before renal infusion of vehicle or capsaicin (1 nmol/min, 20 min). Microinjection of the NAD(P)H oxidase inhibitor apocynin or DPI reduced the baseline RSNA and MAP, but the xanthine oxidase inhibitor allopurinol had no significant effects on these values (Fig. 5A). Bilateral microinjection of apocynin or DPI attenuated the capsaicin-induced ERR, while allopurinol had no significant effect (Fig. 5B). These results suggest that the capsaicin-induced ERR involves NAD(P)H oxidase rather than xanthine oxidase in the PVN.

Effects of Losartan and Renal Denervation on NAD(P)H Oxidase Activity

Microinjection of PBS, losartan (10 nmol), or apocynin (1 nmol) into the PVN was carried out 10 min before renal infusion of vehicle or capsaicin (1 nmol/min, 20 min). A right RD was carried out 60 min before the ipsilateral renal infusion and tissue samples were prepared immediately afterwards. Renal infusion of capsaicin increased NAD(P)H oxidase activity in the bilateral PVN, and this was prevented by bilateral losartan pretreatment (Fig. 6A). Ipsilateral RD abolished the NAD(P)H oxidase activation in the bilateral PVN induced by renal infusion of capsaicin

(Fig. 6B). Moreover, pretreatment with apocynin abolished the capsaicin-induced superoxide anion production in the PVN (Fig. 6C). These results indicate that the NAD(P)H oxidase is responsible for the capsaicin-induced production of superoxide anions in the PVN.

Effects of PVN Microinjection of AP5 or CNQX, or Renal Infusion of Capsazepine, on the ERR

Ionotropic glutamate receptors are divided into NMDARs and non-NMDARs. Our previous studies have shown that both types in the PVN mediate the AAR [22], so it was of interest to determine whether they are also involved in the ERR. Renal infusion of capsaicin (1 nmol/min, 20 min) was carried out to induce the ERR 10 min after treatment with the NMDAR antagonist AP5 (9 nmol) or the non-NMDAR antagonist CNQX (9 nmol). We found that either AP5 or CNQX inhibited the baseline RSNA and reduced the baseline blood pressure (Fig. 7A), but had no significant effect on the ERR (Fig. 7B). These results indicate that ionotropic glutamate receptors are not involved in the capsaicin-induced ERR. On the other hand, transient receptor potential vanilloid subtype 1 receptors (TRPV1Rs) act as sensory mediators, and are activated by capsaicin, heat, and endogenous ligands [34–36]. We therefore used capsazepine, a competitive antagonist of TRPV1Rs to determine whether the capsaicin-induced ERR is mediated by these receptors. Capsaicin (1 nmol/min for 20 min) was infused into the kidney to induce the ERR immediately after the renal infusion of capsazepine (20 nmol/min for 10 min). Capsazepine had no significant effect on the baseline RSNA and MAP (Fig. 7C), but almost completely abolished the ERR (Fig. 7D), suggesting that the capsaicin-induced ERR is mediated by renal TRPV1Rs.

Discussion

We recently showed that chemical stimulation of the kidney with capsaicin elicits the ERR, leading to increases in sympathetic activity and blood pressure. Stimulation of renal afferents with capsaicin promotes c-Fos expression in the bilateral PVN, while lesioning of the bilateral PVN with kainic acid abolishes this capsaicin-induced reflex. Thus, the PVN is an important component of the ERR neural circuitry [11]. The primary novel findings in this study are that the ERR induced by renal infusion of capsaicin is mediated by AT₁Rs in the hypothalamic PVN. AT₁R-dependent NAD(P)H oxidase activation and superoxide anion production in the PVN contribute to the ERR.

It is known that Ang II in the PVN causes sympathetic activation and a pressor response *via* the activation of AT₁Rs [37]. Abundant AT₁Rs have been found in the

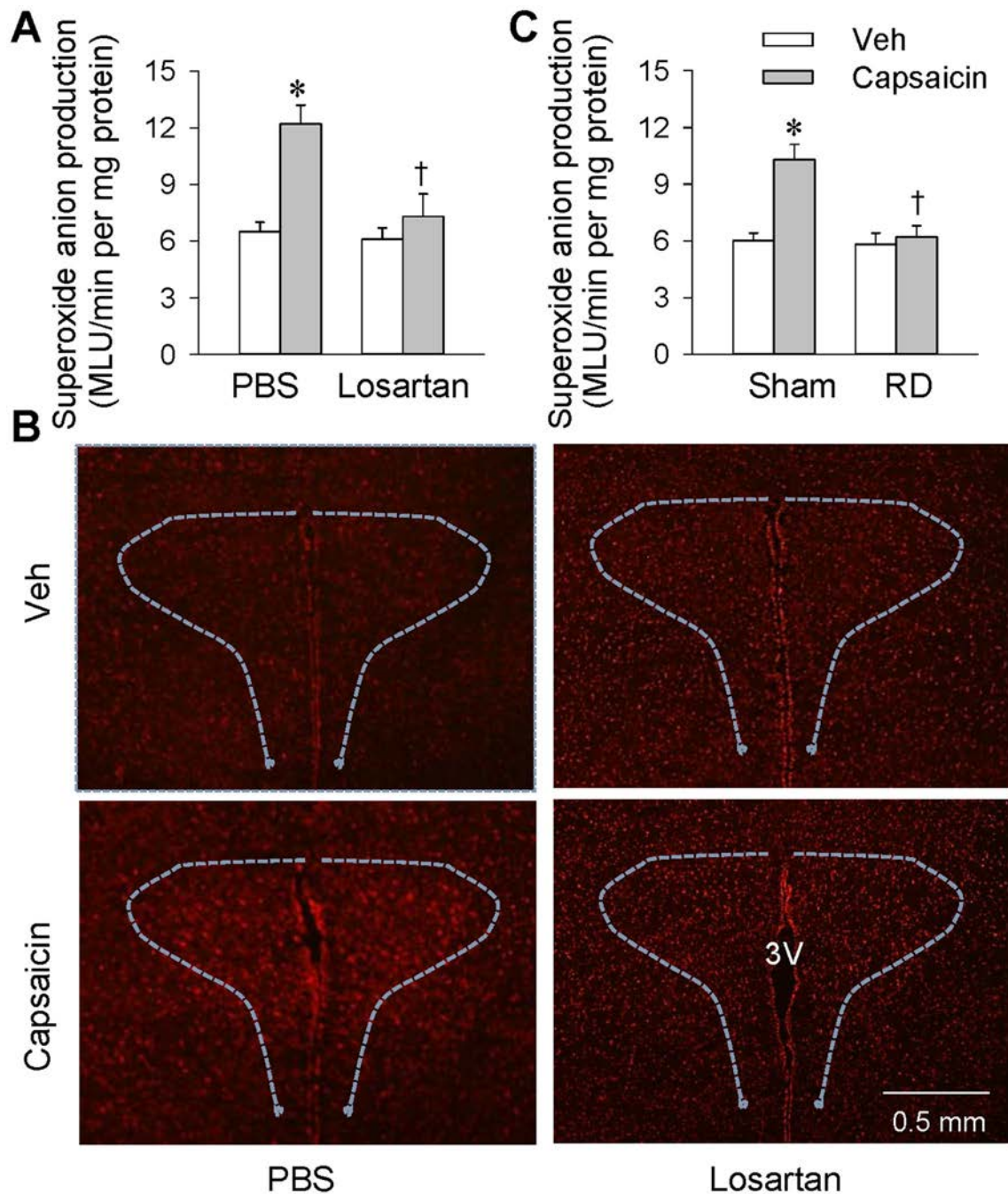


Fig. 4 Effects of losartan and renal denervation (RD) on superoxide anion production in the PVN. **A** Effects of PVN microinjection of losartan (10 nmol) or PBS 10 min before renal infusion of capsaicin at 1 nmol/min for 20 min (* $P < 0.05$ vs Veh; † $P < 0.05$ vs PBS). **B** Representative images of dihydroethidium staining showing the

bilateral PVN [38], and they are upregulated in chronic heart failure [39] and hypertension [21]. We found that blockade of AT_1 Rs or inhibition of Ang II production in the PVN abolished the ERR, indicating that the reflex is mediated by endogenous Ang II and AT_1 Rs in the PVN. Although PVN microinjection of Ang II increased the

changes in ROS levels in the PVN after renal infusion of capsaicin. **C** Effects of right RD 60 min before ipsilateral renal infusion of capsaicin (* $P < 0.05$ vs Veh; † $P < 0.05$ vs Sham). Values are the mean \pm SEM; $n = 6$ per group.

baseline RSNA and MAP, it failed to further augment the sympathetic activation and pressor response induced by renal infusion of capsaicin. A possible explanation is that, given the administration of exogenous Ang II, release of endogenous Ang II due to renal infusion of capsaicin may be unable to induce a further large increase in the Ang II

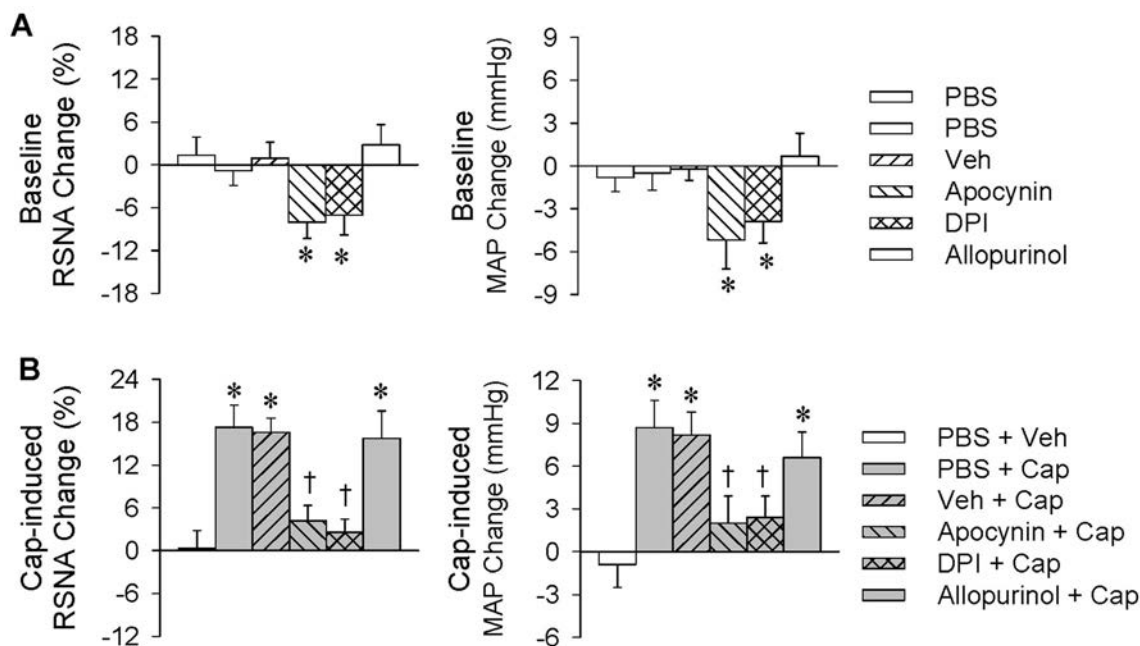
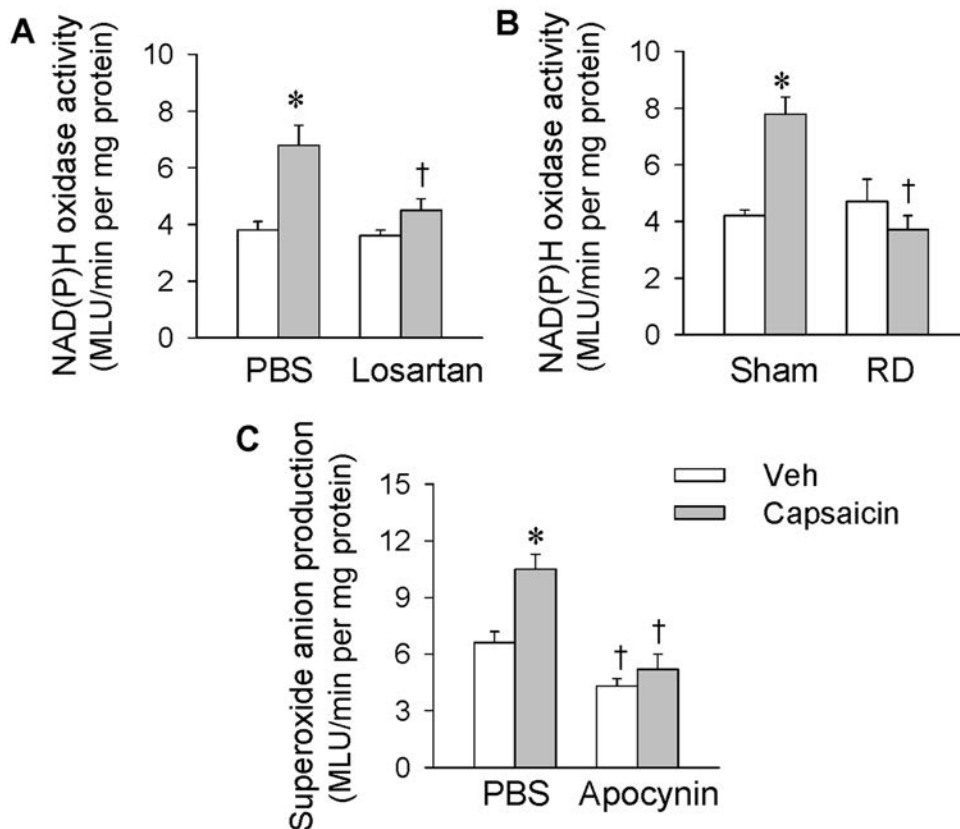


Fig. 5 Roles of NAD(P)H oxidase in the PVN in the capsaicin-induced excitatory renal reflex. The reflex was induced by renal infusion of capsaicin (Cap) at 1 nmol/min for 20 min. The PVN microinjection was carried out 10 min before renal infusion. **A** Baseline RSNA and MAP changes caused by PVN microinjection

of apocynin (1 nmol), DPI (1.5 nmol), or allopurinol (10 nmol) ($*P < 0.05$ vs PBS or Veh). **B** Effects of PVN microinjection of apocynin, DPI, or allopurinol on the reflex ($*P < 0.05$ vs PBS + Veh; $†P < 0.05$ vs PBS + Cap). Values are the mean \pm SEM; $n = 6$ per group.

Fig. 6 Effects of losartan and renal denervation (RD) on NAD(P)H oxidase activity in the PVN and effects of apocynin on superoxide anion production in the PVN. Renal infusion of capsaicin was carried out at 1 nmol/min for 20 min. **A** Effects of PVN microinjection of losartan on NAD(P)H oxidase activity in the PVN. The microinjection of PBS or losartan (10 nmol) was carried out 10 min before renal infusion of capsaicin. **B** Effects of right RD on NAD(P)H oxidase activity in the PVN. The RD was carried out 60 min before ipsilateral renal infusion of capsaicin. **C** Effects of apocynin on the capsaicin-induced superoxide anion production in the PVN ($*P < 0.05$ vs Veh; $†P < 0.05$ vs PBS or Sham; MLU, mean light units). Values are the mean \pm SEM; $n = 6$ per group.



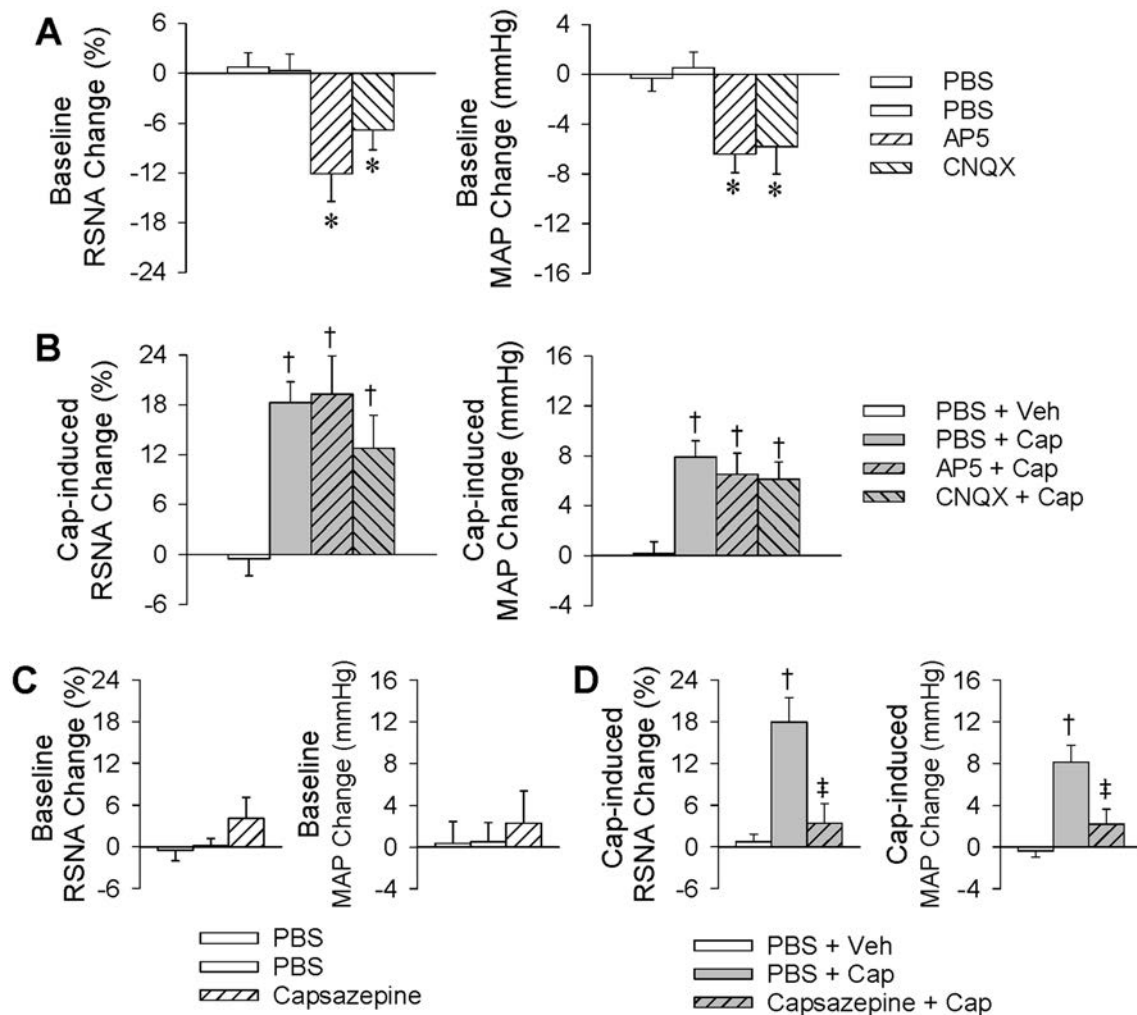


Fig. 7 Effects of PVN microinjection of AP5 or CNQX, or renal infusion of capsazepine, on the capsaicin-induced excitatory renal reflex. The reflex was induced by renal infusion of capsaicin (Cap) at 1 nmol/min for 20 min. **A** Baseline RSNA and MAP changes caused by PVN microinjection of AP5 (9 nmol) or CNQX (9 nmol). **B** Effects of PVN microinjection of AP5 or CNQX on the capsaicin-induced reflex. The PVN microinjection was carried out 10 min

before renal infusion. **C** Baseline RSNA and MAP changes caused by the renal infusion of capsazepine. **D** Effects of renal infusion of capsazepine on the reflex. Renal infusion of Veh or capsaicin for 20 min was carried out immediately after renal infusion of PBS or capsazepine for 10 min (* $P < 0.05$ vs PBS; † $P < 0.05$ vs PBS + Veh; ‡ $P < 0.05$ vs PBS + Cap). Values are the mean \pm SEM; $n = 6$ per group.

content of the PVN. This might be why the total changes caused by the PVN microinjection of Ang II plus renal infusion of capsaicin were not significantly greater than those caused by Ang II or capsaicin alone. These results support the idea that Ang II in the PVN is involved in the ERR. It has been shown that Ang II and AT_1 Rs in the PVN mediate the CSAR [40], but this does not mean that most sympatho-excitatory reflexes due to peripheral afferent activity are mediated by Ang II and its AT_1 Rs in the PVN. An exception is that the AAR induced by infusion of capsaicin into white adipose tissue causes sympathetic activation that is mediated by ionotropic glutamate receptors in the PVN rather than AT_1 Rs [22].

Tempol mimics the role of superoxide dismutase in scavenging superoxide anions [41], and NAC is another antioxidant with superoxide scavenging properties [42]. Ang II is an important stimulus for superoxide anion production in the brain [43] and vasculature [44], and superoxide anion production in the PVN plays a role in the sympathetic activation in hypertension [45]. Furthermore, our previous study has shown that superoxide anions in the PVN contribute to the enhanced CSAR in chronic heart failure [25], so we further investigated whether this mechanism is involved in the ERR. PVN microinjection of tempol or NAC reduced the baseline RSNA and MAP, and prevented the capsaicin-induced ERR. Inhibition of superoxide dismutase with DETC increased the baseline

RSNA and MAP rather than the capsaicin-induced ERR. However, the total RSNA and MAP responses to DETC plus capsaicin were significantly greater than those caused by Ang II or capsaicin alone. More importantly, renal infusion of capsaicin increased superoxide anion production in the PVN, which was prevented by pretreatment with bilateral microinjection of losartan into the PVN or ipsilateral renal denervation. These findings provide evidence that the capsaicin-induced ERR is mediated by the AT₁R activation-dependent production of superoxide anion in the PVN.

NAD(P)H oxidase is expressed in neurons throughout the brain [46], and ROS derived from it play a major role in Ang II signaling [47]. Apocynin prevents the assembly of NAD(P)H oxidase, thereby inhibiting its oxidase activity and superoxide anion formation [48]. Inhibition of NAD(P)H oxidase with apocynin in the PVN reduced the baseline RSNA and MAP, and almost completely abolished the ERR. Similar results were obtained after PVN microinjection of another NAD(P)H oxidase, DPI. However, inhibition of xanthine oxidase with allopurinol in the PVN had no significant effects on the ERR. Renal infusion of capsaicin increased NAD(P)H oxidase activity in the PVN, which was prevented by the bilateral microinjection of losartan or ipsilateral RD. Furthermore, apocynin abolished the superoxide anion production induced by renal infusion of capsaicin. These findings indicate that NAD(P)H oxidase is a key source of the AT₁R-mediated superoxide anion production in the PVN. It is notable that the ERR is mediated by Ang II–AT₁R–NAD(P)H oxidase–ROS rather than NMDARs and non-NMDARs in the PVN, similar to the signaling pathway of the CSAR [21]. However, the signaling pathway of the ERR is different from that of the AAR, which is mediated by both NMDARs and non-NMDARs. In this study, we only focused on the signaling pathway in the PVN, but other central nuclei such as the rostral ventrolateral medulla and the nucleus of the solitary tract may also be involved in the ERR, and this deserves further investigation.

Sympathetic over-activity contributes greatly to the pathogenesis and development of several diseases including chronic kidney disease, chronic heart failure, and hypertension [6]. It has been shown that enhanced renal afferent activity in 2-kidney 1-clip hypertensive mice increases blood pressure and sympathetic nerve activity [49], while renal afferent denervation in the rat prevents the progression of chronic renal failure [50]. Chronic intermittent hypobaric hypoxia attenuates renal vascular hypertension [51], while renal afferent signaling plays a role in chronic intermittent hypoxia-induced hypertension, which is involved in human obstructive sleep apnea syndrome [52]. Increased afferent activity from the kidney might play important roles in the sympathetic over-activity in these

diseases, and this needs further investigation. Ang II, AT₁Rs, NAD(P)H oxidase and superoxide anion production in the PVN may be critical targets in interventions for ERR-related sympathetic activation, and might attenuate some cardiovascular diseases with excessive sympathetic activation.

In conclusion, the capsaicin-induced ERR is mediated by Ang II and AT₁Rs, and their downstream production of NAD(P)H oxidase-derived superoxide anion in the PVN.

Acknowledgements This work was supported by the National Natural Science Foundation of China (31871148, 91639105, 31571167, and 31571168).

Conflict of interest The authors declare no competing or financial interests.

References

1. Grassi G, Ram VS. Evidence for a critical role of the sympathetic nervous system in hypertension. *J Am Soc Hypertens* 2016, 10: 457–466.
2. Zhang DY, Anderson AS. The sympathetic nervous system and heart failure. *Cardiol Clin* 2014, 32: 33–45.
3. Kaur J, Young BE, Fadel PJ. Sympathetic overactivity in chronic kidney disease: consequences and mechanisms. *Int J Mol Sci* 2017, 18: E1682.
4. Kopp UC. Role of renal sensory nerves in physiological and pathophysiological conditions. *Am J Physiol Regul Integr Comp Physiol* 2015, 308: R79–R95.
5. Bie P, Evans RG. Normotension, hypertension and body fluid regulation: brain and kidney. *Acta Physiol (Oxf)* 2017, 219: 288–304.
6. Frame AA, Carmichael CY, Wainford RD. Renal afferents. *Curr Hypertens Rep* 2016, 18: 69.
7. Zheng H, Patel KP. Integration of renal sensory afferents at the level of the paraventricular nucleus dictating sympathetic outflow. *Auton Neurosci* 2017, 204: 57–64.
8. Abdulla MH, Johns EJ. The innervation of the kidney in renal injury and inflammation: a cause and consequence of deranged cardiovascular control. *Acta Physiol (Oxf)* 2017, 220: 404–416.
9. Veelken R, Schmieder RE. Renal denervation—implications for chronic kidney disease. *Nat Rev Nephrol* 2014, 10: 305–313.
10. Carlstrom M. Therapeutic value of renal denervation in cardiovascular disease? *Acta Physiol (Oxf)* 2017, 220: 11–13.
11. Ye C, Qiu Y, Zhang F, Chen AD, Zhou H, Wang JJ, *et al.* Chemical stimulation of renal tissue induces sympathetic activation and pressor response *via* hypothalamic paraventricular nucleus. *Neurosci Bull* 2019. <https://doi.org/10.1007/s12264-019-00417-1>.
12. Pyner S. The paraventricular nucleus and heart failure. *Exp Physiol* 2014, 99: 332–339.
13. Chen WW, Xiong XQ, Chen Q, Li YH, Kang YM, Zhu GQ. Cardiac sympathetic afferent reflex and its implications for sympathetic activation in chronic heart failure and hypertension. *Acta Physiol (Oxf)* 2015, 213: 778–794.
14. Xiong XQ, Chen WW, Zhu GQ. Adipose afferent reflex: sympathetic activation and obesity hypertension. *Acta Physiol (Oxf)* 2014, 210: 468–478.
15. Badoer E. The role of the hypothalamic PVN in the regulation of renal sympathetic nerve activity and blood flow during

- hyperthermia and in heart failure. *Am J Physiol Renal Physiol* 2010, 298: F839–F846.
16. Sun J, Ren XS, Kang Y, Dai HB, Ding L, Tong N, *et al.* Intermedin in paraventricular nucleus attenuates sympathoexcitation and decreases TLR4-mediated sympathetic activation via adrenomedullin receptors in rats with obesity-related hypertension. *Neurosci Bull* 2019, 35: 34–46.
 17. Xu B, Zheng H, Liu X, Patel KP. Activation of afferent renal nerves modulates RVLM projecting PVN neurons. *Am J Physiol Heart Circ Physiol* 2015, 308: 1103–1111.
 18. Zhou JJ, Ma HJ, Shao JY, Pan HL, Li DP. Impaired hypothalamic regulation of sympathetic outflow in primary hypertension. *Neurosci Bull* 2019, 35: 124–132.
 19. Cato MJ, Toney GM. Angiotensin II excites paraventricular nucleus neurons that innervate the rostral ventrolateral medulla: an in vitro patch-clamp study in brain slices. *J Neurophysiol* 2005, 93: 403–413.
 20. Yu XJ, Zhao YN, Hou YK, Li HB, Xia WJ, Gao HL, *et al.* Chronic intracerebroventricular infusion of metformin inhibits salt-sensitive hypertension via attenuation of oxidative stress and neurohormonal excitation in rat paraventricular nucleus. *Neurosci Bull* 2019, 35: 57–66.
 21. Chen AD, Zhang SJ, Yuan N, Xu Y, De W, Gao XY, *et al.* AT₁ receptors in paraventricular nucleus contribute to sympathetic activation and enhanced cardiac sympathetic afferent reflex in renovascular hypertensive rats. *Exp Physiol* 2011, 96: 94–103.
 22. Cui BP, Li P, Sun HJ, Ding L, Zhou YB, Wang JJ, *et al.* Iontropic glutamate receptors in paraventricular nucleus mediate adipose afferent reflex and regulate sympathetic outflow in rats. *Acta Physiol (Oxf)* 2013, 209: 45–54.
 23. Zhang LL, Ding L, Zhang F, Gao R, Chen Q, Li YH, *et al.* Salusin-beta in rostral ventrolateral medulla increases sympathetic outflow and blood pressure via superoxide anions in hypertensive rats. *J Hypertens* 2014, 32: 1059–1067.
 24. Han Y, Fan ZD, Yuan N, Xie GQ, Gao J, De W, *et al.* Superoxide anions in paraventricular nucleus mediate the enhanced cardiac sympathetic afferent reflex and sympathetic activity in renovascular hypertensive rats. *J Appl Physiol* 2011, 110: 646–652.
 25. Han Y, Shi Z, Zhang F, Yu Y, Zhong MK, Gao XY, *et al.* Reactive oxygen species in the paraventricular nucleus mediate the cardiac sympathetic afferent reflex in chronic heart failure rats. *Eur J Heart Fail* 2007, 9: 967–973.
 26. Pereira SC, Parente JM, Belo VA, Mendes AS, Gonzaga NA, do Vale GT, *et al.* Quercetin decreases the activity of matrix metalloproteinase-2 and ameliorates vascular remodeling in renovascular hypertension. *Atherosclerosis* 2018, 270: 146–153.
 27. Li Y, Zhu H, Kuppusamy P, Zweier JL, Trush MA. Mitochondrial electron transport chain-derived superoxide exits macrophages: implications for mononuclear cell-mediated pathophysiological processes. *React Oxyg Species (Apex)* 2016, 1: 81–98.
 28. Harms JE, Kuczumarski JM, Kim JS, Thomas GD, Kaufman MP. The role played by oxidative stress in evoking the exercise pressor reflex in health and simulated peripheral artery disease. *J Physiol* 2017, 595: 4365–4378.
 29. Sheu ML, Shen CC, Chen YS, Chiang CK. Ochratoxin A induces ER stress and apoptosis in mesangial cells via a NADPH oxidase-derived reactive oxygen species-mediated calpain activation pathway. *Oncotarget* 2017, 8: 19376–19388.
 30. Ciarcia R, Damiano S, Florio A, Spagnuolo M, Zacchia E, Squillacioti C, *et al.* The protective effect of apocynin on cyclosporine A-induced hypertension and nephrotoxicity in rats. *J Cell Biochem* 2015, 116: 1848–1856.
 31. Xu S, Zhao Y, Jin C, Yu L, Ding F, Fu G, *et al.* PKC/NADPH oxidase are involved in the protective effect of pioglitazone in high homocysteine-induced paracrine dysfunction in endothelial progenitor cells. *Am J Transl Res* 2017, 9: 1037–1048.
 32. Sun HJ, Zhao MX, Ren XS, Liu TY, Chen Q, Li YH, *et al.* Salusin-beta promotes vascular smooth muscle cell migration and intimal hyperplasia after vascular injury via ROS/NFκB/MMP-9 pathway. *Antioxid Redox Signal* 2016, 24: 1045–1057.
 33. Zhao MX, Zhou B, Ling L, Xiong XQ, Zhang F, Chen Q, *et al.* Salusin-beta contributes to oxidative stress and inflammation in diabetic cardiomyopathy. *Cell Death Dis* 2017, 8: e2690.
 34. Zhong B, Wang DH. N-oleoyldopamine, a novel endogenous capsaicin-like lipid, protects the heart against ischemia-reperfusion injury via activation of TRPV1. *Am J Physiol Heart Circ Physiol* 2008, 295: H728–H735.
 35. Moore C, Gupta R, Jordt SE, Chen Y, Liedtke WB. Regulation of pain and itch by TRP channels. *Neurosci Bull* 2018, 34: 120–142.
 36. Chiu IM. Infection, pain, and itch. *Neurosci Bull* 2018, 34: 109–119.
 37. Li YF, Wang W, Mayhan WG, Patel KP. Angiotensin-mediated increase in renal sympathetic nerve discharge within the PVN: role of nitric oxide. *Am J Physiol Regul Integr Comp Physiol* 2006, 290: R1035–R1043.
 38. Ma H, Chen SR, Chen H, Pan HL. Endogenous AT₁ receptor-protein kinase C activity in the hypothalamus augments glutamatergic input and sympathetic outflow in hypertension. *J Physiol* 2019, 597: 4325–4340.
 39. Wang HJ, Zhang F, Zhang Y, Gao XY, Wang W, Zhu GQ. AT₁ receptor in paraventricular nucleus mediates the enhanced cardiac sympathetic afferent reflex in rats with chronic heart failure. *Auton Neurosci* 2005, 121: 56–63.
 40. Zhu GQ, Gao L, Patel KP, Zucker IH, Wang W. ANG II in the paraventricular nucleus potentiates the cardiac sympathetic afferent reflex in rats with heart failure. *J Appl Physiol* 2004, 97: 1746–1754.
 41. Yamada J, Yoshimura S, Yamakawa H, Sawada M, Nakagawa M, Hara S, *et al.* Cell permeable ROS scavengers, Tiron and Tempol, rescue PC12 cell death caused by pyrogallol or hypoxia/reoxygenation. *Neurosci Res* 2003, 45: 1–8.
 42. Elbini Dhoubi I, Jallouli M, Annabi A, Gharbi N, Elfazaa S, Lasram MM. A minireview on N-acetylcysteine: An old drug with new approaches. *Life Sci* 2016, 151: 359–363.
 43. Capettini LS, Montecucco F, Mach F, Stergiopulos N, Santos RA, da Silva RF. Role of Renin-Angiotensin system in inflammation, immunity and aging. *Curr Pharm Des* 2012, 18: 963–970.
 44. Masi S, Uliana M, Virdis A. Angiotensin II and vascular damage in hypertension: Role of oxidative stress and sympathetic activation. *Vascul Pharmacol* 2019, 115: 13–17.
 45. Yu XJ, Miao YW, Li HB, Su Q, Liu KL, Fu LY, *et al.* Blockade of endogenous angiotensin-(1-7) in hypothalamic paraventricular nucleus attenuates high salt-induced sympathoexcitation and hypertension. *Neurosci Bull* 2019, 35: 47–56.
 46. Serrano F, Kolluri NS, Wientjes FB, Card JP, Klann E. NADPH oxidase immunoreactivity in the mouse brain. *Brain Res* 2003, 988: 193–198.
 47. Griendling KK, Sorescu D, Ushio-Fukai M. NAD(P)H oxidase: role in cardiovascular biology and disease. *Circ Res* 2000, 86: 494–501.
 48. Wang K, Zhu ZF, Chi RF, Li Q, Yang ZJ, Jie X, *et al.* The NADPH oxidase inhibitor apocynin improves cardiac sympathetic nerve terminal innervation and function in heart failure. *Exp Physiol* 2019, 104: 1638–1649.
 49. Ong J, Kinsman BJ, Sved AF, Rush BM, Tan RJ, Carattino MD, *et al.* Renal sensory nerves increase sympathetic nerve activity and blood pressure in 2-kidney 1-clip hypertensive mice. *J Neurophysiol* 2019, 122: 358–367.
 50. Campese VM, Kogosov E, Koss M. Renal afferent denervation prevents the progression of renal disease in the renal ablation

- model of chronic renal failure in the rat. *Am J Kidney Dis* 1995, 26: 861–865.
51. Li N, Guan Y, Tian YM, Ma HJ, Zhang X, Zhang Y, *et al.* Chronic intermittent hypobaric hypoxia ameliorates renal vascular hypertension through up-regulating NOS in nucleus tractus solitarii. *Neurosci Bull* 2019, 35: 79–90.
52. AlMarabeh S, Abdulla MH, O'Halloran KD. Is aberrant renorenal reflex control of blood pressure a contributor to chronic intermittent hypoxia-induced hypertension? *Front Physiol* 2019, 10: 465.



Microglia-Derived NLRP3 Activation Mediates the Pressor Effect of Prorenin in the Rostral Ventrolateral Medulla of Stress-Induced Hypertensive Rats

Li Hu¹ · Shutian Zhang² · Kokwin Ooi² · Xuehai Wu³ · Jiayang Wu¹ · Jian Cai⁴ · Yinggang Sun⁵ · Jijiang Wang² · Danian Zhu² · Fuxue Chen¹ · Chunmei Xia²

Received: 11 June 2019 / Accepted: 14 December 2019 / Published online: 3 April 2020
© The Author(s) 2020

Abstract Increased microglial activation and neuroinflammation within autonomic brain regions such as the rostral ventrolateral medulla (RVLM) have been implicated in stress-induced hypertension (SIH). Prorenin, a member of the brain renin-angiotensin system (RAS), can directly activate microglia. The present study aimed to investigate the effects of prorenin on microglial activation in the RVLM of SIH rats. Rats were subjected to intermittent electric foot-shocks plus noise, this stress was administered for 2 h twice daily for 15 consecutive days, and mean arterial pressure (MAP) and renal sympathetic nerve

activity (RSNA) were monitored. The results showed that MAP and RSNA were augmented, and this paralleled increased pro-inflammatory phenotype (M1) switching. Prorenin and its receptor (PRR) expression and the NLR family pyrin domain containing 3 (NLRP3) activation were increased in RVLM of SIH rats. In addition, PLX5622 (a microglial depletion agent), MCC950 (a NLRP3 inhibitor), and/or PRO20 (a (Pro)renin receptor antagonist) had antihypertensive effects in the rats. The NLRP3 expression in the RVLM was decreased in SIH rats treated with PLX5622. Mito-tracker staining showed translocation of NLRP3 from mitochondria to the cytoplasm in prorenin-stimulated microglia. Prorenin increased the ROS-triggering M1 phenotype-switching and NLRP3 activation, while MCC950 decreased the M1 polarization. In conclusion, upregulated prorenin in the RVLM may be involved in the pathogenesis of SIH, mediated by activation of the microglia-derived NLRP3 inflammasome. The link between prorenin and NLRP3 in microglia provides insights for the treatment of stress-related hypertension.

Li Hu, Shutian Zhang and Kokwin Ooi have contributed equally to this work.

Electronic supplementary material The online version of this article (<https://doi.org/10.1007/s12264-020-00484-9>) contains supplementary material, which is available to authorized users.

✉ Fuxue Chen
chenfuxue@staff.shu.edu.cn

✉ Chunmei Xia
cmxia@fudan.edu.cn

¹ Laboratory of Neuropharmacology and Neurotoxicology, Shanghai Key Laboratory of Bio-Energy Crops, College of Life Science, Shanghai University, Shanghai 200444, China

² Department of Physiology and Pathophysiology, Basic Medicine College, Fudan University, Shanghai 200032, China

³ Department of Neurosurgery, Huashan Hospital, Fudan University, Shanghai 200040, China

⁴ Department of Neurology, Renji Hospital, Shanghai Jiaotong University, Shanghai 200240, China

⁵ Department of Cardiovascular Diseases, Xinhua Hospital Affiliated to Shanghai Jiao Tong University School of Medicine, Shanghai 200025, China

Keywords Stress · NLRP3 · Prorenin · Microglia · Hypertension

Introduction

Evidence shows that chronic psychosocial stress is directly linked to the development of hypertension, cardiovascular disease, and stroke [1]. The activation of various neurogenic pathways, such as stimulation of the sympathetic nervous system (SNS), mediates not only short-term increases in blood pressure (BP), but also the elevation of chronic BP in response to specific stresses [2]. The sympathetic outflow is controlled by key cerebral nuclei

and neural circuits in the central nervous system (CNS), predominantly the rostral ventrolateral medulla (RVLM) [3–5], the nucleus tractus solitarius, and the hypothalamic paraventricular nucleus (PVN), all of which are associated with the activities of the autonomic nervous system [2].

It is well established that increased SNS outflow and enhanced renin-angiotensin system (RAS) activity are common features of hypertension and various pathological settings that predispose individuals to hypertension. In an animal experiment, it has been reported that chronic foot-shock stress upregulates the expression of the RAS components in the CNS and the circulatory system, thereafter increases vasopressin, oxidative stress, and stress hormone levels, which are involved in the development of hypertension [1]. More recently, hypertension has been recognized as an immune condition and evidence suggests that reciprocal communication between the RAS, SNS, and immune systems plays a role in the establishment of hypertension [4, 5]. Increased SNS activity plays the roles of altering immune system responses in pathophysiological settings. Moreover, microglia, the resident central immune cells, also contribute to the increased SNS activity in rodents [6]. However, the cause-effect relationship between central inflammatory responses and the centrally-triggered sympathetic drive remains elusive.

Microglia maintain normal neuronal physiology and homeostasis in the CNS in their resting or immunosurveillant stages [7]. There are M1/pro-inflammatory and M2/immune-regulatory microglial phenotypes. Our previous study showed that the centrally administered anti-inflammatory agent minocycline significantly alleviates M1 microglia activation and hypertension in SIH rats [6]. The main component of RAS, angiotensin II (Ang II) itself, is a powerful inducer of increased pressure. It also triggers microglial activation and boosts the production of pro-inflammatory cytokines [2] and reactive oxygen species (ROS) through mitochondrial damage, which subsequently contributes to the activation of sympathetic nerve activity in hypertension development [8–10]. It has been confirmed that the Ang II/AT1 receptor axis or prorenin directly activates microglia into the M1 immunophenotype. Ang II triggers the immune system *via* shifting the microglia from the M2 to the M1 phenotype by binding to the Ang II receptor type 1 (AT1) [9].

Prorenin as the precursor of renin can directly stimulate microglial activation and pro-inflammatory cytokine production, apart from initiating the RAS cascade, and this may contribute to activation of the pro-inflammatory phenotype (M1) [11–14]. It has been reported that microinjection of human prorenin and activation of the (pro)renin receptor (PRR) in the PVN contribute to the increased sympathetic nerve activity in rats [15]. A PRR agonist can bind both renin and prorenin, which leads to

the non-proteolytic activation of prorenin and local Ang II formation [16]. In addition, it has been noted that while the PRR-(pro)renin complex plays its roles independent of Ang II, it also activates downstream signal transduction pathways such as the NF- κ B and Wnt signaling pathway [11, 17]. Our previous *in vitro* study showed that prorenin induces the disintegration of mitochondria and M1 phenotype switching *via* ROS-overproduction in microglia [18], while its roles in BP regulation warrant further investigation.

The NLR family pyrin domain containing 3 (NLRP3) inflammasomes are multi-protein complexes that comprise the NLRP3 protein, the adaptor molecule apoptosis-associated speck-like protein containing a CARD (caspase recruitment domain) (ASC), and cysteine protease caspase-1 components [19]. NLRP3 inflammasomes are responsible for the maturation of pro-inflammatory cytokines such as interleukin-1 β (IL-1 β) and IL-18 involved in host defense and cellular stress responses [20, 21]. NLRP3 inflammasomes are activated by many mechanisms, such as K⁺ efflux, endoplasmic reticulum stress, intracellular Ca²⁺ and ROS. ROS might activate NLRP3 inflammasomes both as a trigger and an effector, resulting in pathological processes [22]. Zhou *et al.* first reported that the accumulation of damaged mitochondria increases the activation of NLRP3 inflammasomes [23]. NLRP3 was originally thought to be a cytosolic receptor, but it translocates to mitochondria in hypoxic settings [24]. Whether prorenin activates NLRP3 *via* triggering ROS and its translocation profile in the RVLM of SIH rats remain unknown.

Here, we investigated the mechanisms involved in the local effect of prorenin on microglial activation in SIH rats. We demonstrated that stress induced prorenin and PRR upregulation in the RVLM, which triggered microglial activation. We then confirmed that the prorenin-NLRP3 inflammatory signaling in microglia mediated the SNS activation during stress-induced pathology.

Materials and Methods

Drugs and Reagents

N-acetylcysteine (NAC; A7250), dimethyl sulfoxide, 4',6-diamidino-2-phenylindole, and anti- β -actin (A1978) were from Sigma-Aldrich (St. Louis, MO). Recombinant human prorenin was from Abcam (ab93266; Cambridge, MA) and MCC950 (sc-505904) was from Santa Cruz Biotechnology (Santa Cruz, CA). The ROS fluorescent probe-DCFH-DA kit (S0033) and caspase 1 activity assay kit (C1101) were from the Beyotime Institute of Biotechnology (Nanjing, China). The following antibodies were used: sheep monoclonal antiserum against prorenin/renin (GTX7967, Gene Tex, San Antonio, TX); rabbit polyclonal antiserum against

PRR (bs-7691R, Bioss, Beijing, China); rabbit polyclonal antiserum against caspase-1 (D7F10); rabbit anti-ASC monoclonal antibody (#13833), anti-CD86 (#91882), and anti-CD206 (#91992) were from Cell Signaling Technology (Beverly, MA); mouse monoclonal antiserum against CD11b/c (OX42, ab1211), mouse monoclonal to IL-6 (ab9324), iNOS (ab15323), Arg (ab60176), Iba-1 (ab153696), GFAP (ab7260), PGP 9.5 (ab10410), and rabbit polyclonal antiserum against NLRP3 (ab214185) were from Abcam. Donkey anti-sheep IgG H&L Alexa Fluor 555 (ab150178), goat anti-rabbit IgG H&L Alexa Fluor 594 (ab150080), and goat anti-mouse IgG H&L Alexa Fluor 488 (ab150117) were from Abcam. MCC950 was from Adipogen Corp. (San Diego, CA). PLX5622 was from Plexxikon (Berkeley, CA).

Generation of the PRR Peptide Ligand

PRO20 was synthesized by Sangon Biotech (Shanghai) Co., Ltd. (Shanghai, China) as previously described [25].

Animals

Adult Sprague-Dawley rats (male, 8 weeks old, 250–300 g) were purchased from the Animal Laboratory Center of Fudan University. Altogether, 140 animals were used in this study, with a mortality rate of 5% due to intolerance of brain surgery, or death during stress. All experimental procedures were approved by Fudan University Animal Care Committee and conformed to the guidelines of the Institutional Ethics Committee; all efforts were made to minimize the number of animals used and their suffering. The rats were housed under a 12-h light/dark cycle in a temperature-controlled room at 24 °C with standard food and tap water *ad libitum*. They were divided into the following groups (6 rats each): (i) normotensive (Ctrl); (ii) stress-induced hypertensive (SIH); (iii) SIH + aCSF (artificial cerebrospinal fluid); (iv) SIH + MCC950 (a selective NLRP3 inhibitor), (v) Ctrl + MCC950; (vi) SIH + PRO20 (a newly-developed PRR antagonist, 200 $\mu\text{mol/L}$); and (vii) Ctrl + PRO20. PLX5622 was used to eliminate microglia in SIH rats. MCC950 was released into the cisterna magna at 0.15 $\mu\text{L/h}$ from an osmotic mini-pump to maintain a total final concentration of 0.5 $\mu\text{mol/L}$ in the brain [10]. PRO20 or MCC950 was delivered by osmotic minipump once daily for 1 week (from stress day 8 to day 15). PLX5622 was formulated in standard chow by the Department of Laboratory Animal Science, Fudan University, at 1200 ppm, and administered for 7 consecutive days (days 8–15 of stress). Molecular studies were replicated at least 3 times.

In preliminary experiments, we assessed the M1 polarization in the rats. The results showed that the inflammatory microglial marker CD86 and their secreted proteins (iNOS, Arg, and IL-6) did not differ between control and drug treatment (MCC950 or PRO20) groups, implying that the drugs themselves did not have pro- or anti-inflammatory effects in normal rats (Fig. S1). In accord with the guidelines of the Institutional Ethics Committee to minimize the number of animals used and their suffering, further molecular experiments were conducted in the Ctrl, SIH, SIH + vehicle (aSCF), SIH + MCC950, and SIH + PRO20 groups.

SIH was induced as described in our previous publications [4, 5]. Briefly, rats were placed in a cage (22 cm \times 22 cm \times 28 cm) and received intermittent electric shocks (35–75 V, 0.5 ms in duration) every 2–30 s randomly controlled by a computer. Meanwhile, noise (range, 88–98 dB) produced by a buzzer was given as the conditioned stimulus [6]. The rats were subjected to stress for 2 h twice daily for 15 consecutive days. The control group underwent sham stress. Systolic blood pressure (SBP) was recorded in conscious rats using the tail-cuff method. SBP measurements were repeated three times and the average value was taken.

General Procedures for Acute Experiments

As in our previous study [6], rats were anesthetized with sodium pentobarbitone (50 mg/kg) intraperitoneally (i.p.). A catheter was placed in the femoral vein. BP was measured *via* a femoral artery cannula connected to a pressure transducer and a polygraph (PowerLab system, AD Instruments, Bella Vista, NSW, Australia). The HR was automatically derived from the phasic arterial BP wave. Body temperature was maintained at 37 °C by a heating pad.

Implantation of Intracisternal Osmotic Minipump

The procedures were performed as described in our previous study [6]. Briefly, the rats were anesthetized with pentobarbital sodium (50 mg/kg, i.p.). After a midline dorsal neck incision, the dura was perforated with a 22-gauge steel needle and following cerebrospinal fluid leakage, a PE-5 catheter (Clay Adams, Sparks, MD) was advanced 5 mm into the cisterna magna and sealed to the dura with tissue glue. The outer end of the catheter was connected to a micro-osmotic minipump (Alzet 1007D, Durect Co., Cupertino, CA). The PRR antagonist (PRO20) or MCC950 was delivered by osmotic minipump. The rats received procaine penicillin injection (1,000 IU, i.m.) postoperatively. Rats that had progressive weight gain

and were in normal physiological condition after the operation were used in subsequent experiments.

Renal Sympathetic Nerve Activity (RSNA)

Recording

We recorded RSNA when the general procedures for acute experiments were ready. Before a renal sympathetic nerve was exposed, the trachea was cannulated with polyethylene tubing and connected to a pneumotachograph (SAR-830/P, CWE Inc., Ardmore, PA) to maintain normal ventilation. Then, the head was fixed in a model 920 Kopf stereotaxic frame with bars and the body was placed in the lateral position on a heating pad. This approach is similar to that used by Huber and Basu [15]. Briefly, rats were anaesthetized as above and the left kidney was exposed through a retroperitoneal incision. A pair of silver recording electrodes was placed on the isolated left renal sympathetic nerve (Teflon 786500, A-M Systems Inc., Sequim, WA). Subsequently, the exposed nerve and the electrodes were secured with Kwik-Sil gel (World Precision Instruments) and a Grass P55C preamplifier was used to amplify and filter (bandwidth: 100–3,000 Hz) the nerve activity. The maximum activity occurred 1–2 min after the rat was overdosed by narcotic euthanasia. Baseline nerve activity was taken as the percentage of maximum after the noise level was subtracted; the background noise level was recorded 15–20 min after the rat was euthanized using the unit conversion of the PowerLab Chart system (AD Instruments).

Primary Culture of Rat Microglial Cells and *In Vitro* Experimental Design

Primary cultures of microglial cells were prepared as previously described [26]. Briefly, the medulla oblongata covering the RVLM was removed from 1–2-day-old Sprague-Dawley rats after decapitation as we described previously [6]. The RVLM was identified according to the atlas of Watson and Paxinos [27]. Both sides of the RVLM (about 1.5- to 2.5-mm lateral to the midline and medial to the spinal trigeminal tract) were collected using micropunches with a 1-mm inner diameter burr. Next, Hanks balanced salt solution dissecting medium containing glucose, bovine serum albumin (BSA) and HEPES, as well as 0.025% trypsin was used to incubate the minced tissue at 37 °C for 20 min. Then, cells were plated at 3×10^5 cells/cm² in Dulbecco's modified Eagle's medium (DMEM) with GlutaMax and high glucose (4.5 g/L), supplemented with 10% fetal bovine serum, 0.1 mg/mL streptomycin and 100 U/mL penicillin in poly-L-lysine-coated 75 cm² culture flasks. After 3 days, the culture medium was removed and replaced with fresh medium and kept at 37 °C under

95% O₂/5% CO₂. On day 9, the cells were re-suspended after centrifugation (150 × g for 10 min) [28]. Cell viability was evaluated by trypan blue exclusion (Fig. S2). The purity of cultured microglia was >95% when evaluated by flow cytometry.

For the *in vitro* experiments, microglia were divided into to 6 groups: (i) control (Ctrl, vehicle); (ii) prorenin (20 nmol/L for 24 h) treatment (PRO) [13, 18]; (iii) Ctrl + NAC (5 mmol/L); (iv) Ctrl + MCC950 (10 μmol/L); (v) PRO + NAC (5 mmol/L); and (vi) PRO + MCC950 (10 μmol/L). The concentrations of NAC [29] and MCC950 were determined as described previously [30]. We preliminarily investigated the effects of MCC950 and/or NAC on M1 polarization and the release of pro-inflammatory factors (IL-1β and TNF-α) from microglia in the control group. These results showed no significant differences between the vehicle (Ctrl) and drug-treatment (MCC950 and NAC) groups, which implied that the drugs themselves did not affect control-group microglia (Fig. S3). Therefore, further molecular experiments were mainly conducted in the Ctrl, PRO, PRO + NAC, and/or PRO + MCC950 groups.

Flow Cytometry

In order to measure M1 and M2 polarization, primary culture of microglia was carried out as described previously [18, 31]. Microglia were harvested by re-suspension in cold phosphate-buffered saline (PBS) containing 0.5% BSA/0.05% NaN₃, then incubated in 20% DMEM/F12 medium. M1 and M2 phenotype microglia were recognized using monoclonal antibodies specific for CD86-PE and antibodies specific for CD206-APC, respectively. For immunophenotypic analysis, the number of purified microglia was adjusted to 1×10^6 /mL. Primary microglia were incubated for 30 min with 10% fetal bovine serum, followed by incubation with the antibody mixtures for 30 min on ice. Microglia were washed and re-suspended in PBS twice, and then immediately assessed by flow cytometry (Becton Dickinson, Swindon, UK) and analyzed using Flowing software v2.5.1. Flow cytometry analysis of the expression profiles of CD86 and CD206 allowed us to distinguish M1 (CD86⁺) from M2 (CD206⁺) [32].

Double Immunofluorescence Staining and Confocal Microscopic Imaging

Immunofluorescence was performed as described previously [5, 6], to determine the co-localization of NLRP3 with microglia CD11b/c (OX42), astrocytes (GFAP), and neurons (NeuN). Rats were anesthetized with 10% chloral hydrate and perfused through the left ventricle with 200 mL of 0.01 mol/L PBS (pH 7.4), followed by

200 mL of freshly-prepared 4% paraformaldehyde in 0.1 mol/L PB. RVLM sections were collected, post-fixed for 4 h, then placed in 20% and 30% sucrose at 4 °C to dehydrate overnight. Free-floating 30- μ m coronal sections containing the RVLM were cut on a cryostat (Microm, Walldorf, Germany) [33]. The sections were washed in PBS and incubated with 0.3% Triton X-100 for 30 min followed by incubation with 5% horse serum for 1 h at 37 °C to block non-specific protein. The sections were incubated with the polyclonal antibodies CD86, CD206, NLRP3, CD11b/c, GFAP, and PGP9.5 overnight at 4 °C. We used goat anti-mouse IgG H&L Alexa Fluor 488, donkey anti-sheep IgG H&L Alexa Fluor 647, and donkey anti-rabbit IgG H&L Alexa Fluor 594 secondary antiserum. NLRP3 co-localization with mito-tracker was investigated *in vitro*. The fluorescent signals were monitored under a Fluorview FV300 laser scanning confocal microscope (Olympus, Tokyo, Japan); immunoreactivity manifested as specific green or red fluorescence.

Western Blot Analysis

Total RVLM tissue (see Fig. S4 for location of micro-uncures) from each rat was homogenized in lysis buffer with 1% NP40 and 1 mmol/L PMSF. Protein samples of the same amount from each rat were extracted from RVLM homogenates to analyze protein expression by western blot. In brief, the protein samples (20 μ g each) were subjected to SDS/PAGE in 8%–12% gradient gel (Invitrogen, Carlsbad, CA) and transferred to PVDF membrane. Prorenin, PRR, NLRP3, ASC, caspase-1, pro-IL-1 β , IL-1 β , Iba-1, and M1 markers [CD86, IL-6, iNOS, and Arg] in the RVLM and/or cultured microglia were measured. This was followed by incubation with horseradish peroxidase-conjugated goat anti-rabbit IgG or goat anti-mouse IgG. The amount of protein was assessed by ECL detection reagents (WBKLS0050; Millipore) and the immunostaining band was visualized and quantitated by an automatic chemiluminescence image analysis system (Tanon-5200; Tanon Science & Technology, Shanghai, China). The data were normalized by developing the β -actin as loading control. The concentration of all the antibodies was 1:1000 except for β -actin (1:5000).

RNA Extraction and Quantitative Real-Time Polymerase Chain Reaction (PCR)

Total RNA extraction reagent (TaKaRa, Dalian, China) was used to extract the total RNA from the RVLM. The mRNAs of prorenin, PRR, NLRP3, pro-Casp-1, ASC, IL-1 β , TNF- α , IL-10, and TGF- β were analyzed by quantitative real-time PCR. Isolated mRNA was quantified by spectrophotometry and the 260/280 nm optical density

ratio was calculated. The cDNA was synthesized using a high-capacity cDNA reverse transcription kit (Applied Biosystems, ABI). The relative quantification of gene expression was expressed as fold-change *via* normalization against β -actin by using the $2^{-\Delta\Delta CT}$ method. The sequences of primers were designed using Primer Express 2.0 and are listed in Table S1.

DCFH-DA Fluorescent Imaging to Analyze Intracellular ROS Production in Microglia

The ultrastructural mitochondrial morphology showed that prorenin-induced mitochondria had disorientation and cristae breakage (Fig. S5), so we measured ROS production in microglia. Microglia were seeded in a 6-well plate overnight and treated as previously described. DCFH-DA is a ROS-specific fluorescent probe, which we used to measure total intracellular ROS levels. The microglia were incubated with 10 μ mol/L DCFH-DA at 37 °C in a dark room. After washing 3 times with serum-free medium, microglia were analyzed under a Fluorview FV300 laser scanning confocal microscope (Olympus), with an excitation wavelength of 488 nm and an emission wavelength of 525 nm.

Statistical Analysis

Experimental data are expressed as the mean \pm SEM (standard error of the mean). Student's unpaired *t* test was used for experiments that contained two groups of samples. For comparative purposes, one-way or two-way analysis of variance with repeated measures was used to determine differences between groups. This was followed by the Tukey's multiple range tests for *post hoc* assessment of individual means. $P < 0.05$ indicated that the differences were statistically significant. Statistical data were analyzed with GraphPad Prism 5 software.

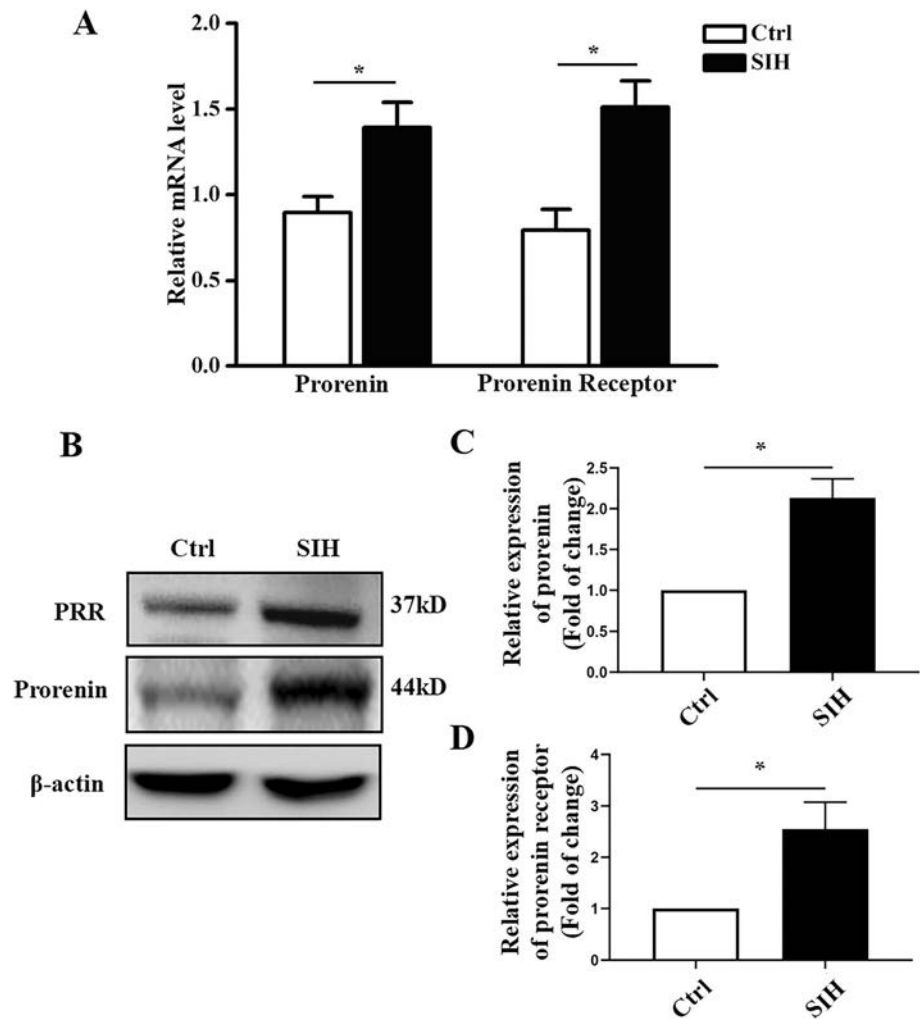
Results

Prorenin and/or PRR Expression is Upregulated in the RVLM of SIH Rats

We measured the protein and mRNA levels of prorenin and/or PRR in the RVLM to determine whether stress caused their abnormal expression. We found that their mRNA levels were increased (Fig. 1A, $P < 0.05$) in the RVLM of SIH rats. Representative immunoblot bands of prorenin and/or PRR in the RVLM are shown in Fig. 1B. Western blotting analysis showed that the protein levels of prorenin and/or PRR were increased 2.1 and 2.5-fold

Fig. 1 Expression of prorenin/PRR in the RVLM of rats.

A qRT-PCR showing both prorenin and PRR are increased in the RVLM of SIH rats. **B** Representative western blots of prorenin and PRR in the RVLM of SIH rats. **C, D** Densitometric quantification showing prorenin and PRR are higher in the SIH group than in controls. Data are presented as the mean \pm SEM. * $P < 0.05$ vs Ctrl, $n = 6$ /group.



respectively (Fig. 1C, D, $P < 0.05$) in SIH rats compared with controls.

Mean Arterial Pressure (MAP) and RSNA are Augmented in SIH rats, and are Attenuated by the PRR Antagonist PRO20

Given the increased prorenin and PRR in the RVLM of SIH rats, we speculated that prorenin/PRR play a potential role in BP regulation. Next, we investigated whether MAP and RSNA are regulated by prorenin/PR. aCSF and the PRR antagonist PRO20 were infused into the cerebellomedullary cistern in SIH rats. Hemodynamic measurements and RSNA recordings showed that the arterial BP, mean MAP and RSNA were higher in the SIH group than in the control group, and these increases were attenuated by cerebellomedullary cistern infusion of PRO20 ($P < 0.05$, Fig. 2).

M1/M2 Ratio and Pro-inflammatory Factors are Increased in the RVLM of SIH Rats, and are Attenuated by the PRR Antagonist PRO20

Activated microglia can be polarized to M1 and/or M2 phenotype [26], and the M1 phenotype indicates neuroinflammatory activity. The immunofluorescent staining showed that activated microglia were present in the RVLM, and we used the CD86 or CD206 antibody to identify the M1 or M2 phenotype of microglial activation (Fig. 3A). Immunofluorescence analysis showed that the ratio of M1 phenotypes was increased and that of M2 phenotypes was decreased in SIH rats (Fig. 3B, $P < 0.05$). Furthermore, neuroinflammation was identified by the release of pro-inflammatory and immune-regulatory factors (Fig. 3C). To determine the effect of PRO20 on neuroinflammation following SIH, we performed qRT-PCR and confirmed that the pro-inflammatory factor release was increased in SIH rats (Fig. 3C, $P < 0.05$), but further decreased in PRO20-treated SIH rats (Fig. 3D, $P < 0.05$).

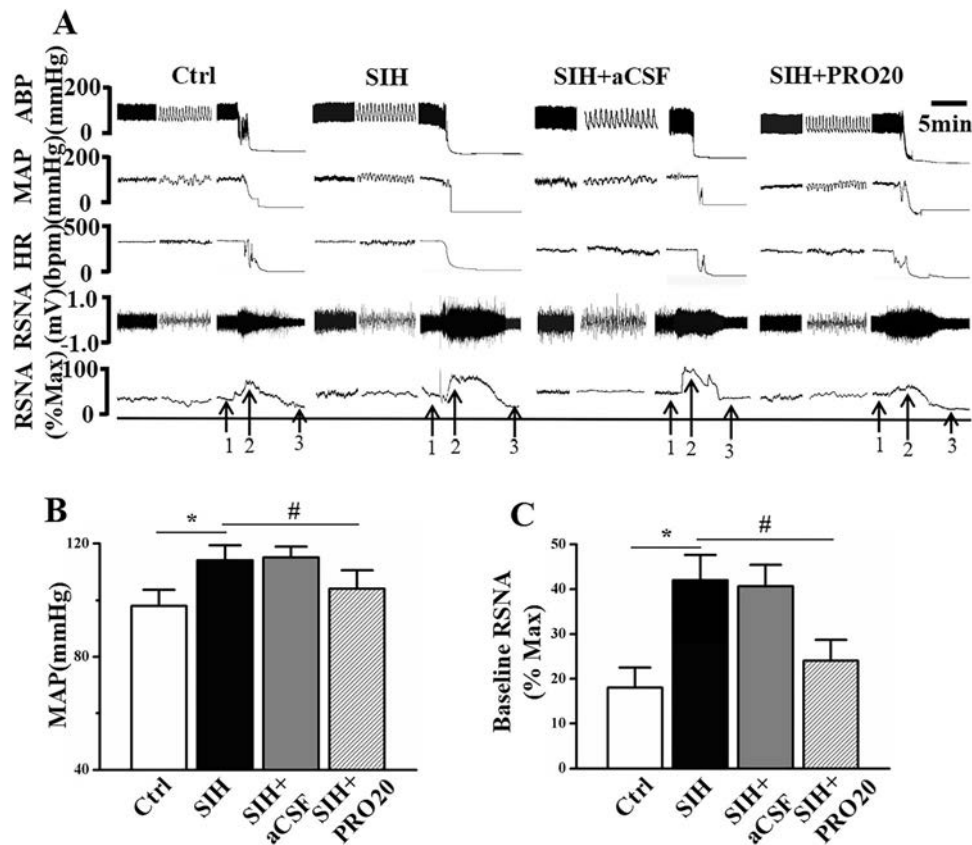


Fig. 2 Effects of intracisternal infusion of PRO20 on the MAP and RSNA in SIH rats. **A** Representative original traces demonstrating the effect of PRO20 infusion on RSNA, MAP, and HR (1, basal RSNA; 2, maximum RSNA; 3, noise level). The maximum occurred 1–2 min after the rat was euthanized. Note that the maximum RSNA did not significantly differ among the 3 groups, while the SIH/SIH + aCSF rats had a greater basal RSNA level than control and/or PRO20-

treated SIH rats, and intracisternal infusion PRO20 attenuated the MAP and baseline RSNA level of SIH rats. **B** Statistical data for MAP. **C** Statistical data for baseline nerve activity. Data represent the mean \pm SEM; $n = 6$; * $P < 0.05$ vs Ctrl; # $P < 0.05$ vs SIH. ABP, arterial blood pressure; MAP, mean arterial pressure; HR, heart rate; RSNA, renal sympathetic nerve activity; SIH, stress-induced hypertensive rats; aCSF, artificial cerebrospinal fluid.

Immunofluorescence analysis confirmed that PRO20 treatment significantly reduced the M1 microglia, as shown by decreased CD86 staining (Fig. 3E, F, $P < 0.05$). These results indicated that PRO20 effectively inhibits the polarization of the M1 phenotype and reduces neuroinflammation in the RVLM of SIH rats.

NLRP3 Inflammasome Expression is Increased in Both Microglia and Neurons in the RVLM of SIH Rats, and is Decreased by the PRR Antagonist PRO20

We first examined the role of PRO20 in NLRP3/ASC/caspase-1 mRNA expression using qRT-PCR analyses. Compared with those of SIH group, the mRNA levels of NLRP3, ASC, and caspase-1 p20 were significantly decreased in the PRO20-treated group (all $P < 0.05$, Fig. 4A). We then assessed the protein expression profiles of NLRP3 inflammasome components in the RVLM, and found that the NLRP3, ASC, and caspase-1 p20 protein

levels (Fig. 4B, C) were significantly increased in SIH rats. Based on these results, double immunofluorescence staining was then performed to investigate which cell type expressed the upregulated NLRP3. We stained NLRP3 along with the microglia, neuron, and astrocyte markers, OX42, PGP9.5, and GFAP, respectively. The double immunofluorescent staining showed that NLRP3 mainly co-localized with microglia (Fig. 4D–F) and/or neurons (Fig. 4G–I) but was not co-expressed with the astrocyte marker GFAP (Fig. 4J, K). Immunofluorescence analysis confirmed that stress induced strong microglial activation and upregulation of NLRP3 expression in the RVLM (Fig. 4D–K, $P < 0.05$), while PRO20 significantly reduced the immunofluorescence density of NLRP3 both in microglia and neurons (Fig. 4F, I, $P < 0.05$). These results indicated that PRO20 effectively inhibits activation of the NLRP3 inflammasome in the RVLM of SIH rats.

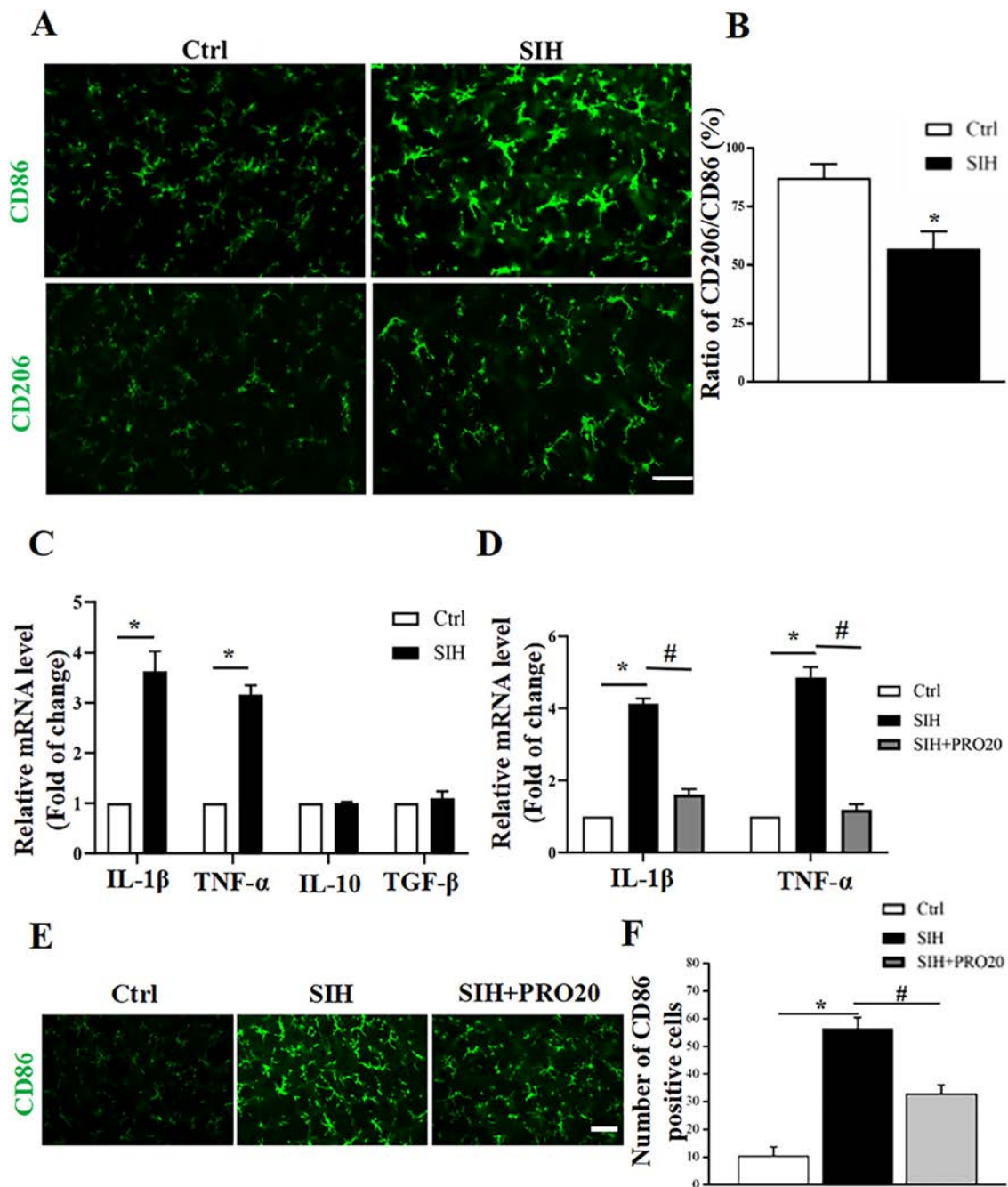


Fig. 3 The ratio of M1/M2 polarization and release of pro-inflammatory/immune-regulatory factors in the RVLM of SIH rats. **A** Immunofluorescence detection of M1 and/or M2 phenotype microglia in the RVLM showed robust switching to M1 phenotype in SIH rats. **B** Relative ratio of M2 versus M1 phenotype microglia in the RVLM expressed as a percentage. **C, D** qRT-PCR showing the release of pro-

inflammatory/immune-regulatory factors was increased in the RVLM of SIH rats. **E, F** The PRR antagonist, PRO20, decreased the M1 polarization in SIH rats. Data represent the mean \pm SEM; $n = 6$; $*P < 0.05$ vs Ctrl; $^{\#}P < 0.05$ vs SIH; scale bars, 200 μ m in (A) and (E).

The Anti-hypertensive Effects of MCC950 Depend on the Presence of Microglia

Since microglia were the predominant cell type expressing NLRP3 following SIH, we further explored whether MCC950, the NLRP3 inflammasome inhibitor, had an

anti-hypertensive effect by targeting microglia. We used a specific CSF1R inhibitor, PLX5622, to eliminate microglia as previously reported [34] after 7 successive days of SIH induction. The effect of microglial depletion by PLX5622 was identified using western blot analysis (Fig. 5A, B) and immunofluorescent staining for the microglia marker Iba-1

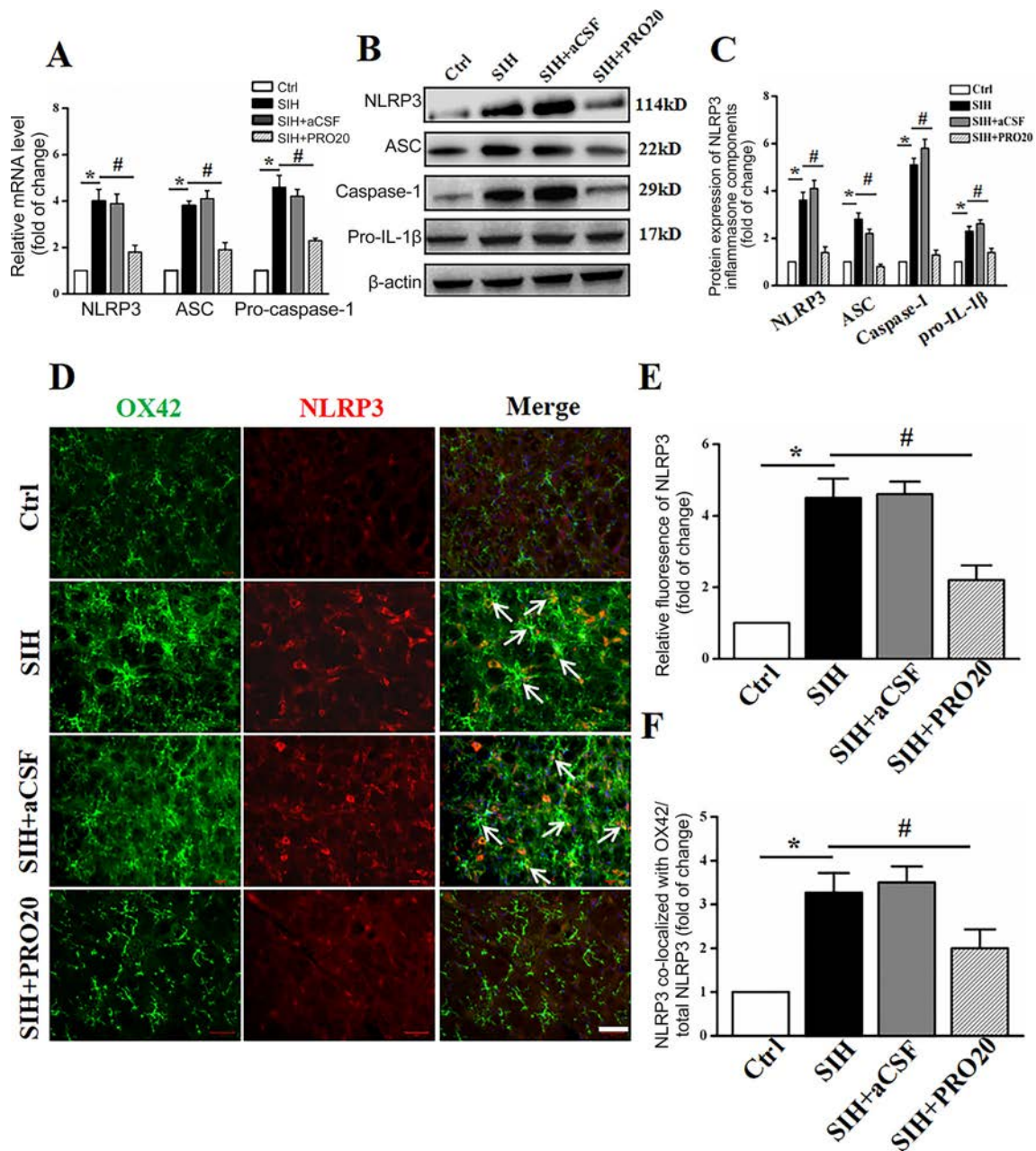


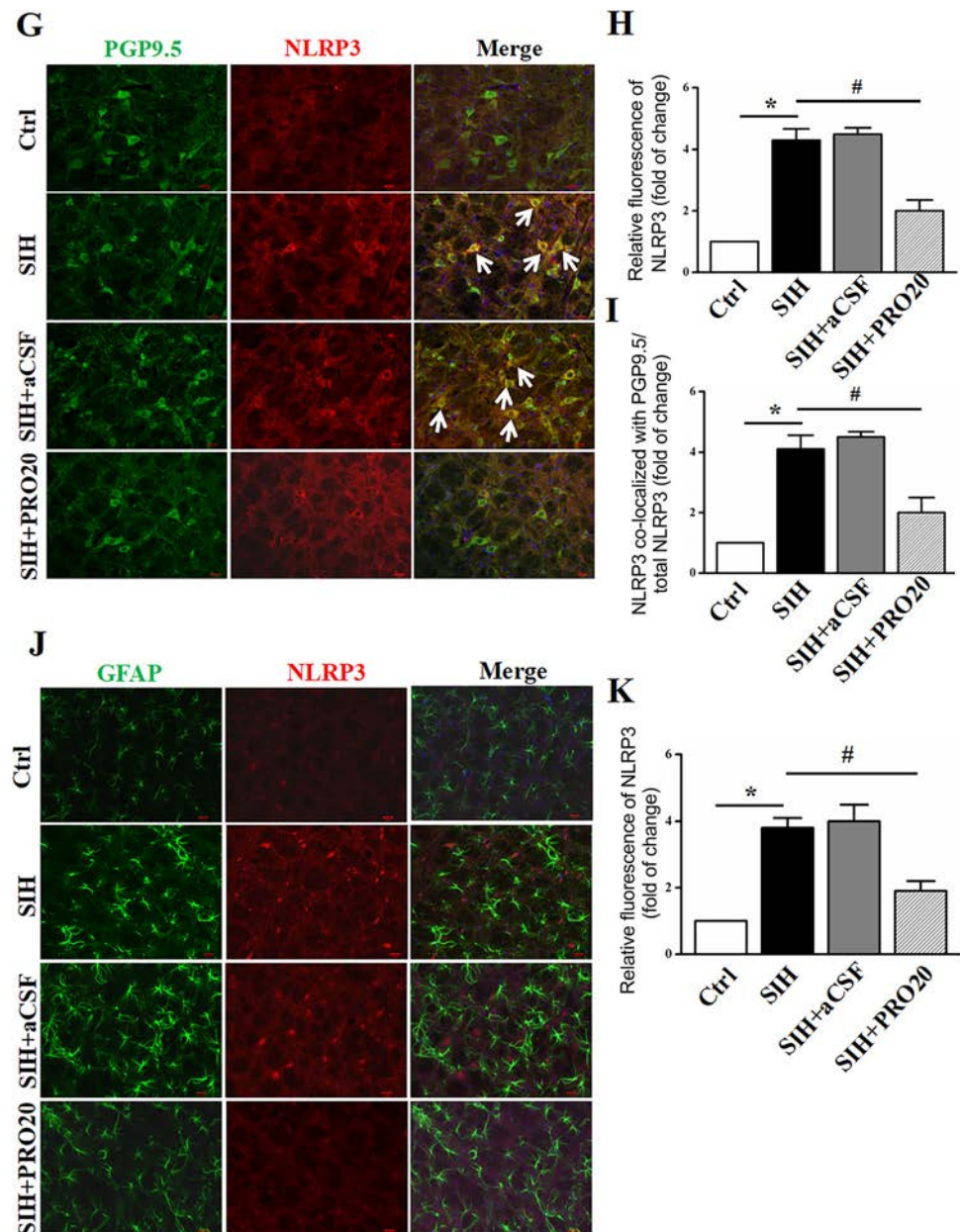
Fig. 4 Expression of NLRP3 is downregulated by PRO20, a PRR antagonist. **A** Effect of PRO20 on the mRNA expression of NLRP3/ASC/caspase-1 using qRT-PCR analyses. **B**, **C** Representative immunoblots and quantitative analysis showing that NLRP3, ASC, caspase-1, and pro-IL-1 β expression in the RVLM of SIH rats was upregulated, while PRO20 treatment downregulated their expression. **D** Representative images showing that NLRP3 (red) co-localized with the microglial marker (OX42). **E**, **F** Relative fluorescence intensity calculation of NLRP3-immunoreactivity with or without OX42-immunoreactivity in different groups. **G–I** Representative images

and quantitative analysis showing co-localization of PGP 9.5 (neuronal marker, green) and NLRP3 (red) in the RVLM. **J**, **K** Representative images of double immunofluorescent staining for GFAP (astrocyte marker, green) and NLRP3 (red) and densitometric quantification of immunoreactivity in the RVLM. Notably, immunofluorescence staining analysis showed that NLRP3 mostly localized with microglia and neurons (arrows). Data represent the mean \pm SEM; $n = 6$; * $P < 0.05$ vs Ctrl; # $P < 0.05$ vs SIH; scale bars, 200 μ m in (**D**), (**G**), and (**J**).

(Fig. 5C, D). Western blot analysis showed that PLX5622 treatment resulted in the elimination of $\sim 85\%$ of microglia and decreased NLRP3 expression in the RVLM of SIH rats (Fig. 5A, B). Immunofluorescent staining also confirmed

that microglia were depleted by $\sim 85\%$. Of note, we found that microglial elimination by PLX5622 attenuated the augmented blood pressure in SIH rats compared with the SIH + aCSF group. In addition, a depressor effect of

Fig. 4 continued



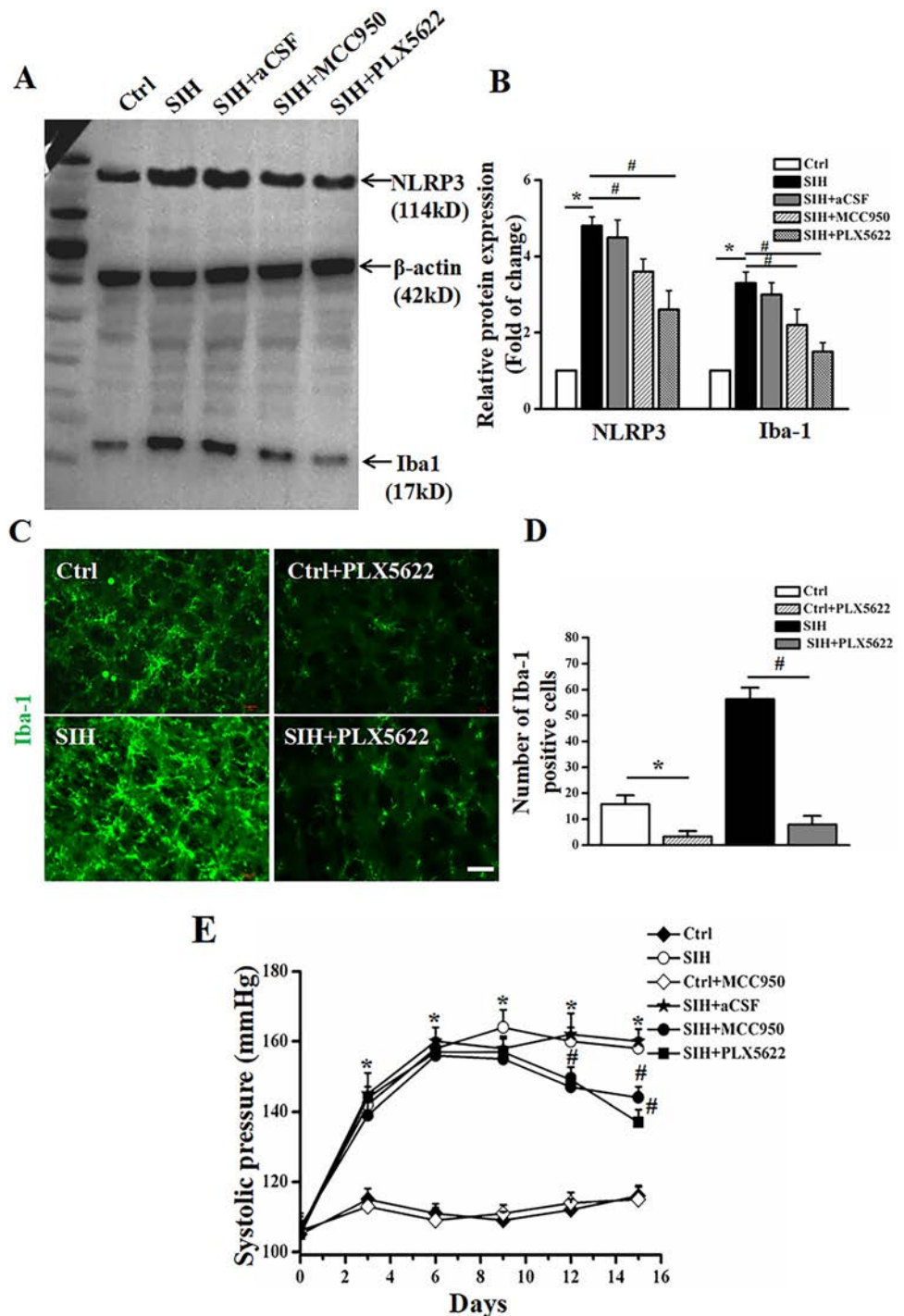
MCC950 was observed in SIH rats (Fig. 5E, all $P < 0.05$). These results implied that microglia partially contribute to the anti-hypertensive effect of MCC950 in SIH rats.

Prorenin Promotes the M2-to-M1 Polarization Transition Via NLRP3 Over-activation *In Vitro*

To investigate whether prorenin regulates microglial polarization *via* NLRP3 activation, we incubated primary microglia cultured from rats with recombinant human prorenin (20 nmol/L) for 24 h. The purity of cultured microglia was $> 94\%$ when evaluated by flow cytometry (Fig. 6A). The M1 and M2 phenotypes were assessed by flow cytometry in the Ctrl, prorenin, and prorenin +

MCC950 groups (Fig. 6B). There was a significant increase in the proportion of M1/M2 in prorenin-treated microglia (from 0.67% to 31.52%, $n = 6$, $P < 0.05$), while co-treatment with prorenin and MCC950 reversed the M1/M2 proportion (from 31.52% to 3.97%, $n = 6$, $P < 0.05$, Fig. 6C). qRT-PCR analysis showed that prorenin in microglia increased the inflammatory factors TNF- α and IL- β (Fig. 6D, $P < 0.05$). Conversely, interference with NLRP3 by its inhibitor MCC950 in microglia resulted in a decrease in M1-related inflammatory factors (Fig. 6D, $P < 0.05$). These results indicated that suppressing NLRP3 activation reduces the ratio of M1 to M2 polarization and pro-inflammatory factor release, which implies

Fig. 5 The NLRP3 inhibitor, MCC950, has an anti-hypertensive effect on SIH, which might be associated with microglia-derived NLRP3. **A, B** Representative immunoblots and densitometric analysis showing that NLRP3 expression is decreased in both MCC950 (NLRP3 inhibitor) and PLX5622 (CSF1R inhibitor)-treated SIH rats. **C, D** The efficiency of microglia elimination by PLX5622 evaluated by decreased microglia marker of Iba-1 using immunofluorescent staining. **E** SBP measurements showing that both MCC950 and PLX5622 had a depressor effect in SIH rats. Data represent the mean \pm SEM; $n = 6$; $*P < 0.05$ vs Ctrl; $\#P < 0.05$ vs SIH.



that prorenin promotes M2-to-M1 polarization *via* NLRP3 over-activation *in vitro*.

Prorenin Increases NLRP3 Activation, and This is Mediated by ROS Overproduction

To investigate whether prorenin directly activates NLRP3 *via* oxidative stress, the ROS scavenger NAC was

administered along with prorenin. Incubation of microglia with prorenin for 24 h elicited a significant increase in ROS production the inflammasomes of function ($n = 6$, $P < 0.05$; Fig. 7A, B). The immunoblot results showed that components of the NLRP3 inflammasome (NLRP3, ASC, caspase-1), pro-IL-1 β , and its mature product IL-1 β were increased in the prorenin-treated group ($n = 6$, $P < 0.05$, Fig. 7C, D). Furthermore, there was increased

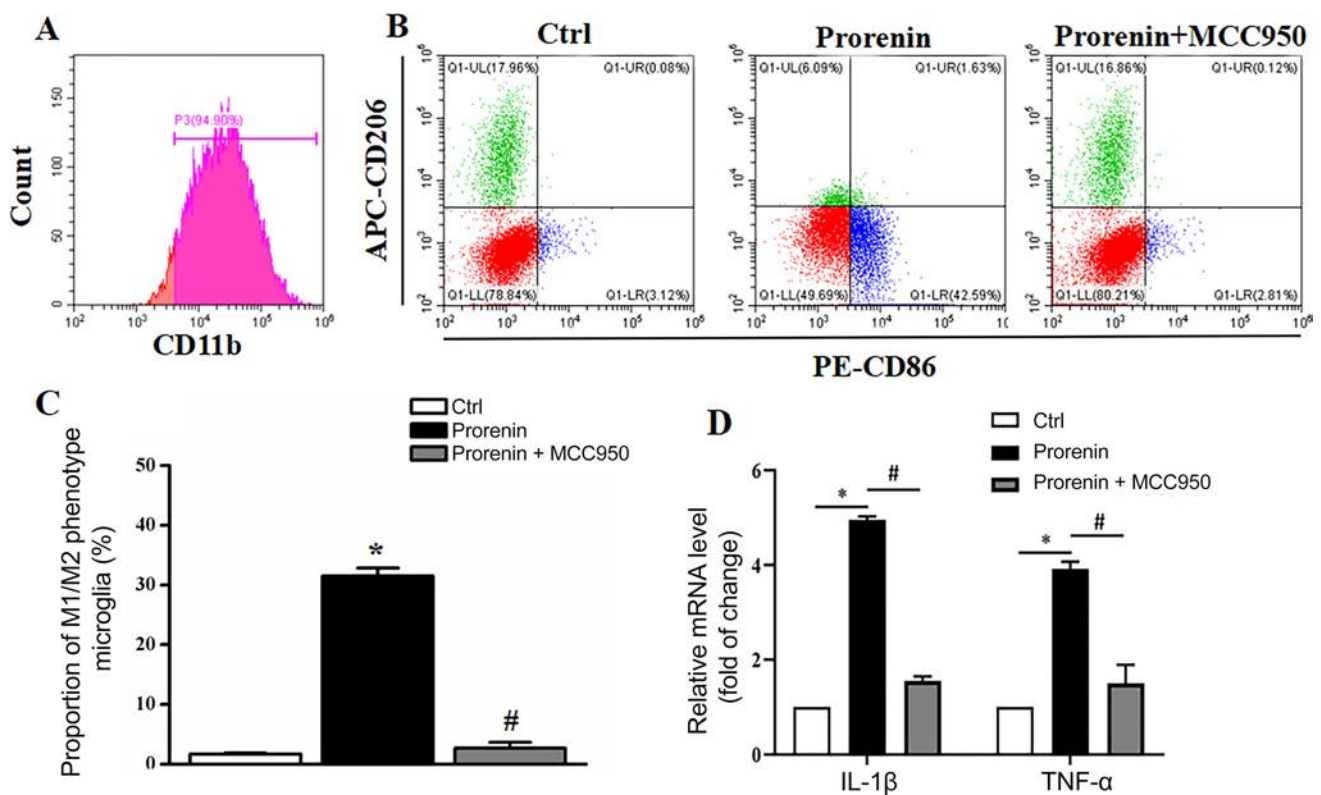


Fig. 6 NLRP3 mediates M1 polarization in prorenin-treated microglia. **A** Analysis of the expression profile of CD11b by flow cytometry confirming that the purity of isolated primary microglia was > 94%. **B** Representative fluorescence-activated cell sorting plots showing the M1 (CD86+) and M2 (CD206+) phenotypes by flow cytometry in Ctrl, prorenin, and prorenin + MCC950-treated microglia. **C** Statistical data showing the proportions of M1/M2

phenotypes in Ctrl, prorenin, and prorenin + MCC950-treated microglia. **D** qRT-PCR analysis showing that the pro-inflammatory factors TNF- α and IL- β are increased in prorenin-treated microglia, while co-treatment with prorenin and MCC950, an NLRP3 inhibitor, decreases the release of TNF- α and IL- β . Data represent the mean \pm SEM; $n = 6$; * $P < 0.05$ vs Ctrl; # $P < 0.05$ vs prorenin.

inflammasome activation in prorenin-treated microglia compared with controls ($n = 6$, $P < 0.05$), as indicated by increased caspase-1 activity (Fig. 7E), and these effects were attenuated by co-treatment with the ROS scavenger NAC. This implied that prorenin increases NLRP3 activation, which is mediated by oxidative stress.

Immunofluorescent staining showed that the co-localization of NLRP3 and ASC components was increased in the prorenin-treated group ($n = 6$, $P < 0.05$, Fig. 8A–C), which was another profile of inflammasome activation. Co-staining for mito-tracker and NLRP3 showed much more NLRP3 translocation from the rest of cytoplasm to mitochondria, which meant that NLRP3 was activated to some extent ($n = 6$, $P < 0.05$, Fig. 8D, E), while the increased co-localization and translocation were attenuated by co-treatment with prorenin and NAC, which resulted in decreased ROS. The above results showed that prorenin

increases ROS-mediated M1 phenotype-switching and NLRP3 activation in microglia *in vitro*.

Discussion

The main purpose of the present study was to study the roles of prorenin in cardiovascular regulation by the RVLM, and further to identify the mechanisms underlying the pressor effect of prorenin. To this end, we measured the expression of endogenous prorenin and NLRP3 complexes in the RVLM of SIH rats. The roles of prorenin in the pathogenesis of SIH were identified using the centrally-administered PRR inhibitor PRO20 [35]. The effect of NLRP3 on BP was investigated using the selective NLRP3 inhibitor MCC950, which specifically inhibits the activation of NLRP3 but not the inflammasomes of AIM2, NLRP4, or NLRP1 [36]. However, with *in vivo* studies it

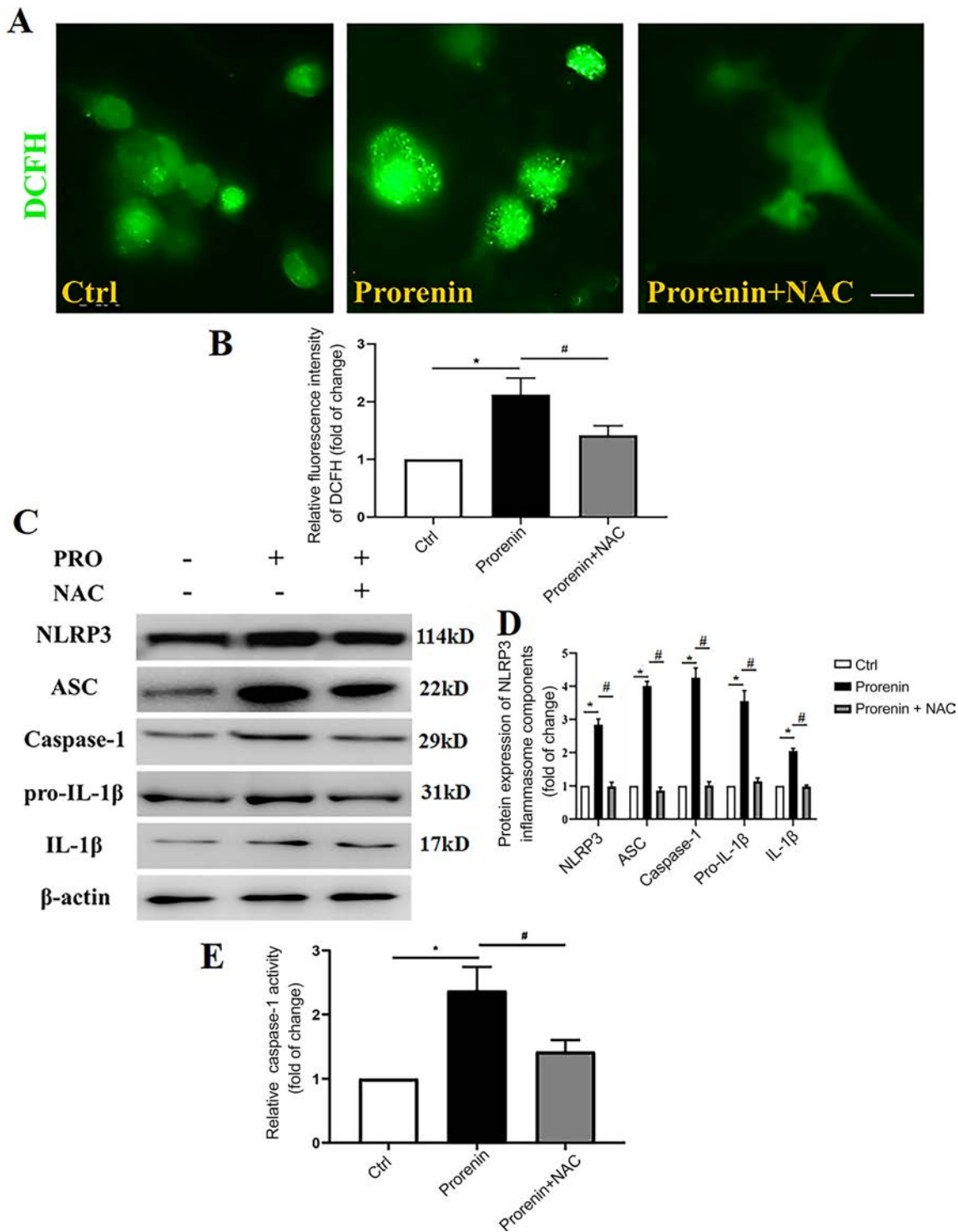


Fig. 7 ROS mediate the prorenin-induced activation of the NLRP3 inflammasome. **A** Representative images of cytoplasmic ROS production in control, prorenin, and prorenin with NAC groups using DCFH-DA-associated fluorescence assays. **B** ROS quantification indicated by fluorescent intensity in the different groups. **C** Immunoblots of the components of the NLRP3 inflammasome (NLRP3,

ASC, and caspase-1), pro-IL-1β, and its mature product IL-1β in prorenin with or without the ROS scavenger NAC. **D** Statistics for experiments as in C. **E** Caspase-1 activity. Data represent the mean ± SEM; *n* = 6, **P* < 0.05 vs Ctrl; #*P* < 0.05 vs prorenin, one-way ANOVA with unpaired *t* test; scale bar, 15 μm.

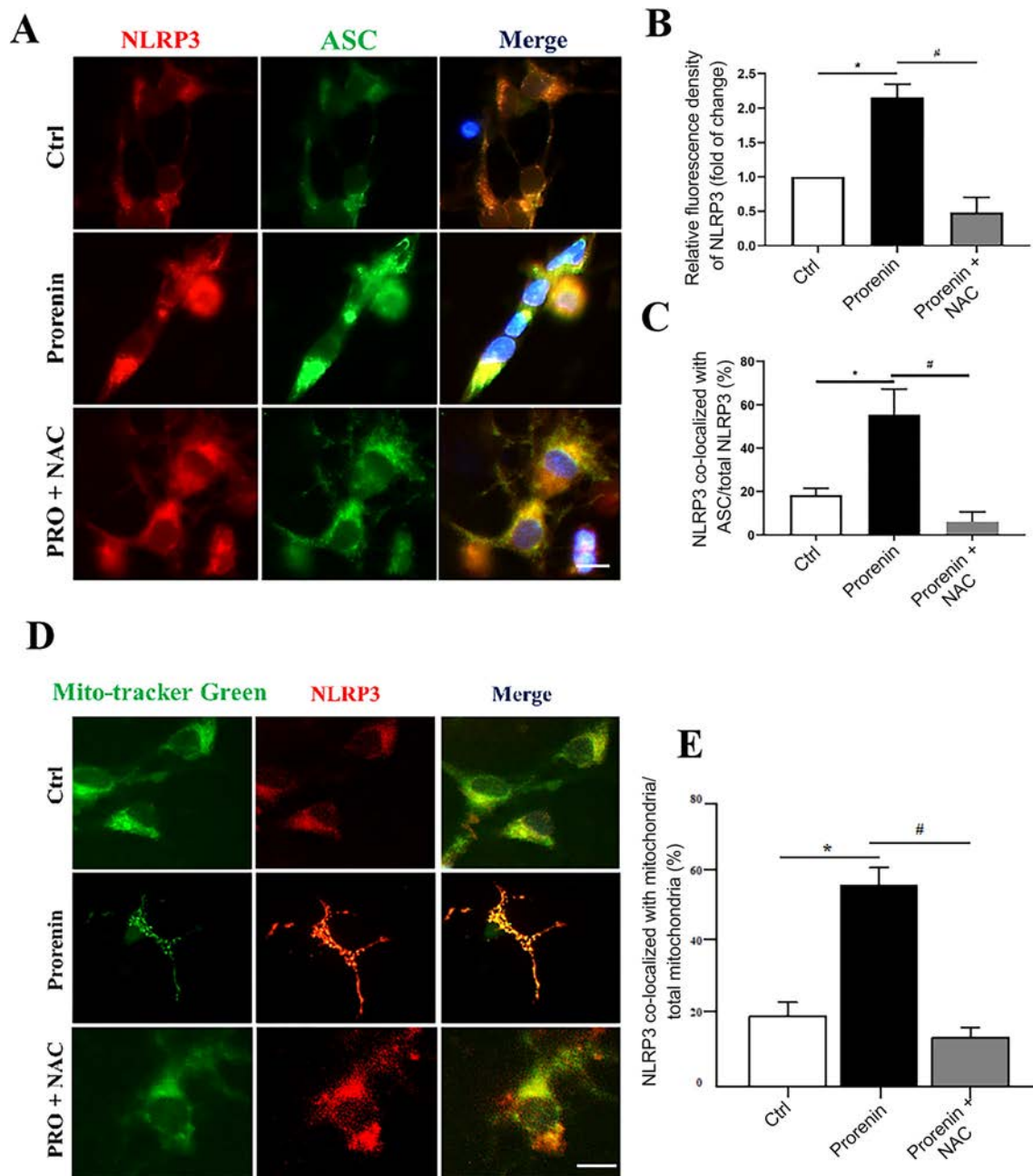


Fig. 8 The increased NLRP3 inflammasome activation and NLRP3 translocation from cytoplasm to mitochondria are attenuated by co-treatment with prorenin and NAC. **A** Representative images of primary microglia co-stained with NLRP3 (red) and ASC (green). **B** Densitometric quantification of immunofluorescent staining for NLRP3 in different groups. **C** Co-localization of NLRP3 and ASC in

control, prorenin, and prorenin plus NAC groups. **D** Representative images of primary microglia stained with NLRP3 (red) and mito-tracker (green). **E** Percentage co-localization of NLRP3 immunoreactivity with mitochondria. Data represent the mean \pm SEM; $n = 6$; $*P < 0.05$ vs Ctrl; $\#P < 0.05$ vs prorenin, one-way ANOVA with unpaired t test; scale bars, 15 μm in **A** and **D**.

has been difficult to reconcile whether these effects are associated with microglia. Accordingly, we used the microglial depletion agent PLX5622 to address this question as reported in the literature [37]. Furthermore, the effect of ROS on triggering NLRP3 activation was elucidated using the ROS scavenger NAC [38] in prorenin-

treated microglia *in vitro*. We used intracisternal infusion to chronically administer pharmacological agents in order to assess their effects as in similar studies [6, 39, 40]. Our major findings were the following: SIH rats manifested increased BP and RSNA, implying increased sympathetic overactivity consistent with stress-induced neurogenic

hypertension; intra-RVLM prorenin and PRR were upregulated, with increased M1 phenotype-switching and NLRP3 inflammasome activation in the RVLM of SIH rats. The microglia-depleting agent PLX5622, the NLRP3 inhibitor MCC950, or the PRR antagonist PRO20 had an antihypertensive effect in SIH rats. NLRP3 in the RVLM was decreased when rats were treated with PLX5622. Furthermore, NLRP3 with mito-tacker staining showed much more NLRP3 translocation from mitochondria to the cytoplasm in prorenin-stimulated microglia *in vitro*. Prorenin increased ROS-triggered M1 phenotype-switching and NLRP3 activation, while MCC950 decreased M1 polarization in prorenin-challenged microglia. We concluded that increased intra-RVLM prorenin might be involved in the pathogenesis of SIH, and is mediated by microglia-derived NLRP3 inflammasome activation.

Microglia supervise and respond rapidly to a change of homeostasis, and play the role of immune response by transition of immune phenotype. Stress in the internal or external environment has profound effects on microglial activation. Microglia express different receptors that allow them to respond to stress hormones including glucocorticoids, epinephrine, and norepinephrine, from both peripheral and central sources [41]. Changes in microglia and related hormones might change the activity of neurons in the CNS. During acute and chronic repetitive psychogenic stress, neural activity might change; for example, restraint water-immersion stress alters the neural activity in the central nucleus of the amygdala in rats [42]. The RVLM is the location of pre-sympathetic neurons. It is a structure that integrates multiple descending fibers and projections to sympathetic preganglionic neurons to regulate sympathetic outflow [43, 44], and our previous study demonstrated that microglia in RVLM of SIH rats are activated, and this contributed to the neuroinflammation in SIH [6].

Stress can activate the local RAS in the brain. The critical importance of brain RAS in regulating sympathetic activity and BP is an emerging field of research [45]. It has been reported that bilateral microinjection of human prorenin into the PVN significantly increases splanchnic sympathetic nerve activity [15]. Shi *et al.* [13] demonstrated that prorenin, the precursor of renin in the RAS component, directly activates hypothalamic microglia *in vitro*, showing that RAS-induced neurogenic hypertension is independent of Ang II. Huber *et al.* found that prorenin incubation with brain neurons dramatically enhances the ROS-AP-1-iNOS signaling pathway; they also suggested that PRR activation in the PVN exerts a sympathoexcitation effect. They provided alternative perspectives on the Ang II-independent effect of local RAS [15]. Given the presence of the blood-brain barrier, brain RAS activity depends on the local synthesis of (pro)renin in the brain rather than uptake from blood.

It has been suggested that the brain synthesizes large quantities of prorenin, the inactive precursor of renin [9]. In the brain, it is assumed that prorenin binds to the PRR, which results in prosegment unfolding, thus allowing Ang-I-generating activity without prosegment removal (non-proteolytic activation) [10, 11]. Contrepas *et al.* [46] using *in situ* hybridization showed a wide distribution of PRR mRNA in adult mouse brain, including the RVLM, PVN, supraoptic nucleus, nucleus of the tractus solitarius, and subformal organ critical for their involvement in the central regulation of cardiovascular function and fluid volume homeostasis. Although neither our studies nor those of others can conclude that pro(re)nin is generated in the CNS, they support the hypothesis that pro(re)nin plays roles in the brain.

Takahashi *et al.* [47] using immunocytochemistry showed that (P)RR protein is expressed in the paraventricular and supraoptic nuclei of the human hypothalamus, and in anterior pituitary cells of the human brain. Evidence for the presence of PRR in the human brain, both in neurons and microglia, and its positive correlation with SBP provides a foundation for future functional studies on brain PRR in human hypertension. Functionally, it has been demonstrated that PRR antagonists are effective in animal models of hypertension [10]. Furthermore, the expression of PRR in neurons and microglia suggests its possible role in regulating not only neuronal activity but also inflammation and hypertension, a new research avenue in humans [48].

Previous investigators have demonstrated that prorenin and PRR are involved in the pathogenesis of renal and cardiac hypertrophy, accompanied by local oxidative stress, inflammation, and NLRP3-IL-1 β -related signals [48, 49]. In chronic inflammation, NLRP3 acts as the primary activator of inflammation, which can trigger the cascade production of other pro-inflammatory cytokines [50, 51]. In salt-induced pre-hypertensive rats, NLRP3 inflammasome activation is associated with hypertension in the PVN [36, 52]. We found that prorenin increased ROS production and triggered microglial M1 phenotype-switching and NLRP3 activation in primary cultured microglia. Furthermore, NLRP3 with mito-tacker staining showed that the translocation of NLRP3 from mitochondria to the cytoplasm was increased in prorenin-challenged microglia. These effects were abolished by co-treatment with the ROS scavenger NAC, an anti-oxidant and anti-inflammatory agent [53]. It should be noted that NAC directly scavenges ROS *via* its sulfhydryl active group; in addition, NAC acts as a glutathione precursor which induces production of the endogenous antioxidant glutathione, thereby reducing the formation of mitochondrial reactive nitrogen species (mROS) [54]. So, NAC can ameliorate mitochondrial dysfunction and decrease oxidative stress in microglia.

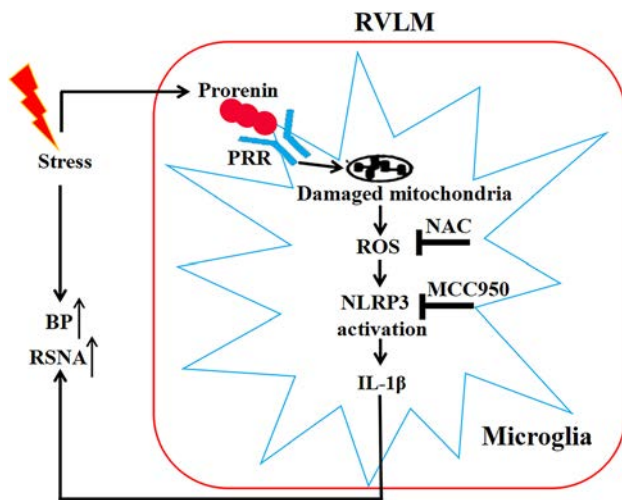


Fig. 9 Schematic diagram illustrating the putative mechanisms of the pressor effect of prorenin *via* ROS-triggered microglia-derived NLRP3-IL-1 β activation in the RVLM. PRR, (pro)renin receptor; ROS, reactive oxygen species; NAC, N-acetylcysteine; NLRP3, NLR family pyrin domain containing 3; ASC, apoptosis-associated speck-like protein containing a caspase recruitment domain; IL-1 β , interleukin-1 β ; BP, blood pressure; RSNA, renal sympathetic nerve activity.

Ultrastructural microscopic imaging showed swollen mitochondria with disorientated and broken cristae in prorenin-stimulated microglia, while NAC attenuated this injury (Fig. S5). However, the relationship between mROS and NLRP3 activation requires further investigation.

In summary, external environmental stress upregulates prorenin and PRR expression in the RVLM of stress-exposed rats. ROS overproduction from injured mitochondria induces activation of the microglial NLRP3 inflammasome, after which much more inflammatory factors are released. The neuroinflammation couples with the increased sympathetic flow to underline the pathogenesis of SIH. Blockade of the prorenin-ROS-NLRP3 pathway attenuates this effect (Fig. 9).

Acknowledgements This work was supported by the National Natural Science Foundation of China (81770423) and the Shanghai Municipal Natural Science Foundation (13ZR1403400).

Conflict of interest The authors confirm that there are no conflicts of interest.

Open Access This article is licensed under a Creative Commons Attribution 4.0 International License, which permits use, sharing, adaptation, distribution and reproduction in any medium or format, as long as you give appropriate credit to the original author(s) and the source, provide a link to the Creative Commons licence, and indicate if changes were made. The images or other third party material in this article are included in the article's Creative Commons licence, unless

indicated otherwise in a credit line to the material. If material is not included in the article's Creative Commons licence and your intended use is not permitted by statutory regulation or exceeds the permitted use, you will need to obtain permission directly from the copyright holder. To view a copy of this licence, visit <http://creativecommons.org/licenses/by/4.0/>.

References

- Wang LH, Dong T, Liu BB, Zhao XD, Chen JW, Murao K, *et al*. Contribution of the renin-angiotensin system in chronic foot-shock induced hypertension in rats. *Life Sci* 2015, 121: 135–144.
- Young CN, Davissou RL. Angiotensin-II, the brain, and hypertension: An update. *Hypertension* 2015, 66: 920–926.
- Deng Y, Tan X, Li ML, Wang WZ, Wang YK. Angiotensin-converting enzyme 2 in the rostral ventrolateral medulla regulates cholinergic signaling and cardiovascular and sympathetic responses in hypertensive rats. *Neurosci Bull* 2019, 35: 67–78.
- Xia CM, Shao CH, Xin L, Wang YR, Ding CN, Wang J, *et al*. Effects of melatonin on blood pressure in stress-induced hypertension in rats. *Clin Exp Pharmacol Physiol* 2008, 35: 1258–1264.
- Zhang CR, Xia CM, Jiang MY, Zhu MX, Zhu JM, Du DS, *et al*. Repeated electroacupuncture attenuating of apelin expression and function in the rostral ventrolateral medulla in stress-induced hypertensive rats. *Brain Res Bull* 2013, 97: 53–62.
- Du D, Hu L, Wu J, Wu Q, Cheng W, Guo Y, *et al*. Neuroinflammation contributes to autophagy flux blockage in the neurons of rostral ventrolateral medulla in stress-induced hypertension rats. *J Neuroinflammation* 2017, 14: 169.
- Fang X, Sun D, Wang Z, Yu Z, Liu W, Pu Y, *et al*. MiR-30a positively regulates the inflammatory response of microglia in experimental autoimmune encephalomyelitis. *Neurosci Bull* 2017, 33: 603–615.
- Biancardi VC, Son SJ, Ahmadi S, Filosa JA, Stern JE. Circulating angiotensin II gains access to the hypothalamus and brain stem during hypertension via breakdown of the blood-brain barrier. *Hypertension* 2014, 63: 572–579.
- Waki H, Gouraud SS, Maeda M, Raizada MK, Paton JF. Contributions of vascular inflammation in the brainstem for neurogenic hypertension. *Respir Physiol Neurobiol* 2011, 178: 422–428.
- Liao B, Zhao W, Beers DR, Henkel JS, Appel SH. Transformation from a neuroprotective to a neurotoxic microglial phenotype in a mouse model of ALS. *Exp Neurol* 2012, 237: 147–152.
- Zubcevic J, Jun JY, Lamont G, Murca TM, Shi P, Yuan W, *et al*. Nucleus of the solitary tract (pro)renin receptor-mediated anti-hypertensive effect involves nuclear factor-kappaB-cytokine signaling in the spontaneously hypertensive rat. *Hypertension* 2013, 61: 622–627. 30.
- Zhu T, Miller AG, Deliyanti D, Berka DR, Agrotis A, Campbell DJ, *et al*. Prorenin stimulates a pro-angiogenic and pro-inflammatory response in retinal endothelial cells and an M1 phenotype in retinal microglia. *Clin Exp Pharmacol Physiol* 2015, 42: 537–548.
- Shi P, Grobe JL, Desland FA, Zhou G, Shen XZ, Shan Z, *et al*. Direct pro-inflammatory effects of prorenin on microglia. *PLoS One* 2014, 9: e92937.
- Uraoka M, Ikeda K, Nakagawa Y, Koide M, Akakabe Y, Nakano-Kurimoto R, *et al*. Prorenin induces ERK activation in endothelial cells to enhance neovascularization independently of the renin-angiotensin system. *Biochem Biophys Res Commun* 2009, 390: 1202–1207.

15. Huber MJ, Basu R, Cecchetti C, Cuadra AE, Chen QH, Shan Z. Activation of the (pro)renin receptor in the paraventricular nucleus increases sympathetic outflow in anesthetized rats. *Am J Physiol Heart Circ Physiol* 2015, 309: H880–887.
16. Nguyen G, Delarue F, Burckle C, Bouzahir L, Gillier T, Sraer JD. Pivotal role of the renin/prorenin receptor in angiotensin II production and cellular responses to renin. *J Clin Invest* 2002, 109: 1417–1427.
17. Cruciat CM, Ohkawara B, Acebron SP, Karaulanov E, Reinhard C, Ingelfinger D, *et al.* Requirement of prorenin receptor and vacuolar H⁺-ATPase-mediated acidification for Wnt signaling. *Science* 2010, 327: 459–463.
18. Hu L, Zhang S, Wen H, Liu T, Cai J, Du D, *et al.* Melatonin decreases M1 polarization *via* attenuating mitochondrial oxidative damage depending on UCP2 31 pathway in prorenin-treated microglia. *PLoS One* 2019, 14: e0212138.
19. Rawat P, Teodorof-Diedrich C, Spector SA. Human immunodeficiency virus Type-1 single-stranded RNA activates the NLRP3 inflammasome and impairs autophagic clearance of damaged mitochondria in human microglia. *Glia* 2019, 67: 802–824.
20. Kim MJ, Jung HO. Pulmonary hypertension: a long-term risk stratifier in primary mitral regurgitation. *Ann Transl Med* 2016, 4: 541.
21. Rodriguez-Iturbe B, Pons H, Johnson RJ. Role of the immune system in hypertension. *Physiol Rev* 2017, 97: 1127–1164.
22. Dai Y, Zhang J, Xiang J, Li Y, Wu D, Xu J. Calcitriol inhibits ROS-NLRP3-IL-1 β signaling axis *via* activation of Nrf2-antioxidant signaling in hyperosmotic stress stimulated human corneal epithelial cells. *Redox Biol* 2018, 21: 101093.
23. Zhou R, Yazdi AS, Menu P, Tschopp J. A role for mitochondria in NLRP3 inflammasome activation. *Nature* 2011, 469: 221–225.
24. Kim SM, Kim YG, Kim DJ, Park SH, Jeong KH, Lee YH, *et al.* Inflammasome-independent role of NLRP3 mediates mitochondrial regulation in renal injury. *Front Immunol* 2018, 9: 2563.
25. Li W, Sullivan MN, Zhang S, Worker CJ, Xiong Z, Speth RC, *et al.* Intracerebroventricular infusion of the (Pro)renin receptor antagonist PRO20 attenuates deoxycorticosterone acetate-salt-induced hypertension. *Hypertension* 2015, 65: 352–361.
26. Slusarczyk J, Trojan E, Glombik K, Piotrowska A, Budziszewska B, Kubera M, *et al.* Targeting the NLRP3 inflammasome-related pathways *via* tianeptine treatment-suppressed microglia polarization to the M1 phenotype in lipopolysaccharide-stimulated cultures. *Int J Mol Sci* 2018, 19: 1965.
27. Paxinos G, Watson CR, Emson PC. AChE-stained horizontal sections of the rat brain in stereotaxic coordinates. *J Neurosci Methods* 1980, 3: 129–149.
28. Grinshpun J, Tveria L, Fleisher-Berkovich S. Differential regulation of prostaglandin synthesis in neonatal rat microglia and astrocytes by somatostatin. *Eur J Pharmacol* 2008, 584: 312–317.
29. Bhat SA, Sood A, Shukla R, Hanif K. AT2R Activation prevents microglia pro-inflammatory activation in a NOX-dependent manner: inhibition of PKC activation and p47(phox) phosphorylation by PP2A. *Mol Neurobiol* 2019, 56: 3005–3023.
30. Lv J, Su W, Yu Q, Zhang M, Di C, Lin X, *et al.* Heme oxygenase-1 protects airway epithelium against apoptosis by targeting the proinflammatory NLRP3-RXR axis in asthma. *J Biol Chem* 2018, 293: 18454–18465.
31. Sarkar S, Malovic E, Plante B, Zenitsky G, Jin H, Anantharam V, *et al.* Rapid and refined CD11b magnetic isolation of primary microglia with enhanced purity and versatility. *J Vis Exp* 2017, 122: e55364.
32. Wei J, Besner GE. M1 to M2 macrophage polarization in heparin-binding epidermal growth factor-like growth factor therapy for necrotizing enterocolitis. *J Surg Res* 2015, 197: 126–138.
33. Wu JX, Tong L, Hu L, Xia CM, Li M, Chen QH, *et al.* Upregulation of Nav1.6 expression in the rostral ventrolateral medulla of stress-induced hypertensive rats. *Hypertens Res* 2018, 41: 1013–1022.
34. Rice RA, Pham J, Lee RJ, Najafi AR, West BL, Green KN. Microglial repopulation resolves inflammation and promotes brain recovery after injury. *Glia* 2017, 65: 931–944.
35. Xu C, Lu A, Lu X, Zhang L, Fang H, Zhou L, *et al.* Activation of renal (pro)renin receptor contributes to high fructose-induced salt sensitivity. *Hypertension* 2017, 69: 339–348.
36. Krishnan SM, Ling YH, Huuskos BM, Ferens DM, Saini N, Chan CT, *et al.* Pharmacological inhibition of the NLRP3 inflammasome reduces blood pressure, renal damage, and dysfunction in salt-sensitive hypertension. *Cardiovasc Res* 2019, 115: 776–787.
37. Elmore MR, Najafi AR, Koike MA, Dagher NN, Spangenberg EE, Rice RA, *et al.* Colony-stimulating factor 1 receptor signaling is necessary for microglia viability, unmasking a microglia progenitor cell in the adult brain. *Neuron* 2014, 82: 380–397.
38. Rodriguez-Perez AI, Borrajo A, Rodriguez-Pallares J, Guerra MJ, Labandeira-Garcia JL. Interaction between NADPH-oxidase and Rho-kinase in angiotensin II-induced microglial activation. *Glia* 2015, 63: 466–482.
39. Wu KL, Chan SH, Chan JY. Neuroinflammation and oxidative stress in rostral ventrolateral medulla contribute to neurogenic hypertension induced by systemic inflammation. *J Neuroinflammation* 2012, 9: 212.
40. Chao YM, Lai MD, Chan JY. Redox-sensitive endoplasmic reticulum stress and autophagy at rostral ventrolateral medulla contribute to hypertension in spontaneously hypertensive rats. *Hypertension* 2013, 61: 1270–1280.
41. Frank MG, Fonken LK, Watkins LR, Maier SF. Microglia: Neuroimmune-sensors of stress. *Semin Cell Dev Biol* 2019, 94: 176–185.
42. He F, Ai H, Wang M, Wang X, Geng X. Altered neuronal activity in the central nucleus of the amygdala induced by restraint water-immersion stress in rats. *Neurosci Bull* 2018, 34: 1067–1076.
43. Lohmeier TE, Iliescu R. Chronic lowering of blood pressure by carotid baroreflex activation: mechanisms and potential for hypertension therapy. *Hypertension* 2011, 57: 880–886.
44. Guyenet PG. The sympathetic control of blood pressure. *Nat Rev Neurosci* 2006, 7: 335–346.
45. Iulita MF, Duchemin S, Vallerand D, Barhoumi T, Alvarez F, Istomine R, *et al.* CD4⁺ regulatory T lymphocytes prevent impaired cerebral blood flow in angiotensin II-induced hypertension. *J Am Heart Assoc* 2019, 8: e009372.
46. Contrepas A, Walker J, Koulakoff A, Franek KJ, Qadri F, Giaume C *et al.* (2009) A role of the (pro)renin receptor in neuronal cell differentiation. *Am J Physiol Regul Integr Comp Physiol* 297:R250–257.
47. Takahashi K, Hiraishi K, Hirose T, Kato I, Yamamoto H, Shoji I *et al.* (2010) Expression of (pro)renin receptor in the human brain and pituitary, and co-localisation with arginine vasopressin and oxytocin in the hypothalamus. *J Neuroendocrinol* 22:453–459.
48. Cooper SG, Trivedi DP, Yamamoto R, Worker CJ, Feng CY, Sorensen JT, *et al.* Increased (pro)renin receptor expression in the subfornical organ of hypertensive humans. *Am J Physiol Heart Circ Physiol* 2018, 314: H796–H804.
49. Campbell DJ. Critical review of prorenin and (pro)renin receptor research. *Hypertension* 2008, 51: 1259–1264.
50. Harrison DG, Guzik TJ, Lob HE, Madhur MS, Marvar PJ, Thabet SR, *et al.* Inflammation, immunity, and hypertension. *Hypertension* 2011, 57: 132–140.
51. Agarwal D, Haque M, Sriramula S, Mariappan N, Pariaut R, Francis J. Role of proinflammatory cytokines and redox homeostasis in exercise-induced delayed progression of hypertension

- in spontaneously hypertensive rats. *Hypertension* 2009, 54: 1393–1400.
52. Wang ML, Kang YM, Li XG, Su Q, Li HB, Liu KL, *et al.* Central blockade of NLRP3 reduces blood pressure *via* regulating inflammation microenvironment and neurohormonal excitation in salt-induced prehypertensive rats. *J Neuroinflammation* 2018, 15: 95.
53. Cazzola M, Calzetta L, Facciolo F, Rogliani P, Matera MG. Pharmacological investigation on the anti-oxidant and anti-inflammatory activity of N-acetylcysteine in an *ex vivo* model of COPD exacerbation. *Respir Res* 2017, 18: 26.
54. Gil-Martinez AL, Cuenca L, Sanchez C, Estrada C, Fernandez-Villalba E, Herrero MT. Effect of NAC treatment and physical activity on neuroinflammation in subchronic Parkinsonism; is physical activity essential? *J Neuroinflammation* 2018, 15: 328.



A Whole-brain Map of Long-range Inputs to GABAergic Interneurons in the Mouse Caudal Forelimb Area

Zhuonan Duan^{1,2} · Anan Li^{1,2,3} · Hui Gong^{1,2,3} · Xiangning Li^{1,2,3}

Received: 19 July 2019 / Accepted: 4 October 2019 / Published online: 19 January 2020
© Shanghai Institutes for Biological Sciences, CAS 2020

Abstract The caudal forelimb area (CFA) of the mouse cortex is essential in many forelimb movements, and diverse types of GABAergic interneuron in the CFA are distinct in the mediation of cortical inhibition in motor information processing. However, their long-range inputs remain unclear. In the present study, we combined the monosynaptic rabies virus system with Cre driver mouse lines to generate a whole-brain map of the inputs to three major inhibitory interneuron types in the CFA. We discovered that each type was innervated by the same upstream areas, but there were quantitative differences in the inputs from the cortex, thalamus, and pallidum. Comparing the locations of the interneurons in two subregions of the CFA, we discovered that their long-range inputs were remarkably different in distribution and proportion. This whole-brain mapping indicates the existence of parallel pathway organization in the forelimb subnetwork and provides insight into the inhibitory processes in forelimb movement to reveal the structural architecture underlying the functions of the CFA.

Electronic supplementary material The online version of this article (<https://doi.org/10.1007/s12264-019-00458-6>) contains supplementary material, which is available to authorized users.

✉ Xiangning Li
lixiangning@mail.hust.edu.cn

- ¹ Britton Chance Center for Biomedical Photonics, Wuhan National Laboratory for Optoelectronics–Huazhong University of Science and Technology, Wuhan 430074, China
- ² Ministry of Education Key Laboratory for Biomedical Photonics, School of Engineering Sciences, Huazhong University of Science and Technology, Wuhan 430074, China
- ³ Huazhong University of Science and Technology–Suzhou Institute for Brainmatics, Suzhou 215125, China

Keywords Forelimb area · Input circuit · Interneuron · Parvalbumin · Somatostatin · Vasoactive intestinal peptide

Introduction

Complex movement patterns, such as forelimb motion, require the coordination of many muscles and joint movements that is specifically associated with neural activity in the cortical forelimb area (CFA) [1–3]. Cytoarchitectonic, electrophysiological, and behavioral experiments have shown that forelimb movements are regulated by several cortical areas, including the CFA [4, 5]. In mice, the CFA includes a portion of the primary motor cortex (CFA_{MOP}) and somatosensory cortex (CFA_{SSp}), which are organized into two central nodes of the cortical forelimb subnetwork [6]. Each cortical area is significantly associated with different muscle groups and specific phases of forelimb motor tasks [3, 4, 7–9].

GABAergic neurons in the neocortex can be classified into three main groups: parvalbumin-positive (PV+), somatostatin-positive (SOM+), and vasoactive intestinal peptide-positive (VIP+). Physiological and functional studies have shown that different cortical interneuron types exhibit distinct and diverse activities in different behavioral states [10] and the long-range inputs to GABAergic interneurons are important in visual, auditory, and somatosensory cortical circuits [11–13]; however, the long-range inputs to different interneuron types in the CFA remain unclear. To illuminate their connective circuit mechanisms in mammalian forelimb subnetworks, it is imperative to map the synaptic inputs to CFA interneurons, including both local and long-range inputs, at the whole-brain level. Conventional neural tracing using retrograde chemical tracers has indicated that the CFA integrates

long-range inputs from several sources including cortical areas and subcortical nuclei [6]; however, these methods have not demonstrated any input connections to specific types of neuron. Mouse lines with different kinds of Cre driver in conjunction with the monosynaptic rabies virus (RV) system [14, 15] provide a stable and reliable approach to map the long-range inputs to GABAergic neurons in the target region at the whole-brain level [16–20]. Therefore, we used monosynaptic RV in the CFA_{MOP} and CFA_{SSp} of three GABAergic Cre lines to investigate the long-range inputs to different interneurons in the CFA.

Materials and Methods

Animals

VIP-Cre [B6J.Cg-Vip^{tm1(cre)Zjh}/AreckJ], PV-Cre [B6;129P2-Pvalb^{tm1(cre)Arbr}/J], and SOM-Cre [B6N.Cg-Sst^{tm2.1(cre)Zjh}/J] transgenic mice were purchased from The Jackson Laboratory (Bar Harbor, ME). All mice were housed in an experimental animal barrier environment with a 12-h light/dark cycle and food and water *ad libitum*. Only adult mice (2–3 months old) were used. All experimental procedures were approved by the Animal Experimentation Ethics Committee of Huazhong University of Science and Technology.

Surgery and Stereotaxic Viral Injection

The mice were anesthetized by intraperitoneal (i.p.) injection of 10% ethylurethane, 2% chloral hydrate, and 1.7 mg/mL xylazine mixed in 0.9% NaCl (0.1 mL/10 g body weight). Then the anesthetized mice were mounted on a stereotaxic holder (item 68030, RWD Life Science, Shenzhen, China), and the angle of the skull was adjusted before craniotomy. We set the bregma and lambda points at the same level and the left and right hemispheres were symmetrical with the center line on the plane. A small hole (~0.5 mm diameter) was bored through the skull above the target region using a dental drill. All the viral tools were injected through a glass micropipette connected to a pressure injection pump (Nanoject II: Drummond Scientific Co., Broomall, PA) at 35 nL/min. After the operation, the wound was treated with lincomycin hydrochloride to prevent inflammation.

The monosynaptic RV system was as described previously [14, 21], and all the viral tools used were provided by BrainVTA Co., Ltd. (Wuhan, China). We first injected 150 nL adeno-associated helper viruses (AAV helper) into the CFA_{MOP} upper limb region [antero-posterior (AP), 1.34 mm from bregma; medio-lateral (ML), 1.75 mm; dorso-ventral (DV), –1.5 mm], or the CFA_{SSp} upper limb region

(AP, 0.14 mm; ML, 2.2 mm; DV, –1.4 mm) in PV-Cre, SOM-Cre, and VIP-Cre mice. The AAV helper was mixed with rAAV2/9-Ef1 α -DIO-BFP-2a-TVA-WPRE-pA and rAAV2/9-Ef1 α -DIO-RG-WPRE-pA at a ratio of 1:2, and the final titer was 2.30×10^{12} viral genomes/mL. Three weeks later, we repeated the operation and injected 300 nL RV- Δ G-EnvA-EGFP in the same area at a titer of 2.00×10^8 infectious units/mL.

Histology

Approximately one week after RV injection, mice were anesthetized and perfused with 0.01 mol/L phosphate-buffered saline (PBS; Sigma-Aldrich, St. Louis, MO) and 4% paraformaldehyde (PFA; Sigma-Aldrich) in 0.01 mol/L PBS. The perfused brains were immersed in 4% PFA for 24 h and then placed in 0.01 mol/L PBS for 4 h at 4 °C before embedding. The procedures of agarose embedding were based on previous research [22]. Briefly, agarose type I (Sigma-Aldrich) was oxidized by stirring in 10 mmol/L sodium periodate (Sigma-Aldrich) for 3 h at room temperature and the oxidized product was then washed repeatedly in PBS at a final concentration of 5%. The brains were embedded in melted oxidized agarose using a silicone mold and maintained at 4 °C for solidification. The embedded brains were sectioned at 50 μ m on a vibrating microtome (Leica VT1200S; Leica Microsystems, Wetzlar, Germany).

For immunohistochemistry, selected sections were blocked with 5% bovine serum albumin (BSA) containing 0.3% Triton in 0.01 mol/L PBS. One hour later, the following primary antibodies were added and incubated for ~12 h at 4 °C: anti-PV (1:1,000, mouse, Millipore, MAB1572; Burlington, MA), anti-SOM (1:200, goat, Santa Cruz, sc-7819; Dallas, TX), and anti-ChAT (1:500, goat, Millipore, AB144P). After rinsing five times in PBS, these sections were incubated with the following fluorophore-conjugated secondary antibodies for 2 h at room temperature: donkey anti-goat (Alexa Fluor 647, 1:500, Invitrogen, Waltham, MA) and goat anti-mouse (Alexa Fluor 647, 1:500, Invitrogen). All the antibodies were diluted in 5% BSA. DAPI at 5 μ g/mL was used to stain nuclei.

Microscopy and Analysis

For whole-brain input counting, 50- μ m sections were mounted with 50% glycerol and visualized using a slide-scanning microscope (\times 4, 0.2 NA objective; Nikon, Tokyo, Japan). For imaging starter cells and immunohistochemistry, selected sections were mounted with 50% glycerol and then imaged on an inverted confocal microscope (\times 10, 0.45 NA objective, Zeiss LSM 710; \times 20,

0.75 NA objective Zeiss LSM 710; Oberkochen, Germany).

The RV-GFP-labeled input neurons were manually counted using the Fiji (NIH, Bethesda, MD) Cell Counter plug-in, and their locations were defined according to the Allen brain atlas [23]. All the abbreviations for brain region used here are listed in Supplementary Table S1. The proportion of input from each brain area was normalized to the total number of long-range inputs.

Statistics

All the graphs were generated in GraphPad Prism v.8.02 (GraphPad Software, San Diego, CA) and statistical results are presented as the mean \pm SEM. The individual data points are shown in histograms and though the data distributions were assumed to be normal, this was not formally tested. The two-tailed Student's *t*-test and one-way analysis of variance (ANOVA) followed by Tukey's *post-hoc* tests were performed using SPSS (version 23; IBM, Armonk, NY). To quantify the similarity in input patterns, we calculated Pearson's correlation coefficients and the significance level was set to $P < 0.05$.

Results

Tracing Monosynaptic Inputs to Different Interneuron Types in the CFA

To label the whole-brain input connection patterns of three interneuron types in the CFA, we used three Cre lines that expressed Cre recombinase in PV+, SOM+, and VIP+ neurons. We delivered AAV as a helper virus carrying specific DNA sequences that coded TVA, BFP, and G proteins (AAV-DIO-BFP-TVA and AAV-DIO-RG) into mouse brains (Fig. 1A,B). The injection sites of all samples were concentrated in the CFA (Fig. 1C). The interneurons that demonstrated Cre recombinase expressed BFP, the avian receptor TVA, and rabies glycoprotein (RG). Three weeks later, we delivered RV-EnvA-GFP into the same region (Fig. 1A,B). Only neurons that expressed TVA and RG simultaneously were infected by RV and spread the virus retrogradely to presynaptic cells. One week after RV injection, we imaged the brains. In each group, the distribution of the majority of starter cells was restricted to the CFA (Fig. 1D). Local input cells in the CFA were labeled with EGFP, while the neurons that co-expressed BFP and EGFP were defined as starter cells (Fig. 1E).

To dissect the layer-specific distribution of starter cells across the three major interneuron types, we measured the distance between each starter cell and the pial surface (Fig. 1F). PV+ starter cells were found throughout the

cortical layers with most located in superficial layers; SOM+ starter cells were primarily distributed in layer V, consistent with the known distribution of SOM+ interneurons in the neocortex [24]; and VIP+ starter cells in the CFA were primarily detected in the superficial layers.

Whole-brain Mapping of Long-range Inputs to Three Interneuron Types in the CFA

Whole-brain mapping of the monosynaptic input neurons was accomplished in 62 discrete nuclei in the three kinds of mice. Representative coronal sections showed that all three interneuron types in the CFA received major long-range inputs from ipsilateral cortical, thalamic, and cerebral nuclei and contralateral cortex that had already been identified (Fig. 2A). We quantified the GFP-labeled neurons in coronal sections of labeled mice. According to the standard mouse brain atlas [23], there were 48,249 PV-Cre (3 mice), 24,706 SOM-Cre (4 mice), and 11,925 VIP-Cre (3 mice) long-range input neurons. Although the CFA_{MOP} contained a large number of GFP-labeled neurons, we could not confirm that these were directly rabies-infected interneurons (TVA+ only) at the injection site.

The ipsilateral cortex was the most important source of long-range input to the three types of interneuron in the CFA_{MOP}, accounting for $\sim 75\%$ of the total long-range inputs (VIP-Cre, $74.5\% \pm 6.4\%$; PV-Cre, $74.4\% \pm 4.2\%$; SOM-Cre, $75.0\% \pm 4.1\%$; Fig. 2B). The majority of the ipsilateral input was derived from the motor-sensory cortex and the thalamus, while fewer input neurons were located in the frontal pole cortex, orbital cortex, cerebral nuclei, hypothalamus, midbrain, pons, and other cortical regions (Fig. 2B). The input neurons in the contralateral hemisphere were mainly distributed in the motor-sensory and orbital cortex; however, almost no RV-GFP-labeled neurons were found in the subcortical area (Fig. 2A, C).

Cortical Input to Three Interneuron Types in the CFA

The cortical PV+, SOM+, and VIP+ interneurons were preferentially located in different cortical layers (Fig. 1E), and previous studies established that cortico-cortical projections have layer-specific patterns [25]. To further analyze the layer-specific patterns of cortical inputs to the CFA, we separated the main motor-sensory cortical inputs into superficial (layers II and III) and deep (V and VI) populations. Deep and superficial cortical inputs were detected in multiple regions, such as the secondary motor cortex, the nose and mouth areas of primary sensory cortex, the upper and lower limb areas of primary sensory cortex, the secondary somatosensory area (SSs), and the barrel cortex (Fig. 2D). A few input neurons were found in layer

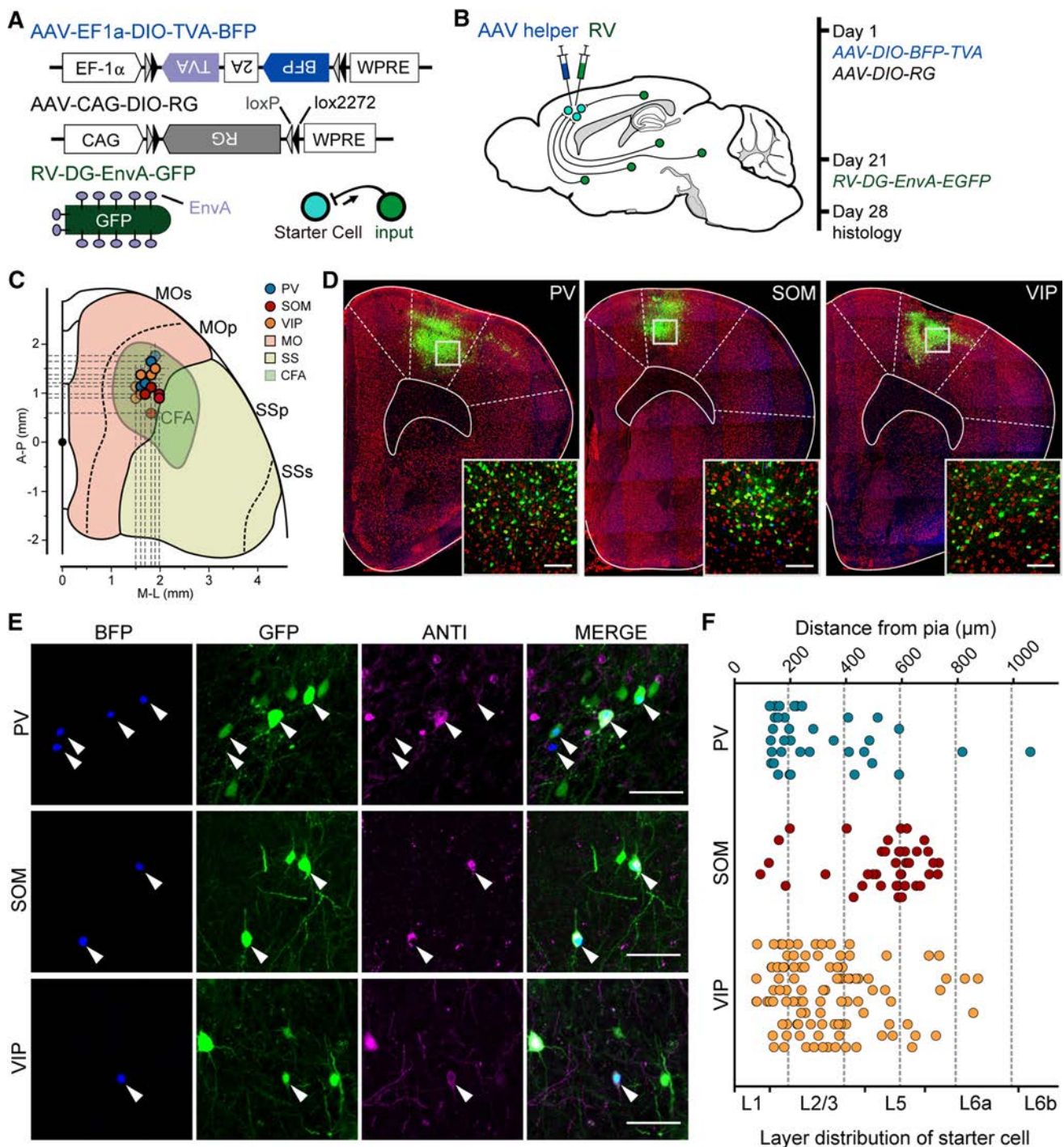


Fig. 1 Strategies for tracing monosynaptic inputs to three interneuron types in the CFA. **A** Recombinant AAV helper viruses and genetically-modified RV. **B** Experimental design. **C** Diagram showing the central coordinates of every injection site in the CFA. Each colored spot indicates one animal, and different colors indicate different Cre lines. **D** Coronal sections showing the injection site and the distribution of starter cells in each group (scale bars, 100 μ m).

E Starter cells of the three interneuron types (arrowheads, scale bars, 50 μ m). **F** Individual layer-specific distribution of starter cells in the three interneuron types. Each line indicates one coronal section (upper x-axis, distance from pia; lower x-axis, layer distribution of each starter cell; each colored spot indicates a single starter cell; blue, PV+; red, SOM+; orange, VIP+ starter cells).

IV, particularly in the nose and mouth areas of primary sensory cortex and SSs, and we clustered them into the superficial input group. Our quantitative analysis showed

no significant difference between the proportion of deep and superficial cortical inputs to each interneuron type (Fig. 2D). Intra-telencephalic neurons, which projected to

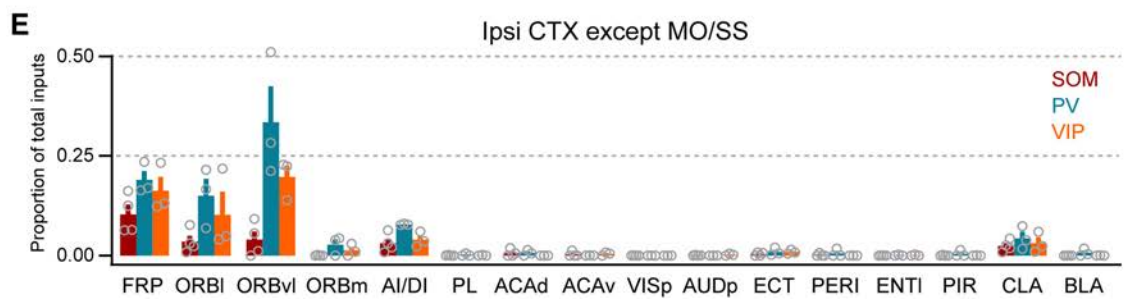
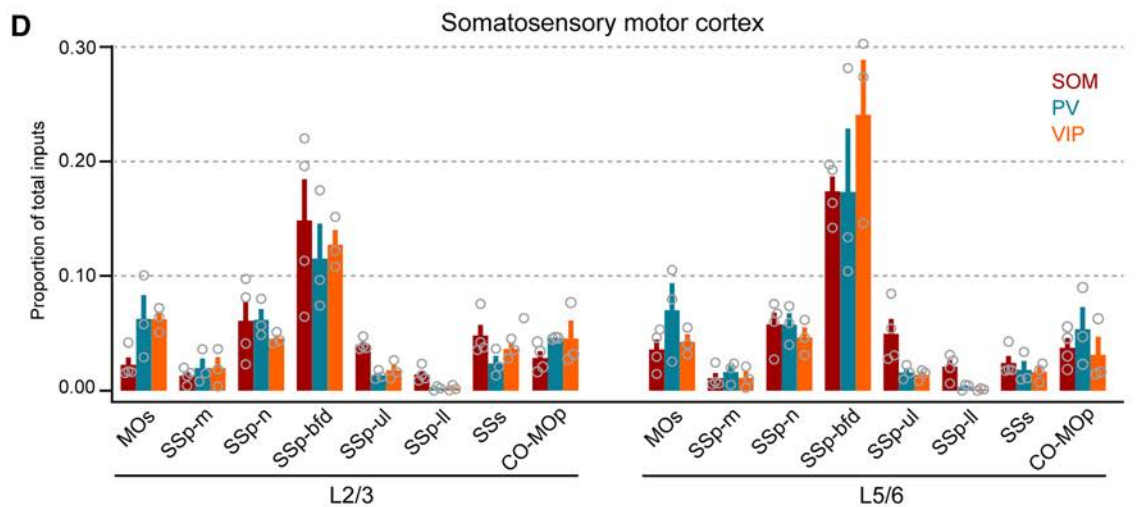
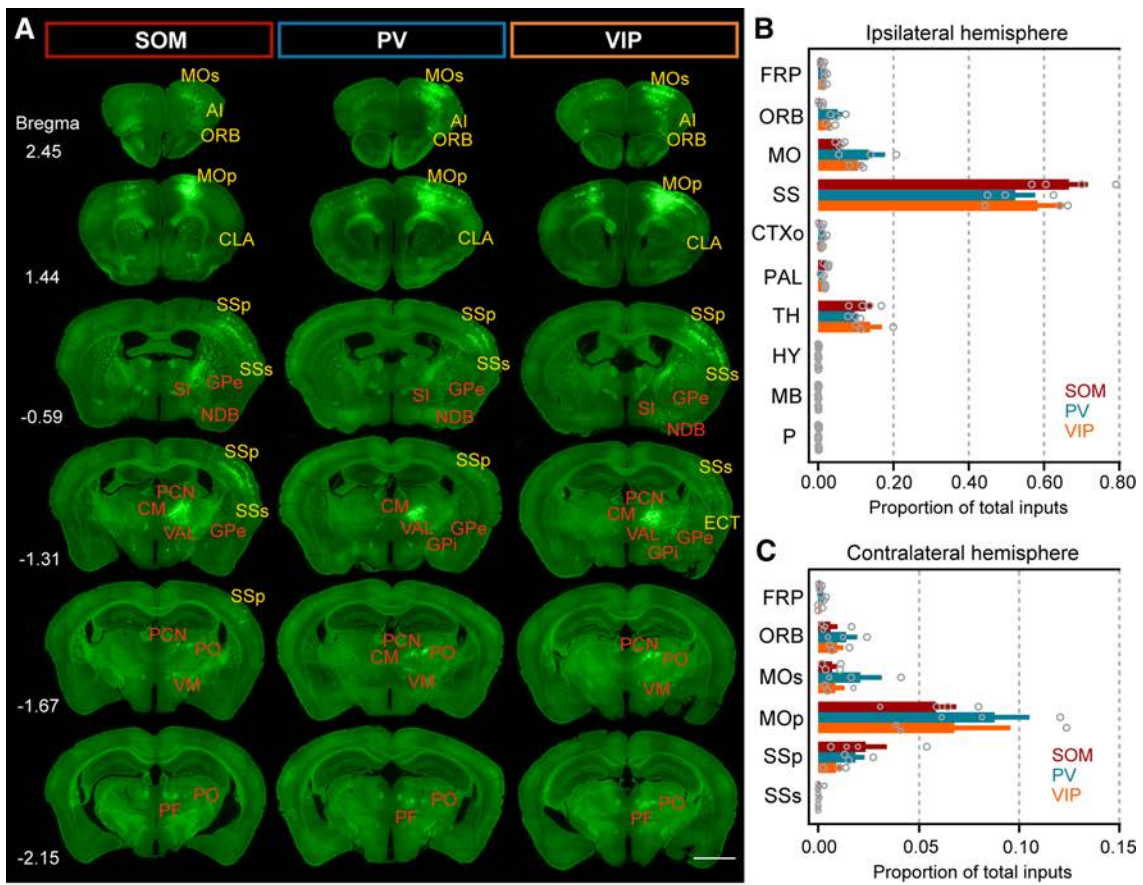


Fig. 2 Overview of whole-brain input connections to three interneuron types in the CFA. **A** Representative coronal sections showing the main long-range inputs to PV+, SST+, and VIP+ interneurons in the CFA (yellow, cortical regions; orange, subcortical regions; scale bar, 2 mm). **B–E** Proportions of input from the ipsilateral hemisphere (**B**), contralateral hemisphere (**C**), deep and superficial ipsilateral motor-sensory cortex (**D**), and ipsilateral cortex except motor-sensory cortex (**E**) to each interneuron type (mean \pm SEM).

the cerebral cortex and striatum, were distributed in layers II/III and V/VI [26]. This result indicates that all three types of CFA interneurons received uniform input from deep and superficial intra-telencephalic neurons.

We also found that SOM+ neurons were most closely associated with the limb-related sensory cortex and received more direct input connections than PV+ ($P = 0.023$) and VIP+ ($P = 0.018$) neurons (Fig. 2D). Moreover, compared to VIP+ neurons, SOM+ and PV+ neurons received more inputs from the orbital cortex and agranular insular area, which are associated with somatosensory and emotional control. Sparse or negligible long-range input neurons were detected within the isocortex, olfactory areas, hippocampal formation, and cortical subplate (Fig. 2E).

Subcortical Input to Three Interneuron Types in the CFA

Subcortical mapping of the RV-GFP-labeled neurons showed that the thalamus and cerebral nuclei were prominent long-range subcortical input sources for CFA interneurons (Fig. 2B), consistent with previous structural studies of CFA pyramidal neurons [25]. In our data, the striatal input was weak or negligible, while major direct input neurons were observed in the pallidum, especially in the external segment of the globus pallidus (GPe). We found that SOM+ neurons received more input from the GPe than PV+ neurons ($P = 0.033$) (Fig. 3A). A similar pattern of GPe input distribution was evident in the different Cre lines, in that RV-GFP-labeled neurons were concentrated in the rostromedial and caudoventral regions (Fig. 3B). As the pallidum is the main source of the corticopetal cholinergic projection [26, 27], we assessed the proportions of neurons co-labeled with choline acetyltransferase (ChAT) antibodies and RV-GFP in PV-Cre (2 mice, 26 cells) and SOM-Cre (2 mice, 7 cells) mice. The results demonstrated proportions $>80\%$ in both groups (Fig. 3C, D), suggesting that the majority of GPe inputs to the CFA SOM+ and PV+ interneurons are corticopetal cholinergic neurons.

The thalamic input accounted for $\sim 10\%$ of the whole-brain input to CFA interneurons (VIP-Cre, $13.8\% \pm 3.1\%$; PV-Cre, $9.7\% \pm 0.9\%$; SOM-Cre, $12.6\% \pm 1.8\%$). Whole-thalamus analysis revealed that CFA interneurons received

equal proportions of thalamic input from the sensory-motor cortex-related thalamus and polymodal association cortex-related thalamus (Fig. 3E). In the latter, each interneuron type received similar proportions of input from all major thalamic input structures, such as the posterior medial nucleus (PO), mediodorsal nucleus, nucleus reuniens, central medial nucleus, paracentral nucleus, and parafascicular nucleus (PF). In the sensory-motor cortex-related thalamus, the major inputs came from the ventral anterior-lateral nucleus (VAL) and the ventral medial nucleus (VM) of the thalamus. Each CFA interneuron type received similar input from the VM, while VIP+ neurons received more inputs from the VAL than the PV+ neurons ($P = 0.048$) (Fig. 3E). This result suggested that higher-order thalamic nuclei forward information equally to each interneuron type in the CFA, while VAL activation might promote the disinhibition of neuronal activity in forelimb movement *via* VIP+ interneurons.

Moreover, we detected a few RV-GFP-labeled neurons in the lateral hypothalamic area, lateral preoptic area, and zona incerta of the hypothalamus; periaqueductal gray, ventral tegmental area, dorsal raphe nucleus, substantia nigra pars compacta, and pedunculopontine nucleus of the midbrain; and the pontine reticular nucleus, superior central raphe nucleus, parabrachial nucleus, laterodorsal tegmental nucleus, and locus ceruleus of the pons (Fig. 3F). These nuclei might be part of the source of cortically-modulated signals.

Distinct Whole-brain Long-range Input to CFA_{MOP} and CFA_{SSp} Interneurons

We divided the CFA into two sub-regions to explore the structural connections between forelimb motor and forelimb sensory activity. We labeled whole-brain monosynaptic input to the interneurons in CFA_{SSp}, which were mainly located in SSp-ul, another somatic sensorimotor node in the upper limb subnetwork [6]. Compared with CFA_{MOP}, we found that interneurons in CFA_{SSp} also received major inputs from the cerebral cortex, cerebral nuclei, and thalamus. Most of CFA_{SSp} input sources also had projections to the CFA_{MOP} (Fig. 4A); however, quantitative analysis indicated that the proportions of input to CFA_{MOP} and CFA_{SSp} were remarkably different in different brain areas (Fig. 4B–F).

Notably, in the cerebral cortex the motor-sensory cortex had the strongest connectivity with both CFA_{MOP} and CFA_{SSp}; however, nose and mouth areas of primary sensory cortex and barrel cortex preferentially projected to the interneurons in the CFA_{MOP} rather than in the CFA_{SSp}, consistent with the actual movement patterns of the mice (Fig. 4B). Furthermore, neurons in anterior cortical regions, such as the frontal association cortex,

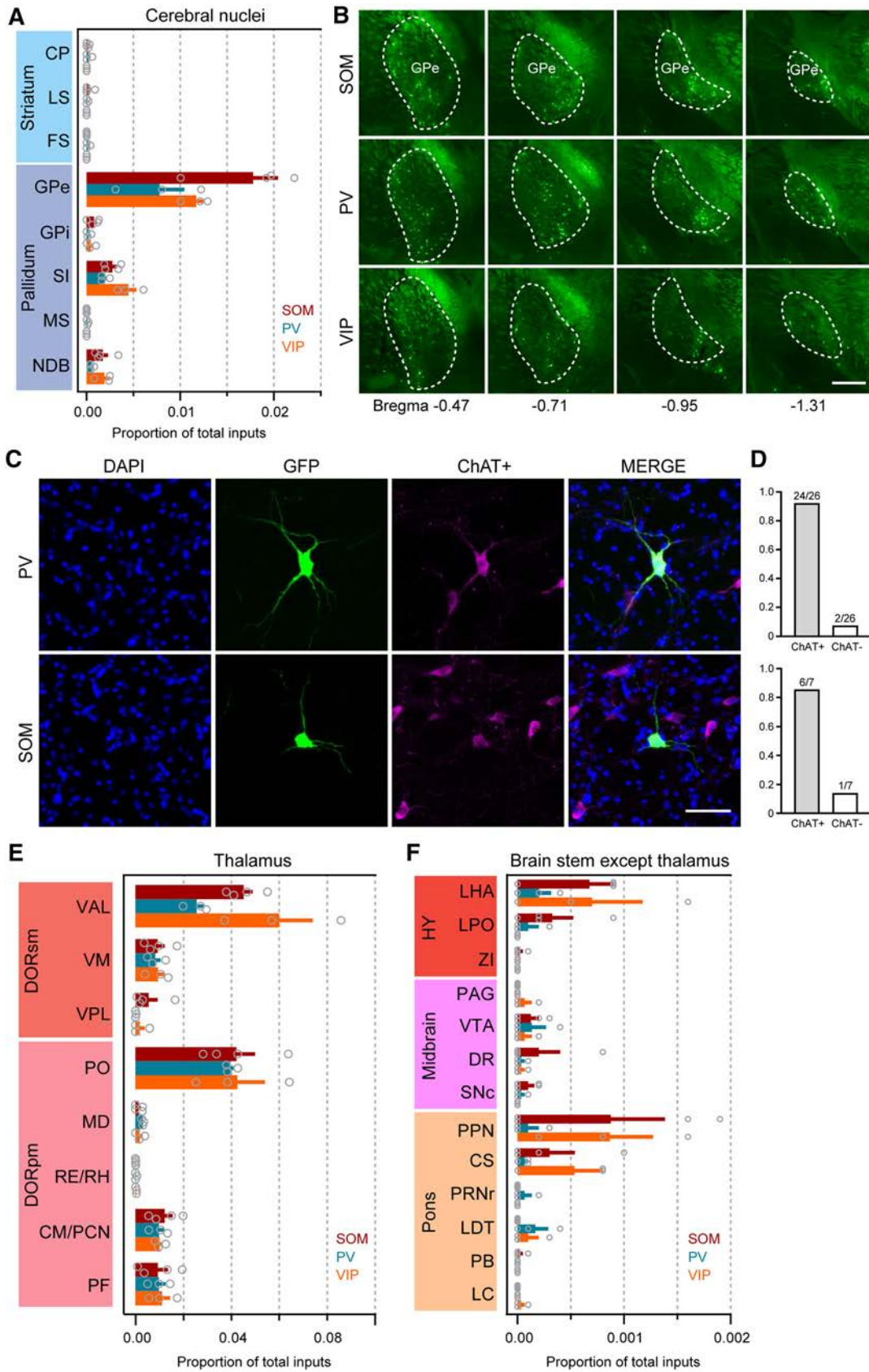


Fig. 3 Subcortical input connections to three interneuron types in the CFA. **A** Proportions of cerebral nuclear input to each interneuron type (mean \pm SEM). **B** Coronal sections showing the distribution of GPe input to each interneuron type (scale bar, 500 μ m). **C** Identification of RV-GFP+/ChAT+ input neurons in the GPe (scale bar, 50 μ m). **D** Proportions of RV-GFP-labeled neurons expressing ChAT in the GPe (mean \pm SEM). **E** Proportions of input from the thalamus (mean \pm SEM). **F** Proportions of input from other brainstem regions except the thalamus (mean \pm SEM).

orbital cortex, agranular insular area, and secondary motor cortex provided more direct projections to the interneurons in the CFA_{MOP}; however, neurons in caudal cortical regions, such as SSs, primary auditory cortex, and the ectorhinal area, had more direct projections to the CFA_{SSp}, which followed the topological structure of the two CFA sub-regions (Fig. 4B). We did not observe CFA_{SSp} interneurons receiving input from the frontal pole and orbital cortex of the contralateral cortex (Fig. 4A, C).

In the cerebral nuclei, we did not observe any striatal input neurons in CFA_{SSp} RV-labeled samples ($n = 3$); in the pallidum, we detected similar proportions of input to the CFA_{MOP} and CFA_{SSp} (Fig. 3D). In the thalamus, the CFA_{MOP} interneurons received input primarily from the VAL ($P = 0.002$), paracentral nucleus ($P = 0.002$), and PF ($P = 0.011$), while the CFA_{SSp} interneurons preferentially received input from the VPL ($P = 0.006$) and PO ($P = 0.008$) (Fig. 4E). In other brainstem regions, the proportion of input to the CFA was $<0.2\%$. The midbrain, especially the ventral tegmental area, is known to contain a high density of dopaminergic neurons and provided more direct projections to the interneurons in the CFA_{SSp} ($P = 0.022$), while few RV-GFP-labeled neurons were detected in the substantia nigra pars compacta (Fig. 4A, F). This result suggests that the dopamine signal in the forelimb subnetwork might primarily arise from the ventral tegmental pathway and innervate CFA_{SSp} interneurons.

Parallel Pathways of Cortical and Thalamic Inputs to the CFA_{MOP} and CFA_{SSp}

Quantitative analysis showed that both CFA_{MOP} and CFA_{SSp} interneurons received a large number of direct inputs from barrel cortex and the SSs; however, the input neurons that projected to the CFA_{MOP} were mainly distributed in the anterolateral barrel cortex, while those that directly projected to the CFA_{SSp} were mainly distributed posterolaterally. Following a similar topological organization, in the SSs the inputs to the CFA_{MOP} were mainly distributed in the anterior area, while the inputs to the CFA_{SSp} were mainly distributed caudally (Fig. 5A, C). These results suggest that the interneurons in CFA_{MOP} and

CFA_{SSp} receive distinct sensory information from two parallel cortical pathways.

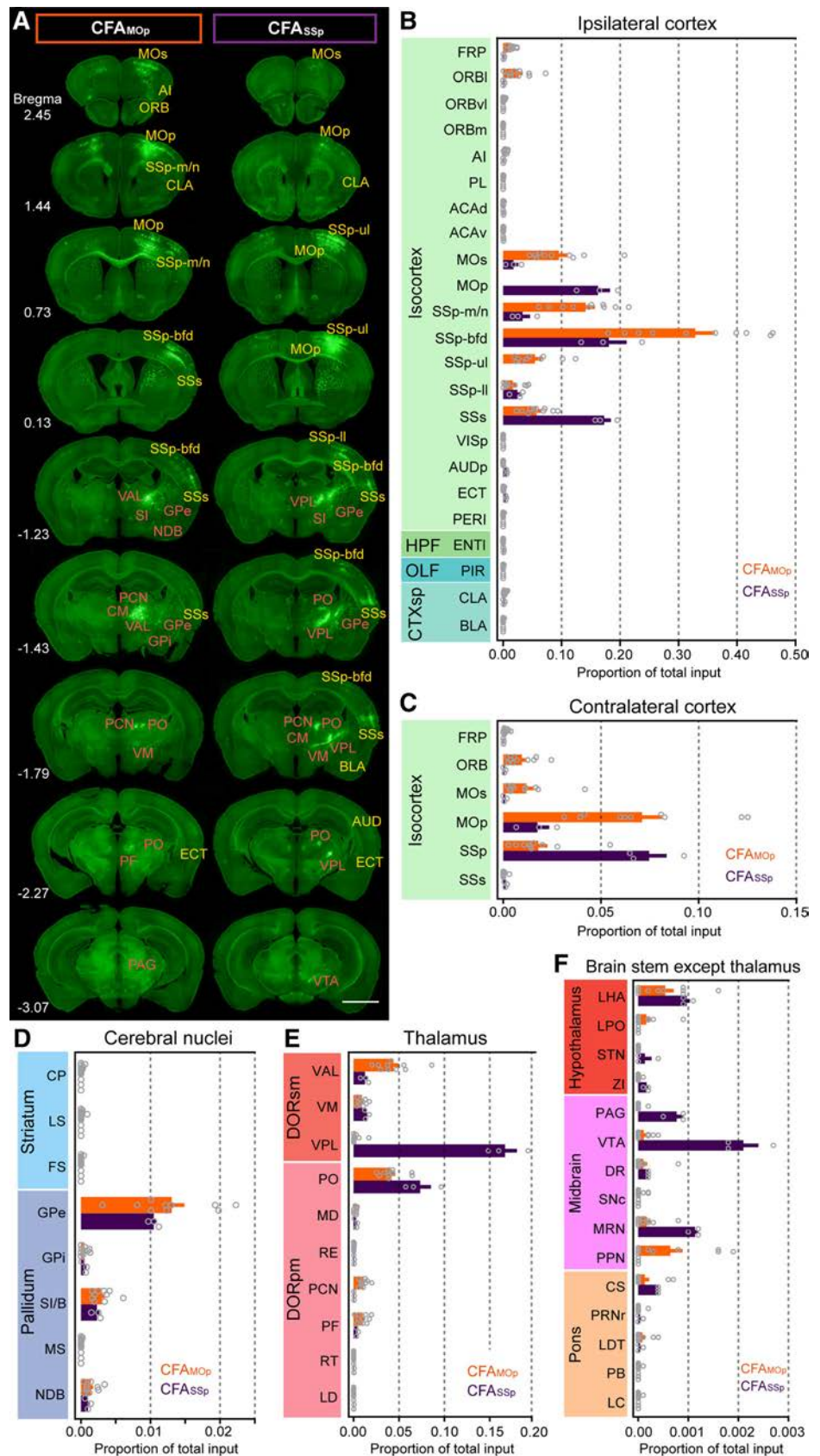
We showed that both CFA_{MOP} and CFA_{SSp} interneurons received major thalamic inputs from the higher-order PO thalamic nuclei (Fig. 3E, 4E). Worthy of mention is that the PO neurons that projected to the CFA_{MOP} were mainly distributed laterally, while the neurons that projected to the CFA_{SSp} were only distributed in the central region (Fig. 5B, D). Interestingly, the separation of thalamus–CFA sub-loops was not only observed in the PO, but also in the VM and PF (Fig. 5D). Consistent with parallel cortical pathways, this result in the thalamus also suggests the existence of parallel pathways in the forelimb subnetwork, which are only related to one another (i.e., not identical). Furthermore, the separation of lateral and central parts in the PO is helpful in understanding the complex higher-order thalamic nuclei.

Discussion

Using the monosynaptic RV system, we studied the long-range input connections of CFA interneurons at the whole-brain level in mice, and generated a comprehensive long-range input atlas of interneurons in the CFA_{MOP} and CFA_{SSp}. All of the PV+, SOM+, and VIP+ interneurons in the CFA received major long-range inputs from the cerebral cortex, pallidum, and thalamus to varying degrees (Fig. 6). Notably, the interneurons in different sub-regions of the CFA received long-range inputs from the cortex and thalamus in remarkably differing distributions and proportions. These differences were not only reflected in the known structures, but also in brain areas that had not yet been subdivided. The anatomical evidence indicated that the interneurons in the CFA_{MOP} and CFA_{SSp} have distinct connectivity subnetworks, and the connectivity mapping provides important guidance for further understanding the inhibitory regulatory processes in forelimb movement and the structural architecture underlying the functions of the CFA.

Diverse GABAergic interneuron types in the neocortex have a characteristically low density and are highly heterogeneous. These interneurons only account for $\sim 20\%$ of cortical neurons, but they are divided into a number of different subtypes according to their morphological, physiological, and biochemical characteristics [25, 28–30]. Although there is still no clear consensus on how many inhibitory cell types there are, PV+, SOM+, and VIP+ are generally considered to be the three major non-overlapping classes of interneuron in the mouse neocortex [29]. Using the monosynaptic RV tracing system, VIP+ interneurons in the barrel cortex received a significantly greater proportion of distant cortical input

Fig. 4 Overview of whole-brain input connections to interneurons in the CFA_{MOP}/CFA_{SSp}. **A** Representative coronal sections showing the contrast of input connections to VIP+ interneurons in the CFA_{MOP} and CFA_{SSp} (yellow, cortical regions; orange, sub-cortical regions; scale bar, 2 mm). **B** Quantitative analysis of the proportions of long-range inputs from the ipsilateral cortex to the CFA_{MOP} and CFA_{SSp} (mean ± SEM). **C** Proportions of input from the contralateral hemisphere (mean ± SEM). **D** Proportions of input from cerebral nuclei (mean ± SEM). **E** Proportions of input from the thalamus (mean ± SEM). **F** Proportions of input from other brainstem regions except the thalamus (mean ± SEM).



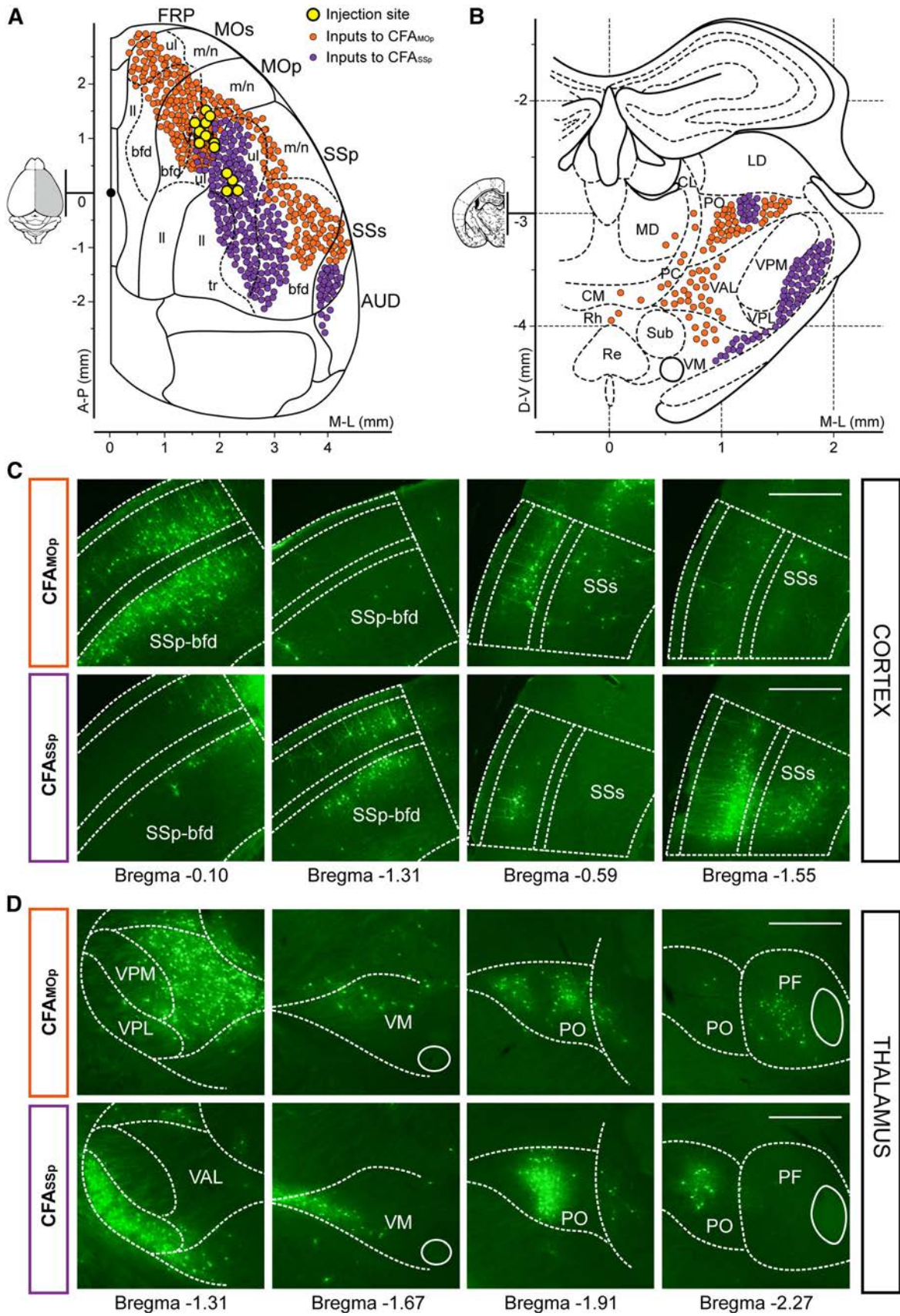


Fig. 5 Cortical and thalamic input connection patterns of CFA interneurons. **A, B** Schematic diagrams of the cortical (**A**) and thalamic (**B**) inputs to CFA_{MOP} or CFA_{SSp} interneurons (yellow, injection sites of AAV and RV; orange, inputs to CFA_{MOP} interneurons; purple, inputs to CFA_{SSp} interneurons). **C** Coronal sections showing the different cortical input connection patterns. Input neurons distributed in anterior (barrel field, bregma -0.10 mm; SSs, -0.59 mm) and caudal regions (barrel field, -1.31 mm; SSs, -1.55 mm) (sections from two VIP-Cre mice; scale bars, 500 μm). **D** Coronal sections showing the different thalamic input connection patterns. Input neurons distributed in VAL/VPL (bregma -1.31 mm), VM (-1.67 mm), PO (-1.91 mm), and PF (-2.27 mm) (sections from two VIP-Cre mice; scale bars, 500 μm).

from deep layers than the PV+ or SOM+ neurons [15]; however, this may not be a common characteristic among all cortical interneurons because we found that the three interneuron types in the CFA_{MOP} received deep cortical inputs in similar proportions (VIP-Cre, 37.5% ± 4.4%; PV-Cre, 35.7% ± 1.6%; SOM-Cre, 37.6% ± 2.2%). We consider that this difference may be due to the distribution of starter cells, but this has not yet been confirmed.

Both the PV+ and SOM+ interneurons in the CFA_{MOP} received direct projections from the GPe, which mainly co-releases GABA and acetylcholine to inhibit and activate interneurons and pyramidal neurons across cortical layers [27]. The cortico-striatal PV+/SOM+ projecting neurons directly innervate striatal dopamine (D1/D2) receptor neurons, while striatal information flows to the internal

segment of the globus pallidus and GPe through D1/D2 receptor neurons from direct and indirect pathways [31, 32]. This suggests that PV+ and SOM+ interneurons in the CFA_{MOP} contribute to the MOP-STR-GPe-MOP inhibitory microcircuit and the neural activity may be modulated by striatal GABAergic spiny projection neurons that bypass the thalamus. Furthermore, CFA_{MOP} interneurons receive direct input from the PF, which projects to both the somatosensory cortex and the dorsolateral striatum [33]; however, our results showed that the PF preferentially innervates the motor rather than the sensory cortex.

Moreover, in the thalamus, PO is the major source of long-range subcortical information to CFA_{MOP} interneurons, and the proportions among the three groups displayed no significant differences. In the somatosensory cortex, the terminals of thalamo-cortical PO neurons were densely assembled in layers I and Va and preferentially innervated PV+ interneurons in layer Va and VIP+ interneurons in layer II [34, 35]. Our structural results in the CFA confirmed that the monosynaptic inputs to SOM+ interneurons were densely distributed in the PO, consistent with both PV+ and VIP+ interneurons in the CFA. The innervation of such structural connections is unclear, but we also provided thalamo-cortical connections that provide a basis for functional research on SOM+ interneurons.

We also compared the distributions and proportions of long-range inputs to interneurons in different CFA sub-regions, and found that the cortex and thalamus were the

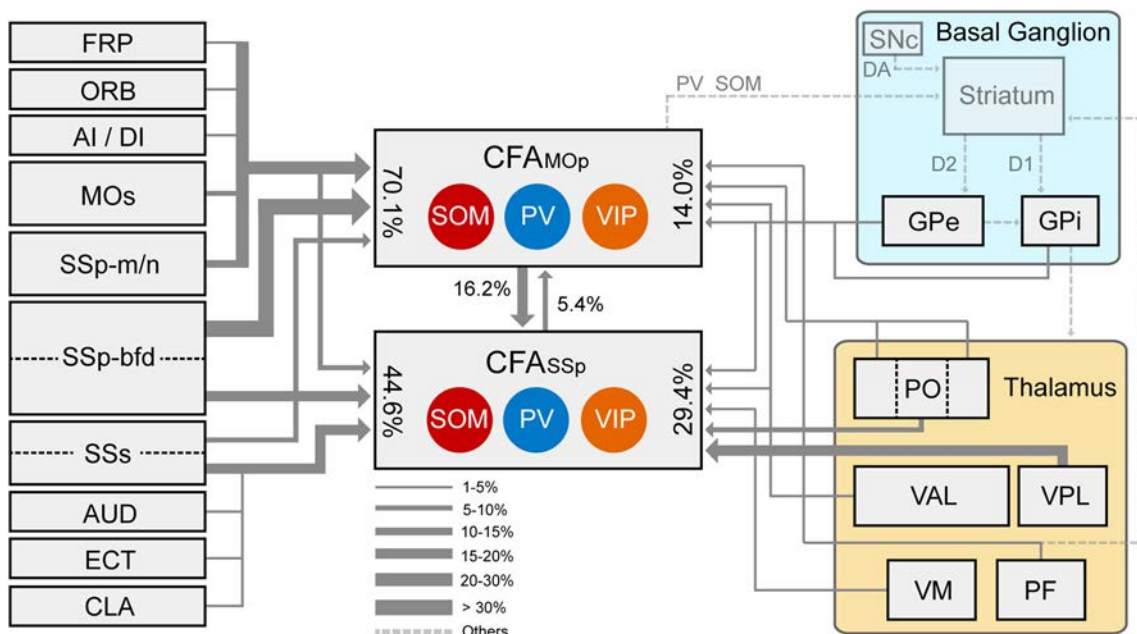


Fig. 6 Schematic of the main long-range input connection patterns to the GABAergic interneurons in the CFA: the cortico-cortical projections (left); the interactions between CFA_{MOP} and CFA_{SSp} (middle); and the inputs from the thalamus and the basal ganglia

(right). Percentages represent the proportion of total long-range inputs at the whole-brain level. Line thickness represents the range of proportions.

most important long-range input sources that connect to the CFA; however, GABAergic interneurons in the CFA_{MOP} received more cortico-cortical projections, while the CFA_{SSp} interneurons received more thalamic inputs (Fig. 6). The proportion of cortical inputs to CFA_{SSp} VIP+ neurons was $70.4\% \pm 1.7\%$, whereas the proportion of CFA_{MOP} VIP+ neurons was $84.1\% \pm 3.1\%$. In contrast, the proportion of input from the thalamus to the CFA_{SSp} was $27.4\% \pm 1.7\%$, and to the CFA_{MOP} was only $13.8\% \pm 3.1\%$. We speculated that the neurons located in the anterior cortex preferentially receive more cortico-cortical inputs and fewer thalamo-cortical inputs than those in the posterior cortex.

The barrel cortex is generally considered to be structurally and functionally equivalent to the somatosensory cortex [12, 15, 35]; in our study, direct input signals from multiple sub-regions of the somatosensory cortex to CFA interneurons were counted separately, and the inputs from barrel cortex and SSs were anatomically organized into two cortical information channels to CFA interneurons. In the thalamus, the higher-order PO thalamic nucleus is subdivided into four subnuclei according to their connection with layer Vb neurons in the barrel cortex [36]; however, we first separated the PO into lateral and central portions in the forelimb-movement subnetwork. The segregation of two CFA–PO loops may also support the concept of parallel pathway organization in the forelimb-movement system.

Acknowledgements We thank Qingtao Sun, Pan Luo, Mei Yao, and Peilin Zhao for help with experiments and data analysis. We thank the Optical Bioimaging Core Facility of Huazhong University of Science and Technology for providing support with data acquisition. This work was supported by the National Natural Science Foundation of China (61721092, 91749209, and 31871088) and the Director Fund of Wuhan National Laboratory for Optoelectronics.

Conflict of interest The authors declare that the research was conducted in the absence of any commercial or financial relationships that could be construed as a potential conflict of interest.

References

- Iwaniuk AN, Whishaw IQ. On the origin of skilled forelimb movements. *Trends Neurosci* 2000, 23: 372–376.
- Lemon RN. Descending pathways in motor control. *Annu Rev Neurosci* 2008, 31: 195–218.
- Wang X, Liu Y, Li X, Zhang Z, Yang H, Zhang Y, *et al.* Deconstruction of corticospinal circuits for goal-directed motor skills. *Cell* 2017, 171: 440–455 e14.
- Tennant KA, Adkins DL, Donlan NA, Asay AL, Thomas N, Kleim JA, *et al.* The organization of the forelimb representation of the C57BL/6 mouse motor cortex as defined by intracortical microstimulation and cytoarchitecture. *Cereb Cortex* 2011, 21: 865–876.
- Touvykine B, Mansoori BK, Jean-Charles L, Deffeyes J, Quessy S, Dancause N. The effect of lesion size on the organization of the ipsilesional and contralesional motor cortex. *Neurorehabil Neural Repair* 2016, 30: 280–292.
- Zingg B, Hintiryan H, Gou L, Song MY, Bay M, Bienkowski MS, *et al.* Neural networks of the mouse neocortex. *Cell* 2014, 156: 1096–1111.
- Ramanathan D, Conner JM, Tuszyński MH. A form of motor cortical plasticity that correlates with recovery of function after brain injury. *Proc Natl Acad Sci U S A* 2006, 103: 11370–11375.
- Harrison TC, Ayling OG, Murphy TH. Distinct cortical circuit mechanisms for complex forelimb movement and motor map topography. *Neuron* 2012, 74: 397–409.
- Hira R, Terada S, Kondo M, Matsuzaki M. Distinct functional modules for discrete and rhythmic forelimb movements in the mouse motor cortex. *J Neurosci* 2015, 35: 13311–13322.
- Sachidhanandam S, Sermet BS, Petersen CCH. Parvalbumin-expressing GABAergic neurons in mouse barrel cortex contribute to gating a goal-directed sensorimotor transformation. *Cell Rep* 2016, 15: 700–706.
- Nelson A, Schneider DM, Takatoh J, Sakurai K, Wang F, Mooney R. A circuit for motor cortical modulation of auditory cortical activity. *J Neurosci* 2013, 33: 14342–14353.
- Lee S, Kruglikov I, Huang ZJ, Fishell G, Rudy B. A disinhibitory circuit mediates motor integration in the somatosensory cortex. *Nat Neurosci* 2013, 16: 1662–1670.
- Zhang S, Xu M, Kamigaki T, Hoang Do JP, Chang WC, Jenvay S, *et al.* Selective attention. Long-range and local circuits for top-down modulation of visual cortex processing. *Science* 2014, 345: 660–665.
- Wickersham IR, Lyon DC, Barnard RJ, Mori T, Finke S, Conzelmann KK, *et al.* Monosynaptic restriction of transsynaptic tracing from single, genetically targeted neurons. *Neuron* 2007, 53: 639–647.
- Wang X, Yang H, Pan L, Hao S, Wu X, Zhan L, *et al.* Brain-wide mapping of mono-synaptic afferents to different cell types in the laterodorsal tegmentum. *Neurosci Bull* 2019, 35: 781–790.
- Wall NR, De La Parra M, Sorokin JM, Taniguchi H, Huang ZJ, Callaway EM. Brain-wide maps of synaptic input to cortical interneurons. *J Neurosci* 2016, 36: 4000–4009.
- Zhang S, Xu M, Chang WC, Ma C, Hoang Do JP, Jeong D, *et al.* Organization of long-range inputs and outputs of frontal cortex for top-down control. *Nat Neurosci* 2016, 19: 1733–1742.
- Su YT, Gu MY, Chu X, Feng X, Yu YQ. Whole-brain mapping of direct inputs to and axonal projections from GABAergic neurons in the parafacial zone. *Neurosci Bull* 2018, 34: 485–496.
- Li Z, Chen Z, Fan G, Li A, Yuan J, Xu T. Cell-type-specific afferent innervation of the nucleus accumbens core and shell. *Front Neuroanat* 2018, 12: 84.
- Luo P, Li A, Zheng Y, Han Y, Tian J, Xu Z, *et al.* Whole brain mapping of long-range direct input to glutamatergic and GABAergic neurons in motor cortex. *Front Neuroanat* 2019, 13: 44.
- Sun Q, Li X, Ren M, Zhao M, Zhong Q, Ren Y, *et al.* A whole-brain map of long-range inputs to GABAergic interneurons in the mouse medial prefrontal cortex. *Nat Neurosci* 2019, 22: 1357–1370.
- Jiang T, Long B, Gong H, Xu T, Li X, Duan Z, *et al.* A platform for efficient identification of molecular phenotypes of brain-wide neural circuits. *Sci Rep* 2017, 7: 13891.
- Oh SW, Harris JA, Ng L, Winslow B, Cain N, Mihalas S, *et al.* A mesoscale connectome of the mouse brain. *Nature* 2014, 508: 207–214.
- Xu X, Roby KD, Callaway EM. Immunohistochemical characterization of inhibitory mouse cortical neurons: three chemically

- distinct classes of inhibitory cells. *J Comp Neurol* 2010, 518: 389–404.
25. Hooks BM, Mao T, Gutnisky DA, Yamawaki N, Svoboda K, Shepherd GM. Organization of cortical and thalamic input to pyramidal neurons in mouse motor cortex. *J Neurosci* 2013, 33: 748–760.
 26. Li X, Yu B, Sun Q, Zhang Y, Ren M, Zhang X, *et al.* Generation of a whole-brain atlas for the cholinergic system and mesoscopic projectome analysis of basal forebrain cholinergic neurons. *Proc Natl Acad Sci U S A* 2018, 115: 415–420.
 27. Saunders A, Oldenburg IA, Berezovskii VK, Johnson CA, Kingery ND, Elliott HL, *et al.* A direct GABAergic output from the basal ganglia to frontal cortex. *Nature* 2015, 521: 85–89.
 28. Feldmeyer D, Qi G, Emmenegger V, Staiger JF. Inhibitory interneurons and their circuit motifs in the many layers of the barrel cortex. *Neuroscience* 2018, 368: 132–151.
 29. Tremblay R, Lee S, Rudy B. GABAergic interneurons in the neocortex: from cellular properties to circuits. *Neuron* 2016, 91: 260–292.
 30. Lee S, Hjerling-Leffler J, Zaghera E, Fishell G, Rudy B. The largest group of superficial neocortical GABAergic interneurons expresses ionotropic serotonin receptors. *J Neurosci* 2010, 30: 16796–16808.
 31. Schmitz Y, Luccarelli J, Kim M, Wang M, Sulzer D. Glutamate controls growth rate and branching of dopaminergic axons. *J Neurosci* 2009, 29: 11973–11981.
 32. Melzer S, Gil M, Koser DE, Michael M, Huang KW, Monyer H. Distinct corticostriatal GABAergic neurons modulate striatal output neurons and motor activity. *Cell Rep* 2017, 19: 1045–1055.
 33. Mandelbaum G, Taranda J, Haynes TM, Hochbaum DR, Huang KW, Hyun M, *et al.* Distinct cortical-thalamic-striatal circuits through the parafascicular nucleus. *Neuron* 2019, 102: 636–652.e7.
 34. Aronoff R, Matyas F, Mateo C, Ciron C, Schneider B, Petersen CC. Long-range connectivity of mouse primary somatosensory barrel cortex. *Eur J Neurosci* 2010, 31: 2221–2233.
 35. Audette NJ, Urban-Ciecko J, Matsushita M, Barth AL. POm thalamocortical input drives layer-specific microcircuits in somatosensory cortex. *Cereb Cortex* 2018, 28: 1312–1328.
 36. Sumser A, Mease RA, Sakmann B, Groh A. Organization and somatotopy of corticothalamic projections from L5B in mouse barrel cortex. *Proc Natl Acad Sci U S A* 2017, 114: 8853–8858.



Test–Retest Reliability of Functional Magnetic Resonance Imaging Activation for a Vergence Eye Movement Task

Cristian Morales¹ · Suril Gohe³ · Xiaobo Li¹ · Mitchell Scheiman² · Bharat B. Biswal¹ · Elio M. Santos¹ · Chang Yaramothu¹ · Tara L. Alvarez¹

Received: 19 July 2019 / Accepted: 18 September 2019 / Published online: 23 December 2019
© Shanghai Institutes for Biological Sciences, CAS 2019

Abstract Vergence eye movements are the inward and outward rotation of the eyes responsible for binocular coordination. While studies have mapped and investigated the neural substrates of vergence, it is not well understood whether vergence eye movements evoke the blood oxygen level-dependent signal reliably in separate experimental visits. The test–retest reliability of stimulus-induced vergence eye movement tasks during a functional magnetic resonance imaging (fMRI) experiment is important for future randomized clinical trials (RCTs). In this study, we established region of interest (ROI) masks for the vergence neural circuit. Twenty-seven binocularly normal young adults participated in two functional imaging sessions measured on different days on the same 3T Siemens scanner. The fMRI experiments used a block design of sustained visual fixation and rest blocks interleaved between task blocks that stimulated eight or four vergence eye movements. The test–retest reliability of task-activation was assessed using the intraclass correlation coefficient (ICC), and that of spatial extent was assessed using the Dice coefficient. Functional activation during the vergence eye movement task of eight movements

compared to rest was repeatable within the primary visual cortex (ICC = 0.8), parietal eye fields (ICC = 0.6), supplementary eye field (ICC = 0.5), frontal eye fields (ICC = 0.5), and oculomotor vermis (ICC = 0.6). The results demonstrate significant test–retest reliability in the ROIs of the vergence neural substrates for functional activation magnitude and spatial extent using the stimulus protocol of a task block stimulating eight vergence eye movements compared to sustained fixation. These ROIs can be used in future longitudinal RCTs to study patient populations with vergence dysfunctions.

Keywords Vergence eye movement · Test–retest reliability · Functional MRI · Vergence region of interest masks

Introduction

Vergence eye movements are the disjunctive inward (convergence) and outward (divergence) rotation of the eyes used to ensure that an object of interest is imaged on the fovea of each eye. The underlying neural substrates that govern such a response have been investigated using single cell recordings in primates [1–5], transcranial magnetic stimulation in humans [6, 7], functional imaging experiments in humans [8, 9] and other primates [10], and case-reports [11–13]. Collectively, these studies suggest that the following regions of interest (ROIs) are functionally active during a vergence response: frontal eye fields (FEF), supplementary eye field (SEF), parietal eye fields (PEF) and cerebellar oculomotor vermis (OV), midbrain, pons, and primary visual cortex [1–3, 5–9, 11–13].

While prior oculomotor functional imaging studies of saccadic movements (conjugate, tandem eye movement) have been conducted to assess the reliability of a saccadic

Electronic supplementary material The online version of this article (<https://doi.org/10.1007/s12264-019-00455-9>) contains supplementary material, which is available to authorized users.

✉ Tara L. Alvarez
tara.l.alvarez@njit.edu

¹ Biomedical Engineering, New Jersey Institute of Technology, Newark, NJ 07102, USA

² Pennsylvania College of Optometry, Salus University, Philadelphia, PA 19027, USA

³ Department of Health Informatics, Rutgers University School of Health Professions, Newark, NJ 07107, USA

task [14, 15], no study has assessed the reliability of the functional activity evoked using vergence eye movements during a functional magnetic resonance imaging (fMRI) experiment. Knowing which ROIs are not only functionally but also reliably active during a vergence response is of great value to researchers investigating therapeutic interventions for patients with a vergence dysfunction. Vergence dysfunctions are commonly reported in the general population [16–22], in brain injury patients [23, 24], those with psychological dysfunctions [25, 26], and patients with attentional deficits [27, 28]. fMRI is one tool that can be used to study the differences in functional activation between patients and normal controls as well as to evaluate the changes in functional activity evoked by therapeutic interventions in numerous clinical populations [29–31]. Longitudinal studies of therapeutic interventions have assessed peak and mean functional activations within an ROI and quantified the spatial extent of an ROI in stimulus-induced fMRI protocols [32–34]. A few pilot studies have assessed functional activity changes as a result of vision therapy in those with vergence dysfunctions [35–37]. However, a gap in the literature is the lack of data about the test–retest reliability of a protocol to stimulate the vergence neural circuit using a stimulus-induced fMRI protocol. Specifically, the variability of the blood oxygenation level-dependent (BOLD) signal evoked by vergence eye movements needs to be assessed between fMRI datasets collected on different days to test the reliability of the signal. A high correlation between the data sets would support the use of BOLD activation as an objective outcome measure in randomized clinical trials (RCTs). This knowledge is important to determine whether potential changes in the BOLD signal are due to therapeutic interventions or simply to variability between visits or habituation from learning the fMRI experimental set-up.

The test–retest reliability of a stimulus-induced fMRI protocol has been investigated by assessing the beta weights (standardized regression coefficients) between and within visits acquired from the same participants on different days, quantifying variance [38], and the voxel-wise intraclass correlation coefficient (ICC) [39] for the peak functional activation within an ROI. Both group-level and individual-level analyses are encouraged to assess test–retest reliability [40]. The test–retest reliability of the spatial extent of stimulus-induced functional activation has been evaluated using the Dice coefficient [38]. The Sørensen–Dice coefficient is a statistical method used to assess the spatial overlap between two samples [41, 42]. These objective methods can be used to assess how reliable and robust a stimulus-induced protocol is in evoking changes within the BOLD signal on different visits on different days.

The primary goal of this study was to assess the test–retest reliability of functional activity within vergence ROI masks by measuring the beta weights of the peak and mean functional activation in an ROI using ICC analysis as well as the test–retest reliability of ROI spatial extent using Dice coefficient analysis. In addition, we assessed the ability of a protocol for stimulus-induced vergence eye movement to evoke functional activation of the vergence neural circuit and to identify ROI masks of the vergence neural substrates in binocularly normal controls for future RCTs of patients with vergence dysfunctions.

Materials and Methods

Participants

All participants signed written informed consent for protocols approved by the Institutional Review Boards of the New Jersey Institute of Technology and Rutgers University (the institutional Ethics Committees) and in accordance with the Declaration of Helsinki. We recruited 27 young adult, binocularly-normal participants, aged between 18 and 35 years (mean 21.8 ± 3.37 years) (5 females, 22 males).

All participants underwent an optometric examination by one of the co-authors (MS), an optometrist. This examination included the following assessments: best-corrected visual acuity at distance and near, non-cycloplegic auto-refraction, Convergence Insufficiency Symptom Survey (CISS) [43, 44], stereopsis (Randot Stereotest), cover/uncover (unilateral cover) test at distance (6 m) and near (40 cm), alternate cover test with prism neutralization at distance and near, negative fusional vergence (blur, break, and recovery) at near, positive fusional vergence (blur, break, and recovery) at near, near point of convergence break and recovery, vergence facility at near, and push-up accommodative amplitude. This battery of tests has been used in previous vergence dysfunction clinical trials [45, 46]. Eligibility criteria for normal binocular vision included best-corrected distance visual acuity of 20/25 in both eyes, CISS score < 21 , difference between near and far phoria $< 6\Delta$, normal positive and negative fusional vergence (PFV/NFV) at near, normal amplitude of accommodation, and random dot stereopsis appreciation of 500 s of arc or better [35, 47]. Normal PFV/NFV is defined as passing Sheard's criterion or $PFV \geq 15\Delta$ base-out break [48]. Normal amplitude of accommodation is defined as a minimum of 15 minus a quarter times the participant's age [49]. Exclusion criteria were other visual dysfunctions such as retinal diseases or oculomotor dysfunction, history of brain injury including concussion, physiological or attentional dysfunctions, or any disease known to affect

accommodation, vergence, or ocular motility, constant strabismus at distance, vertical heterophoria $\geq 2\Delta$ at distance or near, ≥ 2 lines interocular difference in best-corrected visual acuity, manifest or latent nystagmus, history of strabismus surgery or refractive surgery, or inability to comprehend and/or perform the study test.

Materials

fMRI data were acquired with a 3T Siemens TRIO (Siemens Medical Solutions, Parkway Malvern, PA, USA) at Rutgers University Brain Imaging Center. All the scans were acquired using a 12-channel head coil. Monocular right-eye movements were recorded using the Eyelink-1000 system (SR Research, Kanata, ON, Canada) at a sampling frequency of 250 Hz (Fig. 1A) to ensure eye movement compliance. The participant was aligned symmetrically within the bore of the magnet (Fig. 1A) to consistently acquire eye movement data. The visual stimuli were observed by looking into a mirror reflecting a screen 87.5 cm from the nasion of the participant. The fMRI-compatible screen was 36 cm wide and 20.5 cm high. A custom MatLab™ code using Psychtoolbox [50] was executed in the MRI control room on a computer that had a screen resolution of 1920 pixels \times 1080 pixels. Before the scanning protocol began, eye moments were calibrated with 5 pre-designated locations on the screen to convert the pixel values to eye position in degrees.

Vergence Eye Movement Stimuli

The overall timing and sequence of stimuli are shown in Fig. 1B. Participants began with a ‘rest’ block of sustained fixation for 21 s. The visual stimulus was a set of eccentric squares (Fig. 1C) which were adjusted to stimulate the perception of an object far away from (far disparity) or closer to (near disparity) the participant. When fusing the visual target, the participant perceived a converging or diverging set of squares (Fig. 1D). After the rest block, the frequency of low occurrence (FLO) block lasted 18 s and evoked four vergence eye movements. Each vergence stimulus was presented for at least 2 s and up to 5 s, which reduced the anticipatory cues known to modify such eye movements [51, 52] and resulted in an increase of neural activity [9]. The binocularly symmetrical disparity vergence step stimuli of the FLO block were presented in the following order: 4° Convergence (Con), 4° Con, 6° Divergence (Div), and 4° Con. After the FLO block, a ‘rest’ block of sustained fixation was presented. Next, the frequency of high occurrence (FHO) task block lasted for 19 s, where 8 stimuli were presented. For the FHO block, the following order of stimuli was presented: 4° Con, 4°

Con, 6° Div, 4° Con, 4° Con, 6° Div, 4° Con, and 4° Div. The block design of ‘rest’ intermixed between FLO and FHO blocks was similar to that of a prior investigation of saccadic eye movements [53]. These vergence demands were chosen to reduce confounding variables such as phoria on the vergence eye movement responses [54–62]. To familiarize participants with the visual stimuli, they came to the laboratory to practice to ensure that they understood how to fuse the eccentric squares. Based on verbal feedback, all participants were able to fuse the visual stimuli and attain the perception of squares at different convergent or divergent planes as shown in Fig. 1D.

Scanning Protocol

Two experimental sessions were carried out with all participants on each of two different days. The two visits were separated by 1–31 days (mean 7.67 ± 7.72 days) based on the availability of the participant and the imaging center. The two sessions were run consecutively with a short pause between to allow the participant a short rest. An anatomical high-resolution reference volume data set was acquired using a magnetization-prepared rapid acquisition gradient-echo (MP-RAGE) sequence with the following parameters: repetition time (TR) = 1900 ms, echo time (TE) = 2.52 ms, T1 = 900 ms, flip angle = 9°, field of view (FOV) = 256 mm, and spatial resolution = $1.0 \text{ mm}^3 \times 1.0 \text{ mm}^3 \times 1.0 \text{ mm}^3$. A total of 176 slices were acquired for the anatomical scan. Two functional runs were acquired using an echo planar imaging (EPI) sequence with the following parameters: TR = 2000 ms, TE = 13 ms, flip angle = 90°, FOV = 192 mm, spatial resolution = $3.0 \text{ mm}^3 \times 3.0 \text{ mm}^3 \times 3.0 \text{ mm}^3$, 53 slices, and 208 volumes. During each visit, the participant performed two stimulus-induced tasks (run 1 and run 2) that were identical, and each run lasted 416 s (208 volumes). The stimulus-induced task consisted of symmetrical disparity vergence step stimuli.

Pre-processing

The two vergence eye movement runs for each visit were analyzed independently with SPM12 (Wellcome Centre for Human Neuroimaging, UCL, London, UK) using the default parameters unless otherwise noted. For each EPI four-dimensional (4D) volume dataset, all the volumes were realigned to the first volume in the same run. The realigned volumes were then co-registered to the anatomical MP-RAGE image acquired during the same visit. After co-registration, a detailed motion artifact analysis was conducted for all participants for both datasets, measuring motion in the x, y, and z axes and in yaw, pitch, and roll.

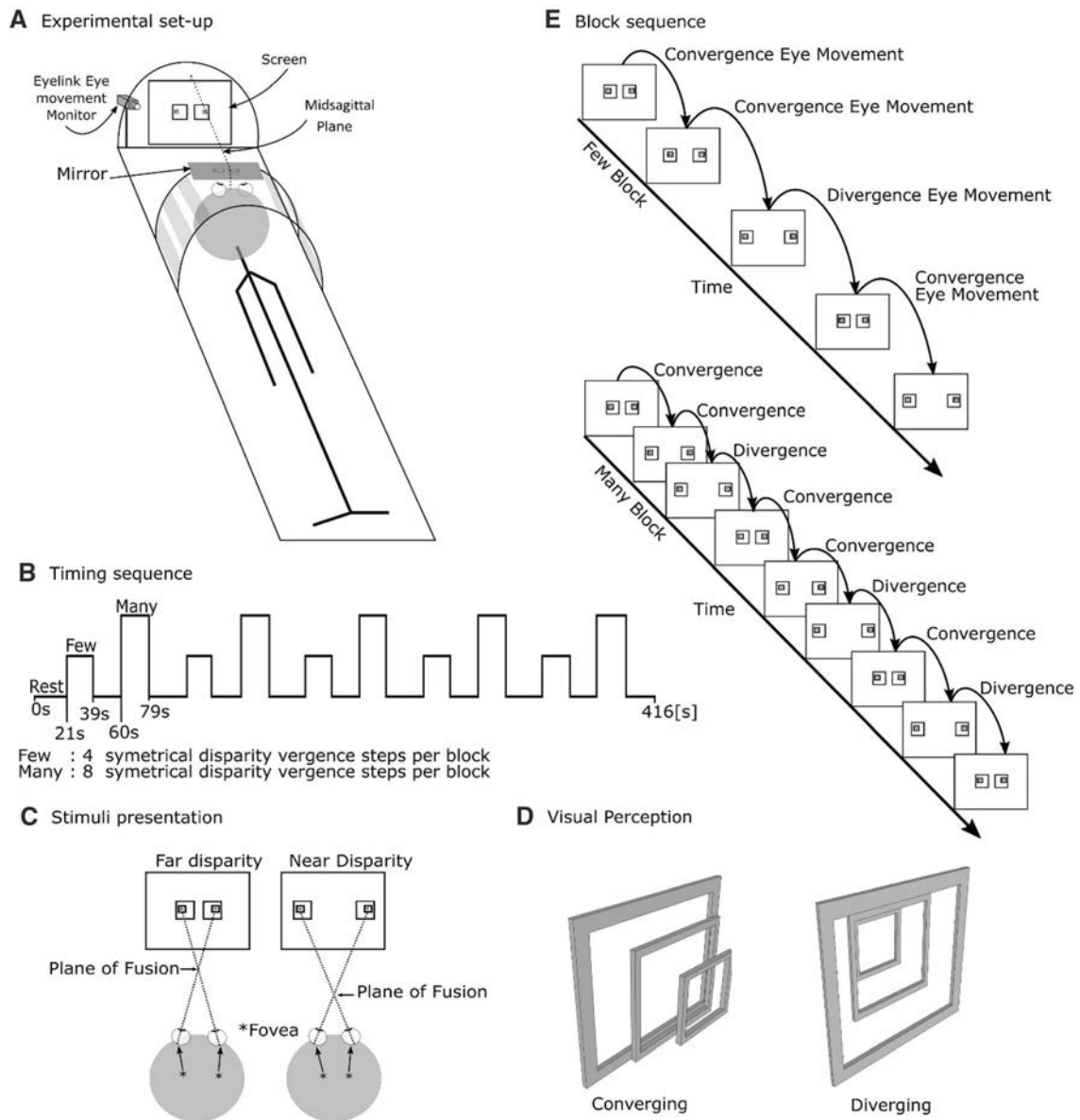


Fig. 1 **A** Experimental set-up. **B** Timing protocol of rest and the stimulus-induced vergence eye movement task. **C** Visual stimulus showing eccentric squares for far disparity and near disparity vergence fixation with how the plane of fixation changes for each type of disparity. **D** Visual perception of eccentric squares converging and diverging. The participant perceives the smallest box closer or

farther away in the plane. **E** Timing sequences of blocks for the frequency of low-occurrence task that stimulated four vergence eye movements and the frequency of high-occurrence task that stimulated eight such movements along with the type and sequence of vergence eye movements.

All participants had a maximum movement of 2 mm or less between time samples. The mean motion across all participants was 0.51 mm ± 0.38 mm for visit 1 and 0.42 mm ± 0.21 mm for visit 2. A paired *t* test of each participant’s average movement in visits 1 and 2 showed no significant difference [$T(26) = 1.35$; $P = 0.2$]. White matter (WM) and cerebrospinal fluid (CSF) were segmented using the MP-RAGE images. Masks for each tissue type were generated using a tissue probability map with a threshold set to ≥ 0.97 . Then, the first five principal

components from principal component analysis were extracted from the CSF mask. This procedure was repeated to find the first five principal components for the WM mask [63]. The Montreal Neurological Institute template (MNI152) was used to map each participant’s native MP-RAGE and fMRI datasets into standardized MNI space. Data were resampled to a $2\text{ mm}^3 \times 2\text{ mm}^3 \times 2\text{ mm}^3$ voxel size using a 4th degree b-spline interpolation function. To reduce the effect of physiological and head motion-related noises on functional activation, a total of 34

nuisance variables were regressed out from the fMRI dataset. Specifically, the following variables were regressed out from the datasets: 6 movement coefficients (yaw, pitch, roll, x, y, z), the corresponding 6 quadratics, 6 auto-regressors and their corresponding 6 quadratics which totaled 24 variables [64, 65], plus the 5 principal components of the CSF and the 5 principal components of the WM [63, 66]. All voxels on the resulting 4D volume data set were high-pass filtered (cutoff frequency $f_c = 0.01$ Hz, or 100 s). The data sets were smoothed with a 6-mm full width at half maximum kernel. The two runs in each visit were then temporally concatenated to increase the statistical power.

Whole-brain Functional Activation Maps and Group-level Statistics

A general linear model was used to generate whole-brain voxel-wise functional activation maps. The canonical waveform of a double gamma function, which is the Statistical Parametric Mapping (SPM) default, was used to calculate the beta weight of each voxel for the rest block compared to the FLO task block and for the rest block compared to the FHO task block. A one-sample T -test was applied to derive group-level activation maps for both the FLO and the FHO paradigms. These functional activation maps were then passed through a threshold of $P < 0.05$ with false discovery rate (FDR) correction for multiple comparisons [67] and overlaid on the anatomical images for visualization purposes.

ROIs

Based on previous studies from our group and others, the brain regions involved in the mediation of a vergence response include the FEF [9, 68], SEF [69], cerebellum [13, 70], PEF [5, 71], and primary visual cortex [72–74], which were the primary ROIs investigated in this study. In addition, Broca's area was investigated as an ROI to test the null hypothesis. A vergence eye movement task was hypothesized to not stimulate functional activity within Broca's area, which was defined using the Analysis of Functional NeuroImages Atlas software [75] and is centered at MNI coordinates $x = -54$, $y = 24$, and $z = 10$ [75–77]. The peak and mean beta weight functional activations were determined for these ROIs. The FEF is at the intersection of the precentral and superior frontal sulci [68, 78, 79]; the PEF is in the vicinity of the intraparietal sulcus [37, 71, 80]; the SEF is the area between the bilateral FEF near the midsagittal plane [81]; and the OV is in the posterior cerebellum along the midline [82, 83].

The beta weights in each vergence ROI mask were assessed for each participant and the peak and mean beta weights for each ROI were measured. A paired t -test is used to assess potential differences between the ROI-level activation between visits 1 and 2. The MNI coordinates of the T value were measured to define the center of the vergence ROI masks that can be used in future functional imaging studies of vergence neural substrates. The vergence ROI masks were defined as a 5 mm radius sphere of 81 voxels centered around the peak activation of the averaged data set from visit 1 using anatomical landmarks. Small radius ROIs (5-mm radius spheres) are recommended for studies investigating smaller neural substrates [84, 85]. A 10-mm radius sphere used to assess the peak ICC values was also used to investigate consistency. However, in this study we report results using a 5-mm sphere since this has been used in a previous oculomotor functional imaging study [86].

Assessment of Test–Retest Reliability

Test–Retest Reliability of the Magnitude of Functional Activation

The ICC is an established method of assessing the test–retest reliability of the magnitude of functional activity within an ROI and has been used in fMRI studies [87, 88]. There are many methods of calculating the ICC. We chose ICC (1,1) because we used the same participants, instrumentation, and stimulus-induced task protocol in two separate visits [89, 90]. The equation for ICC(1,1) is shown below (Eq. 1). MS_B is the mean beta weight squared between participants, MS_W is the mean beta weight squared within participants, and k is the number of participants (27).

$$ICC(1, 1) = \frac{MS_B - MS_W}{MS_B + (k - 1)MS_W} \quad (1)$$

Test–retest reliability is classified as poor (ICC = 0–0.4), fair (ICC = 0.4–0.55), good (ICC = 0.55–0.75), or excellent (ICC = 0.75–1.0) [15, 38, 90, 91]. The ICC values were calculated using the IPN toolbox in MatLab [92, 93].

The ICCs were calculated both at the voxel-level and for each of the vergence ROI masks. For the voxel-level analysis, only voxels that attained an ICC > 0.4 were extracted and plotted superimposed upon the high-resolution anatomical maps for visualization. For each vergence ROI, the maximum ICC was tabulated and compared between visits 1 and 2.

Test–Retest Reliability of Spatial Activation Maps

The test–retest reliability of the whole-brain spatial activation maps was evaluated at the group-level by conducting a Boolean AND gate on the functional activity maps between the two visits that reached a significance threshold of $P < 0.05$ corrected for multiple comparisons using the FDR. These significantly active voxels were overlaid on anatomical images for visualization. This map displayed all the voxels that survived the thresholding in both visits 1 and 2 for the FHO *versus* rest contrast and for the FLO *versus* rest contrast.

The Dice coefficient is a method to assess the test–retest reliability of the spatial extent of functional activity [14, 38, 91]. This coefficient was used to quantify the intersection (also known as overlap) in spatial extent of the activation maps between visits. For this study, the Dice coefficient was calculated for each vergence ROI mask. The participant-level threshold was not corrected for multiple comparison using $[T(202) = 1.65; P < 0.05]$. The activation maps derived in the previous steps were transformed to a binary map where significantly active voxels were encoded as a binary ‘high’ (logical 1) and the other voxels as a binary ‘low’ (logical 0). The Dice coefficient was then calculated using Eq. 2:

$$D = \frac{2 * V_{\text{overlap}}}{V_{\text{visit1}} + V_{\text{visit2}}} \quad (2)$$

V_{overlap} is the summation of the common voxels during both visit 1 and visit 2, V_{visit1} is the sum of all the significantly active voxels during visit 1, and V_{visit2} is the sum of all the significantly active voxels during visit 2 for each specific vergence ROI mask. In previous research, the Dice coefficient is calculated for each individual participant [40]. Hence, we reported the Dice coefficient as the mean of all participants with one standard deviation for each of the individual ROIs. To be more conservative in the calculation of the Dice coefficient, a more stringent motion artifact threshold of < 1 mm of mean movement was used. Since test–retest reliability of spatial extent is sensitive to motion, only participants who had an average head motion of < 1 mm were assessed [38, 94].

Results

Optometric Examination

The clinical optometric examination results are summarized in Table S1 with the 27 participants’ mean, standard deviation, and the minimum and maximum range. Based on these measurements, all participants were considered to have normal binocular vision.

Group-level Functional Activation Maps for the Stimulus Protocol for Vergence Eye Movements

The group-level functional activation maps from the stimulus-induced vergence eye movement task overlaid on the high-resolution anatomical images using FDR ($P < 0.05$) multiple comparison correction are shown in Fig. 2. As expected, no significant functional activity was found in Broca’s area (slice 10S in Fig. 2). The supplementary data (Fig. S1) display the volumes of many slices of functional activation spatial maps to show the whole brain activity during this task.

From the group-level spatial functional activity maps, the peak T -values were extracted for each of the ROIs and the MNI coordinates of the peak T -value are also listed in Table 1. When comparing the MNI coordinates of the peak activation from visits 1 and 2 for both the contrasts of FHO compared to rest and for FLO compared to rest, the coordinates were within 2 functional voxels (within 6 mm for each of the x , y , and z coordinates).

Establishing Vergence ROI Masks

The peak functional activity for visits 1 and 2 were similar in both the magnitude and spatial location of functional activity. In addition, the peak activation was similar in magnitude and location for the FHO *versus* rest task and for the FLO *versus* rest task. For FHO *versus* rest and FLO *versus* rest, a paired t -test revealed no significant differences in the T -value for each of the ROIs (FHO: $T(8) = 1.9; P = 0.1$; FLO: $T(8) = 1.1; P = 0.5$). Hence, the vergence ROI masks for the vergence neural substrates were established. Given the consistency in the datasets, the vergence ROI masks were defined as 5-mm radius spheres centered around the peak activation defined using the MNI coordinates of visit 1 from the FHO *versus* rest contrast (Table 1). The peak T -value results were virtually identical for the 5-mm and 10-mm radius ROIs. Hence, only the values from the 5-mm radius sphere are reported.

Test–Retest Reliability of Functional Activation during a Vergence Eye Movement Task

The maximum ICC for each of the vergence ROI masks are listed in Table 2 with the corresponding MNI coordinates where the peak ICC occurred. The ICC values to assess the test–retest reliability of functional activity from the FHO block *versus* rest task were significantly greater than the FLO block *versus* rest task for most of the vergence ROIs [$T(7) = 2.6, P = 0.04$]. Only the SEF ROI ICC was greater in the FLO task block than in the FHO task block.

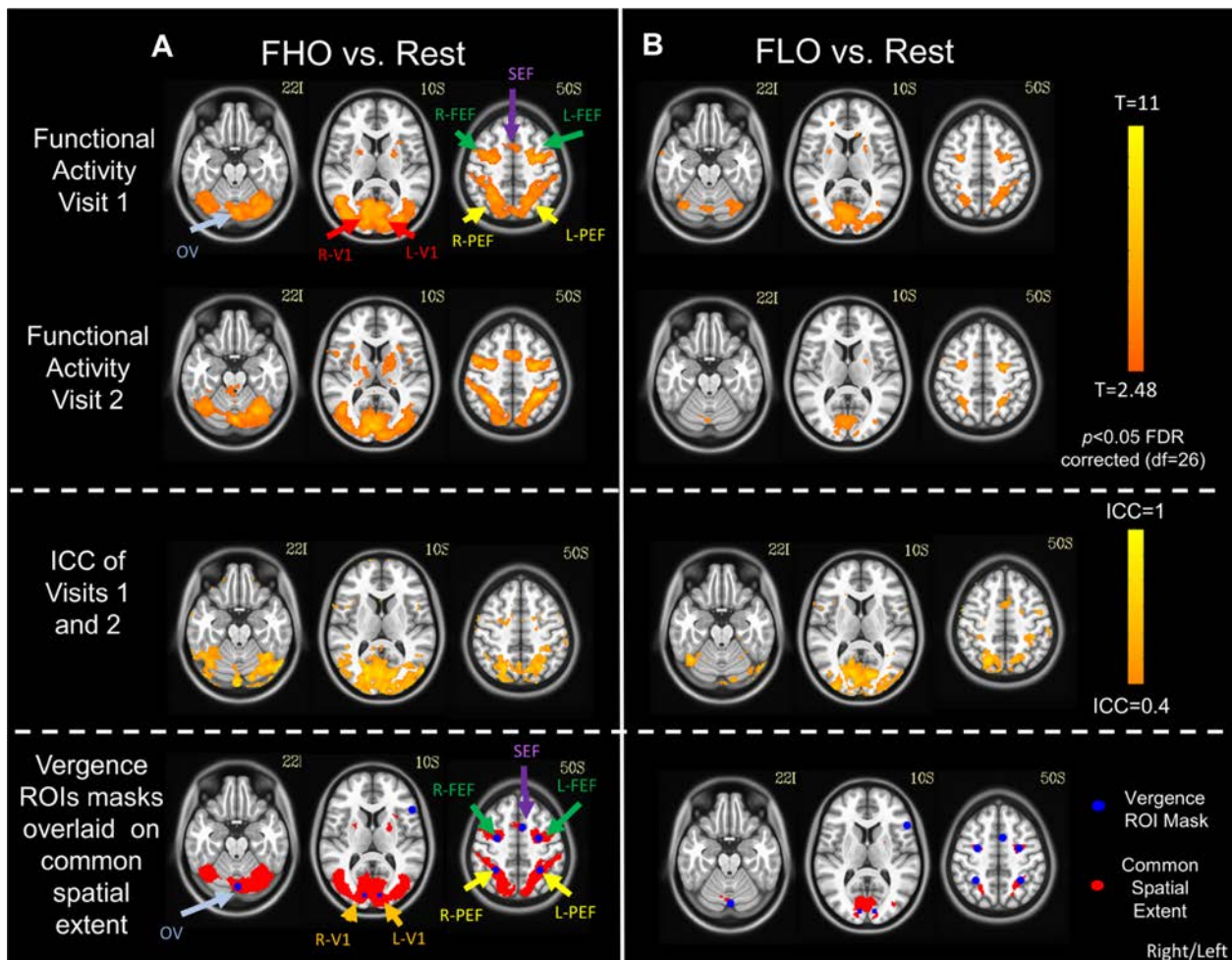


Fig. 2 **A** Functional activity of FHO *versus* rest blocks for the average of 27 binocularly normal participants overlaid on high-resolution anatomical images using a threshold of $P < 0.05$ corrected for multiple comparison with FDR. **B** Functional activity of FLO *versus* rest for the same dataset [arrows indicate oculomotor vermis (OV), right and left primary visual cortex (R/L V1), right and left parietal eye fields (R/L PEF), supplemental eye field (SEF), and right and left frontal eye fields (R/L FEF; upper row, functional activity from visit 1; second row, functional activity from visit 2; third row, ICC maps of functional activity assessing test–retest reliability between visits 1 and

2; fourth row, Boolean AND function of functional activation spatial extent from visits 1 and 2 with the vergence masks]. Axial slice 22 inferior (22I) displays the cerebellar functional activity from the oculomotor vermis (OV) (gray arrow); axial slice 10 superior (10S) displays the right primary visual cortex (R-V1) and left primary visual cortex (L-V1) (red arrows); axial slice 50 superior (50S) displays the following vergence neural substrates: left FEF (L-FEF) and right FEF (R-FEF) (green arrows), SEF (purple arrow), and left PEF (L-PEF) and right PEF (R-PEF) (yellow arrows).

To further assess the test–retest reliability, the beta weights of functional activity within each of the defined vergence ROIs were extracted from each vergence ROI mask using the MNI coordinates from the FHO of Visit 1. Using a paired t -test, no significant difference ($P \geq 0.1$) was found between the peak beta weights from visits 1 and 2 (Fig. 3A1, B1). Next, the beta weights per ROI were averaged. The mean beta weights per ROI for the FHO *versus* rest (Fig. 3A2) and for the FLO *versus* rest (Fig. 3B2) for visits 1 and 2 were also consistent. Using a paired t -test, no significant differences were found for any of the ROIs for the mean beta weights for either task (FHO or FLO vergence eye movements *versus* rest) ($P \geq 0.1$).

Evaluation of Test–Retest Reliability of Spatial Extent during the Vergence Eye Movement Task

The main vergence ROIs V1, PEF, FEF, SEF, and OV showed consistent spatial extent activation for the FHO vergence eye movement task compared to rest (Fig. 2). For the vergence ROIs identified in this study, the FLO vergence eye movement task showed consistent activity in the V1, PEF, FEF, and OV vergence ROI masks. When comparing the FHO and FLO vergence eye movement tasks, increased spatial extent was found in the FHO vergence eye movement task compared to the FLO

Table 1 Peak *T*-values per ROI for Visit 1 and Visit 2 for the FHO *versus* rest block and the FLO *versus* rest block

ROI	Visit 1 FHO <i>vs</i> Rest		Visit 2 FHO <i>vs</i> Rest		Visit 1 FLO <i>vs</i> Rest		Visit 2 FLO <i>vs</i> Rest	
	<i>T</i> Value	MNI coordinates [x y z]						
L-V1	6.7	[- 10 - 88 6]	7.6	[- 8 - 90 2]	5.9	[- 10 - 86 4]	4.1	[- 8 - 86 2]
R-V1	8.4	[10 - 88 6]	8.6	[10 - 86 4]	6.5	[12 - 86 2]	5.4	[8 - 88 2]
L-PEF	5.1	[- 30 - 48 50]	8.8	[- 32 - 44 50]	5.0	[- 28 - 48 50]	5.7	[- 28 - 48 48]
R-PEF	6.3	[30 - 48 50]	8.5	[34 - 48 52]	4.0	[30 - 48 50]	5.1	[30 - 52 52]
L-FEF	7.2	[- 28 - 6 48]	9.1	[- 28 - 6 48]	5.0	[- 32 - 4 48]	7.3	[- 26 - 6 48]
R-FEF	6.9	[28 - 6 52]	6.8	[28 - 6 50]	5.5	[26 - 6 50]	5.7	[28 - 6 48]
SEF	4.3	[- 6 8 50]	5.4	[- 6 8 52]	2.1	[- 10 6 48]	3.8	[- 4 8 52]
Vermis	6.7	[- 2 - 78 - 22]	9.2	[- 2 - 76 - 20]	4.8	[- 2 - 74 - 24]	5.0	[- 4 - 76 - 18]
Broca	- 2.8	[- 54 24 10]	- 3.9	[- 54 24 10]	- 3.1	[- 54 24 10]	- 2.2	[- 54 24 10]

Table 2 Functional activity in visits 1 and 2 using the peak and mean ICC within each vergence ROI for the FHO and FLO *versus* rest tasks in Broca's area

ROI	FHO <i>vs</i> Rest			FLO <i>vs</i> Rest		
	Peak ICC	Mean ICC	MNI coordinate	Peak ICC	Mean ICC	MNI coordinate
L-V1	0.84	0.68	[- 10 - 86 2]	0.69	0.51	[- 8 - 84 4]
R-V1	0.81	0.61	[6 - 88 4]	0.77	0.51	[6 - 88 6]
L-PEF	0.69	0.40	[- 32 - 52 52]	0.49	0.33	[- 34 - 46 50]
R-PEF	0.60	0.30	[26 - 50 48]	0.37	0.19	[28 - 52 50]
L-FEF	0.42	0.24	[- 30 - 2 50]	0.43	0.13	[- 24 - 6 50]
R-FEF	0.54	0.26	[26 - 4 48]	0.41	0.10	[24 - 8 54]
SEF	0.46	0.23	[- 4 10 54]	0.56	0.40	[- 2 10 48]
Vermis	0.61	0.32	[2 - 80 - 22]	0.37	- 0.02	[- 4 - 74 - 20]
Broca	0.00	0.00	[- 54 24 10]	0.00	0.00	[- 54 24 10]

vergence eye movement task (further details in supplementary material).

An individual-level Dice coefficient was calculated for each participant for all of the vergence ROIs (Table 3). The Dice coefficient is susceptible to motion artifacts, hence a more conservative threshold for excluding participants due to motion artifacts was used. Any participant who had on average 1 mm or more of movement was omitted from this analysis. Twenty out of 27 participants who met this more conservative threshold were further analyzed. When comparing the FHO and FLO tasks relative to rest blocks, a larger spatial extent was found for the FHO task than for the FLO task for all 8 vergence ROI masks. A paired *t*-test of the vergence ROIs (excluding Broca's area) showed that the Dice coefficient for the FHO *versus* rest task was significantly greater than that for the FLO *versus* rest task: [$T(7) = 7.1$; $P < 0.001$]. The left and right primary visual cortex had the greatest Dice coefficients among the masks studied. The SEF ROI had the lowest test-retest reliability of spatial extent in the vergence neural circuit. Broca's area did not show significant functional activity.

Discussion

Neural Substrates of Vergence

The stimulus-induced task of rest blocks interleaved between blocks of 8 vergence eye movements (FHO block) and blocks of 4 vergence eye movements (FLO block) stimulated the neural substrates of vergence and the resulting eye movements. The primary visual cortex, PEF, SEF, FEF, and OV were functionally active. The literature shows that these ROIs mediate a vergence eye movement response [1–3, 5–9, 11–13, 79]. The fMRI ROIs presented here were similar to those reported in fMRI studies investigating vergence eye movements in humans stimulated using light-emitting diodes placed for different vergence angular demands [8, 9, 95]. Other ROIs may be explored in future studies.

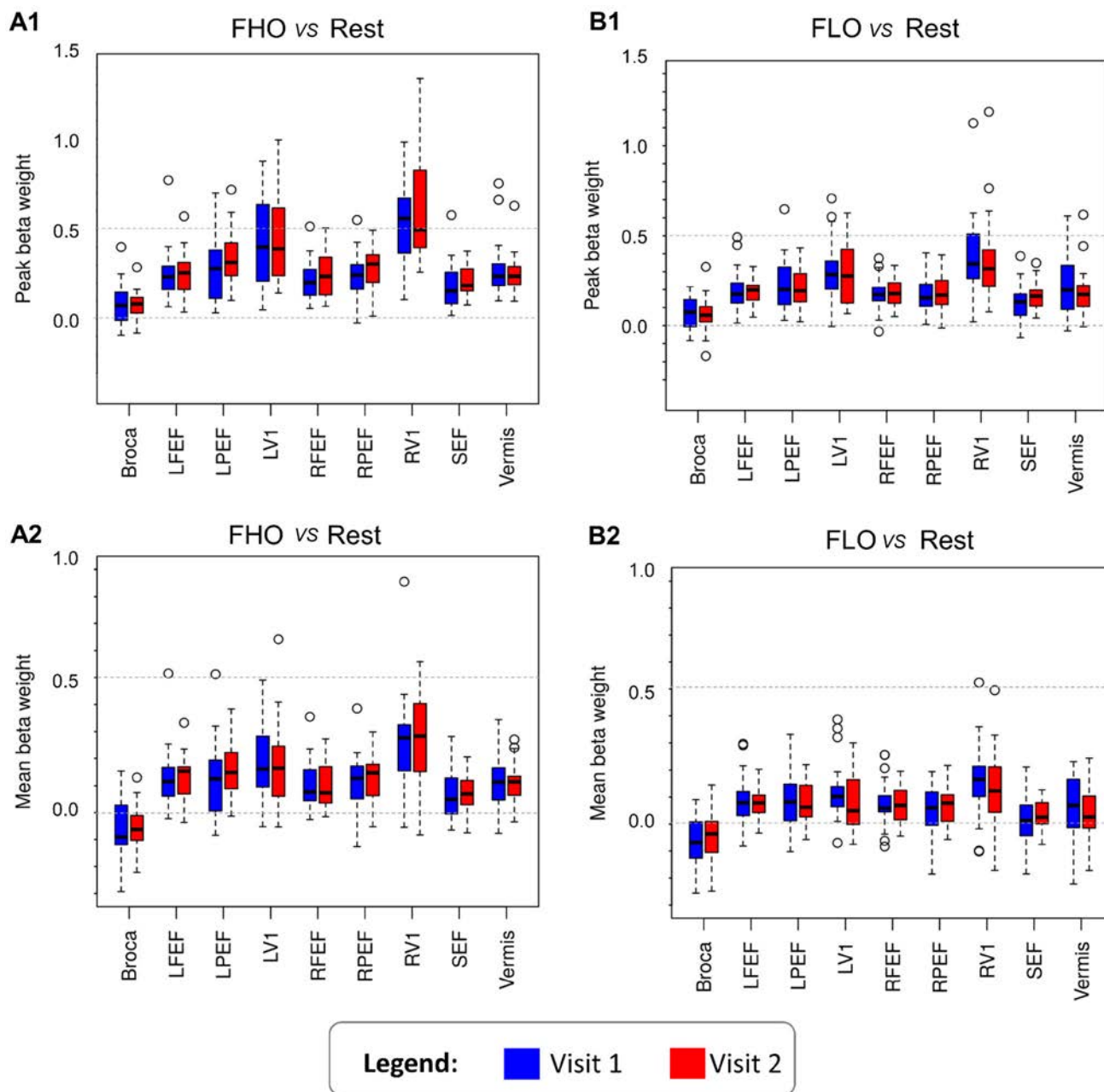


Fig. 3 Box-and-whisker plots showing the mean and upper and lower quartiles for the beta weights per ROI from visit 1 (blue) and visit 2 (red). Outliers are plotted as individual points. **A1, B1** Peak beta weights per vergence ROI mask from the FHO block *versus* rest

blocks (**A1**) and for the LFO *versus* rest blocks (**B1**). **A2, B2** Mean beta weights per ROI from the FHO *versus* rest blocks (**A2**) and FLO *versus* rest blocks (**B2**).

Evaluation of Test–Retest Reliability

Functional imaging is a popular method to non-invasively study metabolic activity of the brain and much research has been conducted to assess its utility for clinical medicine both in terms of biomarkers for disease or dysfunction and as outcome measures for longitudinal studies as reviewed by Dubois and Adolphs [96]. Studies of the reliability of functional imaging strongly encourage both group-level

and individual-level analyses, especially if fMRI is to be used as a biomarker, since individual participants would be compared to normative databases [38, 40]. For the vergence eye movement stimulus-induced protocol described in this study, the functional activation magnitude was assessed using the ICC to have fair test–retest reliability for the FEF and SEF since the ICCs were between 0.4 and 0.55. The PEF had good test–retest reliability, while the primary visual cortex had excellent

Table 3 Dice coefficients of the FHO *versus* rest and FLO *versus* rest tasks for each vergence ROI in 20 participants (mean \pm SD)

ROI	FHO <i>vs</i> Rest $P < 0.05$	FLO <i>vs</i> Rest $P < 0.05$
L-V1	0.59 \pm 0.31	0.48 \pm 0.34
R-V1	0.74 \pm 0.29	0.49 \pm 0.29
L-PEF	0.43 \pm 0.31	0.24 \pm 0.28
R-PEF	0.35 \pm 0.35	0.19 \pm 0.22
L-FEF	0.34 \pm 0.32	0.14 \pm 0.19
R-FEF	0.35 \pm 0.33	0.08 \pm 0.13
SEF	0.15 \pm 0.24	0.09 \pm 0.17
Vermis	0.32 \pm 0.29	0.06 \pm 0.18
Broca's area	0 \pm 0	0 \pm 0

test–retest reliability when evaluating BOLD functional activity signal strength. The beta weights for an individual-level analysis of each participant were similar and no significant differences were found between visits 1 and 2. Hence, functional activity within the defined vergence ROI masks is a reliable measure and suitable for longitudinal studies.

The reproducibility of spatial extent is susceptible to the threshold value, especially for individual-participant analysis [38, 97, 98]. Spatial extent is also susceptible to motion artifacts [38]. The group-level data analysis showed substantial spatial extent overlap. These data support the idea that spatial extent is reliable when the datasets are averaged among participants and group-level analysis can be used in a longitudinal study. However, for the within-participant analysis, the Dice coefficients for the vergence ROIs in the FHO block *versus* rest block were between 0.32 and 0.43 for the FEF, PEF, and OV, which is moderate repeatability. While the primary visual cortex for the individual analysis had good Dice coefficients between 0.6 and 0.7, the SEF had a poor Dice coefficient of 0.15. Therefore, caution should be exercised when studying the spatial extent in individual participants for this vergence task in a longitudinal study. Other studies have reported Dice coefficients for within-participant analyses between 0.7 and 0.8 when analyzing spatial extent for the primary motor cortex during a finger-tapping task [38] and 0.25–0.27 for an intertemporal choice task [40]. The results of our study are similar to others on the test–retest reliability of spatial extent for within-participant analyses [38, 40].

Differences between the FHO and FLO Vergence Eye Movement Tasks

Results from our study support the proposal that a block of 8 vergence eye movements (FHO block) stimulates a

stronger BOLD signal than a block of 4 vergence eye movements (FLO block) both in terms of magnitude and spatial extent. The number of saccades occurring within a block has been shown to be directly proportional to the BOLD signal strength [53]. Kimmig and colleagues suggested that the direct relationship between the frequency of saccades and the amplitude of the BOLD signal is because the BOLD signal is an indication of overall global energy consumption—the more saccades generated, the more energy consumed, and hence, the greater the BOLD signal [53]. Our results on vergence eye movements were similar to those reported for the saccadic eye movement system.

Future Randomized Clinical Trials on Vergence Dysfunction

Vergence dysfunctions such as strabismus, convergence insufficiency, divergence insufficiency, convergence excess, and divergence excess are common in the general population. A meta-analysis of strabismus reports an incidence of 1.93% [99]. Convergence insufficiency is more common, reported in 3.4%–17.6% of the general population [16–22]. The other vergence dysfunctions are less common; specifically, convergence excess is present in 2.3%–2.9% [22, 100], divergence insufficiency in 0.8% [100], and divergence excess in 0.6% [100]. While randomized clinical trials have shown that therapeutic interventions lead to a sustained improvement in the visual symptoms and clinical signs of convergence insufficiency [47, 101–107], the underlying neural mechanism by which vision therapy adapts the neural substrates used to generate a vergence eye movement is not well understood. Small pilot longitudinal studies have been conducted to assess the influence of vision therapy on the underlying functional activity of the brain for convergence insufficiency [35, 36, 108]. However, none of these studies assessed the validity of using fMRI as a potential outcome measure [35, 36]. Future studies can also investigate the neural mechanisms underlying vision therapy in patients with concussion-related visual symptoms [109].

The data presented here identify vergence ROI masks that are reliable at both the group and individual levels for the magnitude of the functional activity evoked using a vergence step protocol of 8 vergence eye movements (FHO eye movement block) compared to sustained fixation (rest block). This protocol was found to be reliable based on the ICC and beta weight analyses of the vergence ROIs. Spatial extent was reliable for group-level analysis. However, our results revealed that caution should be exercised when studying spatial extent for individual-level analysis in a longitudinal study. These results support the conclusion that the magnitude of the functional activity generated by a

stimulus-induced protocol evoking 8 vergence eye movements compared to a sustained fixation task (rest block) is reliable as an outcome measure for RCTs to assess therapeutic interventions for patients with vergence dysfunctions.

Acknowledgements This work was supported by the National Eye Institute of the National Institutes of Health, Department of Health and Human Services, Bethesda, MD, USA (NEI R01EY023261 to TLA).

Conflict of interest All authors claim that there are no conflicts of interest.

References

- Busettini C, Davison RC, Gamlin PDR. Vergence Eye Movements. 1st ed. New York: Encyclopedia of Neuroscience Elsevier, 2009: 75–84.
- Mays LE, Porter JD, Gamlin PD, Tello CA. Neural control of vergence eye movements: neurons encoding vergence velocity. *J Neurophysiol* 1986, 56: 1007–1021.
- May PJ, Warren S, Gamlin PDR, Billig I. An anatomic characterization of the midbrain near response neurons in the macaque monkey. *Invest Ophthalmol Vis Sci* 2018, 59: 1486–1502.
- Mays LE, Gamlin PDR. Neuronal circuitry controlling the near response. *Curr Opin Neurobiol* 1995, 5: 763–768.
- Gamlin PDR. Neural mechanisms for the control of vergence eye movements. *Ann N Y Acad Sci* 2002, 956: 264–272.
- Kapoula Z, Isotalo E, Müri RM, Bucci MP, Rivaud-Péchoix S. Effects of transcranial magnetic stimulation of the posterior parietal cortex on saccades and vergence. *Neuroreport* 2001, 12: 4041–4046.
- Coubard OA, Kapoula Z. Dorsolateral prefrontal cortex prevents short-latency saccade and vergence: a TMS study. *Cereb Cortex* 2006, 16: 425–436.
- Alkan Y, Biswal BB, Taylor PA, Alvarez TL. Segregation of frontoparietal and cerebellar components within saccade and vergence networks using hierarchical independent component analysis of fMRI. *Vis Neurosci* 2011, 28: 247–261.
- Alvarez TL, Alkan Y, Gohel S, Ward DB, Biswal BB. Functional anatomy of predictive vergence and saccade eye movements in humans: A functional MRI investigation. *Vision Res* 2010, 50: 2163–2175.
- Ward MK, Bolding MS, Schultz KP, Gamlin PD. Mapping the macaque superior temporal sulcus: functional delineation of vergence and version eye-movement-related activity. *J Neurosci* 2015, 35: 7428–7442.
- Rambold H, Neumann G, Sander T, Helmchen C. Pontine lesions may cause selective deficits of “slow” vergence eye movements. *Ann N Y Acad Sci* 2005, 1039: 567–570.
- Rambold H, Sander T, Neumann G, Helmchen C. Palsy of “fast” and “slow” vergence by pontine lesions. *Neurology* 2005, 64: 338–340.
- Sander T, Sprenger A, Neumann G, Machner B, Gottschalk S, Rambold H, *et al.* Vergence deficits in patients with cerebellar lesions. *Brain* 2009, 132: 103–115.
- Raemaekers M, Vink M, Zandbelt B, van Wezel RJ, Kahn RS, Ramsey NF. Test-retest reliability of fMRI activation during prosaccades and antisaccades. *Hum Brain Mapp* 2007, 36: 532–542.
- Lukasova K, Sommer J, Nucci-Da-Silva MP, Vieira G, Blanke M, Bremmer F, *et al.* Test-retest reliability of fMRI activation generated by different saccade tasks. *J Magn Reson Imaging* 2014, 40: 37–46.
- Cooper J, Jamal N. Convergence insufficiency—a major review. *Optometry* 2012, 83: 137–158.
- Hussaindeen JR, Rakshit A, Singh NK, George R, Swaminathan M, Kapur S, *et al.* Prevalence of non-strabismic anomalies of binocular vision in Tamil Nadu: report 2 of BAND study. *Clin Exp Optom* 2017, 100: 642–648.
- Wajuihian SO, Hansraj R. Vergence anomalies in a sample of high school students in South Africa. *J Optom* 2016, 9: 246–257.
- Rouse MW, Borsting EJ, Hyman L, Hussein M, Cotter SA, Flynn M, *et al.* Frequency of convergence insufficiency among fifth and sixth graders. The Convergence Insufficiency and Reading Study (CIRS) group. *Optom Vis Sci* 1999, 76: 643–649.
- Davis AL, Harvey EM, Twelker JD, Miller JM, Leonard-Green T, Campus I. Convergence insufficiency, accommodative insufficiency, visual symptoms, and astigmatism in Tohono O’odham students. *J Ophthalmol* 2016, 2016: 1–7.
- Nunes AF, Monteiro PML, Ferreira FBP, Nunes AS. Convergence insufficiency and accommodative insufficiency in children. *BMC Ophthalmol* 2019, 19: 19–58.
- García-Muñoz Á, Carbonell-Bonete S, Cantó-Cerdán M, Cacho-Martínez P. Accommodative and binocular dysfunctions: prevalence in a randomised sample of university students. *Clin Exp Optom* 2016, 99: 313–321.
- Master CL, Scheiman M, Gallaway M, Goodman A, Robinson RL, Master SR, *et al.* Vision diagnoses are common after concussion in adolescents. *Clin Pediatr (Phila)* 2016, 55: 260–267.
- Alvarez TL, Kim EH, Vicci VR, Dhar SK, Biswal BB, Barrett AM. Concurrent vision dysfunctions in convergence insufficiency with traumatic brain injury. *Optom Vis Sci* 2012, 89: 1740–1751.
- Bolding MS, Lahti AC, White D, Moore C, Gurler D, Gawne TJ, *et al.* Vergence eye movements in patients with schizophrenia. *Vision Res* 2014, 102: 64–70.
- Chrobak A, Siuda K, Biela M, Arciszewska A, Siwek M, Pilecki MW, *et al.* Convergence insufficiency with unilateral exophoria at near in schizophrenia and bipolar disorder—a preliminary study. *Psychiatr Pol* 2015, 48: 1143–1154.
- Granet DB, Gomi CF, Ventura R, Miller-Scholte A. The relationship between convergence insufficiency and ADHD. *Strabismus* 2005, 13: 163–168.
- Borsting E, Rouse M, Chu R. Measuring ADHD behaviors in children with symptomatic accommodative dysfunction or convergence insufficiency: a preliminary study. *Optom J Am Optom Assoc* 2005, 76: 588–592.
- Lin Y, Li M, Zhou Y, Deng W, Ma X, Wang Q, *et al.* Age-related reduction in cortical thickness in first-episode treatment-naïve patients with schizophrenia. *Neurosci Bull* 2019, 35: 688–696.
- Su W, Guo J, Zhang Y, Zhou J, Chen N, Zhou M, *et al.* A longitudinal functional magnetic resonance imaging study of working memory in patients following a transient ischemic attack: A preliminary study. *Neurosci Bull* 2018, 34: 963–971.
- Sexton CE, Sykara K, Karageorgiou E, Zitser J, Rosa T, Yaffe K, *et al.* Connections between insomnia and cognitive aging. *Neurosci Bull* 2019. <https://doi.org/10.1007/s12264-019-00401-9>
- Hamzei F, Liepert J, Dettmers C, Weiller C, Rijntjes M. Two different reorganization patterns after rehabilitative therapy: An

- exploratory study with fMRI and TMS. *Neuroimage* 2006, 31: 710–720.
33. Laatsch L, Krisky C. Changes in fMRI activation following rehabilitation of reading and visual processing deficits in subjects with traumatic brain injury. *Brain Inj* 2006, 20: 1367–1375.
 34. Sheng B, Lin M. A longitudinal study of functional magnetic resonance imaging in upper-limb hemiplegia after stroke treated with constraint-induced movement therapy. *Brain Inj* 2009, 23: 65–70.
 35. Alvarez TL, Vicci VR, Alkan Y, Kim EH, Gohel S, Barrett AM, *et al.* Vision therapy in adults with convergence insufficiency: Clinical and functional magnetic resonance imaging measures. *Optom Vis Sci* 2010, 87: 985–1002.
 36. Widmer DE, Oechsli TS, Limbachia C, Kulp MT, Toole AJ, Kashou NH, *et al.* Post-therapy functional magnetic resonance imaging in adults with symptomatic convergence insufficiency. *Optom Vis Sci* 2018, 95: 505–514.
 37. Alvarez TL, Jaswal R, Gohel S, Biswal BB. Functional activity within the frontal eye fields, posterior parietal cortex, and cerebellar vermis significantly correlates to symmetrical vergence peak velocity: An ROI-based, fMRI study of vergence training. *Front Integr Neurosci* 2014, 8: 1–12.
 38. Gorgolewski KJ, Storkey AJ, Bastin ME, Whittle I, Pernet C. Single subject fMRI test—retest reliability metrics and confounding factors. *Neuroimage* 2013, 69: 231–243.
 39. Shrout PE, Fleiss JL. Intraclass correlations: uses in assessing rater reliability. *Psychol Bull* 1979, 86: 420–428.
 40. Fröhner JH, Teckentrup V, Smolka MN, Kroemer NB. Addressing the reliability fallacy in fMRI: Similar group effects may arise from unreliable individual effects. *Neuroimage* 2019, 195: 174–189.
 41. Dice LR. Measures of the amount of ecologic association between species. *Ecology* 1945, 26: 297–302.
 42. Sorensen T. A method of establishing groups of equal amplitude in plant sociology based on similarity of species content. *Biol Skr K danske Vindensk Selsk* 1948, 4: 1–34.
 43. Rouse MW, Borsting EJ, Mitchell GL, Cotter SA, Kulp M, Scheiman M, *et al.* Validity of the convergence insufficiency symptom survey: a confirmatory study. *Optom Vis Sci* 2009, 86: 357–363.
 44. Rouse MW, Borsting EJ, Lynn Mitchell G, Scheiman M, Cotter SA, Cooper J, *et al.* Validity and reliability of the revised convergence insufficiency symptom survey in adults. *Ophthalmic Physiol Opt* 2004, 24: 384–390.
 45. CITT-ART Investigator Group, Scheiman M, Mitchell GL, Cotter SA, Kulp M, Chase C, *et al.* Convergence insufficiency treatment trial—attention and reading trial (CITT-ART): design and methods. *Vis Dev Rehabil* 2015, 1: 214–228.
 46. Convergence Insufficiency Treatment Trial (CITT) Study Group. The convergence insufficiency treatment trial: design, methods, and baseline data. *Ophthalmic Epidemiol* 2008, 15: 24–36.
 47. Convergence Insufficiency Treatment Trial Study Group. Randomized clinical trial of treatments for symptomatic convergence insufficiency in children. *Arch Ophthalmol* 2008, 126: 1336–1349.
 48. Sheard C. Zones of ocular comfort. *Am J Optom* 1930, 7: 9–25.
 49. Hofstetter HW. A comparison of Duane's and Donders' tables of the amplitude of accommodation. *Optom Vis Sci* 1944, 21: 345–363.
 50. Cornelissen FW, Peters EM, Palmer J. The Eyelink Toolbox: eye tracking with MATLAB and the Psychophysics Toolbox. *Behav Res Methods Instrum Comput* 2002, 34: 613–617.
 51. Alvarez TL, Semmlow JL, Yuan W, Munoz P. Comparison of disparity vergence system responses to predictable and non-predictable stimulations. *Cah Psychol Cogn* 2002, 21: 243–261.
 52. Kumar AN, Han Y, Garbutt S, Leigh RJ. Properties of anticipatory vergence responses. *Invest Ophthalmol Vis Sci* 2002, 43: 2626–2632.
 53. Kimmig H, Greenlee M, Gondan M, Schira M, Kassubek J, Mergner T. Relationship between saccadic eye movements and cortical activity as measured by fMRI: quantitative and qualitative aspects. *Exp Brain Res* 2001, 141: 184–194.
 54. Kim EH, Vicci VR, Han SJ, Alvarez TL. Sustained fixation induced changes in phoria and convergence peak velocity. *PLoS One* 2011, 6: e20883.
 55. Alvarez TL, Semmlow JL, Yuan W, Munoz P. Disparity vergence double responses processed by internal error. *Vision Res* 2000, 40: 341–347.
 56. Kim EH, Vicci VR, Granger-Donetti B, Alvarez TL. Short-term adaptations of the dynamic disparity vergence and phoria systems. *Exp Brain Res* 2011, 212: 267–278.
 57. Alvarez TL, Kim EH, Granger-Donetti B. Adaptation to progressive additive lenses: potential factors to consider. *Sci Rep* 2017, 7: 2529.
 58. Kim EH, Granger-Donetti B, Vicci VR, Alvarez TL. The relationship between phoria and the ratio of convergence peak velocity to divergence peak velocity. *Investig Ophthalmol Vis Sci* 2010, 51: 4017–4027.
 59. Alvarez TL, Kim EH, Yaramothu C, Granger-Donetti B. The influence of age on adaptation of disparity vergence and phoria. *Vision Res* 2017, 133: 1–11.
 60. Chen YF, Lee YY, Chen T, Semmlow JL, Alvarez TL. Behaviors, models, and clinical applications of vergence eye movements. *J Med Biol Eng* 2010, 30: 1–15.
 61. Alvarez TL, Kim EH. Analysis of saccades and peak velocity to symmetrical convergence stimuli: binocularly normal controls compared to convergence insufficiency patients. *Investig Ophthalmology Vis Sci* 2013, 54: 4122–4135.
 62. Semmlow JL, Chen YF, Granger-Donetti B, Alvarez TL. Correction of saccade-induced midline errors in responses to pure disparity vergence stimuli. *J Eye Movement Res* 2009, 21: 1–13.
 63. Behzadi Y, Restom K, Liao J, Liu TT. A component based noise correction method (CompCor) for BOLD and perfusion based fMRI. *Neuroimage* 2007, 37: 90–101.
 64. Friston KJ, Williams S, Howard R, Frackowiak RS, Turner R. Movement-related effects in fMRI time-series. *Magn Reson Med* 1996, 35: 346–355.
 65. Yan CG, Cheung B, Kelly C, Colcombe S, Craddock RC, Di Martino A, *et al.* A comprehensive assessment of regional variation in the impact of head micromovements on functional connectomics. *Neuroimage* 2013, 76: 183–201.
 66. Servatius RJ, Spiegler KM, Handy JD, Pang KCH, Tsao JW, Mazzola CA. Neurocognitive and fine motor deficits in asymptomatic adolescents during the subacute period after concussion. *J Neurotrauma* 2018, 35: 1008–1014.
 67. Benjamini Y, Hochberg Y. Controlling the false discovery rate: a practical and powerful approach to multiple testing. *J R Stat Soc Ser B* 1995, 57: 289–300.
 68. Gamlin PDR, Yoon K. An area for vergence eye movement in primate frontal cortex. *Nature* 2000, 407: 1003–1007.
 69. Fukushima J, Akao T, Takeichi N, Kurkin S, Kaneko CR, Fukushima K. Pursuit-related neurons in the supplementary eye fields: discharge during pursuit and passive whole body rotation. *J Neurophysiol* 2004, 91: 2809–2825.
 70. Zhang H, Gamlin PD. Neurons in the posterior interposed nucleus of the cerebellum related to vergence and

- accommodation. I. Steady-state characteristics. *J Neurophysiol* 1998, 79: 1255–1269.
71. Gnadt JW, Mays LE. Neurons in monkey parietal area LIP are tuned for eye-movement parameters in three-dimensional space. *J Neurophysiol* 1995, 73: 280–297.
 72. Nienborg H, Bridge H, Parker AJ, Cumming BG. Receptive field size in V1 neurons limits acuity for perceiving disparity modulation. *J Neurosci* 2004, 24: 2065–2076.
 73. Prince SJ, Pointon AD, Cumming BG, Parker AJ. The precision of single neuron responses in cortical area V1 during stereoscopic depth judgments. *J Neurosci* 2000, 20: 3387–3400.
 74. Prince SJD, Cumming BG, Parker AJ. Range and mechanism of encoding of horizontal disparity in macaque V1. *J Neurophysiol* 2002, 87: 209–221.
 75. Cox RW. AFNI: Software for analysis and visualization of functional magnetic resonance neuroimages. *Comput Biomed Res* 1996, 29: 162–173.
 76. Binkofski F, Amunts K, Stephan KM, Posse S, Schormann T, Freund HJ. Broca's region subserves imagery of motion: A combined cytoarchitectonic and fMRI study. *Hum Brain Mapp* 2000, 11: 273–285.
 77. Santi A, Grodzinsky Y. Working memory and syntax interact in Broca's area. *Neuroimage* 2007, 37: 8–17.
 78. Paus T. Location and function of the human frontal eye-field: a selective review. *Neuropsychologia* 1996, 34: 475–483.
 79. Vernet M, Quentin R, Chanes L, Mitsumasu A, Valero-Cabré A. Frontal eye field, where art thou? Anatomy, function, and non-invasive manipulation of frontal regions involved in eye movements and associated cognitive operations. *Front Integr Neurosci* 2014, 8: 1–24.
 80. Pierrot-Deseilligny C, Milea D, Müri RM. Eye movement control by the cerebral cortex. *Curr Opin Neurol* 2004, 17: 17–25.
 81. Grosbras MH, Lobel E, Van de Moortele PF, LeBihan D, Berthoz A. An anatomical landmark for the supplementary eye fields in human revealed with functional magnetic resonance imaging. *Cereb Cortex* 1999, 9: 705–711.
 82. Gamlin PDR, Clarke RJ. Single-unit activity in the primate nucleus reticularis tegmenti pontis related to vergence and ocular accommodation. *J Neurophysiol* 1995, 73: 2115–2119.
 83. Takagi M, Tamargo R, Zee DS. Effects of lesions of the cerebellar oculomotor vermis on eye movements in primate: binocular control. *Prog Brain Res* 2003, 142: 19–33.
 84. Poldrack RA. Region of interest analysis for fMRI. *Soc Cogn Affect Neurosci* 2007, 2: 67–70.
 85. Tong Y, Chen Q, Nichols TE, Rasetti R, Callicott JH, Berman KF, *et al.* Seeking optimal region-of-interest (roi) single-value summary measures for fMRI studies in imaging genetics. *PLoS One* 2016, 11: e0151391.
 86. Abrahamsson M, Ohlsson J, Björndahl M, Abrahamsson H. Clinical evaluation of an eccentric infrared photorefractor: the PowerRefractor. *Acta Ophthalmol Scand* 2003, 81: 605–610.
 87. Bennett CM, Miller MB. How reliable are the results from functional magnetic resonance imaging? *Ann N Y Acad Sci* 2010, 1191: 133–155.
 88. Caceres A, Hall DL, Zelaya FO, Williams SC, Mehta MA. Measuring fMRI reliability with the intra-class correlation coefficient. *Neuroimage* 2009, 45: 758–768.
 89. Koo TK, Li MY. A Guideline of selecting and reporting intraclass correlation coefficients for reliability research. *J Chiropr Med* 2016, 15: 155–163.
 90. Li L, Zeng L, Lin Z, Cazzell M, Liu H. Tutorial on use of intraclass correlation coefficients for assessing intertest reliability and its application in functional near-infrared spectroscopy-based brain imaging. *J Biomed Opt* 2015, 20: 050801.
 91. Morrison MA, Churchill NW, Cusimano MD, Schweizer TA, Das S, Graham SJ. Reliability of task-based fMRI for preoperative planning: a test-retest study in brain tumor patients and healthy controls. *PLoS One* 2016, 11: e0149547.
 92. Zuo XN, Di Martino A, Kelly C, Shehzad ZE, Gee DG, Klein DF, *et al.* The oscillating brain: Complex and reliable. *Neuroimage* 2010, 49: 1432–1445.
 93. Zuo XN, Kelly C, Adelstein JS, Klein DF, Castellanos FX, Milham MP. Reliable intrinsic connectivity networks: Test – retest evaluation using ICA and dual regression approach. *Neuroimage* 2010, 49: 2163–2177.
 94. Taylor PA, Gohel S, Di X, Walter M, Biswal BB. Functional covariance networks: obtaining resting-state networks from intersubject variability. *Brain Connect* 2012, 2: 203–217.
 95. Jaswal R, Gohel S, Biswal BB, Alvarez TL. Task-modulated coactivation of vergence neural substrates. *Brain Connect* 2014, 4: 595–607.
 96. Dubois J, Adolphs R. Building a science of individual differences from fMRI. *Trends Cogn Sci* 2016, 20: 425–443.
 97. Duncan KJ, Pattamadilok C, Knierim I, Devlin JT. Consistency and variability in functional localisers. *Neuroimage* 2009, 46: 1018–1026.
 98. Fernández G, Specht K, Weis S, Tendolkar I, Reuber M, Fell J, *et al.* Intrasubject reproducibility of presurgical language lateralization and mapping using fMRI. *Neurology* 2003, 60: 969–975.
 99. Hashemi H, Khabazkhoob M, Nabovati P, Shahraki FA, Ostadimoghaddam H, Faghihi M, *et al.* Accommodative insufficiency in a student population in Iran. *J Optom* 2019, 12: 161–167.
 100. Atowa UC, Wajuihian SO, Hansraj R. Vergence profile and prevalence of non-strabismic vergence anomalies among school children in Abia State, Nigeria. *Ophthalmic Epidemiol* 2019, 26: 121–131.
 101. Scheiman M, Rouse MW, Kulp MT, Cotter S, Hertle R, Mitchell GL. Treatment of convergence insufficiency in childhood: a current perspective. *Optom Vis Sci* 2009, 86: 420–428.
 102. Scheiman M, Cotter S, Rouse M, Mitchell GL, Kulp M, Cooper J, *et al.* Randomised clinical trial of the effectiveness of base-in prism reading glasses versus placebo reading glasses for symptomatic convergence insufficiency in children. *Br J Ophthalmol* 2005, 89: 1318–1323.
 103. Scheiman M, Mitchell GL, Cotter S, Kulp MT, Cooper J, Rouse M, *et al.* A randomized clinical trial of vision therapy/orthoptics versus pencil pushups for the treatment of convergence insufficiency in young adults. *Optom Vis Sci* 2005, 82: E583–E595.
 104. Pediatric Eye Disease Investigator Group. Home-based therapy for symptomatic convergence insufficiency in children. *Optom Vis Sci* 2016, 93: 1457–1465.
 105. Nehad T, Salem T, Elmohamady MN. Combined office-based vergence therapy and home therapy system for convergence insufficiency in Egyptian children. *Open Ophthalmol J* 2018, 12: 12–18.
 106. Scheiman M, Gwiazda J, Li T. Non-surgical interventions for convergence insufficiency. *Cochrane Database Syst Rev* 2011, 3: CD006768.
 107. Convergence Insufficiency Treatment Trial (CITT) Study Group. Long-term effectiveness of treatments for symptomatic convergence insufficiency in children. *Optom Vis Sci* 2009, 86: 1096–1103.
 108. Scheiman M, Talasan H, Alvarez TL. Objective assessment of disparity vergence after treatment of symptomatic convergence insufficiency in children. *Optom Vis Sci* 2019, 96: 3–16.
 109. Scheiman MM, Talasan H, Mitchell GL, Alvarez TL. Objective assessment of vergence after treatment of concussion-related CI: A pilot study. *Optom Vis Sci* 2017, 94: 74–88.



Role of T-type Calcium Channels in Generating Hyperexcitatory Behaviors during Emergence from Sevoflurane Anesthesia in Neonatal Rats

Feng-Yan Shen¹ · Byung-Gun Lim² · Wen Wen³ · Yu Zhang¹ · Bo Cao⁵ · Yue-Guang Si⁵ · Li-Qing Ma¹ · Meng Deng¹ · Yang In Kim⁴ · Young-Beom Kim⁴ · Ying-Wei Wang¹

Received: 14 June 2019 / Accepted: 6 November 2019 / Published online: 17 January 2020
© Shanghai Institutes for Biological Sciences, CAS 2020

Abstract In the current study, we sought to investigate whether T-type Ca^{2+} channels (TCCs) in the brain are involved in generating post-anesthetic hyperexcitatory behaviors (PAHBs). We found that younger rat pups (postnatal days 9–11) had a higher incidence of PAHBs and higher PAHB scores than older pups (postnatal days 16–18) during emergence from sevoflurane anesthesia. The power spectrum of the theta oscillations (4 Hz–8 Hz) in the prefrontal cortex was significantly enhanced in younger pups when PAHBs occurred, while there were no significant changes in older pups. Both the power of theta oscillations and the level of PAHBs were significantly reduced by the administration of TCC inhibitors. Moreover, the sensitivity of TCCs in the medial dorsal thalamic

nucleus to sevoflurane was found to increase with age by investigating the kinetic properties of TCCs *in vitro*. TCCs were activated by potentiated GABAergic depolarization with a sub-anesthetic dose of sevoflurane (1%). These data suggest that (1) TCCs in the brain contribute to the generation of PAHBs and the concomitant electroencephalographic changes; (2) the stronger inhibitory effect of sevoflurane contributes to the lack of PAHBs in older rats; and (3) the contribution of TCCs to PAHBs is not mediated by a direct effect of sevoflurane on TCCs.

Keywords Emergence agitation · Neonatal rat · General anesthesia · Sevoflurane · T-type calcium channel · Theta wave

Feng-Yan Shen, Byung-Gun Lim and Wen Wen have contributed equally to this work.

✉ Young-Beom Kim
floweransi@korea.ac.kr

✉ Ying-Wei Wang
wangyingwei@yahoo.com

¹ Department of Anesthesiology, Huashan Hospital, Fudan University, Shanghai 200040, China

² Department of Anesthesiology and Pain Medicine, Korea University Guro Hospital, College of Medicine, Korea University, Seoul 08308, Korea

³ Department of Anesthesiology, Xinhua Hospital, School of Medicine, Shanghai Jiaotong University, Shanghai 200092, China

⁴ Department of Physiology and Neuroscience Research Institute, College of Medicine, Korea University, Seoul 02841, Korea

⁵ Institute of Brain Functional Genomics, East China Normal University, Shanghai 200062, China

Introduction

With the development of new anesthetic formulations and techniques, general anesthesia has become widely available in pediatric surgery. Sevoflurane is a popular volatile anesthetic used in pediatric surgery because of its many advantages including hemodynamic stability, sweet smell, lack of respiratory irritation, and rapid onset of action [1]. However, a high risk of emergence agitation (EA) or delirium induced by sevoflurane has been extensively reported [2].

EA is a well-documented phenomenon in the immediate postoperative period in humans, particularly in preschool-age children [3]. This condition manifests as an unconscious state accompanied by a series of hyperexcitatory behaviors that often spontaneously resolve [4]. However, EA can be urgent when children become uncontrollable during emergence from general anesthesia, and may hurt themselves by accident. EA unavoidably contributes to

extension in hospital stay, and may place additional burdens on both patients and medical staff [5]. Furthermore, EA may be associated with postoperative psychological problems in children, such as eating or sleeping disorders, anxiety, apathy, and aggression [6]. Although many adjunct agents (e.g., dexmedetomidine, remifentanyl, ketamine, and nalbuphine) have demonstrated some effectiveness against EA [7–9], the underlying mechanism is not yet clear.

In a previous study, we reported EA-like behaviors, which we named post-anesthetic hyperexcitatory behaviors (PAHBs), during emergence from sevoflurane anesthesia in neonatal rats [10]. We developed a scale for evaluating such behaviors and demonstrated that PABHs present features similar to EA in humans. We found that sevoflurane-induced PABHs are closely associated with GABAergic (GABA, γ -aminobutyric acid) depolarization/excitation in the neocortical neurons of neonatal rats. However, sevoflurane-potentiated depolarizing potentials cannot activate action potentials alone because of the limited reversal potential of GABA. Nonetheless, these potentials are able to elicit action potentials, presumably by evoking other subthreshold events. Low-threshold Ca^{2+} spikes, which are mediated by the T-type Ca^{2+} channel (TCC), result in a neuron reaching the threshold for burst firing in the central nervous system [11]. Therefore, we sought to investigate whether TCCs are involved in generating PABHs in neonatal rats.

Materials and Methods

Animal Care

Pregnant Sprague-Dawley rats from the Key Laboratory of Brain Functional Genomics affiliated with East China Normal University (Shanghai, China) were housed in a temperature-controlled (22°C–24°C) vivarium on a 12 h/12 h light-dark cycle. Male pups born of these rats were used. The day of birth was defined as postnatal day 0 (P0). The experimental procedures described below were in accordance with the ARRIVE (Animals in Research: Reporting *In Vivo* Experiments) guidelines and were approved by the Animal Care and Use Committee of Fudan University in Shanghai (201802130S). All possible efforts were made to minimize the number of animals and their suffering.

PAHB Model and Assessment

Neonatal Sprague-Dawley rats were used in the behavioral test and were divided into younger (P9–P11) and older pups (P16–P18). PABH modeling and scoring were the same as we described in the previous study [10]. In brief,

anesthesia was induced in rat pups with 6% (*v/v*) sevoflurane gas over 1 min and was then maintained with 3% sevoflurane gas for 9 min. These gases were generated with a calibrated sevoflurane and oxygen-fed commercial vaporizer (Penlon, Abingdon, OX14, UK) and were supplied to the anesthesia chamber at 3 L/min. PABH scores were based on behavioral type [0, none; 1, trembling; 2, head bobbing or stereotypy; 3, unilateral forelimb or hindlimb clonus; 4, bilateral forelimb or hindlimb clonus; 5, side-to-side rolling; 6, wandering (i.e., scrambling along the monitoring chamber walls)], and a bonus score of 0, 0.5, or 1 was given on the basis of its subgrade (0, mild; 0.5, moderate; 1, severe). The sum of the main and bonus scores constituted the behavioral score. We also introduced an open field system to evaluate PABHs. The observation apparatus consisted of four plastic boxes (26 cm \times 26 cm) with a field bordered by 37-cm high sidewalls. Movement distance and movement duration were monitored in each rat for 6 min and analyzed using the Truscan system (Coulbourn, Holliston, MA).

Electroencephalogram (EEG) Recording

To determine the changes in cortical activity in the frontal lobe during the peri-anesthesia period, rat pups were fitted with instrumentation for EEG recording. A head rack and recording electrodes were mounted on each pup under sevoflurane anesthesia 6 h prior to EEG recording. The entire surgical process took no more than 15 min. Each pup's head was fixed on a turntable with a respiratory mask connected to the calibrated sevoflurane and oxygen-fed commercial vaporizer (Penlon Sigma Elite). EEG recording was generally composed of four stages that lasted 10 min each, acclimation, awakening (baseline recording), anesthesia, and emergence. The EEG signals were amplified by a Model 3000 amplifier (A.M. Carlsborg, WA) and digitized and sampled at 200- μ s intervals (Digidata 1440, pClamp 10.2; Molecular Devices, San Jose, CA). The power values were calculated from power spectra generated using Fourier analysis in MatLab software (MathWorks, Natick, MA).

Test of Drug Effects on PABHs and EEGs

To investigate the potential roles of TCCs in generating PABHs, we examined the effects of the TCC inhibitors NNC 55-0396 and ethosuximide on PABHs and EEGs. Intracerebroventricular microinjection (ICVM) of saline or NNC 55-0396 (0.1 μ g/kg body weight) was performed 5 min prior to sevoflurane anesthesia. For ICVM, a 26-gauge cannula made of polyethylene tubing (PE-10: inner diameter 0.28 mm and outer diameter 0.61 mm) was inserted into the lateral cerebral ventricle (stereotaxic coordinates:

0.4 mm lateral to the midline, 0.4 mm posterior to bregma, and 2.5 mm ventral to the skull surface [12]) and secured to the skull with surgical glue 24 h before the behavioral test or EEG recording. Ethosuximide (0.2 g/kg body weight) was administered intraperitoneally 5 min before sevoflurane anesthesia.

Thalamic Slice Preparation

Animals were anesthetized with sodium pentobarbitone (100 mg/kg body weight, i.p.), and the brain was quickly removed and submerged in ice-cold artificial cerebrospinal fluid (ACSF, in mmol/L: 124 NaCl, 1.3 MgSO₄, 3 KCl, 1.25 NaH₂PO₄, 26 NaHCO₃, 2.4 CaCl₂, and 10 glucose). After being chilled for 1–2 min, the brain was trimmed to a block containing the thalamus. Then, coronal slices (400 μm) were cut in ice-cold ACSF using a vibro-slicer (Leica VT1000, Buffalo Grove, IL). Slices containing the medial dorsal thalamic nucleus (MDTN) were transferred to a gas interface recording chamber perfused with aerated ACSF (95% O₂/5% CO₂; 22°C–24°C) containing (in μmol/L) 30 bicuculline methiodide, 2 nimodipine, 3 ω-conotoxin MVIIC, and 0.5 tetrodotoxin to screen out TCC currents [13]. To record GABA_A receptor-mediated responses in isolation, we included AP-5 [DL-2-amino-5-phosphopentanoic acid, an NMDA (N-methyl-D-aspartate) receptor antagonist, 100 μmol/L], DNQX (6,7-dinitroquinoxaline-2,3-dione, a non-NMDA receptor antagonist, 20 μmol/L), and CGP 54626 hydrochloride (a GABA_B receptor antagonist, 1 μmol/L) in the perfusion medium. ACSF for recording was perfused by a peristaltic pump-driven or gravity-fed bath-perfusion system at 0.5–1 mL/min. Humidified 95% O₂/5% CO₂ was continuously blown over the slices to further ensure the adequate oxygenation of cells in the tissue.

Intracellular Recording

Voltage-clamp recordings were obtained from neurons in MDTN slices equilibrated for 1 h–6 h in the recording chamber. Whole-cell recordings (series resistance, 6 MΩ–12 MΩ) of TCC currents were obtained with micropipettes (tip diameter, 1.5 μm–2.0 μm; resistance, 4 MΩ–6 MΩ) filled with an internal solution (pH 7.3) composed of (in mmol/L) 140 K-gluconate, 10 HEPES, 2 MgCl₂, 1 CaCl₂, 11 EGTA, and 2 K₂ATP, while the internal solution for gramicidin (50 μg/mL)-perforated patch clamp recording (series resistance, 30 MΩ–90 MΩ) was composed of (in mmol/L) 143 K-gluconate, 2 KCl, 10 HEPES, and 0.5 EGTA, pH 7.2–7.3. GABA_A receptor-mediated postsynaptic potentials were elicited by electrically stimulating a site near the recorded cell with a custom-made, bipolar tungsten electrode; constant current (0.1 mA–0.5 mA) or

voltage (5 V–20 V) pulses (biphasic square wave, 0.5-ms duration) were used for stimulation. Voltage errors resulting from series resistance were compensated offline for voltage-clamp recordings and online for current-clamp recordings by using a bridge circuit. The signals from neurons were amplified by an Axoclamp-700B amplifier (Molecular Devices) (bandwidth filter set to 10 kHz for current-clamp recordings and 1 kHz for voltage-clamp recordings) and were digitized and sampled at 50-μs intervals (Digidata 1440, pClamp 10.2; Molecular Devices). Activation/inactivation kinetic curves were fitted with the Boltzmann equation, where I_{max} is the maximum current, $V_{1/2}$ is the half-activation/inactivation potential, and k is the steepness constant.

Drugs

All drugs used in this study were from Sigma-Aldrich (St. Louis, MO), except for sevoflurane (Abbott, Queenborough, Kent, UK). For the direct application of sevoflurane to recorded neurons, we prepared sevoflurane-containing solutions by bubbling gas mixtures of sevoflurane and 95% O₂/5% CO₂ generated by the calibrated commercial vaporizer in ACSF for >30 min. The concentration of sevoflurane in the ACSF bubbled with gas mixtures containing 1% sevoflurane, as determined by gas chromatography, was 0.184 mmol/L, which was 92%–94% of the theoretical concentration. The sevoflurane-containing solutions with or without NNC 55-0396 (20 μmol/L) were focally applied to recorded neurons by the “Y-tube” method. To minimize the loss of sevoflurane, we used high-quality polytetrafluorethylene tubing and valves.

Statistical Analysis

Numerical data are expressed as the mean ± SEM. Student's *t*-test was used to compare two independent datasets with normal distributions, while paired *t*-tests were used to compare two dependent datasets with normal distributions. Two-way analysis of variance (ANOVA) and pairwise comparison with the Bonferroni method were performed to compare multiple independent datasets. The categorical data were compared using Fisher's exact test. $P \leq 0.05$ was considered significant.

Results

Enhanced Spontaneous Movements in Younger Pups During Emergence from Sevoflurane Anesthesia

Coincident with our previous findings [10], younger (P9–P11) pups had a high incidence of PAHBs (8 of 8 animals) and high PAHB scores (6.1 ± 0.25), while older pups (P16–P18) were placid during emergence from sevoflurane anesthesia (Fig. 1A, B).

To obtain a more objective evaluation, we examined PAHBs in the open-field test. According to the analysis of the results for movement distance and movement duration in the open field, we found that younger pups showed an eruption of spontaneous movement in the second minute after sevoflurane withdrawal. However, this phenomenon did not occur in older pups (movement distance in the second minute: P9–P11 vs P16–P18 = 0.2 ± 0.04 m vs 0.09 ± 0.05 m, $P = 0.003$; movement duration in the second minute: P9–P11 vs P16–P18 = 32.6 ± 4.53 s vs 9.8 ± 4.06 s, $P \leq 0.001$, $n = 8$, two-way ANOVA followed by Bonferroni's t -test, Fig. 1C, D).

Involvement of TCCs in Generating PAHBs

To investigate the contribution of TCCs to generating PAHBs, we delivered NNC 55-0396, a selective TCC inhibitor by ICVM [14]. We found that spontaneous movements 1 min–3 min after sevoflurane withdrawal were significantly inhibited (movement distance: Saline vs NNC 55-0396 = 0.4 ± 0.05 m vs 0.1 ± 0.04 m, $P \leq 0.001$; movement duration: Saline vs NNC 55-0396 = 65.1 ± 4.50 s vs 25.0 ± 5.69 s, $n = 6-7$, $P \leq 0.001$, Student's t -test, Fig. 2A, B). Moreover, the PAHB score of the NNC 55-0396 group was much lower than that of the saline group (Saline vs NNC 55-0396 = 6.1 ± 0.25 vs 4.2 ± 0.28 , $n = 6$ per group, $P \leq 0.001$, Student's t -test, Fig. 2C). We also found that PAHBs were controlled by the intraperitoneal administration of ethosuximide, an anti-absence seizure drug that functions by blocking TCC currents [15] (PAHB score: saline vs ethosuximide = 5.9 ± 0.30 vs 3.8 ± 0.66 , $n = 6$ per group, $P = 0.009$, Student's t -test, Fig. 2D). These data indicated that TCCs in the brain are involved in generating PAHBs.

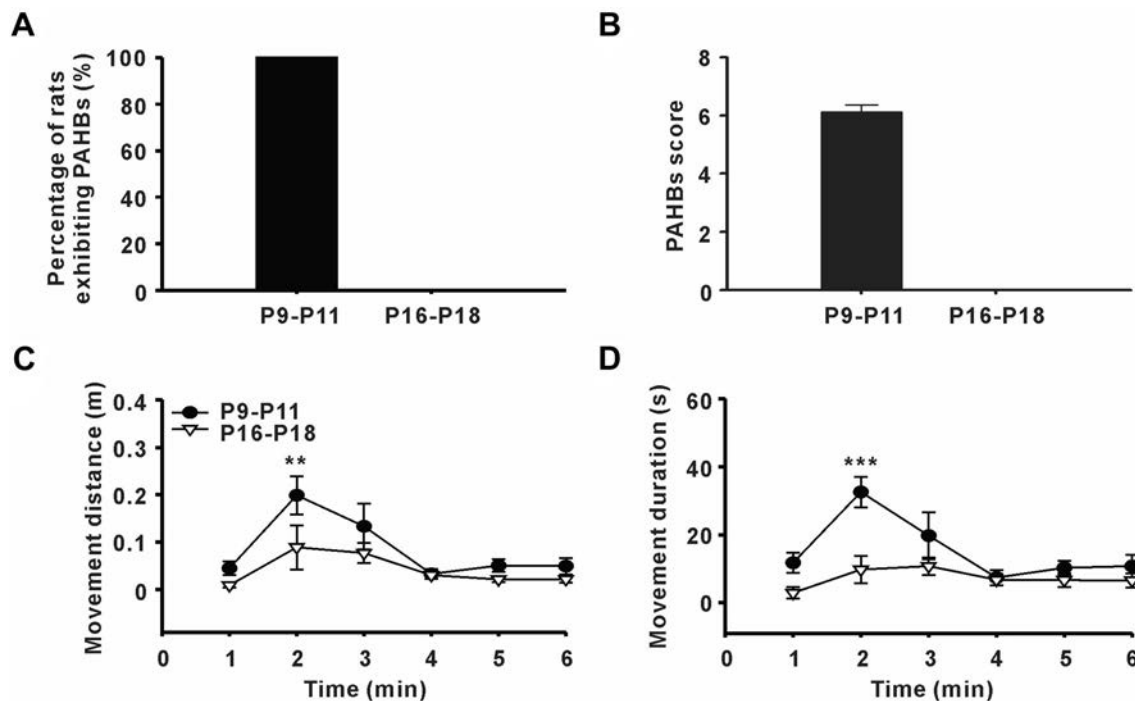


Fig. 1 Enhanced spontaneous movements in younger pups during emergence from sevoflurane anesthesia. **A** Incidence of post-anesthetic hyperexcitatory behaviors (PAHBs) in younger rat pups (P9–P11) and older rat pups (P16–P18) ($n = 8$ per group). **B** PAHB scores

in younger and older pups. **C, D** Movement distance and movement duration in younger and older pups after sevoflurane withdrawal in the open field test ($n = 8$ per group; ** $P \leq 0.01$, *** $P \leq 0.001$ vs P16–P18, two-way ANOVA followed by Bonferroni's t -test).

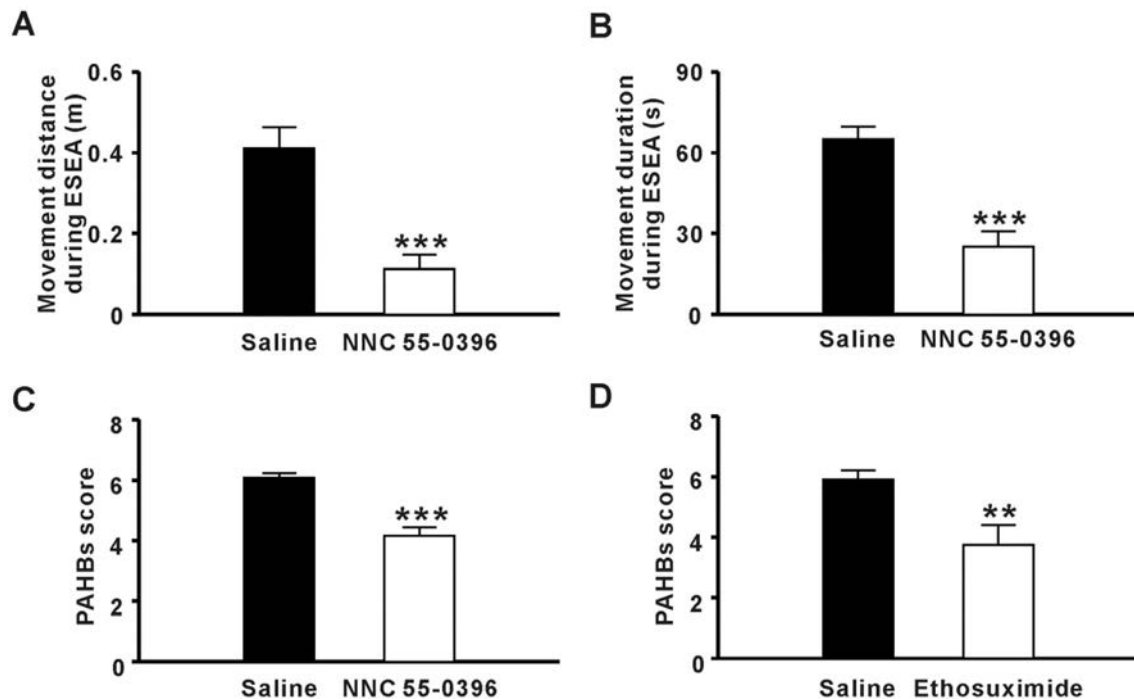


Fig. 2 Involvement of T-type Ca^{2+} channels in generating post-anesthetic hyperexcitatory behaviors (PAHBs). **A, B** Effect of NNC 55-0396 on movement distance and movement duration during early stage of emergence from anesthesia (ESEA) ($n = 6-7$; *** $P < 0.001$

vs saline, Student's *t*-test). **C** Effect of NNC 55-0396 on PAHB score ($n = 6$ per group; *** $P \leq 0.001$ vs saline Student's *t*-test). **D** Effect of ethosuximide on PAHB score ($n = 6$ per group; ** $P \leq 0.01$ vs saline, Student's *t*-test).

Potentiated Theta Oscillations in EEG When Generating PAHBs

It has been demonstrated that TCCs allow for continuous rhythmic bursts in the thalamus [16]. Synchronized bursting from masses of neurons in the thalamus produces abnormal theta oscillations that propagate to the neocortex through thalamo-cortical efferents [17]. So, we further recorded EEG during the peri-anesthesia period to determine whether abnormal activity occurs during PAHBs (Fig. 3A, B).

One to three minutes after sevoflurane withdrawal (early stage of emergence from anesthesia, ESEA), the period in which PAHBs clustered, younger pups showed potentiated long-term bursts in the frontal lobe, a specific EEG pattern that rarely occurred under other conditions or in the older pups (Fig. 3C). Spectral analysis showed that the power of the theta oscillations was significantly higher in younger pups during ESEA than during the awakening stage, while there were no significant changes in the older pups (Fig. 3D, E; Table 1). Moreover, there were no significant changes in the other frequency bands in either group (Fig. 3F; Table 1).

Next, we investigated whether blocking TCCs could affect the abnormal EEG activity during ESEA. As expected, the potentiated power of theta oscillations was attenuated by both ICVM with NNC 55-0396 and the

intraperitoneal administration of ethosuximide [Saline vs NNC 55-0396 = $(4.0 \pm 0.84) \times 10^{-10} \text{ V}^2/\text{Hz}$ vs $(1.6 \pm 0.28) \times 10^{-10} \text{ V}^2/\text{Hz}$, $n = 7-8$, $P = 0.009$; saline vs ethosuximide = $(2.9 \pm 0.54) \times 10^{-10} \text{ V}^2/\text{Hz}$ vs $(1.0 \pm 0.47) \times 10^{-10} \text{ V}^2/\text{Hz}$, $n = 6$ per group, $P = 0.027$, Student's *t*-test, Fig. 3G, H]. These results suggested that potentiated theta oscillations in the frontal lobe are relevant to PAHBs.

Effect of Sub-anesthetic Dose of Sevoflurane on TCCs

According to our previous study, PAHBs can be continually induced by 1% sevoflurane administration [10]. Here, we found that theta oscillations in young pups were also potentiated during 1% sevoflurane administration (Ctrl vs Sevo-1% = 1.0 ± 0.22 vs 1.6 ± 0.40 , $n = 6$, $P = 0.032$, paired *t*-test, Fig. 4A). Therefore, we investigated whether a sub-anesthetic dose (1%) of sevoflurane activated TCCs in younger rats. Because TCCs are expressed at high levels in thalamic relay cells [18], we performed *in vitro* patch clamp recording in the MDTN (Fig. 4B). Our results showed that the relative amplitude of the maximum TCC current in MDTN neurons was attenuated by 1% sevoflurane in both groups (P9–P11: Ctrl vs Sevo-1% = 1.0 ± 0.14 vs 0.8 ± 0.14 , $n = 8$, $P \leq 0.001$; P16–P18: Ctrl vs Sevo-1% = 1.0 ± 0.07 vs 0.8 ± 0.05 , $n = 8$, $P \leq 0.001$, paired *t*-test, Fig. 4C, D).

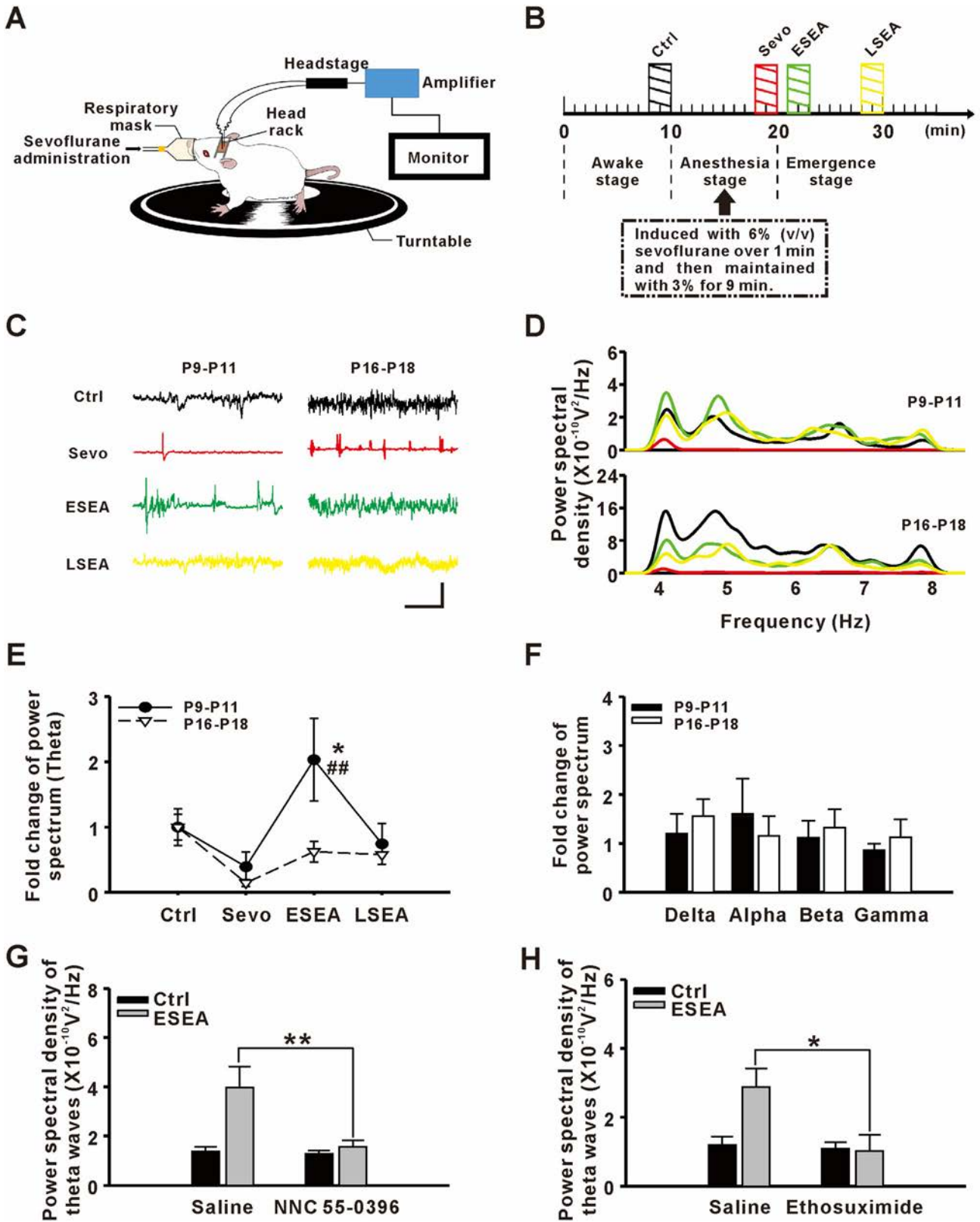


Fig. 3 Potentiated theta oscillations in the frontal lobe when generating post-anesthetic hyperexcitatory behaviors (PAHBs). **A** Sketch of EEG recording during the peri-anesthesia period. **B** Schematic of the EEG recording process. Shaded bars indicate periods of EEG analysis: Ctrl (black, baseline recording), Sevo (red, recording under sevoflurane anesthesia), ESEA (green, recording at the early stage of emergence from anesthesia), and LSEA (yellow, recording at a later stage of emergence from anesthesia). **C** Samples of EEGs from different groups and stages (scale bars: 0.2 mV and 5 s; color coding as in **B**). **D** Power spectra of theta oscillations in different groups and stages. **E** Fold-changes of power spectra of theta oscillations ($n = 8-10$; $*P \leq 0.05$ vs Ctrl; $^{##}P \leq 0.01$ vs P16-P18, two-way ANOVA followed by Bonferroni's *t*-test). **F** Fold changes of power spectra of delta, alpha, beta, and gamma oscillations. **G** Effect of NNC 55-0396 on the power spectrum of theta oscillations at ESEA ($n = 7-8$; $^{***}P \leq 0.01$ vs saline, Student's *t*-test). **H** Effect of ethosuximide on the power spectrum of theta oscillations at ESEA ($n = 6$ per group; $*P \leq 0.05$ vs saline, Student's *t*-test).

To further investigate the kinetic properties of TCCs, we fitted the activation/inactivation curves of the ion channels and found that the activation curves were only slightly right-shifted by 1% sevoflurane application in P9–P11 rats (half activation potential: Ctrl vs Sevo-1% = 69.1 ± 1.01 mV vs 67.2 ± 0.99 mV, $P = 0.039$; half inactivation potential: Ctrl vs Sevo-1% = 76.8 ± 1.38 mV vs 77.2 ± 1.16 mV, $P = 0.76$, paired *t*-test, Fig. 4E, F). Both activation (right-shifted) and inactivation curves (left-shifted) were clearly changed in P16–P18 rats, showing that the kinetic properties of TCCs were significantly inhibited by 1% sevoflurane (half activation potential: Ctrl vs Sevo-1% = 71.0 ± 1.48 mV vs 67.5 ± 1.46 mV, $P \leq 0.001$; half inactivation potential: Ctrl vs Sevo-1% = 77.5 ± 2.46 mV vs 79.4 ± 2.39 mV, $P = 0.016$, paired *t*-test, Fig. 4G, H). In brief, the sensitivity of TCCs to sevoflurane increased with age. In other words, the stronger inhibitory effect of sevoflurane might contribute to the lack of PAHBs in older rats.

Effect of Sub-anesthetic Dose of Sevoflurane on Neuronal Activity in the MDTN

In the introduction, we hypothesized that GABAergic depolarization might be able to elicit action potentials by evoking TCC current. In order to test this possibility, we examined the fast GABAergic postsynaptic potentials and the effects of 1% sevoflurane on neuronal activity in the MDTN using gramicidin-perforated patch clamp recording. We found that 7 of 9 cells in younger pups were depolarized in GABAergic potential, while this occurred in only 1 of 10 cells in older pups ($P = 0.005$, Fisher's exact test, Fig. 5A, B). Moreover, burst firing was elicited in 9 of 12 MDTN neurons by 1% sevoflurane administration in younger pups, while this firing was completely suppressed (0 of 9 neurons) by NNC 55-0396 ($P = 0.001$, Fisher's exact test, Fig. 5C, D). These data indicate that the contribution of TCCs to PAHB is not mediated by the direct effect of sevoflurane on TCCs. Nonetheless, TCCs contribute to neuronal excitability in the presence of a sub-anesthetic concentration of sevoflurane.

Discussion

PAHBs were found in an animal model in our previous work, and when we attempted to compare them to EA in humans, we found that their incidence depends on the age of the animal, type of anesthetic, and duration of anesthesia [10]. These characteristics conform to the features of EA in humans. To evaluate PAHBs, we initially developed a scale that was a modified version of a scale used for quantifying seizure behaviors [19]. Scale methods can sometimes be influenced by subjectivity and can be scored differently by different investigators. Therefore, we introduced an open field system to evaluate the PAHBs beyond the use of this score. We found that younger rats with a high incidence of PAHBs showed an eruption of spontaneous movement in the second minute after sevoflurane withdrawal. Concurrently, we recorded potentiated EEG bursting patterns and enhanced theta oscillation power in

Table 1 Relative power in different frequency bands in the waking state (Ctrl) and the early stage of emergence from anesthesia (ESEA).

Relative power spectrum		Delta (0–4 Hz)	Theta ^a (4–8 Hz)	Alpha (8–13 Hz)	Beta (13–30 Hz)	Gamma (30–80 Hz)
P9–P11 ($n = 10$)	Ctrl	1.0 ± 0.30	1.0 ± 0.28	1.0 ± 0.29	1.0 ± 0.26	1.0 ± 0.23
	ESEA	1.2 ± 0.40	2.0 ± 0.63	1.6 ± 0.72	1.1 ± 0.35	0.9 ± 0.14
P16–P18 ($n = 8$)	Ctrl	1.0 ± 0.42	1.0 ± 0.20	1.0 ± 0.24	1.0 ± 0.28	1.0 ± 0.38
	ESEA	1.6 ± 0.35	0.6 ± 0.16	1.2 ± 0.40	1.3 ± 0.38	1.1 ± 0.37

^aP9–11: Ctrl vs ESEA, $P = 0.022$; P16–18: Ctrl vs ESEA, $P = 0.446$; ESEA: P9–11 vs P16–18, $P = 0.004$, two-way ANOVA followed by Bonferroni's *t*-test

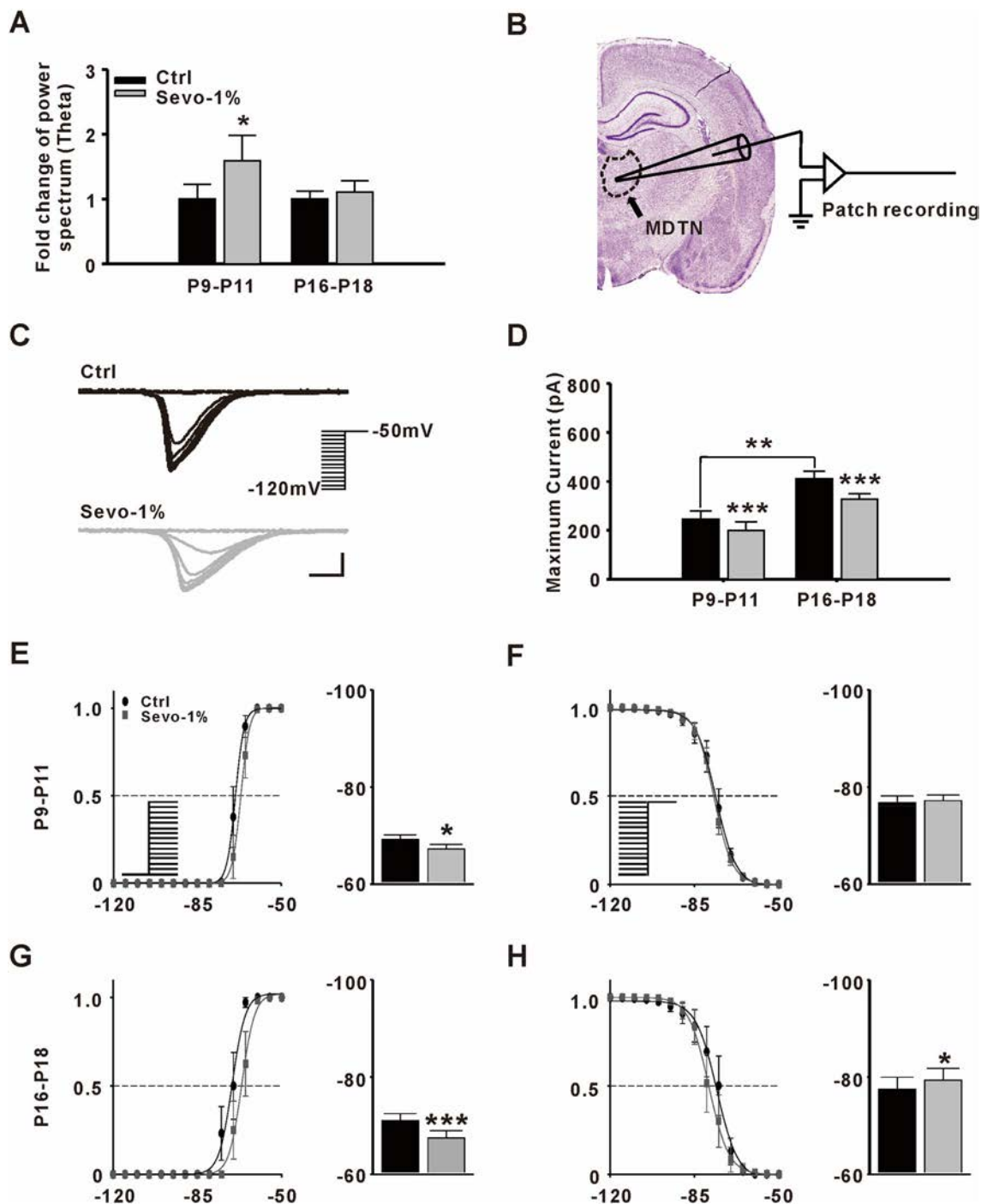


Fig. 4 Effect of sevoflurane on T-type Ca^{2+} channel (TCC) currents. **A** Fold-changes in power spectrum of theta oscillations with 1% sevoflurane (Sevo-1%). A two-minute period of EEG was analyzed before and after a 10-min Sevo-1% application ($n = 6$, $*P \leq 0.05$ vs Ctrl, paired t -test). **B** Sketch of *in vitro* patch clamp recording in the medial dorsal thalamic nucleus (MDTN). **C** Samples of evoked TCC currents from MDTN neurons before (black) and after (gray) Sevo-1% application. TCC currents were gradually inactivated by transient depolarization from various holding potentials to -50 mV (scale bars, 100 pA and 100 ms). **D** Fold-changes in maximum TCC currents after

Sevo-1% application in different groups ($n = 8$ per group, $**P \leq 0.01$ vs P9–P11, Student's t -test; $***P \leq 0.001$ vs Ctrl, paired t -test). **E**, **F** Steady-state activation/inactivation of TCC currents recorded from the MDTN in younger rat pups (P9–P11) (left panels, activation/inactivation curves; right panels, half-activation/inactivation potentials; $n = 8$ per group; $*P \leq 0.05$ vs Ctrl, paired t -test). **G**, **H** Steady-state activation/inactivation of TCC currents recorded from the MDTN in older rat pups (P16–P18) ($n = 8$ per group; $*P \leq 0.05$, $***P \leq 0.001$ vs Ctrl, paired t -test).

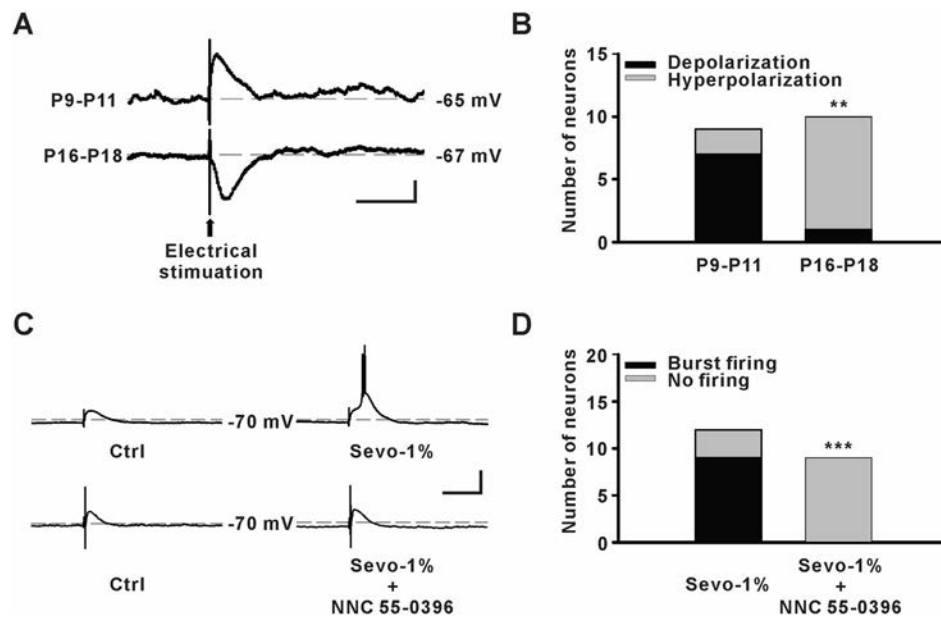


Fig. 5 Effect of sevoflurane on neuronal activity in the medial dorsal thalamic nucleus (MDTN). **A** Samples of evoked GABAergic potentials from MDTN neurons (scale bars, 5 mV and 200 ms). **B** Numbers of GABAergic depolarization in MDTN neurons (P9–11: $n = 7$ of 9 neurons; P16–18: $n = 1$ of 10 neurons, $**P \leq 0.01$, Fisher's exact test). **C** Samples of success or failure to evoke burst firing by

1% sevoflurane (Sevo-1%) without or with NNC 55-0396 (20 $\mu\text{mol/L}$), respectively (scale bars, 20 mV and 200 ms). **D** Numbers of MDTN neurons showing sevoflurane-evoked burst firing (P9–11: $n = 9$ of 12 neurons; P16–18: $n = 0$ of 9 neurons, $***P \leq 0.001$, Fisher's exact test).

the same time window, indicating that sevoflurane-induced abnormalities in EEG are related to PAHBs.

A clinical study reported increased frontal lobe cortical functional connectivity in children with EA during emergence from sevoflurane anesthesia [20]. The authors suggested that internally and externally imposed stimuli may result in increased network connectivity. Meanwhile, a variety of EEG patterns occurred during the emergence stage. Although they did not summarize specific EEG patterns for EA in children, their results revealed that theta activity was evident in 3 of the 4 cases.

EEG activity encompasses the synchronous signals of thousands or millions of neurons from the same cortical area. It has been well documented that sevoflurane causes epileptiform EEG activity in both humans and rodents [21, 22]. Thalamo-cortical dysrhythmia is a theoretical framework that can be used to explain many neurological disorders, including epilepsy [23]. Thalamo-cortical dysrhythmia is caused by an imbalance of synaptic inputs, including GABAergic transmission, to thalamic nuclei. Such conditions may create membrane hyperpolarization to de-inactivate TCCs. Therefore, low-threshold Ca^{2+} spikes could be elicited *via* TCCs to drive thalamic neurons into a low-frequency bursting mode [24].

Bursting is a common type of neuronal firing in the MDTN [25]. Due to the low threshold, burst firing may amplify sensory-signal transmission from the MDTN to the neocortex to avoid signal attenuation [26]. The MDTN

makes reciprocal connections with cells in the prefrontal, limbic, and motor cortices [27], such that a functional imbalance within this neural circuit induced by general anesthetics may lead to abnormal behaviors. Therefore, according to our findings that blocking TCCs attenuated PAHBs and the concomitant EEG changes, we speculated that TCCs may contribute to the generation of PAHBs by potentiating theta activity in the brain. Since TCC inhibitors completely prevented the increased theta waves but only partially prevented the PAHB behaviors after sevoflurane anesthesia, we considered that theta activity might only partially contribute to PAHBs, and other mechanisms independent of the theta activity might contribute.

However, some questions remain unanswered. Why do such hyperexcitatory behaviors (EA or PAHBs) occur more frequently in children or younger pups? Why do they occur during emergence from general anesthesia?

It has been demonstrated that GABAergic action shifts from depolarization/excitation to hyperpolarization/inhibition during the maturation of the central nervous system [28]. In previous work, we showed that sevoflurane-induced PAHBs are strongly associated with GABAergic depolarization/excitation in the neocortical neurons of neonatal rats [10]. However, the depolarizing GABAergic postsynaptic potentials potentiated by sevoflurane in most of these cortical neurons, as well as in neurons in the MDTN (in 7 of 9 cells, $E_{\text{GABA}} = -60.3 \pm 3.04$ mV), were

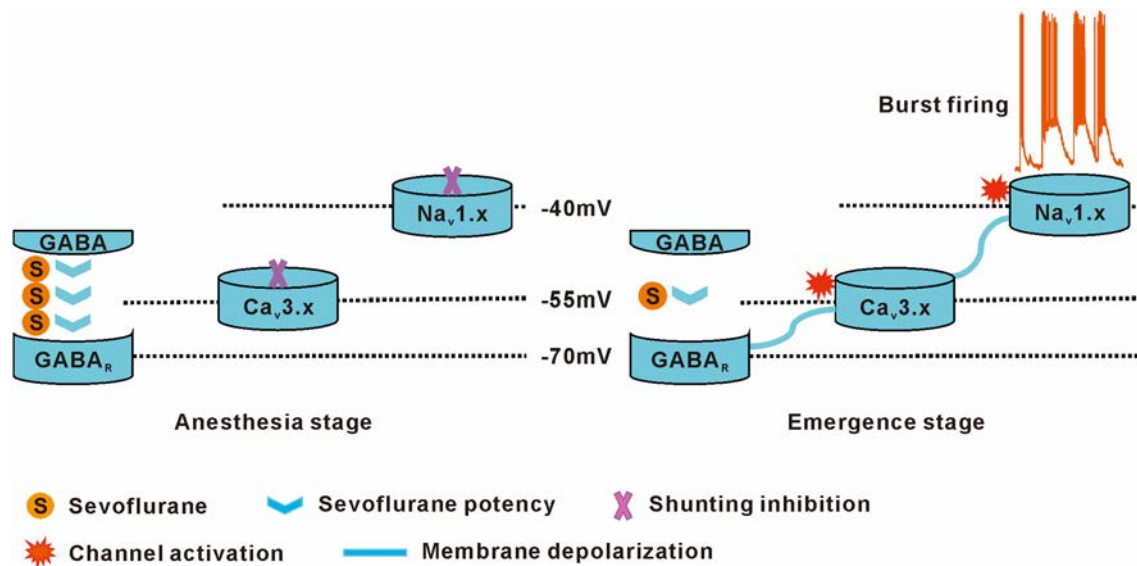


Fig. 6 The hypothesis of sevoflurane-induced post-anesthetic hyperexcitatory behaviors.

subthreshold. In other words, action potentials cannot be activated by GABAergic depolarization alone. Nonetheless, these GABAergic potentials are able to elicit action potentials, presumably by evoking low-threshold Ca^{2+} spikes that are mediated by TCCs, as it has been demonstrated that TCCs are the molecular determinant of the excitatory effects of GABA in the peripheral somatosensory system [29]. We found that TCCs were less sensitive to sevoflurane in younger than in older pups. Together with GABAergic depolarization, the neurophysiological properties of TCCs may determine the high incidence of PAHBs in younger pups. In addition, the stronger inhibitory effect of sevoflurane might contribute to the lack of PAHBs in older rats.

In addition to the hyperpolarizing inhibition, there is another form of inhibition called shunting, which may reduce excitatory synaptic responses and inactivate voltage-gated ion channels *via* a local increase in conductance across the plasma membrane [30]. Therefore, a high concentration of GABA would increase the tonic conductance of the plasma membrane, resulting in shunting-mediated inhibition [31]. Sevoflurane acts as a GABA_A receptor agonist that potentiates the GABA_A channel current [32]. Isoflurane, a volatile anesthetic that has actions similar to those of sevoflurane, is able to shunt voltage-gated Na^+ and Ca^{2+} channels, including TCCs [33]. Therefore, sevoflurane may shunt TCCs *via* GABA_A receptors during deep anesthesia. However, we found that ~80% of T-type currents remained active under a sub-anesthetic dose (1%) of sevoflurane.

According to the results noted above, we hypothesize the following. In a young pup, sevoflurane inhibits neuronal activity *via* shunting inhibition during deep

anesthesia. When sevoflurane is withdrawn, the excitatory voltage channels recover from inhibition, and potentiated GABAergic depolarization by a sub-anesthetic dose of sevoflurane triggers TCCs, such that burst firing is elicited by the TCC current (Fig. 6).

In the present study, we revealed a possible role of TCCs in the brain in generating hyperexcitatory behaviors during emergence from sevoflurane anesthesia in neonatal rats. However, ICVM or intraperitoneal injection of TCC inhibitors are limited in not providing the contributions of the exact subtypes and their locations. Thus, a gene-editing technique should be used for further investigation. Nonetheless, our conclusion provides a new target for EA management in the clinical setting. For instance, ethosuximide may be considered a candidate for further clinical study.

Acknowledgements This work was supported by the National Natural Science Foundation, Beijing, People's Republic of China (81671058 and 81730031 to YW and 81401089 to MD); the National Research Foundation of Korea grants funded by the Republic of Korea (2019R111A1A01057744 to YK); and the Foundation of Shanghai Municipal Science and Technology Commission (19ZR1407500 to FS).

Conflict of interest The authors claim that there are no conflicts of interest.

References

1. Sakai EM, Connolly LA, Klauck JA. Inhalation anesthesiology and volatile liquid anesthetics: focus on isoflurane, desflurane, and sevoflurane. *Pharmacotherapy* 2005, 25: 1773–1788.
2. Costi D, Cyna AM, Ahmed S, Stephens K, Strickland P, Ellwood J, *et al.* Effects of sevoflurane versus other general anaesthesia on

- emergence agitation in children. *Cochrane Database Syst Rev* 2014, 12: CD007084.
3. Moore AD, Anghelescu DL. Emergence delirium in pediatric anesthesia. *Paediatr Drugs* 2017, 19: 11–20.
 4. Veyckemans F. Excitation phenomena during sevoflurane anaesthesia in children. *Curr Opin Anaesthesiol* 2001, 14: 339–343.
 5. Vlajkovic GP, Sindjelic RP. Emergence delirium in children: many questions, few answers. *Anesth Analg* 2007, 104: 84–91.
 6. Kain ZN, Caldwell-Andrews AA, Weinberg ME, Mayes LC, Wang SM, Gaal D, *et al.* Sevoflurane versus halothane: postoperative maladaptive behavioral changes: a randomized, controlled trial. *Anesthesiology* 2005, 102: 720–726.
 7. Hauber JA, Davis PJ, Bendel LP, Martyn SV, McCarthy DL, Evans MC, *et al.* Dexmedetomidine as a rapid bolus for treatment and prophylactic prevention of emergence agitation in anesthetized children. *Anesth Analg* 2015, 121: 1308–1315.
 8. Aouad MT, Al-Alami AA, Nasr VG, Souki FG, Zbeidy RA, Siddik-Sayid SM. The effect of low-dose remifentanyl on responses to the endotracheal tube during emergence from general anesthesia. *Anesth Analg* 2009, 108: 1157–1160.
 9. Dalens BJ, Pinard AM, Letourneau DR, Albert NT, Truchon RJ. Prevention of emergence agitation after sevoflurane anesthesia for pediatric cerebral magnetic resonance imaging by small doses of ketamine or nalbuphine administered just before discontinuing anesthesia. *Anesth Analg* 2006, 102: 1056–1061.
 10. Lim BG, Shen FY, Kim YB, Kim WB, Kim YS, Han HC, *et al.* Possible role of GABAergic depolarization in neocortical neurons in generating hyperexcitatory behaviors during emergence from sevoflurane anesthesia in the rat. *ASN Neuro* 2014, 6: 127–136.
 11. Chemin J, Cazade M, Lory P. Modulation of T-type calcium channels by bioactive lipids. *Pflug Arch* 2014, 466: 689–700.
 12. Varma A, He J, Weissfeld L, Devaskar SU. Postnatal intracerebroventricular exposure to neuropeptide Y causes weight loss in female adult rats. *Am J Physiol Regul Integr Comp Physiol* 2003, 284: R1560–R1566.
 13. Shen FY, Chen ZY, Zhong W, Ma LQ, Chen C, Yang ZJ, *et al.* Alleviation of neuropathic pain by regulating T-type calcium channels in rat anterior cingulate cortex. *Mol Pain* 2015, 11: 8.
 14. Huang L, Keyser BM, Tagmose TM, Hansen JB, Taylor JT, Zhuang H, *et al.* NNC 55-0396 [(1S,2S)-2-(2-(N-[(3-benzimidazol-2-yl)propyl]-N-methylamino)ethyl)-6-fluoro-1,2,3,4-tetrahydro-1-isopropyl-2-naphthyl] cyclopropanecarboxylate dihydrochloride]: a new selective inhibitor of T-type calcium channels. *J Pharmacol Exp Ther* 2004, 309: 193–199.
 15. Huguenard JR. Block of T-type Ca(2+) channels is an important action of succinimide antiabsence drugs. *Epilepsy Curr* 2002, 2: 49–52.
 16. [16] Contreras D. The role of T-channels in the generation of thalamocortical rhythms. *CNS Neurol Disord Drug Targets* 2006, 5: 571–585.
 17. van Wijngaarden JB, Zucca R, Finnigan S, Verschure PF. The impact of cortical lesions on thalamo-cortical network dynamics after acute ischaemic stroke: a combined experimental and theoretical study. *PLoS Comput Biol* 2016, 12: e1005048.
 18. Huguenard JR. Low-threshold calcium currents in central nervous system neurons. *Annu Rev Physiol* 1996, 58: 329–348.
 19. Bough KJ, Gudi K, Han FT, Rathod AH, Eagles DA. An anticonvulsant profile of the ketogenic diet in the rat. *Epilepsy Res* 2002, 50: 313–325.
 20. Martin JC, Liley DT, Harvey AS, Kuhlmann L, Sleight JW, Davidson AJ. Alterations in the functional connectivity of frontal lobe networks preceding emergence delirium in children. *Anesthesiology* 2014, 121: 740–752.
 21. Constant I, Seeman R, Murat I. Sevoflurane and epileptiform EEG changes. *Paediatr Anaesth* 2005, 15: 266–274.
 22. Mohanram A, Kumar V, Iqbal Z, Markan S, Pagel PS. Repetitive generalized seizure-like activity during emergence from sevoflurane anesthesia. *Can J Anaesth* 2007, 54: 657–661.
 23. Llinas RR, Ribary U, Jeanmonod D, Kronberg E, Mitra PP. Thalamocortical dysrhythmia: a neurological and neuropsychiatric syndrome characterized by magnetoencephalography. *Proc Natl Acad Sci U S A* 1999, 96: 15222–15227.
 24. Llinas RR, Steriade M. Bursting of thalamic neurons and states of vigilance. *J Neurophysiol* 2006, 95: 3297–3308.
 25. Wei H, Bonjean M, Petry HM, Sejnowski TJ, Bickford ME. Thalamic burst firing propensity: a comparison of the dorsal lateral geniculate and pulvinar nuclei in the tree shrew. *J Neurosci* 2011, 31: 17287–17299.
 26. Hull C, Isaacson JS, Scanziani M. Postsynaptic mechanisms govern the differential excitation of cortical neurons by thalamic inputs. *J Neurosci* 2009, 29: 9127–9136.
 27. Saalmann YB. Intralaminar and medial thalamic influence on cortical synchrony, information transmission and cognition. *Front Syst Neurosci* 2014, 8: 83.
 28. Kaila K, Price TJ, Payne JA, Puskarjov M, Voipio J. Cation-chloride cotransporters in neuronal development, plasticity and disease. *Nat Rev Neurosci* 2014, 15: 637–654.
 29. Aptel H, Hilaire C, Pieraut S, Boukhaddaoui H, Mallie S, Valmier J, *et al.* The Cav3.2/alpha1H T-type Ca2+ current is a molecular determinant of excitatory effects of GABA in adult sensory neurons. *Mol Cell Neurosci* 2007, 36: 293–303.
 30. Ben-Ari Y, Gaiarsa JL, Tyzio R, Khazipov R. GABA: a pioneer transmitter that excites immature neurons and generates primitive oscillations. *Physiol Rev* 2007, 87: 1215–1284.
 31. Song I, Savtchenko L, Semyanov A. Tonic excitation or inhibition is set by GABA(A) conductance in hippocampal interneurons. *Nat Commun* 2011, 2: 376.
 32. Lecker I, Yin Y, Wang DS, Orser BA. Potentiation of GABA_A receptor activity by volatile anaesthetics is reduced by alpha5GABA_A receptor-preferring inverse agonists. *Br J Anaesth* 2013, 110 Suppl 1: i73–i81.
 33. Ries CR, Puil E. Mechanism of anesthesia revealed by shunting actions of isoflurane on thalamocortical neurons. *J Neurophysiol* 1999, 81: 1795–1801.



METHOD

Expression Patterns of Inducible Cre Recombinase Driven by Differential Astrocyte-Specific Promoters in Transgenic Mouse Lines

Neng-Yuan Hu¹ · Ya-Ting Chen¹ · Qian Wang¹ · Wei Jie¹ · Yi-Si Liu¹ · Qiang-Long You¹ · Ze-Lin Li¹ · Xiao-Wen Li¹ · Sophie Reibel² · Frank W. Pfrieger³ · Jian-Ming Yang¹ · Tian-Ming Gao¹

Received: 22 June 2019 / Accepted: 19 September 2019 / Published online: 11 December 2019
© Shanghai Institutes for Biological Sciences, CAS 2019

Abstract Astrocytes are the most abundant cell type in the central nervous system (CNS). They provide trophic support for neurons, modulate synaptic transmission and plasticity, and contribute to neuronal dysfunction. Many transgenic mouse lines have been generated to obtain astrocyte-specific expression of inducible Cre recombinase for functional studies; however, the expression patterns of inducible Cre recombinase in these lines have not been systematically characterized. We generated a new astrocyte-specific *Aldh11l1*-CreER^{T2} knock-in mouse line and compared the expression pattern of Cre recombinase between this and five widely-used transgenic lines (*hGfap*-CreER^{T2} from The Jackson Laboratory and The Mutant Mouse Resource and Research Center, *Glast*-CreER^{T2},

Cx30-CreER^{T2}, and *Fgfr3*-iCreER^{T2}) by crossing with Ai14 mice, which express tdTomato fluorescence following Cre-mediated recombination. In adult *Aldh11l1*-CreER^{T2}:Ai14 transgenic mice, tdTomato was detected throughout the CNS, and five novel morphologically-defined types of astrocyte were described. Among the six evaluated lines, the specificity of Cre-mediated recombination was highest when driven by *Aldh11l1* and lowest when driven by *hGfap*; in the latter mice, co-staining between tdTomato and NeuN was observed in the hippocampus and cortex. Notably, evident leakage was noted in *Fgfr3*-iCreER^{T2} mice, and the expression level of tdTomato was low in the thalamus when Cre recombinase expression was driven by *Glast* and in the capsular part of the central amygdaloid nucleus when driven by *Cx30*. Furthermore, tdTomato was clearly expressed in peripheral organs in four of the lines. Our results emphasize that the astrocyte-specific CreER^{T2} transgenic lines used in functional studies should be carefully selected.

Electronic supplementary material The online version of this article (<https://doi.org/10.1007/s12264-019-00451-z>) contains supplementary material, which is available to authorized users.

✉ Jian-Ming Yang
jimmyoung@smu.edu.cn

✉ Tian-Ming Gao
tgao@smu.edu.cn

¹ State Key Laboratory of Organ Failure Research, Key Laboratory of Mental Health of the Ministry of Education, Guangdong–Hong Kong–Macao Greater Bay Area Center for Brain Science and Brain-Inspired Intelligence, Guangdong Key Laboratory of Psychiatric Disorders, Collaborative Innovation Center for Brain Science, Department of Neurobiology, School of Basic Medical Sciences, Southern Medical University, Guangzhou 510515, China

² Chronobiotron – UMS 3415, University of Strasbourg, 67084 Strasbourg, France

³ Institute of Cellular and Integrative Neurosciences, CNRS UPR 3212, University of Strasbourg, 67084 Strasbourg, France

Keywords Astrocytes · Cre recombinase · Expression pattern · *Aldh11l1* · Morphology

Introduction

Astrocytes are the largest group of glial cells, accounting for 20%–40% of the total number of glial cells in the human brain [1–3]. For a long time, they have been assumed to be a homogenous population [1], but a growing body of evidence suggests that astrocytes exhibit high heterogeneity across and within brain regions [4–8]. This heterogeneity is reflected in their morphologies, gene expression profiles, and functions [9]. Particularly, our understanding of astrocytic functions is increasing

dramatically, and many more novel functions have recently been discovered and assigned [7, 10–13].

To elucidate the role of astrocytes *in vivo*, many transgenic mouse lines have been generated to achieve the astrocyte-specific expression of Cre recombinase in order to manipulate the gene functions and/or the activity of astrocytes by using the Cre-loxp system [14]. However, most existing astrocyte Cre lines, such as glial fibrillary acidic protein (GFAP)-Cre, do not meet the requirement of astrocyte-specific expression of Cre recombinase, in part due to the fact that most of the astrocyte promoters used to drive Cre recombinase expression are also expressed by non-astrocytes during early development [15–17]. Thus, there is a persistent need to develop new tools to target astrocytes efficiently with high spatial and temporal specificity [18]. To this end, many astrocyte-specific CreER^{T2} transgenic mouse lines, such as human *Gfap* (h*Gfap*)-CreER^{T2}, glutamate aspartate transporter (*Glast*)-CreER^{T2}, connexin 30 (*Cx30*)-CreER^{T2}, fibroblast growth factor receptor 3 (*Fgfr3*)-iCreER^{T2}, and aldehyde dehydrogenase 1 family member L1 (*Aldh1l1*)-CreER^{T2}, have been generated and characterized [19–23]. However, so far, no studies have been carried out to systematically compare the spatial and temporal expression of Cre recombinase in these astrocyte-specific CreER^{T2} transgenic mouse lines, making it difficult to choose an ideal mouse line for functional studies of astrocytes in the central nervous system (CNS).

Aldh1l1 is responsible for formate oxidation *in vivo* and catalyzes the conversion of 10-formyltetrahydrofolate, NADP, and water to tetrahydrofolate, NADPH, and CO₂ [24, 25]. It is expressed primarily by glia, especially astrocytes and ventricular ependymal cells [26] and is considered to be a highly specific marker for astrocytes with a substantially broader expression pattern than the traditional astrocyte marker GFAP. Moreover, *Aldh1l1* has not been detected in oligodendrocytes, oligodendrocyte precursor cells, or neurons based on transcriptome data [27, 28]. These studies suggest that *Aldh1l1* is a highly useful genetic locus to express tamoxifen-inducible CreER^{T2} for spatiotemporally-controlled astrocyte-specific genetic manipulation.

To achieve astrocyte-specific expression of inducible Cre recombinase, we used CRISPR-Cas9 technology to generate knock-in mice driving CreER^{T2} expression by the endogenous *Aldh1l1* promoter. Using this mouse line, we systematically characterized the morphology of astrocytes and compared the specificity and efficiency of Cre-mediated recombination between this and five widely-used astrocyte-specific CreER^{T2} lines.

Materials and Methods

Animals

Fgfr3-iCreER^{T2} transgenic mice were a gift from Professor William D. Richardson (University College London, UK). Two h*Gfap*-CreER^{T2} transgenic mice were purchased from The Jackson Laboratory (The Jackson Laboratory, Bar Harbor, ME, No: 012849) [29] and the Mutant Mouse Resource and Research Center (Mutant Mouse Resource and Research Center, USA, No: 016992-MU) [19]. *Glast*-CreER^{T2} and *Cx30*-CreER^{T2} transgenic mice were generously provided by Professor Frank W. Pfrieger (University of Strasbourg, France) [18]. To evaluate the expression patterns of inducible Cre recombinase, we crossed the astrocyte-specific CreER^{T2} mice with a fluorescent reporter line (Ai14, The Jackson Laboratory, Stock No: 007914). All mice were maintained under specific pathogen-free conditions. Three to four mice were housed in a cage with an individual ventilated caging system at (24 ± 1) °C. The mice were maintained under standard laboratory conditions (12-h light–dark cycle, lights on from 07:00 to 19:00) with free access to food and water unless otherwise indicated. All experiments were conducted in accordance with the regulations for the administration of affairs concerning experimental animals (China) and approved by the Southern Medical University Animal Ethics Committee.

Construction, Generation, and Screening of the *Aldh1l1*-CreER^{T2} Knock-in Mouse Line

The *Aldh1l1*-CreER^{T2} knock-in mouse line was generated by the Model Animal Research Center of Nanjing University (Nanjing, China). The targeting strategy is shown in Fig. 1A. Briefly, *Aldh1l1*-CreER^{T2} knock-in mice were generated *via* a CRISPR/Cas9 system [30, 31] using Cas9 mRNA, sgRNA (CCAGGTCTGTGCCCAATACTGG), and a donor, which were co-injected into C57BL/6 zygotes using microinjection methods. Then, these zygotes were transplanted into pseudopregnant mice [32]. sgRNA-directed Cas9 endonuclease cleavage occurred near the termination codon and created a double-strand break [33]. These breaks were subsequently repaired and resulted in a T2A-CreER^{T2} insertion before the stop codon of the *Aldh1l1* gene. The mice were screened through PCR analysis using specific primers (Fig. S1A–C).

Tamoxifen Treatment

Tamoxifen (Sigma-Aldrich, St. Louis, MO, #T5648) was used to induce CreER^{T2}-mediated recombination. Tamoxifen was dissolved in 10% ethanol (Sigma-Aldrich,

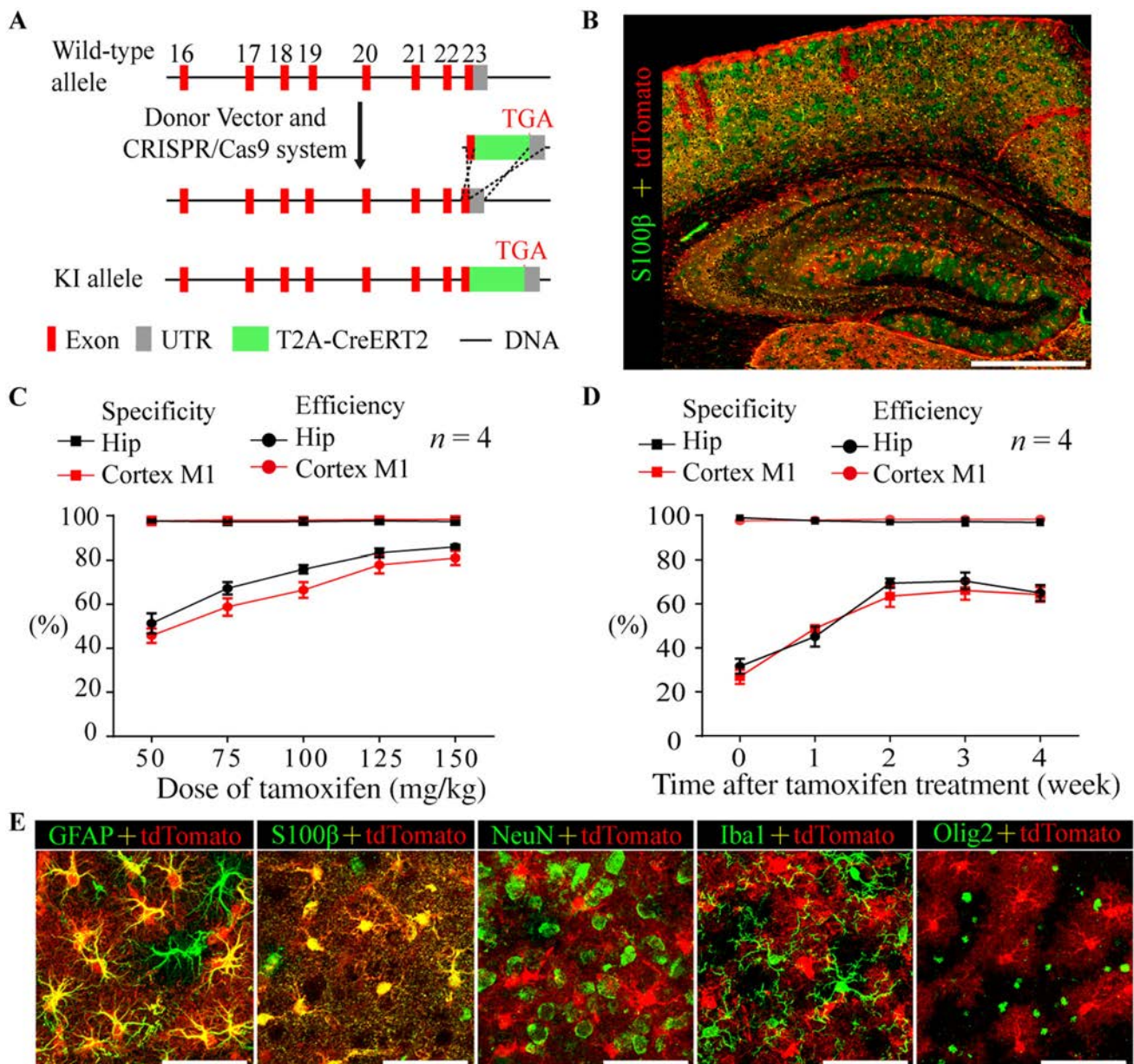


Fig. 1 Creation and characterization of *Aldh1l1*-CreER^{T2} knock-in mice. **A** Schematic showing the generation of *Aldh1l1*-CreER^{T2} knock-in mice *via* the CRISPR/Cas9 system. **B** Representative montage of the cortex and hippocampus in an *Aldh1l1*-CreER^{T2}:Ai14 double-transgenic mouse injected with tamoxifen and stained for S100 β (green) (scale bar, 200 μ m). **C** Graph showing the specificity (percentage of tdTomato-positive cells expressing S100 β) and efficiency (percentage of S100 β -positive cells expressing tdTomato)

of Cre-mediated recombination in the hippocampus and M1 cortex of *Aldh1l1*-CreER^{T2}:Ai14 transgenic mice as a function of the dose of tamoxifen (mean \pm SEM, $n = 4$). **D** As in **(C)** but shown as a function of time after treatment with 100 mg/kg tamoxifen (mean \pm SEM, $n = 4$). **E** Representative high-magnification images of cortical astrocytes in *Aldh1l1*-CreER^{T2}:Ai14 transgenic mice showing co-staining with GFAP and S100 β but not NeuN, Iba1, or Olig2 (scale bars, 50 μ m).

#32205) and 90% sunflower oil (Sigma-Aldrich, #S5007) to reach a final concentration of 20 mg/mL. Adult mice (postnatal days P56–60) were given an intraperitoneal (i.p.) injection of 100 mg/kg tamoxifen (unless otherwise stated) once a day for 7 consecutive days. Expression of Cre recombinase was assessed 2 weeks after the last dose of tamoxifen (unless otherwise stated). In mice aged P7, P14,

and P21, two i.p. doses of 100 mg/kg tamoxifen were given 24 h apart, and the expression of Cre recombinase was assessed 5 days later.

Virus Injection

The recombinant adeno-associated virus (AAV) vectors (AAV2/9 CAG-DIO-GFP, titers 1×10^{13} particles per mL) were packaged by SunBio (Shanghai, China). Mice were deeply anesthetized with 1% sodium pentobarbital (i.p.) (Sigma-Aldrich, #P3761) and placed in a stereotaxic instrument (RWD Life Science Inc., Shenzhen, China). The scalp was removed, and a 1-mm diameter hole was drilled through the skull with a dental drill at the following coordinates: CA1 (anterior, -2.0 mm; lateral, ± 1.5 mm; ventral, -1.5 mm), CA3 (anterior, -2.0 mm; lateral, ± 2.5 mm; ventral, -2.0 mm), and dentate gyrus (DG) (anterior, -2.0 mm; lateral, ± 1.15 mm; ventral, -2.0 mm). The AAV solution was injected using a Hamilton syringe with a microinjector pump (KDS, Stoelting, Wood Dale, IL); in all experiments, $0.3 \mu\text{L}$ of virus solution was injected at 0.05 mL/min . After the injection was completed, the needle was raised 0.1 mm and maintained in position for an additional 10 min to allow the virus to diffuse at the injection site; the needle was then slowly withdrawn [34]. One week later, tamoxifen was administered as described above.

Tissue Sections

For tissue fixation, animals were deeply anesthetized with 1% sodium pentobarbital (Sigma, #P3761) and then intracardially perfused with 4°C saline (0.9% NaCl) followed by 4% paraformaldehyde (PFA) in phosphate-buffered saline (PBS). After dissection, the tissues were postfixed overnight in 4% PFA in PBS at 4°C and then in 30% sucrose in PBS at 4°C . The tissues were subsequently embedded in OCT compound (Tissue-Tek, UK, #4583) and cryo-sectioned (Leica, Germany, #CM1850-1-1) at $20 \mu\text{m}$ for immunohistochemical staining or $100 \mu\text{m}$ for morphological analysis. For each brain area, one in every seven slides was collected into a 5-mL centrifuge tube. Tissue slides were stored at -80°C or washed three times in PBS prior to staining.

Immunohistochemistry

The sections were washed in PBS and then incubated while shaking for 2 h in PBS containing 5% BSA and 1% Triton X-100 at room temperature. They were then washed three times for 5 min each in PBS, incubated with primary antibodies overnight at 4°C , washed three times for 5 min each with PBS, incubated with secondary antibodies for 2 h at room temperature, and finally washed three times for 5 min each with PBS. The following primary antibodies were used: anti-NeuN ($1:500$, Cell Signaling Technology, Beverly, MA, #24307), anti-GFAP ($1:500$, Cell Signaling

Technology, #3670S), anti-calcium-binding protein B ($\text{S100}\beta$, $1:100$, Abcam, UK, #ab52642), anti-Iba1 ($1:500$, Wako, Japan, #019-19741), anti-Olig2 ($1:500$, Abcam, #Ab42453), anti-SOX2 ($1:1000$, Abcam, #ab97959), anti-doublecortin (DCX, $1:500$, Cell Signaling Technology, #4604), anti-excitatory amino acid transporter 1 (Glast, $1:50$, Proteintech, USA, #20785-1-AP), anti-parvalbumin (PV, $1:5000$, Swant, Switzerland, #PV27) and anti-Aldh111 ($1:50$, Proteintech, #17390-1-AP); and the following secondary antibodies were used: goat anti-mouse IgG with Alexa Fluor 594 or 488 ($1:2000$, Life Technologies, Carlsbad, CA, #A11005 or #A11001) and goat anti-rabbit IgG (H + L) with Alexa Fluor 594 or 488 ($1:2000$, Life Technologies, #A11012 or #A11008). Sections were placed on coverslips, embedded in Vectashield mounting medium (Vectorlabs, Burlingame, CA, #H-1200) and inspected by confocal microscopy (Nikon C2, Japan).

Cell Counting

Three to five sections containing each brain area were obtained from each mouse, and three to four mice were used in each experiment. Image allocations were blinded for analysis. Cells labeled by specific markers were counted using the “Cell Counter” plugin in ImageJ 1.50i software. Identification of cells was ensured by nuclear DAPI labeling. The specificity of Cre recombinase activity in each mouse line was defined as the number of marker- and tdTomato-positive cells divided by the total number of tdTomato⁺ cells. The efficiency was defined as the number of tdTomato⁺ cells divided by the total number of marker-positive cells.

Morphological Analysis

To sparsely label and evaluate the morphological architecture of astrocytes, laser confocal 3D imaging was applied in *Aldh111-CreER*^{T2}:Ai14 mice treated with a low dose of tamoxifen (50 mg/kg). After perfusion-based fixation, tissues were cut into $100 \mu\text{m}$ -thick coronal/sagittal sections on a cryostat microtome (Leica, CM1850-1-1). To increase the light transmittance of the tissue, the slides were washed in PBS and then incubated while shaking for 2 days in PBS containing 5% BSA and 2% Triton X-100 at 4°C . The solution was changed once a day. Single cells were imaged by confocal microscopy (Nikon C2) using a $40 \times$ or $60 \times$ objective. Image stacks were obtained at 100-nm steps to obtain optimal z-axis resolution. Morphometric parameters were analyzed using the image analysis software Imaris 8.1 (Bitplane, Belfast, UK).

Statistical Analysis

Student's *t* test and one-way ANOVA were used to compare the means of two and multiple independent samples, respectively, using SPSS 22.0 software (Chicago, IL). The number of experimental animals is indicated by 'n'. Data shown in the text and figures are expressed as the mean \pm standard error of the mean (SEM) (unless otherwise stated). $P < 0.05$ was considered statistically significant, and GraphPad Prism 6.0 (La Jolla, CA) was used to generate graphs.

Results

Generation and Characterization of *Aldh11l*-CreER^{T2} Knock-in Mouse Line

To obtain a knock-in mouse line expressing inducible Cre recombinase in astrocytes with high selectivity and efficiency, T2A-CreER^{T2}, a fragment obtained from a donor, was inserted before the stop codon of the endogenous *Aldh11l* gene using the CRISPR/Cas9 system (Fig. 1A). The *Aldh11l*-CreER^{T2} knock-in mice were identified through PCR analysis (Fig. S1A–C). The sizes of the PCR products obtained from the 5' homology arm, the 3' homology arm, and WT tissue were 2126 bp, 1457 bp, and 452 bp, respectively (Fig. S1B, C). Homozygotes and heterozygotes displayed no alterations in growth, fertility, or behavior.

The expression pattern of inducible Cre recombinase in the CNS was visualized by crossing *Aldh11l*-CreER^{T2} knock-in mice with an Ai14 reporter line following tamoxifen treatment [35] (Table 1, Fig. S2A). In adult *Aldh11l*-CreER^{T2}:Ai14 transgenic mice, the Cre reporter tdTomato was not detected in the absence of tamoxifen treatment (Fig. S3B), indicating the absence of leaky reporter expression. Tamoxifen-induced Cre recombination occurred throughout the CNS with high specificity in astrocytes as shown by co-localization of tdTomato with the astrocyte markers GFAP and S100 β (Fig. 1C–E; Table 1). To examine the expression patterns of endogenous *Aldh11l*, we stained for Aldh11l in the M1 cortex and hippocampus of adult *Aldh11l*-CreERT2:Ai14 mice. Almost all tdTomato⁺ cells were Aldh11l⁺ (~ 98%); however, Aldh11l⁺/tdTomato⁻ cells were also occasionally observed, similar to the results with S100 β (Fig. S1D, E). This suggested that the expression pattern of Cre recombinase faithfully recapitulated that of the endogenous *Aldh11l* promoter. The efficiency of Cre recombination was dependent on the dose of tamoxifen (Fig. 1C) and approached a plateau at two weeks after treatment with 100 mg/kg tamoxifen (Fig. 1B, D), while the specificity

was stable regardless of the dose or time after treatment (Fig. 1C, D). Increasing the dose of tamoxifen to > 150 mg/kg resulted in significant weight loss in mice (data not shown).

To assess whether inducible Cre recombinase was expressed in cells other than astrocytes, we also co-stained for markers of neurons (NeuN), microglia (Iba1), and oligodendrocytes (Olig2) in adult *Aldh11l*-CreER^{T2}:Ai14 mice (Fig. 1E; Table 1). We only very occasionally observed co-localization of tdTomato and NeuN in the M1 region of cortex, but no co-labeling was found in other cortical areas (Fig. 3A; Table 1). A small number of tdTomato⁺ cells were also Iba1⁺ (Table 1). In contrast, the percentage of tdTomato⁺ cells that co-expressed Olig2 was relatively high, especially in the olfactory bulb (Table 1), possibly because astrocytes and oligodendrocytes share a common origin, and because Olig2 is expressed in glial-restricted precursors giving rise to oligodendrocyte or astrocyte precursors [36, 37].

Previous studies have reported that the expression level of *Aldh11l* is highest during early development, but decreases after one month of age [38]. To further examine the astrocyte targeting specificity and efficiency of *Aldh11l*-CreER^{T2} knock-in mice during development, *Aldh11l*-CreER^{T2}:Ai14 mice aged P7, P14, and P21 were used. The results showed that, while the specificity of Cre recombinase expression was high (> 90%) during early development (Fig. S2A, B), the efficiency was lower in young mice than in adults (Fig. S2A, C), possibly due to the low dose of tamoxifen administered to young mice.

As an alternative approach to reporter lines, we also studied the specificity of Cre targeting using AAV-mediated transduction of a Cre-dependent GFP construct (AAV2/9-CAG-DIO-GFP). Cre-induced expression of GFP was observed in the hippocampus in *Aldh11l*-CreER^{T2} knock-in mice after intracranial injections of AAV followed by tamoxifen treatment. GFP was consistently co-expressed with S100 β in CA1 (95.08% \pm 0.88% of GFP⁺ cells, $n = 3$) and CA3 (98.69% \pm 0.31% of GFP⁺ cells, $n = 3$) (Fig. S1G) but not with NeuN. However, 9.36% \pm 1.38% of GFP⁺ cells co-expressed NeuN in the DG region (Fig. S1F), possibly because the virus transduced neuronal precursor cells in neurogenic areas.

Morphological Diversity of Astrocytes in *Aldh11l*-CreER^{T2}:Ai14 Mice

Astrocytes have highly variable and complex morphologies. To examine this aspect, we sparsely labeled astrocytes with tdTomato by treating *Aldh11l*-CreER^{T2}:Ai14 mice with a low dose of tamoxifen (50 mg/kg). tdTomato labeled not only protoplasmic astrocytes in grey matter and fibrous astrocytes in white matter, but also perivascular

Table 1 Astroglia-specific induction of Cre recombination by tamoxifen (%).

Brain region	GFAP		S100β		NeuN		Iba1		Olig2	
	Efficiency	Specificity	Efficiency	Specificity	Efficiency	Specificity	Efficiency	Specificity	Efficiency	Specificity
Olfactory bulb	-	-	57.84 ± 7.62	77.84 ± 0.36	0	0	1.38 ± 0.36	0.81 ± 0.13	6.1 ± 4.01	7.42 ± 4.51
Cortex	-	-	54.05 ± 1.41	96.12 ± 1.37	0.09 ± 0.01	0.59 ± 0.07	1.57 ± 0.43	1.23 ± 1.51	2.58 ± 1.46	4.23 ± 1.29
Hippocampus	66.86 ± 1.48	95.84 ± 1.02	64.75 ± 1.32	97.51 ± 1.3	0	0	2.44 ± 1.79	1.51 ± 0.85	1.64 ± 0.7	2.38 ± 1.31
BLA	-	-	62.96 ± 2.72	96.94 ± 1.51	0	0	1.30 ± 1.54	1.15 ± 1.40	3.17 ± 1.94	4.55 ± 2.01
PFC	-	-	59.75 ± 2.41	96.71 ± 0.24	0	0	1.67 ± 1.13	1.52 ± 1.44	2.98 ± 1.68	3.15 ± 1.88
VTA	-	-	53.57 ± 3.58	95.6 ± 1.09	0	0	2.71 ± 1.01	2.14 ± 1.94	2.95 ± 1.62	3.44 ± 1.28
Thalamus	-	-	95.28 ± 2.64	97.16 ± 1.18	0	0	3.57 ± 1.8	2.63 ± 1.51	3.21 ± 1.93	3.98 ± 1.75
Hypothalamus	69.01 ± 3.75	44.67 ± 6.02	61.03 ± 7.7	76.37 ± 1.6	0	0	3.92 ± 0.94	2.82 ± 1.45	3.08 ± 1.55	3.81 ± 1.42
Midbrain	-	-	64.82 ± 3.77	95.39 ± 2.48	0	0	1.97 ± 1.54	1.55 ± 1.81	2.96 ± 1.08	3.17 ± 1.26
Cerebellum (Bergmann glia)	-	-	92.17 ± 0.41	97.29 ± 1.49	0	0	2.53 ± 0.53	1.91 ± 0.47	2.24 ± 1.06	2.51 ± 1.67
Medulla	-	-	50.23 ± 0.63	90.54 ± 2.59	0	0	0.88 ± 0.15	0.92 ± 0.36	2.85 ± 1.92	3.11 ± 1.83
Spinal cord	79.18 ± 4.76	56.17 ± 2.57	46.94 ± 3.38	78.51 ± 7.15	0	0	2.40 ± 0.61	1.69 ± 0.63	1.84 ± 1.05	2.47 ± 1.68

Aldh1l1-CreER^{T2};Ai14 transgenic mice were induced by tamoxifen, and immunofluorescence with GFAP, S100β, NeuN and Iba1, then imaged by confocal laser scanning microscopy. The specificity of Cre recombinase activity was defined as the number of marker- and tdTomato-positive cells divided by the total number of tdTomato⁺ cells. The efficiency was defined as the number of tdTomato⁺ cells divided by the total number of marker-positive cells. Data are shown as mean ± SEM, *n* = 3.

glia, which were closely opposed to blood vessels through their end-feet (Fig. S3C). We identified all the morphologically-defined types of astrocyte that were reported previously, including pia mater glia, tanycytes, marginal astrocytes, and Bergmann glia (data not shown) [3, 5, 39]. In addition, we identified five novel morphologically-distinct types that have never been reported; these were habenular nucleus (Hb) glia, inner capsule (ic) fibrous glia, bundle glia, and spinal cord short/long fibrous glia (Fig. 2A–E).

Nearly all Hb glia expressed GFAP (98.4% ± 0.6%, *n* = 3), but only 71.4% ± 0.4% were co-stained with S100β (Fig. 2A; Table 2). These cells filled the Hb, in which they had dense and distinct boundaries, but relatively small diameters (26.5 μm ± 3.1 μm) and they covered an area (715.0 μm² ± 209.8 μm²) smaller than that of the other fibrous glia types (Fig. 2A; Table 2). Their processes formed clusters that were interspersed among each other and that surrounded the cell bodies of neurons.

Most of the ic fibrous glia co-expressed GFAP (96.2% ± 0.8%, *n* = 3), and 82.5% ± 0.6% of them also co-expressed S100β (Fig. 2B; Table 2). These cells were located in the internal capsule, which contains axons that project to and from the cerebral cortex (Fig. 2G). Most of the ic fibrous glia had ~ 5 branches (Table 2) that did not cover “bushy” territories. The processes of adjacent cells formed a network that was flattened and oriented perpendicular to the sagittal plane (Fig. 2B) indicating that these cells support axonal functions.

Bundle glia co-localized with S100β but not with GFAP (Fig. 2C). These cells were located at the surface of the dorsal medulla oblongata and ran as bundles into the medulla. Bundle glia had the most abundant branches (8.81 ± 2.44 branches/cell) but had no secondary branches (Table 2).

Spinal cord short/long fibrous glia co-expressed GFAP but not S100β (Fig. 2D, E). These cells were located in the white matter of the spinal cord, with the shorter more superficial than the longer (Fig. 2G). The short fibrous glia had thicker branches than other fibrous glia, and the long fibrous glia had the longest branches (171 μm ± 42.75 μm) among all morphologically-defined types of astrocyte (Table 2).

Differences in Inducible Cre Recombination Among Astrocyte-specific CreER^{T2} Lines

Astrocyte-specific gene recombination has been widely used to study the functions of genes in astrocytes [14, 40], but very little is known about the differences in the expression patterns of inducible Cre recombinase driven by different promoters. To address this issue, we crossed five widely-used astrocyte-specific CreER^{T2} lines [*hGfap*-

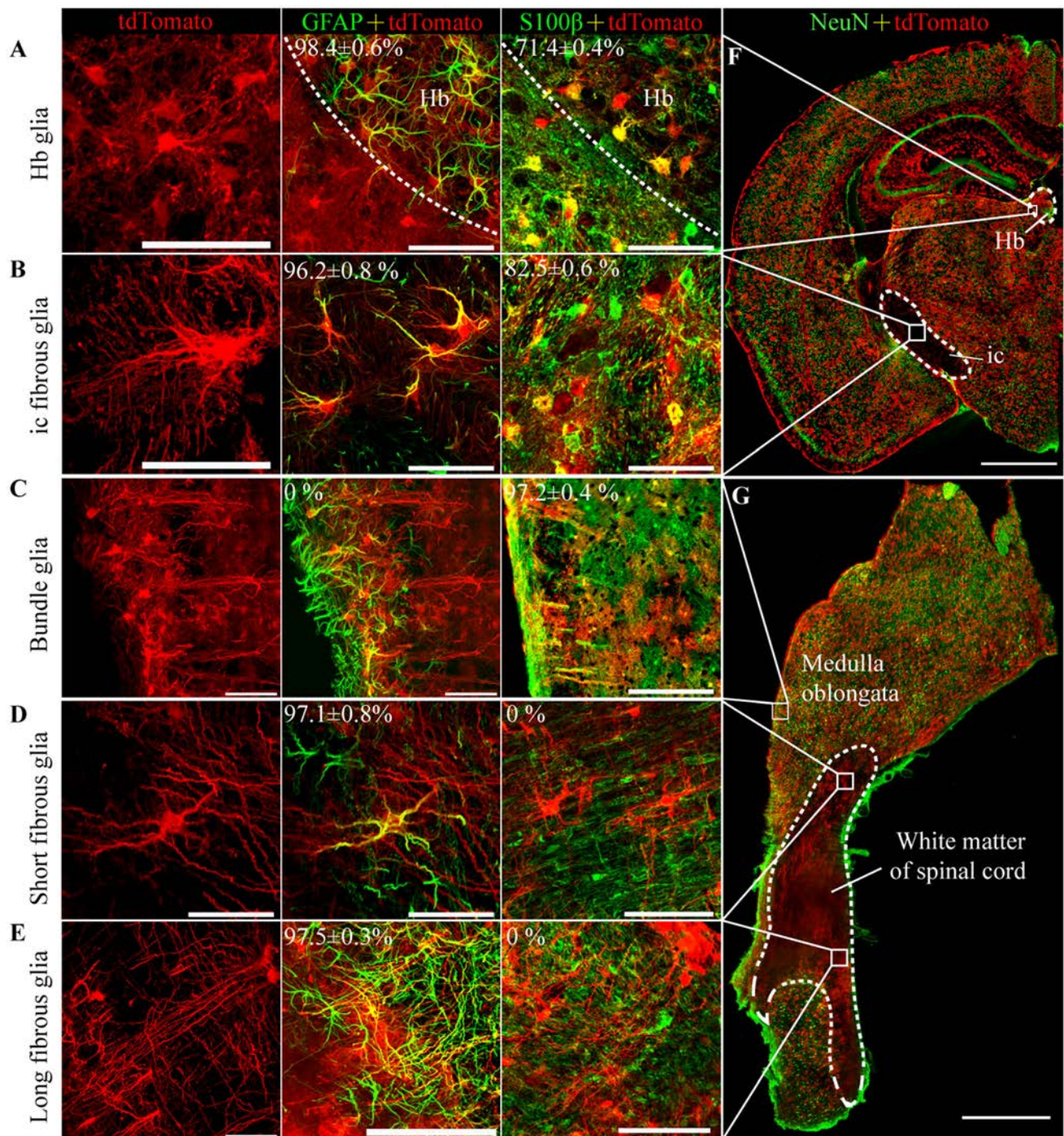


Fig. 2 Characterization of five novel astrocyte morphologies in *Aldh1l1-CreER^{T2};Ai14* transgenic mice. **A** Habenular nucleus (Hb) glia co-stained with GFAP (98.4% ± 0.6%) or S100β (71.4% ± 0.4%) but not NeuN (scale bar, 50 μm). **B–E** As in (A), but in inner capsule (ic) fibrous glia (B), bundle glia (C), short fibrous

glia (D), and long fibrous glia (E) (scale bars, 50 μm). **(F)** Distribution of Hb astrocytes and ic fibrous glia (scale bar, 1 mm). **(G)** Distribution of bundle glia, short fibrous glia, and long fibrous glia in the sagittal plane (scale bar, 1 mm).

CreER^{T2} (from the MMRRC, *MhGfap-CreER^{T2}*), *hGfap-CreER^{T2}* (from The Jackson Laboratory, *JhGfap-CreER^{T2}*), *Glast-CreER^{T2}*, *Cx30-CreER^{T2}* and *Fgfr3-iCreER^{T2}*] with Ai14 reporter mice to create *MhGfap-CreER^{T2};Ai14*,

JhGfap-CreER^{T2};Ai14, *Glast-CreER^{T2};Ai14*, *Cx30-CreER^{T2};Ai14*, and *Fgfr3-iCreER^{T2};Ai14* mice.

All the transgenic lines were treated with 100 mg/kg tamoxifen for 7 days at P56–P60, and the specificity and efficiency of CreER^{T2}-mediated recombination was then

assessed in the M1 cortex and hippocampus 2 weeks after the last dose of tamoxifen (Figs. 3A–F and S4–6). The *Aldh1l1*- and *Glast*-CreER^{T2} lines had the highest specificity in the M1 cortex as shown by co-staining for S100β and NeuN (one-way ANOVA, *P* < 0.05) (Fig. 3G, I). Similarly high specificity was detected in the *Aldh1l1*-, *Cx30*-, and *Fgfr3*-iCreER^{T2} lines in the hippocampus (Fig. 3G, I). Unexpectedly, the *JhGfap*- and *MhGfap*-CreER^{T2} lines had the lowest specificity, as many tdTomato⁺ cells were also NeuN⁺ in the M1 cortex and hippocampus (one-way ANOVA, *P* < 0.0001) (Fig. 3I). These mouse lines were not used in subsequent experiments. In the *Glast*-CreER^{T2} line, the specificity was high in the cortex, but there was co-localization between tdTomato and NeuN in the DG (Fig. S6B). In the *Cx30*-CreER^{T2} line, some neurons in the M1 cortex also expressed tdTomato, and these cells were distributed mainly in layer V (Fig. 3C, G–I). The *Aldh1l1* line showed the lowest expression efficiency and the *Fgfr3*-iCreER^{T2} line the highest in both the cortex and hippocampus (Fig. 3A, G–I).

Some unique properties of the astrocyte-specific CreERT2 lines were identified. In the *Glast*-CreER^{T2} line, the expression efficiency of Cre-mediated recombination was lowest in the thalamus (Figs. 4A, B and S7A) and recombination occurred mainly in areas of the thalamus that lacked PV-positive cells (Fig. S7B). In the *Cx30*-CreER^{T2} line, “cavitation areas” in the capsular part of the central amygdaloid nucleus (CeC) were observed (54.31% ± 3.95%, *n* = 5), even at higher doses (56.70% ± 3.21%, *n* = 5; Fig. 4C, D). Leaky Cre recombination in neurons and astrocytes not treated with tamoxifen was detected only in the *Fgfr3*-iCreER^{T2} line (Fig. 4E, F). In addition, many tdTomato⁺ cells were observed in the choroid plexus of the *Aldh1l1*-CreER^{T2} line, while tdTomato⁺ ependymal cells were observed in the *Cx30*-CreERT2 and *Fgfr3*-iCreER^{T2} lines, and to a lesser extent, in the *Glast*-CreER^{T2} line (Fig. S7C).

Cre-mediated Recombination in Neural Stem Cells in Adult Astrocyte-specific CreER^{T2}:Ai14 Mice

Neural stem cells persist in the rostral migratory stream (RMS), subventricular zone (SVZ), and subgranular zone (SGZ) of the adult rodent brain. Stem cells in the SVZ and RMS migrate to the cortex and the olfactory bulb, where they become mature neurons or astrocytes in adult mice [41, 42]. In addition, neuroblasts from the SGZ migrate and differentiate into DG granule cells [43]. It has been reported that *Aldh1l1*, *Glast*, and *Fgfr3* are expressed in neural stem cells in adult animals [18, 20, 44]. To examine Cre-mediated recombination in neural stem cells in adult astrocyte-specific CreER^{T2} lines, we co-stained tissue

Table 2 Quantification of characteristics of the novel morphologically-defined types of astrocytes in the *Aldh1l1*-CreER^{T2}:Ai14 transgenic mice.

Cell type	Distribution	Efficiency (%)		Cell number	Max diameter (μm)	Body area (μm ²)	Territory area (μm ²)	Branch number	Branch series
		GFAP	S100B						
Hb glia	Hb	98.4 ± 0.6	71.4 ± 0.4	12	26.45 ± 3.05	57.78 ± 11.22	714.95 ± 209.79	5.08 ± 1.08	2.58 ± 0.51
	ic	96.2 ± 0.8	82.5 ± 0.6	16	45.81 ± 11.55	71.28 ± 18.42	2618.11 ± 408.64	4.96 ± 0.71	3.1 ± 0.86
Bundle glia*	Medulla	0	97.2 ± 0.4	12	122.42 ± 10.5	76.72 ± 14.89	3724.11 ± 591.47	8.81 ± 2.44	1
	oblongata								
Spinal cord short fibrous glia	Spinal cord	97.1 ± 0.8	0	16	90.84 ± 32.16	109.73 ± 23.37	11,039.79 ± 2731.6	3.5 ± 1.22	2.83 ± 0.41
Spinal cord long fibrous glia	Spinal cord	97.5 ± 0.3	0	14	171 ± 42.75	95.63 ± 13.57	11,080.35 ± 6708.94	2.25 ± 0.5	2.75 ± 0.5

The efficiency was defined as the number of tdTomato⁺ cells divided by the total number of marker-positive cells. *Hb* Habenular nucleus, *ic* inner capsule. Data are shown as mean ± SD.

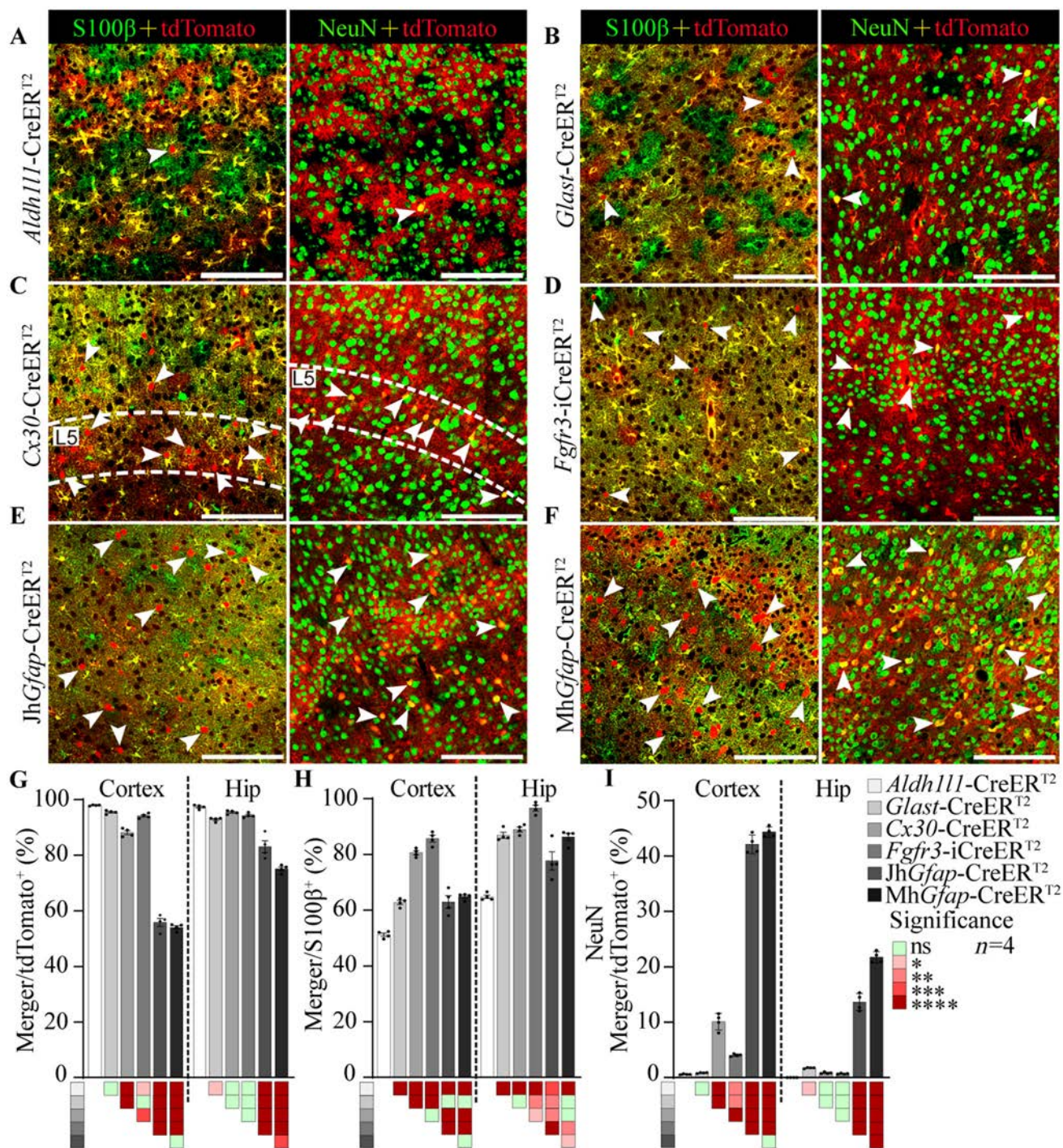


Fig. 3 Comparison of the specificity and efficiency of CreER^{T2}-mediated recombination in the cortex and hippocampus among astrocyte-targeting transgenic mice. **A–F** Representative staining for S100β or NeuN (green) in the M1 cortex of *Aldh111-* (**A**), *Glact-* (**B**), *Cx30-* (**C**), *Fgfr3-i* (**D**), *JhGfap-* (**E**), and *MhGfap-* CreER^{T2}:Ai14 (**F**) double-transgenic mice (arrowheads indicate single cells positive for tdTomato (left) and co-staining with NeuN (right); scale bars, 50 μm). **G, H** Specificity (**G**) and efficiency (**H**) of CreER^{T2}-

mediated recombination in the M1 cortex and hippocampus in astrocyte-specific CreER^{T2}:Ai14 transgenic mice. **I** Percentage of tdTomato-positive cells expressing NeuN in the M1 cortex and hippocampus in astrocyte-specific CreER^{T2}:Ai14 transgenic mice. In **G–I**, data are shown as the mean ± SEM, *n* = 4; colored squares, **P* < 0.05, ***P* < 0.01, ****P* < 0.001, *****P* < 0.0001 (one-way ANOVA followed by Tukey's test).

from the RMS, SVZ (Fig. 5A, B), and SGZ (Figs. S5A–D and S1H) with NeuN (marker for mature neurons) or DCX

(marker for neuronal precursor cells). As described above and reported previously [18], in the *Glact-CreER^{T2}* line,

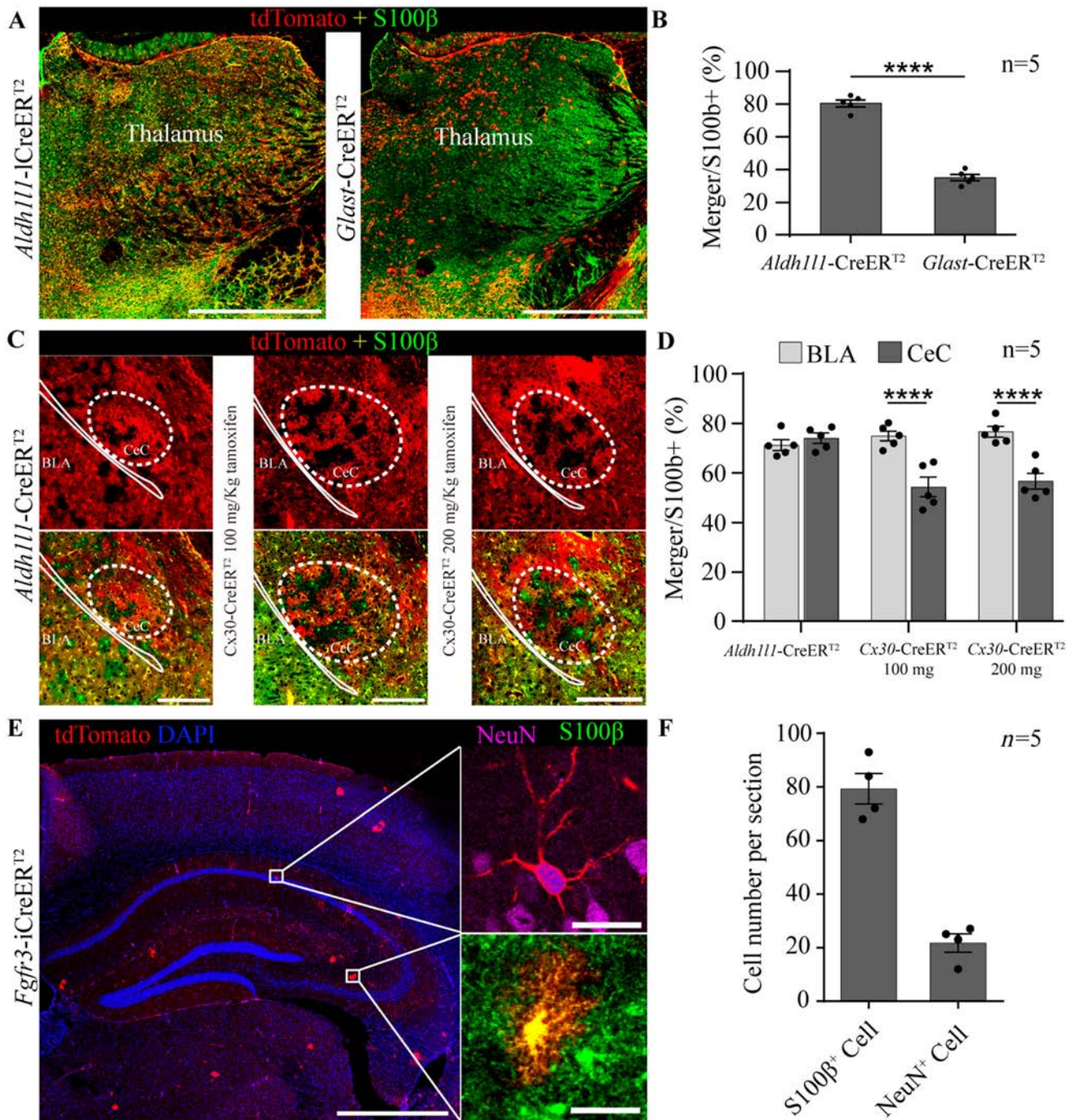


Fig. 4 Unique properties of astrocyte-specific CreER^{T2}:Ai14 transgenic mice. **A** Representative staining for S100β in the thalamus of *Aldh111-* and *Glact-* CreER^{T2}:Ai14 mice (scale bars, 1 mm). **B** Bar graphs showing that the efficiency of CreER^{T2}-mediated recombination in *Glact-CreER^{T2}*:Ai14 mice was lower than in *Aldh111-CreER^{T2}*:Ai14 mice in the thalamus. **C** Representative staining for S100β in the basal lateral amygdala (BLA) and capsular part of the central amygdaloid nucleus (CeC) in *Aldh111-* and *Cx30-CreER^{T2}*:Ai14 mice treated with 100 mg/kg or 200 mg/kg tamoxifen once per day for 5 consecutive days (scale bars, 200 μm). **D** Bar graphs showing

the efficiency of CreER^{T2}-mediated recombination in *Cx30-CreER^{T2}*:Ai14 mice was significantly reduced in the CeC. **E** Representative staining for NeuN and S100β in *Fgfr3-iCreER^{T2}*:Ai14 mice not treated with tamoxifen [scale bars, 1 mm (right) and 10 μm (left)]. **F** Bar graphs showing the numbers of astrocytes (S100β⁺, 79.25 ± 5.71 cells) and neurons (NeuN⁺, 21.75 ± 3.35 cells) per hippocampal section in *Fgfr3-iCreER^{T2}*:Ai14 mice not treated with tamoxifen. In **B**, **D**, and **F**, the data are shown as the mean ± SEM; *****P* < 0.0001, Student's *t* test.

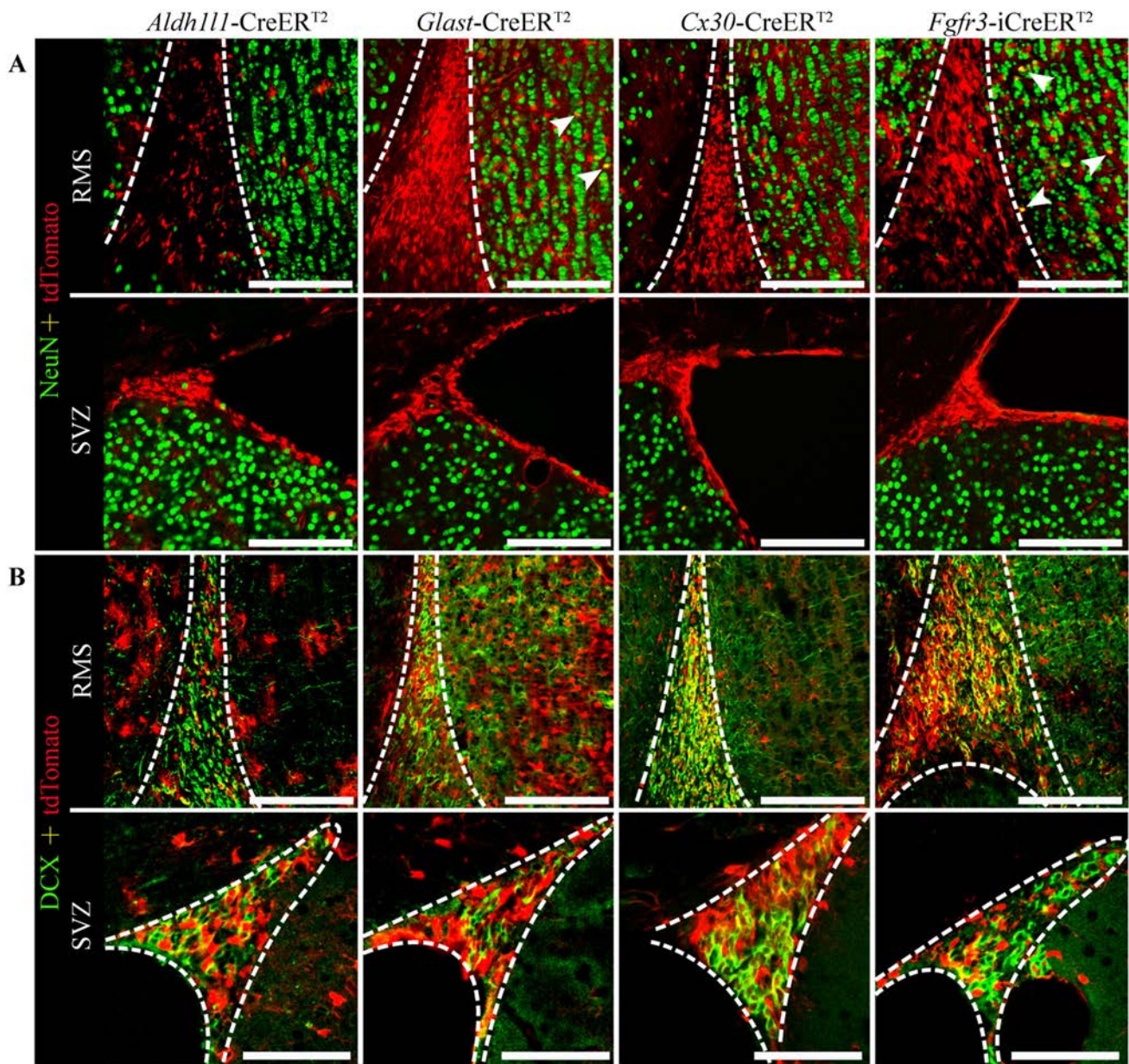


Fig. 5 Cre-mediated recombination in neural stem cells in astrocyte-specific CreER^{T2}:Ai14 transgenic mice. **A** Representative staining for NeuN (green) in the rostral migratory stream (RMS) and subventricular zone (SVZ) in *Aldh111*-, *Glact*-, *Cx30*-, and *Fgfr3-i* CreER^{T2}:Ai14 mice (scale bars, 50 μm). **B** Representative staining for DCX (green) in the RMS and SVZ in *Aldh111*-, *Glact*-, *Cx30*-, and *Fgfr3-i* CreER^{T2}:Ai14 mice (scale bars, 50 μm).

CreER^{T2}:Ai14 mice (arrows indicate cells co-stained with NeuN; scale bars, 50 μm). **B** Representative staining for DCX (green) in the RMS and SVZ in *Aldh111*-, *Glact*-, *Cx30*-, and *Fgfr3-i* CreER^{T2}:Ai14 mice (scale bars, 50 μm).

many cells in the DG were co-stained with NeuN (Figs. 3I, S6B), but this was not observed in the DG of the *Aldh111*-CreER^{T2} line (Fig. S6A–D), and almost no cells in the *Aldh111*-CreER^{T2} line were co-stained for DCX (1.66% ± 0.13% of DCX⁺ cells, *n* = 4; Fig. S1H). In addition, some cells in the granular cell layer were co-stained with NeuN in both the *Glact*-CreER^{T2} and *Fgfr3-i*CreER^{T2} lines (Fig. 5A). As expected, *Aldh111*-CreER^{T2} mediated recombination in neural stem cells of the RMS and SVZ, as demonstrated by the co-localization of

tdTomato with DCX. Similar results were obtained in the *Glact*-, *Cx30*-, and *Fgfr3-i*CreER^{T2} lines (Fig. 5B).

Cre-mediated Recombination in Peripheral Organs of Astrocyte-specific CreER^{T2} Mice

Previous studies have suggested that *Aldh111* is expressed in organs such as the spleen and liver, as well as interstitial cells [45, 46]. Consistent with these reports, we found a high level of Cre reporter expression in the liver of mice in

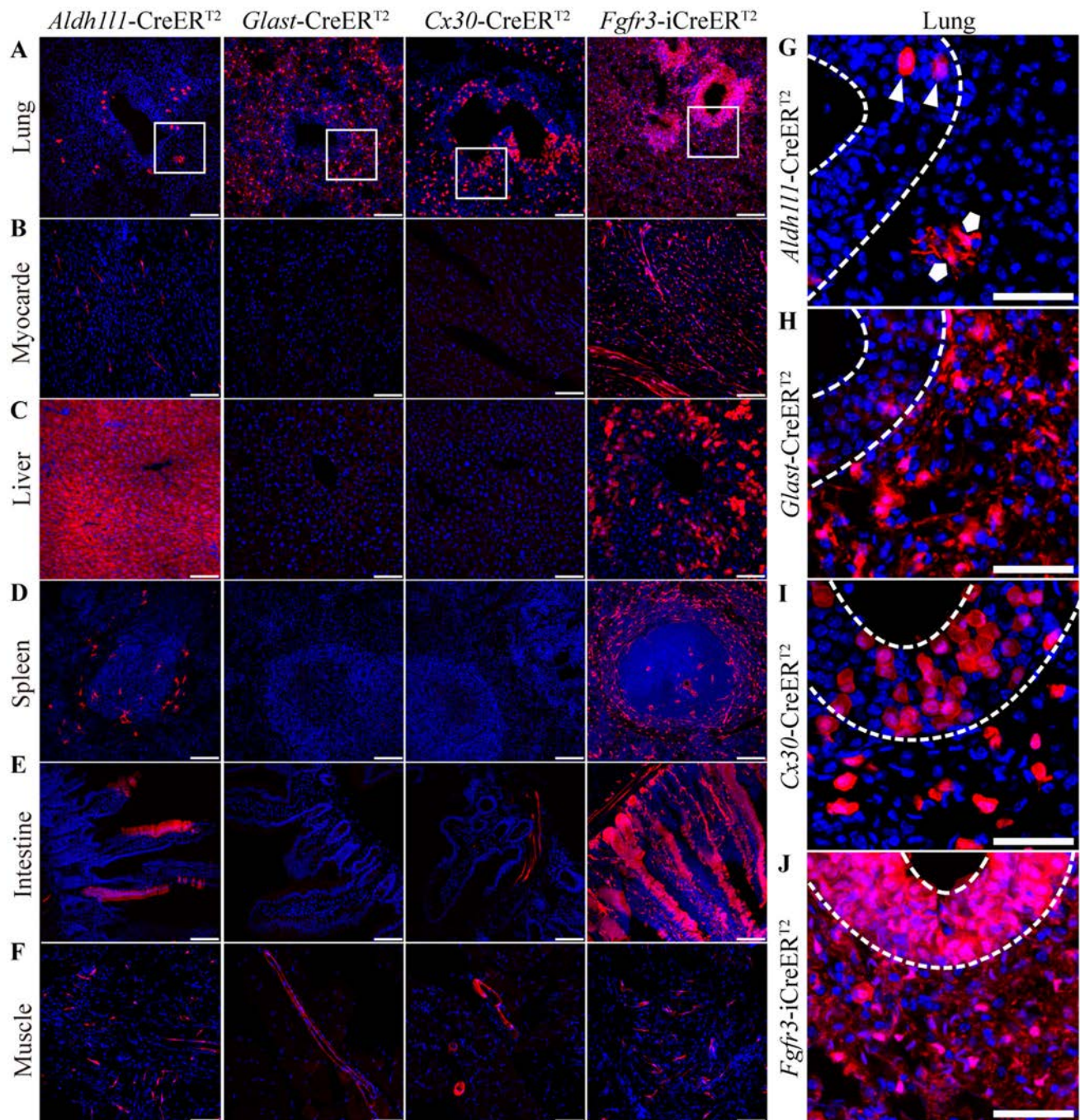


Fig. 6 Cre-mediated recombination in the organs of astrocyte-specific CreER^{T2}:Ai14 transgenic mice. **A–F** Recombination in the lung (**A**), myocardium (**B**), liver (**C**), spleen (**D**), intestine (**E**), and muscle (**F**) in *Aldh111*-, *Glact*-, *Cx30*-, and *Fgfr3-i* CreER^{T2}:Ai14 mice (scale bars, 100 μ m). **G–J** Representative high-magnification images of lung in the *Aldh111*-, *Glact*-, *Cx30*-, and *Fgfr3-i*

CreER^{T2}:Ai14 mice. Two morphologically distinct cell types, round (triangles) and branching cells (pentagons), were sparsely distributed in the *Aldh111*-CreER^{T2}:Ai14 mice (**G**) but densely distributed in the *Fgfr3-i* CreER^{T2}:Ai14 mice (**J**); however, only branching cells were observed in the *Glact*-CreER^{T2}:Ai14 mice (**H**), and only round cells in the *Cx30*-CreER^{T2}:Ai14 mice (**I**) (scale bars, 50 μ m).

the *Aldh111*-CreER^{T2} line (Fig. 6C), but only moderate levels of tdTomato expression in the lung (Fig. 6A), heart (Fig. 6B), spleen (Fig. 6D), intestine (Fig. 6E), and muscle (Fig. 6F). In the *Fgfr3-i*CreER^{T2} line, many tdTomato⁺ cells were found in the liver, spleen, lung, small intestine,

and heart (Fig. 6A–F). In the *Glact*- and *Cx30*-CreER^{T2} lines, there were many tdTomato⁺ cells in the lungs (Fig. 6A, G–J) and a few in blood vessel walls in muscles (Fig. 6F). In addition, sporadic tdTomato⁺ cells were

present on the blood vessel walls of the small intestine in the *Cx30*-CreER^{T2} line (Fig. 6E).

Surprisingly, morphologically distinct cells were found to express tdTomato in the lungs of CreER^{T2} lines (Fig. 6G–J). In the *Aldh111*-CreER^{T2} line, two different cell types were sparsely labeled with tdTomato; these were called branching cells and round cells and were located in the lung lining and on the surface of the trachea, respectively. Interestingly, we found that branching cells were specifically labeled in the *Glast*-CreER^{T2} line (Fig. 6H), while round cells were specifically labeled in the *Cx30*-CreER^{T2} line (Fig. 6I).

Discussion

In this study, we generated a new astrocyte-specific *Aldh111*-CreER^{T2} knock-in mouse line using CRISPR-Cas9 technology and assessed the efficiency and specificity of Cre recombinase in the whole CNS. Five novel morphologically-defined types of astrocyte were then characterized using this line. By comparing the *Aldh111*-CreER^{T2} line with five widely-used astrocyte-specific CreER^{T2} transgenic lines, we discovered that *Aldh111*-CreER^{T2} knock-in mice had the highest astrocyte specificity, highlighting its utility for future functional studies; however, the relatively low efficiency may limit its practical application.

In *Aldh111*-CreER^{T2} knock-in mice, Cre recombination covered almost all brain areas, showed no leakage, and had a high degree of astrocyte specificity. While the expected insertion site was detected by sequencing (data not shown), we cannot exclude the possibility that CRISPR-mediated insertion of CreER may result in non-specific modification of the endogenous genome. However, Cre-positive cells were almost all co-labeled with Aldh111, suggesting that Cre recombination expression is strictly controlled by the activity of the endogenous Aldh111 promoter. Recently, two other lines of *Aldh111*-CreER^{T2} mice were independently generated by two labs using bacterial artificial chromosome (BAC)-based transgene technology [22, 23]. One group inserted the CreER^{T2} cDNA into the start codon of the ALDH1L1 gene, but the specificity and efficiency of the inducible Cre recombinase in the whole CNS were not evaluated through crossing with a fluorescent reporter line [23]. The other group substituted the open reading frame of exon 2 with the CreER^{T2} cDNA, resulting in low expression specificity in cortex (12% of Cre⁺ cells were S100β⁻) and cerebellum, in which 3.3% of PV⁺ cells in the molecular layer showed Cre recombination. In addition, Cre recombination was also observed in some neurons in the DG and olfactory bulb [22]. These differences may result from the fact that CreER^{T2} was inserted into different

locations. Moreover, BAC-based transgenes are randomly inserted, which may affect the expression of other genes, and multiple copies of the gene are commonly inserted [47, 48]. In contrast, CRISPR/Cas9-based gene knock-in is a fixed-point insertion and usually a single copy of the gene is inserted, having less effect on other endogenous genes [49, 50].

Our study provides new evidence for the diversity of astrocyte morphology. Reichenbach and Wolburg described 12 subtypes of astrocyte based on morphology [3, 39, 51]. Emsley and Macklis imaged astrocytes in *hGfap*-GFP mice to provide a morphological characterization of this cell type in the whole CNS and showed region-specific differences [5]. However, they did not describe these morphological features quantitatively or in detail. By evaluating astrocytes sparsely-labeled with tdTomato due to treatment with a low dose of tamoxifen (50 mg/kg) in adult *Aldh111*-CreER^{T2}:Ai14 mice, we identified all of the morphologically-defined types of astrocyte reported previously [3–5, 39] and additionally described five new morphologically-distinct types: Hb glia with crossing processes, ic fibrous glial cells perpendicular to coronal sections, bundle glial cells in the medulla, and spinal cord short and long fibrous glia (Fig. 2A–F; Table 2). Whether these cell types have different physiological characteristics and functions needs further study.

Our data showed that different astrocyte-specific promoters give rise to different Cre recombination patterns. The highest specificity was obtained when Cre recombinase was driven by *Aldh111*, suggesting that this line is ideal for functional research; however, its lower efficiency may miss some astrocyte subtypes. When inducible Cre recombinase was driven by *Glast* or *Cx30*, it was expressed at low levels in the thalamus or CeC, respectively. The data obtained in the *Glast*-CreER^{T2} line were consistent with previous reports [18], and the expression of Cre recombinase was concentrated in areas negative for PV in the thalamus (Fig. S7B). It has been suggested that there are two astrocyte subtypes in the thalamus, similar to the *Glast*⁺ and *Glast*⁻ astrocytes in the cortex [8], and coordinated with the different neurons around them. In addition, *Cx30*⁻ astrocytes lack gap junctions and do not express *Cx30* but instead express other connexins in the CeC that are relevant to specific functions [52, 53]. When driven by *Fgfr3*, Cre recombinase showed leakage throughout the brain, and this may trigger developmental effects. However, this leakage does not occur in *Fgfr3*-iCreER^{T2}:R26R-EYFP mice [20]. This discrepancy may be due to the different genetic backgrounds of the transgenic mice [54]. The R26R-EYFP mice were a mixture of 129X1/SvJ and C57BL/6 J strains [55], but Ai14 mice were congenic on the C57BL/6 J genetic background and showed stronger fluorescence than R26R-EYFP [35]. It

should be noted that the lowest specificity among all these lines was achieved by *hGfap* (Fig. 3G, I). A possible explanation is that *Gfap* promoter sequences exert direct activity in neurons [56]. These findings put into question conclusions that are obtained with *hGfap*-CreER^{T2} lines, especially in behavioral and electrophysiological experiments.

In tissues outside the brain, inducible Cre recombinase was expressed at high levels in the liver (Fig. 6C) when driven by *Aldh1l1*, potentially because the *Aldh1l1* CpG island is methylation-free in DNA extracted from hepatocytes [45]. Therefore, future studies on *Aldh1l1*-CreER^{T2} line-driven knockouts should consider potential effects on the liver. Interestingly, inducible Cre recombinase occurred in two morphologically distinct lung cells, one each in the *Glast*- and *Cx30*-CreER^{T2} lines. These data suggest that astrocyte-specific Cre recombination may also affect peripheral tissues.

Acknowledgements This work was supported by Grants from the National Natural Science Foundation of China (31430032, 31830033, 81971080, and 81671356), the Program for Changjiang Scholars and Innovative Research Teams in University (IRT_16R37), the Science and Technology Program of Guangdong (2018B030334001), and the Guangzhou Science and Technology Project (201707020027, 201704020116). Thanks to Professor William D. Richardson (University College London, UK) for the *Fgfr3*-iCreER^{T2} line.

Conflict of interest The authors declare that the research was conducted in the absence of any commercial or financial relationships that could be construed as a potential conflict of interest.

References

- Herculano-Houzel S. The glia/neuron ratio: how it varies uniformly across brain structures and species and what that means for brain physiology and evolution. *Glia* 2014, 62: 1377–1391.
- Rowitch DH, Kriegstein AR. Developmental genetics of vertebrate glial-cell specification. *Nature* 2010, 468: 214–222.
- Verkhratsky AN, Butt A. *Glial Physiology and Pathophysiology*. Chichester, West Sussex, UK; Hoboken, NJ, USA: Wiley-Blackwell, 2013.
- Bailey MS, Shipley MT. Astrocyte subtypes in the rat olfactory bulb: morphological heterogeneity and differential laminar distribution. *J Comp Neurol* 1993, 328: 501–526.
- Emsley JG, Macklis JD. Astroglial heterogeneity closely reflects the neuronal-defined anatomy of the adult murine CNS. *Neuron Glia Biol* 2006, 2: 175–186.
- Buosi AS, Matias I, Araujo APB, Batista C, Gomes FCA. Heterogeneity in synaptogenic profile of astrocytes from different brain regions. *Mol Neurobiol* 2018, 55: 751–762.
- Ben Haim L, Rowitch DH. Functional diversity of astrocytes in neural circuit regulation. *Nat Rev Neurosci* 2017, 18: 31–41.
- Morel L, Men Y, Chiang MSR, Tian Y, Jin S, Yelick J, *et al.* Intracortical astrocyte subpopulations defined by astrocyte reporter mice in the adult brain. *Glia* 2019, 67: 171–181.
- Zhang Y, Barres BA. Astrocyte heterogeneity: an underappreciated topic in neurobiology. *Curr Opin Neurobiol* 2010, 20: 588–594.
- Wang Q, Jie W, Liu JH, Yang JM, Gao TM. An astroglial basis of major depressive disorder? An overview. *Glia* 2017, 65: 1227–1250.
- Cui Y, Yang Y, Ni Z, Dong Y, Cai G, Foncelle A, *et al.* Astroglial Kir4.1 in the lateral habenula drives neuronal bursts in depression. *Nature* 2018, 554: 323–327.
- Tso CF, Simon T, Greenlaw AC, Puri T, Mieda M, Herzog ED. Astrocytes regulate daily rhythms in the suprachiasmatic nucleus and behavior. *Curr Biol* 2017, 27: 1055–1061.
- Niu B, Zhang T, Hu HQ, Cao BZ. Transcriptome sequencing reveals astrocytes as a therapeutic target in heat-stroke. *Neurosci Bull* 2017, 33: 627–640.
- Jahn HM, Scheller A, Kirchhoff F. Genetic control of astrocyte function in neural circuits. *Front Cell Neurosci* 2015, 9: 310.
- Guo ZB, Su YY, Lou HF. GFAP-positive progenitor cell production is concentrated in specific encephalic regions in young adult mice. *Neurosci Bull* 2018, 34: 769–778.
- Casper KB, McCarthy KD. GFAP-positive progenitor cells produce neurons and oligodendrocytes throughout the CNS. *Mol Cell Neurosci* 2006, 31: 676–684.
- Hirrlinger PG, Scheller A, Braun C, Hirrlinger J, Kirchhoff F. Temporal control of gene recombination in astrocytes by transgenic expression of the tamoxifen-inducible DNA recombinase variant CreERT2. *Glia* 2006, 54: 11–20.
- Slezak M, Goritz C, Niemiec A, Frisen J, Chambon P, Metzger D, *et al.* Transgenic mice for conditional gene manipulation in astroglial cells. *Glia* 2007, 55: 1565–1576.
- Casper KB, Jones K, McCarthy KD. Characterization of astrocyte-specific conditional knockouts. *Genesis* 2007, 45: 292–299.
- Young KM, Mitumori T, Pringle N, Grist M, Kessar N, Richardson WD. An *Fgfr3*-iCreER(T2) transgenic mouse line for studies of neural stem cells and astrocytes. *Glia* 2010, 58: 943–953.
- Mori T, Tanaka K, Buffo A, Wurst W, Kuhn R, Gotz M. Inducible gene deletion in astroglia and radial glia—a valuable tool for functional and lineage analysis. *Glia* 2006, 54: 21–34.
- Winchenbach J, Dukung T, Berghoff SA, Stumpf SK, Hulsmann S, Nave KA, *et al.* Inducible targeting of CNS astrocytes in *Aldh1l1*-CreERT2 BAC transgenic mice. *F1000Research* 2016, 5: 2934.
- Srinivasan R, Lu TY, Chai H, Xu J, Huang BS, Golshani P, *et al.* New transgenic mouse lines for selectively targeting astrocytes and studying calcium signals in astrocyte processes *in situ* and *in vivo*. *Neuron* 2016, 92: 1181–1195.
- Lee KM, Lan Q, Krickler A, Purdue MP, Grulich AE, Vajdic CM, *et al.* One-carbon metabolism gene polymorphisms and risk of non-Hodgkin lymphoma in Australia. *Hum Genet* 2007, 122: 525–533.
- Lim U, Wang SS, Hartge P, Cozen W, Kelemen LE, Chanock S, *et al.* Gene-nutrient interactions among determinants of folate and one-carbon metabolism on the risk of non-Hodgkin lymphoma: NCI-SEER case-control study. *Blood* 2007, 109: 3050–3059.
- Neymeyer V, Tephly TR, Miller MW. Folate and 10-formyltetrahydrofolate dehydrogenase (FDH) expression in the central nervous system of the mature rat. *Brain Res* 1997, 766: 195–204.
- Cahoy JD, Emery B, Kaushal A, Foo LC, Zamanian JL, Christopherson KS, *et al.* A transcriptome database for astrocytes, neurons, and oligodendrocytes: a new resource for understanding brain development and function. *J Neurosci* 2008, 28: 264–278.
- Zhang Y, Chen K, Sloan SA, Bennett ML, Scholze AR, O’Keefe S, *et al.* An RNA-sequencing transcriptome and splicing database of glia, neurons, and vascular cells of the cerebral cortex. *J Neurosci* 2014, 34: 11929–11947.

29. Ganat YM, Silbereis J, Cave C, Ngu H, Anderson GM, Ohkubo Y, *et al.* Early postnatal astroglial cells produce multilineage precursors and neural stem cells *in vivo*. *J Neurosci* 2006, 26: 8609–8621.
30. Shen B, Zhang J, Wu H, Wang J, Ma K, Li Z, *et al.* Generation of gene-modified mice via Cas9/RNA-mediated gene targeting. *Cell Res* 2013, 23: 720–723.
31. Ma Y, Zhang X, Shen B, Lu Y, Chen W, Ma J, *et al.* Generating rats with conditional alleles using CRISPR/Cas9. *Cell Res* 2014, 24: 122–125.
32. Cui L, Zhang Z, Sun F, Duan X, Wang M, Di K, *et al.* Transcervical embryo transfer in mice. *J Am Assoc Lab Anim Sci* 2014, 53: 228–231.
33. Wei C, Liu J, Yu Z, Zhang B, Gao G, Jiao R. TALEN or Cas9 - rapid, efficient and specific choices for genome modifications. *J Genet Genomics* 2013, 40: 281–289.
34. Chen YH, Lan YJ, Zhang SR, Li WP, Luo ZY, Lin S, *et al.* ErbB4 signaling in the prefrontal cortex regulates fear expression. *Transl Psychiatry* 2017, 7: e1168.
35. Madisen L, Zwingman TA, Sunkin SM, Oh SW, Zariwala HA, Gu H, *et al.* A robust and high-throughput Cre reporting and characterization system for the whole mouse brain. *Nat Neurosci* 2010, 13: 133–140.
36. Liu Y, Wu Y, Lee JC, Xue H, Pevny LH, Kaprielian Z, *et al.* Oligodendrocyte and astrocyte development in rodents: an in situ and immunohistological analysis during embryonic development. *Glia* 2002, 40: 25–43.
37. Molofsky AV, Krencik R, Ullian EM, Tsai HH, Deneen B, Richardson WD, *et al.* Astrocytes and disease: a neurodevelopmental perspective. *Genes Dev* 2012, 26: 891–907.
38. Yang Y, Vidensky S, Jin L, Jie C, Lorenzini I, Frankl M, *et al.* Molecular comparison of GLT1 + and ALDH1L1 + astrocytes *in vivo* in astroglial reporter mice. *Glia* 2011, 59: 200–207.
39. Matyash V, Kettenmann H. Heterogeneity in astrocyte morphology and physiology. *Brain Res Rev* 2010, 63: 2–10.
40. Tran CHT, Peringod G, Gordon GR. Astrocytes integrate behavioral state and vascular signals during functional hyperemia. *Neuron* 2018, 100: 1133–1148 e1133.
41. Chaboub LS, Deneen B. Developmental origins of astrocyte heterogeneity: the final frontier of CNS development. *Dev Neurosci* 2012, 34: 379–388.
42. Bayraktar OA, Fuentealba LC, Alvarez-Buylla A, Rowitch DH. Astrocyte development and heterogeneity. *Cold Spring Harb Perspect Biol* 2014, 7: a020362.
43. Obernier K, Alvarez-Buylla A. Neural stem cells: origin, heterogeneity and regulation in the adult mammalian brain. *Development* 2019, 146: dev156059.
44. Foo LC, Dougherty JD. Aldh1L1 is expressed by postnatal neural stem cells *in vivo*. *Glia* 2013, 61: 1533–1541.
45. Oleinik NV, Krupenko NI, Krupenko SA. Epigenetic silencing of ALDH1L1, a metabolic regulator of cellular proliferation, in cancers. *Genes Cancer* 2011, 2: 130–139.
46. Boesmans W, Rocha NP, Reis HJ, Holt M, Vanden Berghe P. The astrocyte marker Aldh1L1 does not reliably label enteric glial cells. *Neurosci Lett* 2014, 566: 102–105.
47. Beil J, Buch T. Generation of bacterial artificial chromosome (BAC) transgenic mice. *Methods Mol Biol* 2014, 1194: 157–169.
48. Yang XW, Gong S. An overview on the generation of BAC transgenic mice for neuroscience research. *Curr Protoc Neurosci* 2005, Chapter 5: 5–20.
49. Kesavan G, Chekuru A, Machate A, Brand M. CRISPR/Cas9-mediated zebrafish knock-in as a novel strategy to study midbrain-hindbrain boundary development. *Front Neuroanat* 2017, 11: 52.
50. Platt RJ, Chen S, Zhou Y, Yim MJ, Swiech L, Kempton HR, *et al.* CRISPR-Cas9 knockin mice for genome editing and cancer modeling. *Cell* 2014, 159: 440–455.
51. Reichenbach A, Wolburg H. *Neuroglia*, 2nd ed. Oxford, UK: Oxford University Press, 2004.
52. Pannasch U, Dossi E, Ezan P, Rouach N. Astroglial Cx30 sustains neuronal population bursts independently of gap-junction mediated biochemical coupling. *Glia* 2019, 67: 1104–1112.
53. Clasadonte J, Haydon PG. Connexin 30 controls the extension of astrocytic processes into the synaptic cleft through an unconventional non-channel function. *Neurosci Bull* 2014, 30: 1045–1048.
54. Yoshiki A, Moriwaki K. Mouse phenome research: implications of genetic background. *ILAR J* 2006, 47: 94–102.
55. Srinivas S, Watanabe T, Lin CS, Williams CM, Tanabe Y, Jessell TM, *et al.* Cre reporter strains produced by targeted insertion of EYFP and ECFP into the ROSA26 locus. *BMC Dev Biol* 2001, 1: 4.
56. Su M, Hu H, Lee Y, d’Azzo A, Messing A, Brenner M. Expression specificity of GFAP transgenes. *Neurochem Res* 2004, 29: 2075–2093.



METHOD

In Vivo Two-photon Calcium Imaging in Dendrites of Rabies Virus-labeled V1 Corticothalamic Neurons

Yajie Tang^{1,2,3} · Liang Li^{2,3} · Leqiang Sun^{2,3} · Jinsong Yu^{2,3} · Zhe Hu² · Kaiqi Lian¹ · Gang Cao^{2,3,4,5} · Jinxia Dai^{2,3,4,5}

Received: 3 July 2019 / Accepted: 4 October 2019 / Published online: 5 December 2019
© Shanghai Institutes for Biological Sciences, CAS 2019

Abstract Monitoring neuronal activity *in vivo* is critical to understanding the physiological or pathological functions of the brain. Two-photon Ca²⁺ imaging *in vivo* using a cranial window and specific neuronal labeling enables real-time, *in situ*, and long-term imaging of the living brain. Here, we constructed a recombinant rabies virus containing the Ca²⁺ indicator GCaMP6s along with the fluorescent protein DsRed2 as a baseline reference to ensure GCaMP6s signal reliability. This functional tracer was applied to retrogradely label specific V1–thalamus circuits and detect spontaneous Ca²⁺ activity in the dendrites of V1 corticothalamic neurons by *in vivo* two-photon Ca²⁺ imaging. Notably, we were able to record single-spine spontaneous Ca²⁺ activity in specific circuits. Distinct spontaneous

Ca²⁺ dynamics in dendrites of V1 corticothalamic neurons were found for different V1–thalamus circuits. Our method can be applied to monitor Ca²⁺ dynamics in specific input circuits *in vivo*, and contribute to functional studies of defined neural circuits and the dissection of functional circuit connections.

Keywords *In vivo* Ca²⁺ imaging · Cranial window · Two-photon microscopy · Rabies virus · Dendrite · Primary visual cortex · Corticothalamic projection · Neural circuit tracing

Introduction

The mammalian brain is an extremely sophisticated structure composed of a highly-complex neural network. Dissecting the structure and function of neural circuits from this complex network is pivotal for understating brain functions such as sensation, movement, learning, and memory [1–7]. In functional studies of neural circuits, it is important to monitor neural activity *in vivo*, and Ca²⁺ imaging is a useful technique for monitoring the dynamics of such activity [8–11]. Ca²⁺ imaging *in vivo* is greatly facilitated by sensitive Ca²⁺ indicators like the genetically-encoded Ca²⁺ indicators (GCaMP family proteins) and the specific labeling of neurons in defined neural circuits based on genetic manipulation and/or neurotrophic virus tracers [11–14].

Among the Ca²⁺ indicators, conventional small synthetic dye molecules are the most sensitive, but they are invasive, hard to target at specific cell types and subcellular locations, and impossible for long-term detection, limiting their application *in vivo* [15–17]. The genetically-encoded Ca²⁺ indicators (GECIs) can be relatively non-invasive,

Electronic supplementary material The online version of this article (<https://doi.org/10.1007/s12264-019-00452-y>) contains supplementary material, which is available to authorized users.

✉ Jinxia Dai
jxdai@mail.hzau.edu.cn

- ¹ Academician Workstation of Animal Disease Control and Nutrition Immunity in Henan Province, Henan Joint International Research Laboratory of Veterinary Biologics Research and Application, Anyang Institute of Technology, Anyang 455000, China
- ² State Key Laboratory of Agricultural Microbiology, Huazhong Agricultural University, Wuhan 430070, China
- ³ College of Veterinary Medicine, Huazhong Agricultural University, Wuhan 430070, China
- ⁴ Biomedical Center, Huazhong Agricultural University, Wuhan 430070, China
- ⁵ Key Laboratory of Development of Veterinary Diagnostic Products, Ministry of Agriculture, College of Veterinary Medicine, Huazhong Agricultural University, Wuhan 430070, China

accessible to specific neurons and subcellular locations, and amenable to long-term recording, making them ideal for *in vivo* studies [17–19]. New generations of GECIs, including GCaMP6 and jGCaMP7 family members, displaying sensitivity and kinetics similar to synthetic dyes, have been developed for assessing neuronal activity at high temporal resolution [20].

Due to the limitations of genetic mouse lines, labeling of defined neural circuits with GECIs is increasingly dependent on the use of diverse neurotropic viruses, including adeno-associated virus (AAV), retrograde tracing AAV, and rabies virus (RV) [13, 21, 22]. Based on the high expression level of GECIs induced by neurotropic viruses, the neural activity of labeled neural circuits at the cellular and subcellular levels (dendrites, spines, and axonal boutons) can be detected *via in vivo* Ca^{2+} imaging by means of live two-photon microscopy or miniscope implementation in anesthetized, awake, and even freely-behaving mice [23–26]. With the help of the cranial window technique, *in vivo* Ca^{2+} imaging by two-photon microscopy can be realized without any invasion of brain tissue [27, 28].

Here, by combining the advantages of GCaMP6s ultra-sensitivity in assessing Ca^{2+} dynamics and RV in retrograde tracing and fine structure labeling due to high-level expression of fluorescent proteins, we aimed to monitor the subcellular activity in neurons in specific RV-labeled circuits by *in vivo* two-photon Ca^{2+} imaging.

Materials and Methods

Animals

All the animal experiments were approved by the Research Ethics Committee, Huazhong Agricultural University, Hubei, China (HZAUMO-2016-021) and were carried out in accordance with the Guide for the Care and Use of Laboratory Animals of the Research Ethics Committee, Huazhong Agricultural University.

Virus Construction and Preparation

The genetically-encoded Ca^{2+} indicators GCaMP6s and red fluorescent protein DsRed2 genes were each cloned into multiple cloning sites at AscI/SacII and SbfI/NheI of the pSAD- Δ G-F3 backbone (a kind gift from Dr. Fuqiang Xu, Wuhan Institute of Physics and Mathematics, Chinese Academy of Sciences, and Dr. Edward Callaway, The SALK Institute, USA) to generate the pSAD- Δ G-GCaMP6s-DsRed2 plasmid. Recombinant rabies virus rRV- Δ G-GCaMP6s-DsRed2 was rescued following the protocol of the Callaway laboratory [29]. Briefly, pSAD-

Δ G-GCaMP6s-DsRed2 and helper plasmids (B19N, B19P, B19G, and B19L) were co-transfected into B7GG cells (kind gifts from Drs Xu and Callaway) and cultured for 7 days–10 days. The viral supernatant was harvested and centrifuged at 70,000g for 3 h, then the pellet was suspended in Dulbecco's modified Eagle's medium and spun again on the top of a 20% sucrose solution. Finally, rRV- Δ G-GCaMP6s-DsRed2 was re-suspended in phosphate-buffered saline, aliquoted, and stored at $-80^{\circ}C$. The titer of rRV- Δ G-GCaMP6s-DsRed2 was adjusted to 10^9 plaque-forming units/mL for mouse brain injection.

Stereotaxic Microinjection

C57BL/6C male mice (8 weeks–10 weeks old) were anesthetized with a mixture of anesthetics (7.5 g urethane, 3 g chloral hydrate, and 75 mg xylazine in 100 mL ddH₂O) at 900 μ L per 100 g body weight by intraperitoneal injection. After the scalp was shaved, the head was fixed in stereotaxic instruments (68025; RWD Life Science, Shenzhen, China) and cleaned with 70% ethanol. For virus injection, a 0.5 mm diameter hole was drilled through the skull with a microdrill (78001; RWD Life Science) at sites for the dorsal lateral geniculate nucleus (dLGN; AP, -2.35 mm; ML, 2.26 mm; DV, -2.70 mm), the lateral posterior nucleus (LP; AP, -2.22 mm; ML, 1.60 mm; DV, -2.62 mm), and the lateral dorsal nucleus (LD; AP, -1.32 mm; ML, 1.40 mm; DV, -2.65 mm). The injector was a 10 μ L syringe (Shanghai Gaoge Industrial and Trading Co., Shanghai, China) fused with a glass needle pulled by PC-10 puller (DL Naturegene Life Sciences, Newbury Park, CA) and filled with mineral oil. A total of 300 nL virus (10^9 focus-forming units/mL) was injected by a KDS LegatoTM 130 micro-pump (KD Scientific Inc., Holliston, MA) at 18 nL/min.

Cranial Window and *In Vivo* Two-photon Calcium Imaging

A cranial window was created over the primary visual cortex (V1) on day 7 after virus injection for *in vivo* Ca^{2+} imaging of corticothalamic neuron dendrites, based on previous reports [30, 31]. Briefly, the skull over the V1 region was polished to a transparent area ~ 10 μ m thick and ~ 4 mm in diameter. A drop of agarose gel was applied to protect the polished area. Finally, a piece of coverslip, 5 mm in diameter and 0.13 mm thick, was placed on the gel and sealed with glue before covering with dental cement.

For Ca^{2+} imaging on day 10 after virus injection, the glass and agarose gel were removed and the skull was wetted with normal saline for imaging with an FV1200MPE multiphoton microscope (Olympus, Tokyo,

Japan). Meanwhile, a scaffold for fastening the mouse head was attached to the skull with dental cement before imaging. Each mouse was anesthetized with 0.2% isoflurane mixed with 200 mL/min O₂ flow and wrapped in a heating pad to keep the body temperature at 37 °C. The optimal laser wavelength to stimulate both GCaMP6s and DsRed2 was 920 nm, while their emission was collected at 495 nm–540 nm and 575 nm–630 nm, respectively.

Data Analysis

All data were analyzed using ImageJ software (National Institutes of Health, Bethesda, MD) with the Time series analyzer V3 plugin. The quantified data are presented as the mean \pm SEM using Graphpad Prism (San Diego, CA). Changes in GCaMP6s and DsRed2 fluorescence intensity were quantified as $\Delta F/F_0$, where ΔF is the difference between a spike and baseline fluorescence and F_0 is the baseline fluorescence. To calibrate GCaMP6s signal distortion, the fluorescence change (GCaMP6s $\Delta F/F_0$) was divided by the DsRed2 intensity (DsRed2 $\Delta F/F_0$) to acquire the calibrated intensity ($\Delta R/R_0$) of GCaMP6s fluorescence. For each imaging area, 300 frames were acquired at a scan speed of 2 μ s/pixel with a frame resolution of 800 \times 800 pixels. The spike frequency of each dendrite was calculated as spike number per minute by dividing the total number of spikes in 5 min by 5.

Results

Retrograde Labeling of V1 Corticothalamic Neurons by Recombinant rRV- Δ G-GCaMP6s-DsRed2 Functional Tracer

In order to monitor Ca²⁺ dynamics at subcellular resolution in specific retrogradely-labeled neural circuits, we constructed a rabies virus-based Ca²⁺ indicator (rRV- Δ G-GCaMP6s-DsRed2), in which the GCaMP6s and DsRed2 genes were tandemly inserted into the RV vector (Fig. 1A). Simultaneous expression of GCaMP6s and DsRed2 proteins was confirmed by their co-distribution in the same B7GG cells (Fig. 1B). DsRed2 fluorescence was used to show the detailed morphology of the whole neuron and served at the same time as a baseline to calibrate the GCaMP6s signal distortion mainly caused by respiratory vibration and thermal drift during two-photon live imaging. This combination of the ultrasensitive GCaMP6s, the stable signal of DsRed2, and retrograde labeling of RV allowed us to monitor live Ca²⁺ activity in specific input circuits to a specific nucleus.

Due to light-scattering and aberrations originating from tissue, the penetration depth of two-photon imaging is limited to a few hundred micrometers [32, 33], so live Ca²⁺ imaging is usually restricted to the superficial cortical layers in mice. Here, we selected V1 corticothalamic

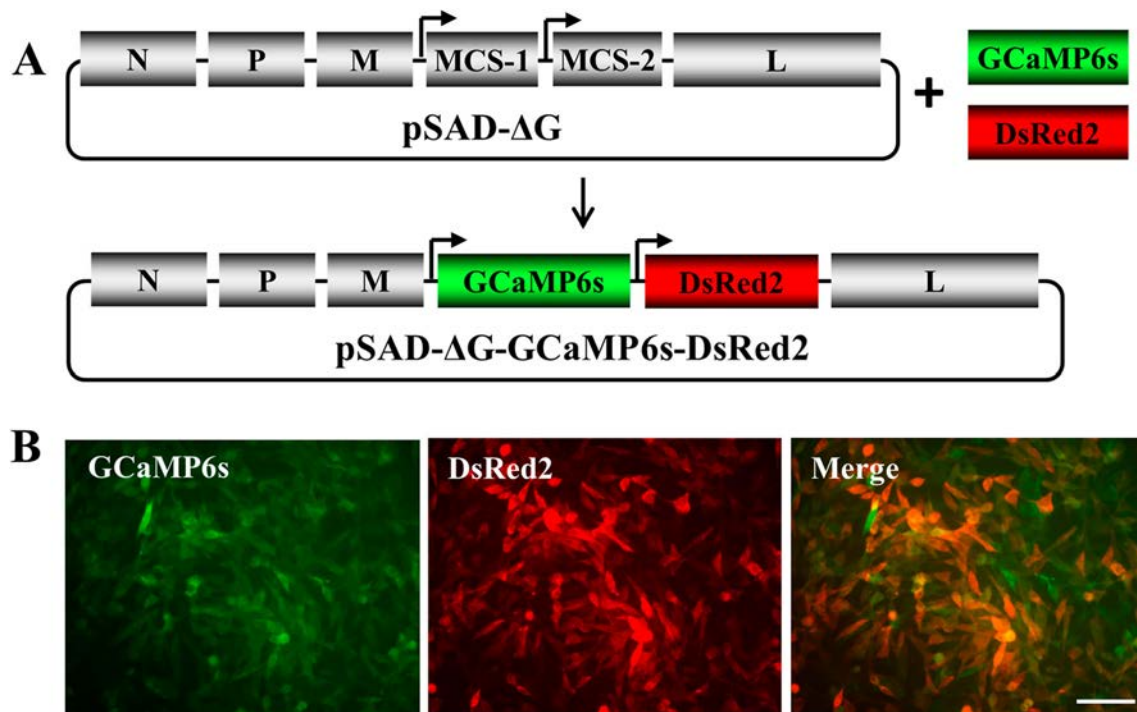


Fig. 1 Construction of the retrograde functional tracer rRV- Δ G-GCaMP6s-DsRed2. **A** Schematic of recombinant RV plasmid construction. The GCaMP6s and DsRed2 genes were cloned into the

G-deleted (Δ G) RV vector pSAD- Δ G to generate the pSAD- Δ G-GCaMP6s-DsRed2 plasmid. **B** Co-expression of GCaMP6s and DsRed2 proteins in the same B7GG cells (scale bar, 100 μ m).

neurons labeled by rRV- Δ G-GCaMP6s-DsRed2 for monitoring subcellular spontaneous activity by two-photon *in vivo* Ca^{2+} imaging. V1 corticothalamic neurons were retrogradely labeled by rRV- Δ G-GCaMP6s-DsRed2 from their thalamic targets (dLGN, LP, and LD; Fig. 2A). Co-expression of GCaMP6s and DsRed2 proteins was observed in all the neurons infected with rRV- Δ G-GCaMP6s-DsRed2 (supplemental Fig. S1). Based on the reports that no significant alteration in neuronal activity of RV-labeled neuron occurs within 5 days–11 days after

Fig. 3 Spontaneous Ca^{2+} dynamics in dendrites and spines of V1 corticothalamic neurons detected by *in vivo* two-photon microscopy. **A** Dendrites of rRV- Δ G-GCaMP6s-DsRed2-labeled V1 neurons (dashed area magnified in **B** and **D**; scale bar, 20 μm). **B** Time-lapse Ca^{2+} imaging of spontaneous dendritic activity (scale bar, 5 μm). **C** Left panel, GCaMP6s and DsRed2 fluorescence in a single dendrite of the V1 corticothalamic neuron in **B**; right panel, GCaMP6s signal calibrated by ratio of GCaMP6s to DsRed2 intensity. **D** Time-lapse Ca^{2+} imaging of spontaneous spine activity [white arrows, Ca^{2+} fluorescence of the activated spine (scale bar, 5 μm)]. **E** Left, quantification of GCaMP6s and DsRed2 fluorescence in a single spine of the V1 corticothalamic neuron in **D**; right, calibrated GCaMP6s signal in the spine.

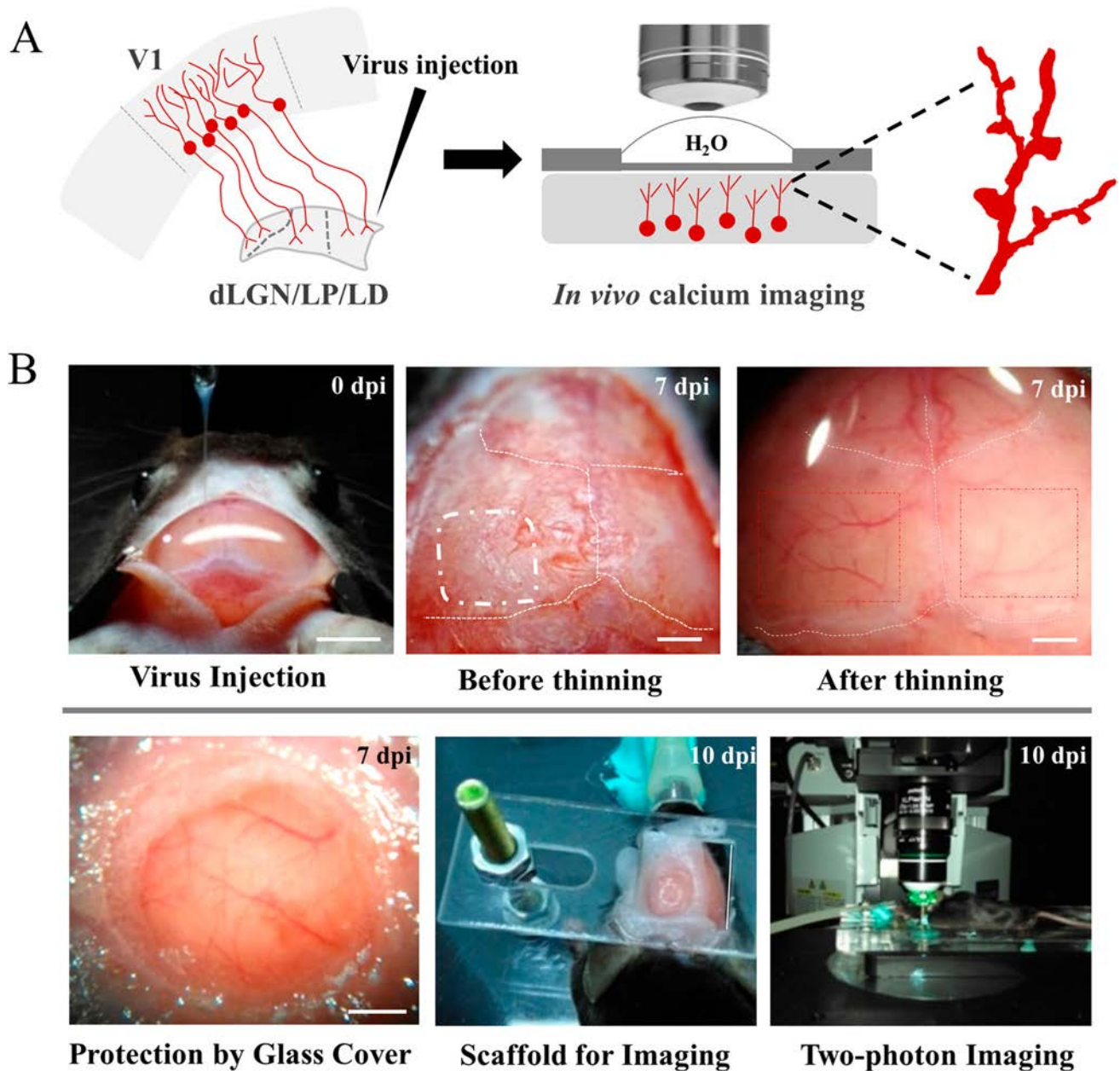
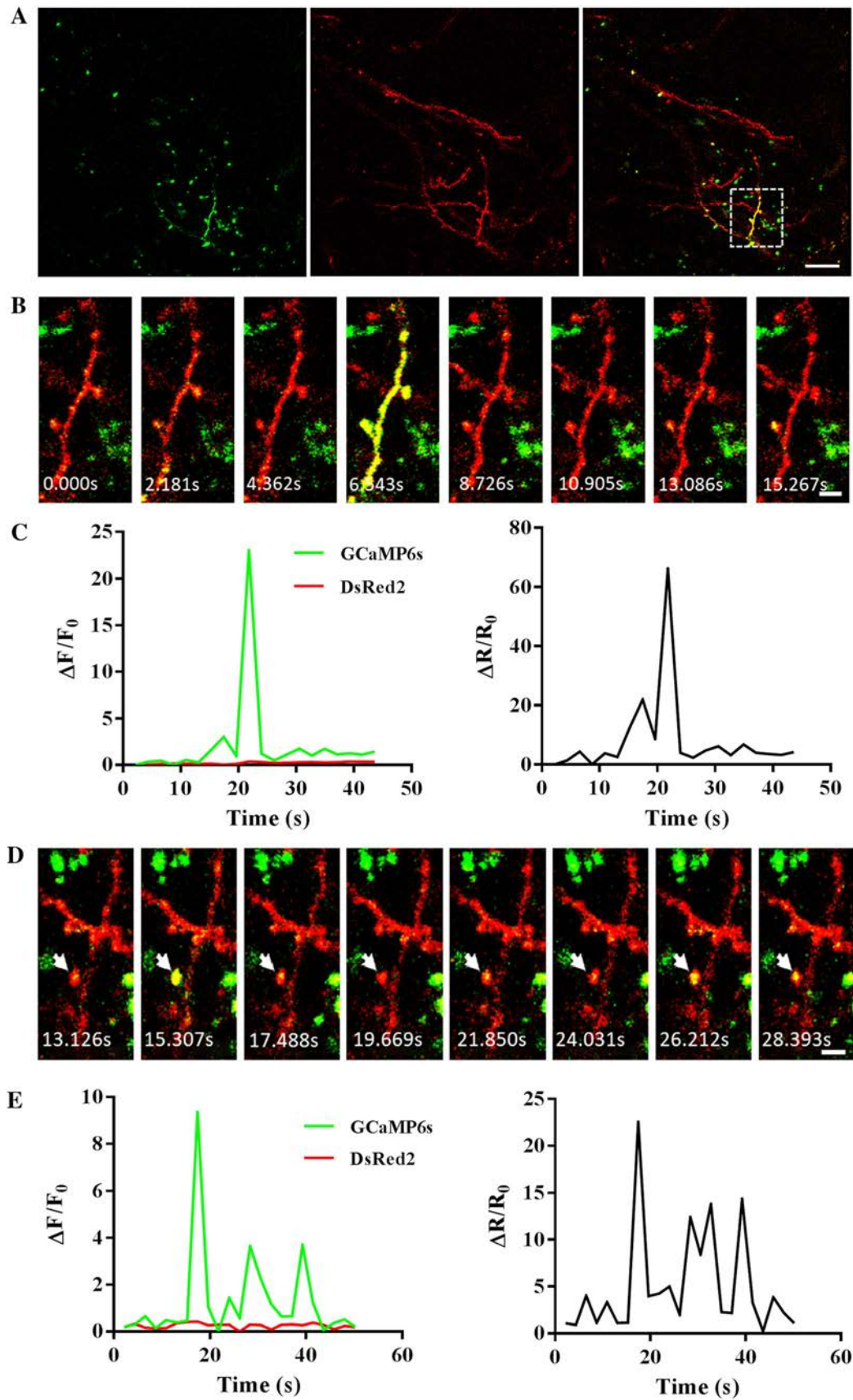


Fig. 2 Method for imaging the activity in dendrites of rRV- Δ G-GCaMP6s-DsRed2-labeled V1 corticothalamic neurons by *in vivo* two-photon microscopy. **A** Schematic of retrograde labeling of different corticothalamic neurons in V1 (V1-dLGN, V1-LP, and V1-LD) by

rRV- Δ G-GCaMP6s-DsRed2 and *in vivo* Ca^{2+} imaging. **B** Sequence of virus injection, cranial window thinning, and two-photon imaging (scale bars, 3 mm for virus injection, 1 mm for thinning, 500 μm for protection by glass cover; dpi, days post-infection).



virus injection based on electrophysiological recording [34], we performed two-photon *in vivo* Ca^{2+} imaging on day 10 after injection to monitor the dendritic Ca^{2+} activity of retrogradely-labeled V1 corticothalamic neurons (Fig. 2B).

In Vivo Two-photon Calcium Imaging to Monitor Spontaneous Activity in Dendrites of Corticothalamic Neurons in V1 Labeled with rRV- Δ G-GCaMP6s-DsRed2

V1 corticothalamic neurons are located in the deep layers (V and VI) of the cortex [35], so *in vivo* Ca^{2+} imaging of the retrogradely-labeled cell bodies was hard to realize due to the limited penetration depth of two-photon microscopy. Thus, we performed Ca^{2+} imaging on the dendrites in the upper layers of rRV- Δ G-GCaMP6s-DsRed2-labeled corticothalamic neurons in mice under anesthesia. The dendrites and spines of V1-dLGN neurons were clearly observed by the bright DsRed2 fluorescence *via* two-photon microscopy (Fig. 3A). Strong green fluorescence (GCaMP6s) was monitored in some DsRed2-positive dendrites and spines (Fig. 3A), indicating increased local activity of neurons with Ca^{2+} influx. Spontaneous Ca^{2+} sparks in dendrites and spines lasting for several seconds were detected, and the baseline of DsRed2 fluorescence was stable during Ca^{2+} imaging (Fig. 3B, D, supplementary videos 1 and 2). The ratio of $\Delta F/F0_{\text{GCaMP6s}}$ to $\Delta F/F0_{\text{DsRed2}}$, $\Delta R/R0$, was calculated to calibrate GCaMP6s signal distortion (Fig. 3C, E). Spontaneous increases of Ca^{2+} concentration in local dendrites and spines may reflect excitatory input from presynaptic terminals in the resting state.

Further, we monitored the spontaneous Ca^{2+} dynamics in the dendrites of corticothalamic neurons from distinct V1-thalamus circuits (V1-dLGN, V1-LP, and V1-LD) (Fig. 4A). For each V1-thalamus circuit, the data from three mice with accurate labeling and successful cranial windows were analyzed. Dendritic Ca^{2+} responses in each mouse were recorded randomly in different fields of V1. The spontaneous Ca^{2+} dynamics of the different groups of corticothalamic neurons displayed distinct patterns of spike amplitude and frequency (Fig. 4). The frequency of Ca^{2+} spikes in the spontaneously active dendrites of V1-LP neurons was higher than those of V1-LD and V1-dLGN neurons (mean \pm SEM; V1-LP, 4.27 ± 0.43 spikes/min; V1-LD, 2.9 ± 0.45 spikes/min; V1-dLGN, 1.5 ± 0.46 spikes/min; V1-LP *vs* V1-LD, $P = 0.047$; V1-LP *vs* V1-dLGN, $P = 0.0013$; Fig. 4B). And the spike frequency of V1-LD neurons was also higher than that of V1-dLGN neurons ($P = 0.0486$). Meanwhile, the amplitude of Ca^{2+} spikes in the dendrites of V1-LD neurons was higher than that from V1-LP and V1-dLGN neurons ($\Delta F/F0$, 2.04 ± 0.1 for V1-LP, 2.78 ± 0.3 for V1-LD,

1.49 ± 0.16 for V1-dLGN; V1-LD *vs* V1-LP, $P = 0.003$; V1-LD *vs* V1-dLGN, $P = 0.0058$). Moreover, the spike amplitude in the dendrites of V1-LP neurons was also higher than that of V1-dLGN neurons ($P = 0.04$). The higher frequencies and amplitudes of Ca^{2+} spikes in the dendrites of V1-LP neurons suggest more active input from upstream neuron terminals. During the whole recording procedure (~ 11 min), no significant fluorescence bleaching of GCaMP6s and DsRed2 was detected (Fig. S2).

Discussion

In functional studies of the brain, *in vivo* Ca^{2+} imaging has become an important method of detecting neuronal activity under physiological and pathological conditions. Two-photon microscopy has emerged as a useful method for *in vivo* Ca^{2+} imaging with high spatial resolution to explore long-term neural function [36]. To study the activity of specific neurons, especially those in specific neural circuits, simply relying on transgenic animals cannot meet the challenge. Based on the advantages of viral tracers (better signals, selectivity, capacity for exogenous gene engineering, and trans-synaptic tracing), their application to functional studies of the brain has turned out to be practical and effective [37, 38].

Rabies virus [21] is one of the most widely-used retrograde tracing viruses due to its high neurotropism. Here, we constructed the rRV- Δ G-GCaMP6s-DsRed2 functional tracer and combined it with *in vivo* Ca^{2+} two-photon imaging to assess spontaneous activity in the dendrites of corticothalamic neurons from different V1-thalamus circuits. As reference fluorescence, DsRed2 was used to calibrate the GCaMP6s signal distortion caused by respiratory vibration and heating to ensure GCaMP6s signal reliability. Meanwhile, DsRed2 protein traced the whole morphology of neurons, providing clear subcellular details including dendrites and dendritic spines. Although fluorescent proteins are photobleached during two-photon microscopic imaging, the bleaching rates for GCaMP6s and DsRed2 showed no significant deviation in 10 min at a scan speed of $2 \mu\text{s}/\text{pixel}$. Moreover, infection with viral tracers may affect neural activity, so observations during a certain time window are required for functional studies [39]. For RV tracing, functional studies within 5 days–11 days after virus injection are reliable [34, 37]. During this time window, RV-labeled neurons are alive (they began to die at ~ 16 days after infection) and neuronal activity is normal as no significant changes in the electrophysiological properties of infected neurons are detectable [34]. Therefore, we performed two-photon *in vivo* Ca^{2+} imaging in this window.

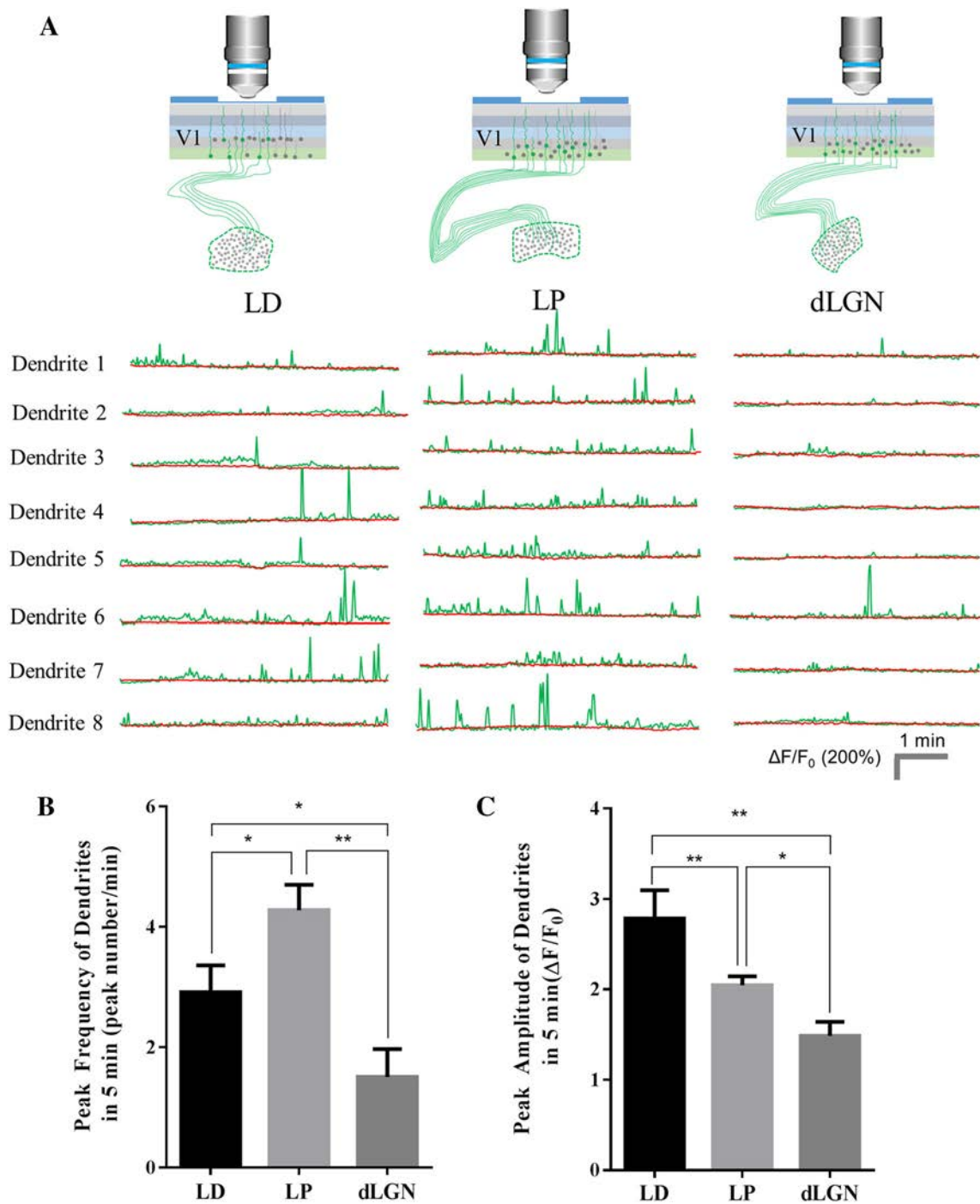


Fig. 4 Distinct spontaneous Ca^{2+} dynamics in corticothalamic neuron dendrites in different V1–thalamic circuits. **A** Schematic of Ca^{2+} imaging in dendrites of neurons from V1–LD, V1–LP, and V1–dLGN circuits and spontaneous Ca^{2+} traces in 5 min for 8 dendrites in each circuit. The green traces indicate Ca^{2+} dynamics, and the red

traces indicate DsRed2 fluorescent signals. **B** Statistics for Ca^{2+} spike frequency during 5-min recording. **C** Statistics for Ca^{2+} spike amplitude of dendrites in 5 min (mean \pm SEM; * $P < 0.05$, ** $P < 0.01$; unpaired t tests).

Due to light-scattering and aberrations originating from tissue, the penetration depth of two-photon imaging is usually limited to the upper cortical layers in mice. For the deeply-localized somata of corticothalamic neurons, monitoring dendrites is easier. And with the ultra-sensitivity of

GCaMP6s to Ca^{2+} , local Ca^{2+} dynamics measurement in dendrites is feasible. It has been reported that the combination of two-photon microscopy with red-shifted fluorescent Ca^{2+} indicator labeling can be used to monitor somatic activity deep in the brain [40]. So, for the deep

somata of corticothalamic neurons, live Ca^{2+} imaging can be performed with the help of a red-shifted fluorescent Ca^{2+} indicator. Moreover, miniscope implementation, which enables Ca^{2+} imaging in deeper brain nuclei *in vivo* [23, 41], is another promising solution for the measurement of somatic activity in corticothalamic neurons *in vivo*.

Our *in vivo* two-photon Ca^{2+} imaging in dendrites of RV-labeled corticothalamic neurons is a simple but robust method for imaging subcellular Ca^{2+} dynamics in specific neurons in viral tracer-labeled neural circuits *in vivo*. This contributes to functional studies of specific neural circuits, and helps to understand the integration of information between neural circuits in the intact brain, especially the subcellular details, under physiological and pathological conditions.

Acknowledgements We thank Dr. Fuqiang Xu (Wuhan Institute of Physics and Mathematics, Chinese Academy of Sciences) and Dr. Edward Callaway (The SALK Institute, USA) for the rRV packing system. This work was supported by the National Natural Science Foundation of China (31700934 and 31371106).

Conflict of interest The authors declare no potential conflicts of interest with respect to the research, authorship, and/or publication of this article.

References

- Knoblich U, Huang L, Zeng H, Li L. Neuronal cell-subtype specificity of neural synchronization in mouse primary visual cortex. *Nat Commun* 2019, 10: 2533.
- Luo L, Callaway EM, Svoboda K. Genetic dissection of neural circuits. *Neuron* 2008, 57: 634–660.
- Huang L, Yuan T, Tan M, Xi Y, Hu Y, Tao Q, *et al.* A retinoraphe projection regulates serotonergic activity and looming-evoked defensive behaviour. *Nat Commun* 2017, 8: 14908.
- Zhang J, Tan L, Ren Y, Liang J, Lin R, Feng Q, *et al.* Presynaptic excitation via GABAB receptors in habenula cholinergic neurons regulates fear memory expression. *Cell* 2016, 166: 716–728.
- Yamada T, Yang Y, Valnegri P, Juric I, Abnoui A, Markwalter KH, *et al.* Sensory experience remodels genome architecture in neural circuit to drive motor learning. *Nature* 2019, 569: 708–713.
- Tomoda T, Sakurai T. Neural circuitry and brain functions. *Clin Calcium* 2018, 28: 844–850.
- Shadmehr R. Distinct neural circuits for control of movement vs. holding still. *J Neurophysiol* 2017, 117: 1431–1460.
- Gobel W, Helmchen F. *In vivo* calcium imaging of neural network function. *Physiology (Bethesda)* 2007, 22: 358–365.
- Yang W, Yuste R. *In vivo* imaging of neural activity. *Nat Methods* 2017, 14: 349–359.
- Tischbirek CH, Birkner A, Konnerth A. *In vivo* deep two-photon imaging of neural circuits with the fluorescent $\text{Ca}(2+)$ indicator Cal-590. *J Physiol* 2017, 595: 3097–3105.
- Broussard GJ, Liang R, Tian L. Monitoring activity in neural circuits with genetically encoded indicators. *Front Mol Neurosci* 2014, 7: 97.
- Daigle TL, Madisen L, Hage TA, Valley MT, Knoblich U, Larsen RS, *et al.* A suite of transgenic driver and reporter mouse lines with enhanced brain-cell-type targeting and functionality. *Cell* 2018, 174: 465–480.e22.
- Fosque BF, Sun Y, Dana H, Yang CT, Ohyama T, Tadross MR, *et al.* Labeling of active neural circuits *in vivo* with designed calcium integrators. *Science* 2015, 347: 755.
- Gazda K, Bazala M, Wegierski T. Microscopic imaging of calcium ions with genetically encoded calcium indicators. *Postepy Biochem* 2017, 63: 34–43.
- Perry JL, Ramachandran NK, Utama B, Hyser JM. Use of genetically-encoded calcium indicators for live cell calcium imaging and localization in virus-infected cells. *Methods* 2015, 90: 28–38.
- Tada M, Takeuchi A, Hashizume M, Kitamura K, Kano M. A highly sensitive fluorescent indicator dye for calcium imaging of neural activity *in vitro* and *in vivo*. *Eur J Neurosci* 2014, 39: 1720–1728.
- Germond A, Fujita H, Ichimura T, Watanabe TM. Design and development of genetically encoded fluorescent sensors to monitor intracellular chemical and physical parameters. *Biophys Rev* 2016, 8: 121–138.
- Dana H, Chen TW, Hu A, Shields BC, Guo C, Looger LL, *et al.* Thy1-GCaMP6 transgenic mice for neuronal population imaging *in vivo*. *PLoS One* 2014, 9: e108697.
- Tian L, Hires SA, Looger LL. Imaging neuronal activity with genetically encoded calcium indicators. *Cold Spring Harb Protoc* 2012, 2012: pdb.top069609.
- Dana H, Sun Y, Mohar B, Hulse BK, Kerlin AM, Hasseman JP, *et al.* High-performance calcium sensors for imaging activity in neuronal populations and microcompartments. *Nat Methods* 2019, 16: 649–657.
- Tervo DGR, Hwang BY, Viswanathan S, Gaj T, Lavzin M, Ritola KD, *et al.* A designer AAV variant permits efficient retrograde access to projection neurons. *Neuron* 2016, 92: 372–382.
- Chen SH, Haam J, Walker M, Scappini E, Naughton J, Martin NP. Production of viral constructs for neuroanatomy, calcium imaging, and optogenetics. *Curr Protoc Neurosci* 2019, 87: e66.
- Chen JL, Andermann ML, Keck T, Xu NL, Ziv Y. Imaging neuronal populations in behaving rodents: paradigms for studying neural circuits underlying behavior in the mammalian cortex. *J Neurosci* 2013, 33: 17631–17640.
- Peters AJ, Lee J, Hedrick NG, O’Neil K, Komiyama T. Reorganization of corticospinal output during motor learning. *Nat Neurosci* 2017, 20: 1133–1141.
- Ranganathan GN, Apostolides PF, Harnett MT, Xu NL, Druckmann S, Magee JC. Active dendritic integration and mixed neocortical network representations during an adaptive sensing behavior. *Nat Neurosci* 2018, 21: 1583–1590.
- Takahashi N, Oertner TG, Hegemann P, Larkum ME. Active cortical dendrites modulate perception. *Science* 2016, 354: 1587–1590.
- Yang G, Pan F, Parkhurst CN, Grutzendler J, Gan WB. Thinned-skull cranial window technique for long-term imaging of the cortex in live mice. *Nat Protoc* 2010, 5: 201–208.
- Holtmaat A, Bonhoeffer T, Chow DK, Chuckowree J, De Paola V, Hofer SB, *et al.* Long-term, high-resolution imaging in the mouse neocortex through a chronic cranial window. *Nat Protoc* 2009, 4: 1128–1144.
- Osakada F, Mori T, Cetin AH, Marshel JH, Virgen B, Callaway EM. New rabies virus variants for monitoring and manipulating activity and gene expression in defined neural circuits. *Neuron* 2011, 71: 617–631.
- Wilson DE, Whitney DE, Scholl B, Fitzpatrick D. Orientation selectivity and the functional clustering of synaptic inputs in primary visual cortex. *Nat Neurosci* 2016, 19: 1003–1009.

31. Sofroniew NJ, Flickinger D, King J, Svoboda K. A large field of view two-photon mesoscope with subcellular resolution for *in vivo* imaging. *Elife* 2016, 5.
32. Birkner A, Tischbirek CH, Konnerth A. Improved deep two-photon calcium imaging *in vivo*. *Cell Calcium* 2017, 64: 29–35.
33. Nemoto T. Development of novel two-photon microscopy for living brain and neuron. *Microscopy (Oxf)* 2014, 63 Suppl 1: i7–i8.
34. Wickersham IR, Finke S, Conzelmann KK, Callaway EM. Retrograde neuronal tracing with a deletion-mutant rabies virus. *Nat Methods* 2007, 4: 47–49.
35. Kim J, Matney CJ, Blankenship A, Hestrin S, Brown SP. Layer 6 corticothalamic neurons activate a cortical output layer, layer 5a. *J Neurosci* 2014, 34: 9656–9664.
36. Svoboda K, Yasuda R. Principles of two-photon excitation microscopy and its applications to neuroscience. *Neuron* 2006, 50: 823–839.
37. Wickersham IR, Lyon DC, Barnard RJO, Mori T, Finke S, Conzelmann KK, *et al.* Monosynaptic restriction of transsynaptic tracing from single, genetically targeted neurons. *Neuron* 2007, 53: 639–647.
38. Osakada F, Callaway EM. Design and generation of recombinant rabies virus vectors. *Nat Protoc* 2013, 8: 1583–1601.
39. Ugolini G. Advances in viral transneuronal tracing. *J Neurosci Methods* 2010, 194: 2–20.
40. Birkner A, Konnerth A. Deep two-photon imaging *in vivo* with a red-shifted calcium indicator. *Methods Mol Biol* 2019, 1929: 15–26.
41. Zhang L, Liang B, Barbera G, Hawes S, Zhang Y, Stump K, *et al.* Miniscope GRIN lens system for calcium imaging of neuronal activity from deep brain structures in behaving animals. *Cur Protoc Neurosci* 2019, 86: e56.



RESEARCH HIGHLIGHT

Norepinephrine from the Locus Coeruleus Regulates Microglia Dynamics During Wakefulness

Yaling Hu¹ · Peng Shi² · Zhihua Gao¹

Received: 3 November 2019 / Accepted: 20 November 2019 / Published online: 2 January 2020
© Shanghai Institutes for Biological Sciences, CAS 2020

Microglia, the brain's “busy bees”, continuously survey the microenvironment by extending and retracting their ramified processes to maintain brain homeostasis [1, 2]. Upon disease or injury, microglia quickly transform their morphology and extend their processes towards the disease/injury sites to clear damage [2]. The mechanisms underlying the high motility of microglial processes and the rapid morphological transformation of microglia have been extensively investigated. However, studies on microglial dynamics *in vivo* have predominantly been carried out in anesthetized animals, and how microglia behave under awake conditions remained unknown. Using two-photon microscopy to track microglia dynamics in awake mice, two independent studies published recently [3, 4] have demonstrated that during wakefulness, microglia exhibit shorter arborization, reduced motility, and diminished responsiveness to injury compared to those under anesthesia. Moreover, both studies showed that norepinephrine (NE), a neurotransmitter released from the axon terminals of locus coeruleus (LC) neurons, directly regulates microglial motility through β_2 -adrenergic receptor (β_2 -AR) signaling in the awake condition [3, 4].

To determine whether microglial dynamics differ in the awake and anesthetized conditions, Stowell *et al.* [3] and Liu *et al.* [4] carefully analyzed microglial dynamics under

both conditions, using the CX3CR1^{GFP/+} transgenic mouse line in which microglia are fluorescently labeled by GFP. Surprisingly, both groups found that microglia in the awake mice survey a smaller territory with shorter arbors, reduced motility, and attenuated responsiveness to acute injury than those in brains anesthetized with isoflurane or a fentanyl cocktail [3, 4]. To exclude the possibility that general anesthesia-related circulatory and respiratory effects influence microglial activity, Liu *et al.* [4] tracked microglial responses using different anesthetics such as ketamine/xylazine and urethane. In parallel, since the fentanyl cocktail produces a slow-wave-dominated state with both analgesic and sedative effects, Stowell *et al.* [3] recorded the microglial dynamics in mice anesthetized with the sedative-only dexmedetomidine (DEX). Consistently, both groups reported enhanced velocity and surveillance of microglial processes within 10 min–15 min of anesthesia induction, regardless of the type of anesthetic, suggesting that anesthesia may relieve an inhibitory signal affecting microglial dynamics during wakefulness.

Given that general anesthesia reduces neuronal activity, Liu *et al.* [4] investigated whether the enhanced microglial surveillance during anesthesia results from the suppressed neuronal activity. They imaged the dynamics of microglial processes in the barrel cortex of mice with unilaterally trimmed whiskers. Thirty minutes after trimming, the neuronal activity in the contralateral barrel cortex was substantially reduced based on Ca^{2+} imaging from neurons expressing GCamp6 (a fluorescent sensor reflecting the intracellular Ca^{2+} level). Meanwhile, microglia also robustly increased their process areas and surveyed greater territories in the contralateral but not in the ipsilateral barrel cortex. To directly address whether neuronal activity regulates microglial process dynamics, Liu *et al.* [4] suppressed the neuronal network activity with muscimol

✉ Zhihua Gao
zhihuagao@zju.edu.cn

¹ Neuroscience Research Center and Department of Neurology, The Second Affiliated Hospital, Key Laboratory of Medical Neurobiology of Zhejiang Province, Zhejiang University School of Medicine, Hangzhou 310058, China

² Department of Cardiology, The Second Affiliated Hospital, Zhejiang University School of Medicine, Hangzhou 310058, China

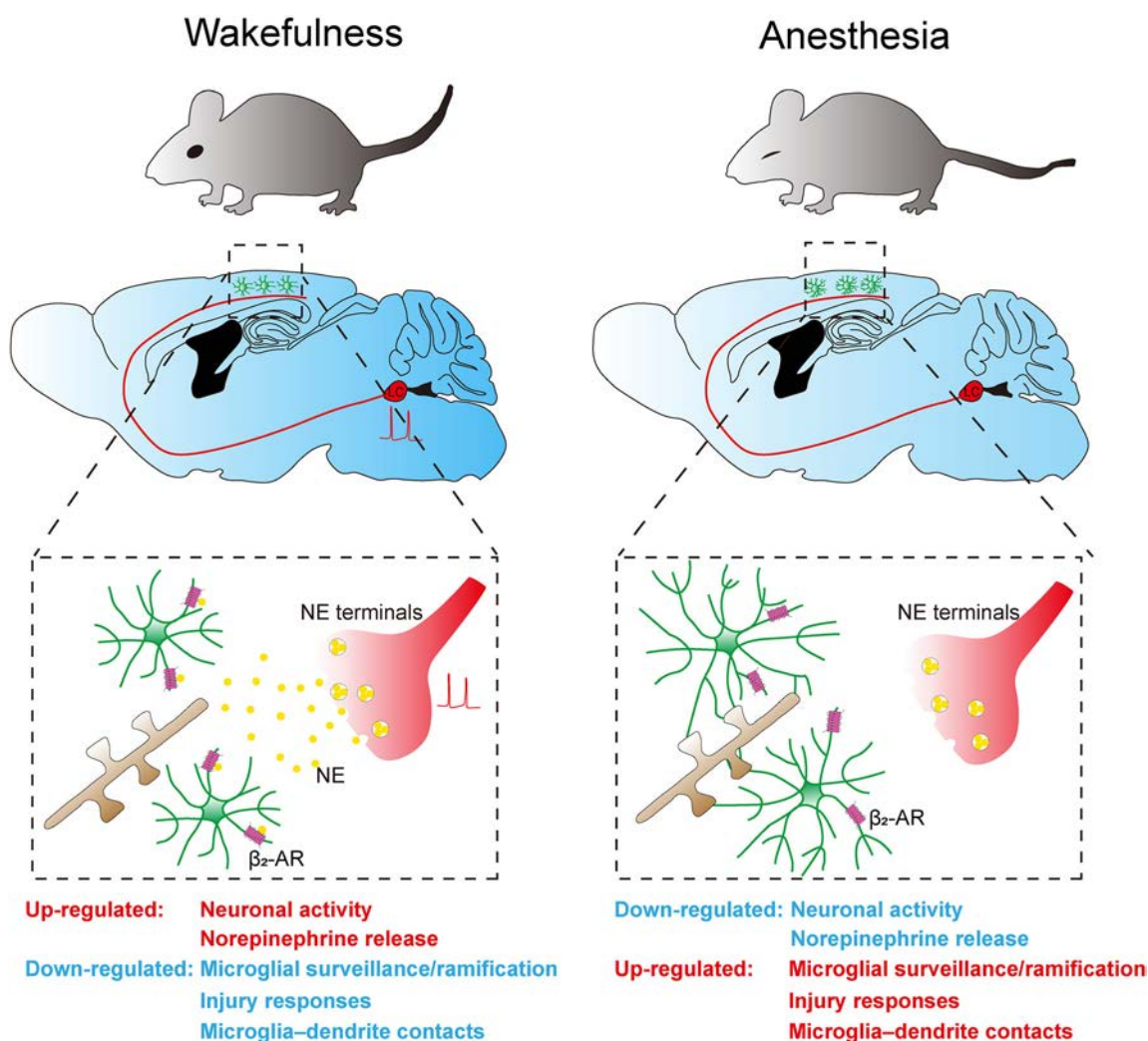


Fig. 1 Regulation of microglial dynamics by norepinephrine (NE)- β_2 adrenergic receptor (β_2 -AR) signaling. During wakefulness, tonic activation of NE neurons in the LC releases NE in the brain. Binding of NE to the β_2 -ARs on microglia restricts microglial surveillance and ramification, injury responses, and microglia-dendrite contacts.

(a GABA_A receptor agonist), tetrodotoxin (an inhibitor of voltage-gated Na⁺ channels), or optogenetic activation of GABAergic neurons. They found that reduced neuronal activity was accompanied by increased process dynamics and surveillance of microglia, reminiscent of the changes during anesthesia, suggesting that reduced neuronal activity triggers enhanced microglial dynamics and surveillance.

To reveal the mechanisms that underlie the differences between microglial dynamics in the awake and anesthetized states, both studies tested whether P2Y₁₂ and fractalkine-CX3CR1 signaling, important pathways known to regulate microglial dynamics [2], are involved and found that neither contributed to the changes. Since NE is an important mediator of wakefulness and DEX is known to reduce NE release from the LC, Stowell *et al.* [3] tested whether NE regulates microglial responses. They ablated

Under anesthesia, reduced NE neuronal activity decreases the levels of NE in the brain, releasing the inhibition of microglia by β_2 -AR signaling, thereby enhancing microglial surveillance and ramification, injury responses, and microglia-dendrite contacts.

NE neurons in the LC using the neurotoxin N-(2-chloroethyl)-N-ethyl-2-bromobenzylamine (DSP4) and found that pre-ablation of LC projections eliminated the DEX-elicited increased arborization and surveillance of microglia. Conversely, optogenetic stimulation of NE release from LC axons reduced microglia arborization and surveillance in DEX-treated animals, suggesting that endogenous NE release from the LC inhibits microglial dynamics and surveillance during wakeful states. Liu *et al.* [4] reached the same conclusion by applying a wide range of neurotransmitters known to be reduced during anesthesia, including acetylcholine, dopamine, NE, and serotonin to the imaging area. They found that only NE prevented the anesthesia-enhanced microglial process surveillance. On the contrary, inhibition of NE release from NE neurons in the LC by chemogenetic manipulation in awake mice

enhanced the microglial process dynamics, further supporting the hypothesis that NE is the inhibitory signal that limits microglial surveillance during wakefulness.

NE exerts diverse actions through a wide range of receptors. Interestingly, microglia express much higher levels of β_2 -ARs than other brain cell types [5] and previous studies *in vitro* have suggested that β_2 -AR signaling inhibits microglial chemotaxis towards ATP [6]. Stowell *et al.* [3] then treated anesthetized mice with a selective β_2 -AR agonist, clenbuterol, and found significantly reduced microglial motility and persistent process retraction, mimicking the changes in the awake condition [3]. By contrast, both studies showed that antagonizing β_2 -ARs with ICI-118, 551 in awake mice produced changes that resemble the anesthetized state with enhanced microglial motility and parenchymal surveillance [3, 4]. Moreover, the effects of clenbuterol were absent in β_2 -AR-ablated microglia [3], suggesting that endogenous NE acts directly on β_2 -ARs to inhibit microglial ramification and process motility during wakefulness.

Microglia shape neuronal circuits by modulating synapse formation, plasticity, and pruning through process arborization and surveillance [7]. Notably, Liu *et al.* [4] reported that enhanced microglial process surveillance increases microglia–dendrite interactions under anesthetized conditions, indicating that changes in microglial surveillance may result in modifications in synaptic plasticity. To determine whether NE– β_2 -AR signaling regulates microglia-mediated synaptic plasticity, Stowell *et al.* [3] examined ocular dominance plasticity (ODP) after 4 days of monocular deprivation when β_2 -AR was pharmacologically activated or inhibited. Interestingly, chronic activation of β_2 -ARs by clenbuterol impaired ODP; however, chronic blockade of β_2 -ARs by ICI-118, 551 had no effect on ODP, suggesting that sustained stimulation of β_2 -ARs interferes with microglia–dendrite contacts, but β_2 -ARs may not be required for ODP. These data provide functional significance for β_2 -ARs-regulated microglia dynamics in the modulation of synaptic plasticity (Fig. 1).

Although microglial dynamics have been described for more than a decade, these two studies are the first to uncover the different behaviors of microglia under anesthetized and awake conditions. Despite the fact that microglia express a wide range of neurotransmitter receptors [8], these studies are the first to reveal how microglia tune their dynamics *in vivo* in response to the release of a neurotransmitter, NE. Together, these results highlight the importance of real-time imaging in awake animals and

reveal the impact of neuronal activity on microglial dynamics in different states. These studies also raise important questions regarding whether the loss or gain of NE signaling in different contexts contributes to the aberrant microglial functions implicated in multiple diseases. For example, loss of NE neurons in the LC, an early sign in Alzheimer's and Parkinson's diseases [9], may enhance microglial dynamics and surveillance, whereas chronic stress or sleep deprivation may inhibit microglial surveillance by increased NE release [10]. Whether and how NE– β_2 -AR signaling contributes to pathology through aberrant regulation of microglial activity in these conditions needs further attention and investigation.

Acknowledgements This work was supported by the National Natural Science Foundation of China (31671057) and the Fundamental Research Funds for the Central Universities (2019FZA7009).

References

1. Nimmerjahn A, Kirchhoff F, Helmchen F. Resting microglial cells are highly dynamic surveillants of brain parenchyma *in vivo*. *Science* 2005, 308: 1314–1318.
2. Davalos D, Grutzendler J, Yang G, Kim JV, Zuo Y, Jung S, *et al.* ATP mediates rapid microglial response to local brain injury *in vivo*. *Nat Neurosci* 2005, 8: 752–758.
3. Stowell RD, Sipe GO, Dawes RP, Batchelor HN, Lordy KA, Whitelaw BS, *et al.* Noradrenergic signaling in the wakeful state inhibits microglial surveillance and synaptic plasticity in the mouse visual cortex. *Nat Neurosci* 2019, 22: 1782–1792.
4. Liu YU, Ying Y, Li Y, Eyo UB, Chen T, Zheng J, *et al.* Neuronal network activity controls microglial process surveillance in awake mice via norepinephrine signaling. *Nat Neurosci* 2019, 22: 1771–1781.
5. Zhang Y, Chen K, Sloan SA, Bennett ML, Scholze AR, O'Keefe S, *et al.* An RNA-sequencing transcriptome and splicing database of glia, neurons, and vascular cells of the cerebral cortex. *J Neurosci* 2014, 34: 11929–11947.
6. Gyoneva S, Traynelis SF. Norepinephrine modulates the motility of resting and activated microglia via different adrenergic receptors. *J Biol Chem* 2013, 288: 15291–15302.
7. Wu Y, Dissing-Olesen L, MacVicar BA, Stevens B. Microglia: dynamic mediators of synapse development and plasticity. *Trends Immunol* 2015, 36: 605–613.
8. Pockock JM, Kettenmann H. Neurotransmitter receptors on microglia. *Trends Neurosci* 2007, 30: 527–535.
9. Heneka MT, Nadrigny F, Regen T, Martinez-Hernandez A, Dumitrescu-Ozimek L, Terwel D, *et al.* Locus ceruleus controls Alzheimer's disease pathology by modulating microglial functions through norepinephrine. *Proc Natl Acad Sci U S A* 2010, 107: 6058–6063.
10. Kvetnansky R, Sabban EL, Palkovits M. Catecholaminergic systems in stress: structural and molecular genetic approaches. *Physiol Rev* 2009, 89: 535–606.



RESEARCH HIGHLIGHT

Meningeal Lymphatic Vessels: A Drain of the Brain Involved in Neurodegeneration?

Yuan Cheng¹ · Yan-Jiang Wang^{1,2,3} 

Received: 20 August 2019 / Accepted: 17 October 2019 / Published online: 1 January 2020
© Shanghai Institutes for Biological Sciences, CAS 2020

Neurodegenerative diseases include several kinds of neurological disorder that are caused by the progressive death of neurons in different regions of the brain. Such diseases affect millions of people worldwide and impose a heavy health burden on modern societies. However, their pathogenesis remains elusive, and disease-modifying methods are not currently available to prevent, halt, or reverse them [1]. A common feature of neurodegenerative diseases is that the abnormal accumulation of misfolded proteins, such as amyloid beta (A β), tau, α -synuclein, fused in sarcoma (FUS), and TAR DNA-binding protein 43 (TDP-43) in the brain leads to selective neuronal degeneration and dysfunction. Dysfunction in the removal of these misfolded proteins from the brain is thought to be a major cause of neurodegenerative diseases and a major therapeutic target for their cure.

Nearly all the tissues and organs, except for the central nervous system (CNS), have been found to include a lymphatic vasculature, which removes the metabolic waste from the tissue to the blood circulation. The CNS was traditionally thought to be devoid of parenchymal lymphatic vessels. For years, there had been speculation about the existence of lymphatic vessels in the brain, but clear evidence was lacking and this remained a puzzle.

A recent breakthrough in this field was the discovery of the glymphatic system [2], which was identified as a clearance pathway in the rodent brain. This route moves cerebrospinal fluid (CSF) into the brain along arterial perivascular spaces and successively into the interstitium, then guides flow towards the venous perivascular spaces, eventually removing metabolic waste in the parenchyma to the CSF. This system was named the “glymphatic” system due to the glial-like water flux and its lymphatic system-like function. It is not a true lymphoid tissue, so sometimes it is referred to as “lymphoid-like” tissue. Another milestone was achieved in 2015 when two studies in mice provided direct evidence that the brain does, in fact, have a lymphatic system [3, 4]. These lymphatic vessels extend through the dura mater and run along the peri-sinus space of the superior sagittal and transverse sinuses. Nevertheless, the major exit route for CSF was unknown. Recently, researchers have shown that lymphatic vessels at the base of the rodent skull are specialized to drain CSF and allow waste and other macromolecules to leave the brain. This provides a deeper understanding of the anatomy and functions of the lymphatic system in the brain, and represents a novel therapeutic approach for neurodegenerative diseases, according to a new research recently published in Nature [5].

Due to the complicated bony architecture at the base of the skull, research in this area remains technically difficult. A study in mice has shown that, from very early days after birth, meningeal lymphatic vessels (mLVs) grow from the base of the skull along the blood vessels into a complex network that extends to the dorsal part of the skull. Based on this finding, Ahn *et al.* [5] explored the function of brain lymphatic vessels using Prox1–GFP lymphatic reporter mice, which express green fluorescent protein under the promoter of Prox1, a key gene in lymphatic development,

✉ Yan-Jiang Wang
yanjiang_wang@tmmu.edu.cn

¹ Department of Neurology and Center for Clinical Neuroscience, Daping Hospital, Third Military Medical University, Chongqing 400042, China

² Chongqing Key Laboratory of Aging and Brain Diseases, Chongqing 400042, China

³ The Institute of Brain and Intelligence, Third Military Medical University, Chongqing 400042, China

and enable researchers to expediently visualize the detailed structure and morphology of lymphatic vessels. The authors demonstrated that dorsal mLVs show mostly a continuously-sealed zipper-like junctional pattern of lymphatic endothelial cells, while the basal mLVs consist principally of a discontinuously-sealed button-like junctional pattern similar to that of lymphatic capillaries in peripheral organs, suggesting that they are suitable for taking up CSF macromolecules. Furthermore, studies have shown that large molecular tracers, when infused into the lateral ventricle, rapidly reach lymph nodes *via* perineural routes through foramina in the skull. However, Ahn and colleagues reported that the basal mLVs drain directly into the deep cervical lymph nodes. Next, the authors assessed the drainage function of mLVs. When they followed the CSF drainage using contrast agents with magnetic resonance in rats, and a fluorescently-labeled tracer in mice, they found that tracers injected into the interstitial fluid of brain tissue were absorbed by the basal meningeal vessels and then drained out of the brain. Moreover, the researchers did not see any uptake by dorsal vessels. Overall, based on these anatomical and functional experiments, the authors came to the conclusion that basal rather than dorsal mLVs are the main route for macromolecule uptake and drainage of CSF into the peripheral lymphatic system [5].

What is the pathophysiological significance of the brain lymphatic system? It has been suggested that aged mice have reduced turnover and drainage of CSF, and such a decline in drainage might have implications for neurodegenerative diseases. Although lymphatic vessels show extraordinary plasticity, the changes in mLVs associated with aging remain unclear. Ahn and colleagues, therefore, compared the changes in basal and dorsal mLVs with age using young and aged mice, and found that the aged mice show clear regression of dorsal mLVs compared with young mice. By contrast, the basal mLVs in aged mice are enlarged and more branched and hyperplastic compared with young mice. This misshapen pattern may compensate for poor drainage. A previous study reported that disrupted lymphatic endothelial cell junctions always occur when lymphatic drainage is impaired and this has been proposed to be one of the initial factors for age-related lymphatic vessel dysfunction and degeneration. So, what happens to these structures with age? The authors showed that the transport of tracer through the basal mLVs in aged mice is significantly lower than in young mice, although lymphatic endothelial cells in aged basal mLVs have fewer zipper-type junctions and more button-type junctions, suggesting that these age-related changes in basal mLVs are associated with decreased CSF drainage in aged mice. Nevertheless, the breakthrough in the precise routes for CSF drainage is a

critical step towards understanding how metabolic waste is cleared from the CNS.

Accumulation of toxic protein aggregates is the common pathological hallmark of neurodegenerative diseases such as Alzheimer's disease (AD), Parkinson's disease, Huntington's disease, and motor neuron diseases. In AD, an imbalance between A β production and clearance is regarded as the cause of A β accumulation. Findings in recent years suggest that extracellular A β deposits are removed from the brain by various means, including enzymatic degradation, phagocytosis by microglia, glymphatic clearance from parenchyma to CSF, a blood–brain barrier (BBB) route, and the recently-identified lymphatic pathway (Fig. 1). The BBB and brain lymphatic pathways are approaches for transporting metabolic waste from the brain to the periphery, but the extent of their contribution to removing waste remains largely unclear. Recent studies suggest that ~40% of the A β peptide generated in the brain is cleared by transport to the periphery [6], as is ~19% of the pathological tau protein in the brain [7]. These findings imply that there are physiological mechanisms to transport both intracellular and extracellular pathological proteins from the brain to the periphery for clearance. Therefore, the transportation between brain and periphery would play a critical role in the clearance of metabolic waste and the maintenance of homeostasis in the brain. In this regard, dysfunction of the draining system would be an important factor leading to the development of neurodegenerative diseases. It is important to note that the function of the brain lymphatic system draining the CSF from the brain to the periphery declines during aging as shown in Ahn's study and a previous study, leading to the accumulation of A β in the brain of AD mice [5, 8]. These findings shed light on the pathophysiological action of the brain lymphatic system.

A critical question is how important the lymphatic system is in clearing metabolic waste from the brain. There are several pathways for substance exchange between the brain and the periphery, including the BBB, choroid plexus, subarachnoid granulations, and the lymphatic system. However, it is essential to determine how the lymphatic system cooperates with other clearance mechanisms in the brain to clear metabolites. We need to know how much CSF is drained into the peripheral circulation *via* the lymphatic system. If this amount is limited, the brain lymphatic system may mainly function in immune regulation rather than waste clearance. The answer to this basic question will pave the way to understanding the roles of the brain lymphatic system in the pathogenesis of neurodegenerative diseases as well as the development of therapeutics and interventions.

Although the relative contribution of each of these systems to overall clearance is unknown, they work

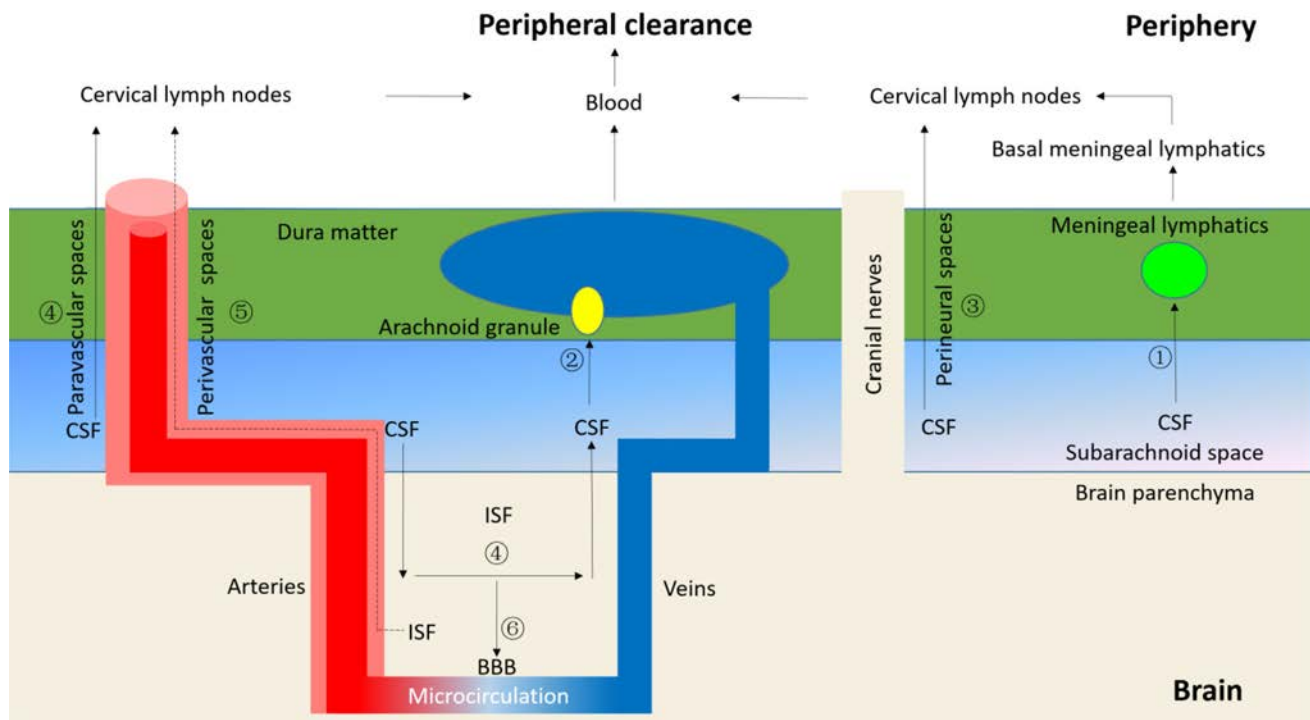


Fig. 1 Pathways of cerebrospinal fluid (CSF) drainage from the brain to the periphery. ① Meningeal lymphatics pathway: CSF flows to meningeal lymphatic vessels mainly *via* the basal component, and then flows to the deep cervical lymph nodes. ② Venous sinus pathway: CSF drains directly into the venous sinuses *via* arachnoid villi. ③ Perineural pathway: CSF drains to the cervical lymph nodes along cranial nerves (such as the olfactory, optic, and trigeminal nerves). ④ Glymphatic and paravascular pathways: CSF flows from the subarachnoid space into the brain parenchyma *via* peri-arterial spaces, exchanges with interstitial fluid (ISF), then flows back to the

subarachnoid space *via* peri-venous spaces. ⑤ Perivascular pathway: ISF diffuses through extracellular spaces in the brain, enters through basement membranes in the tunica media of arteries, and eventually drains from the brain parenchyma to the cervical lymph nodes along perivascular pathways. ⑥ Blood-brain barrier (BBB) pathway: ISF drains from the brain parenchyma into the blood *via* the BBB. Impairment of these pathways is thought to result in the abnormal accumulation of metabolic waste and pathological proteins, such as A β and phosphorylated tau, in the brain.

together to drain pathological proteins from the brain to the periphery, suggesting that the peripheral tissues and organs are physiologically important in maintaining homeostasis in the brain [9]. However, how the pathological proteins of neurodegeneration such as A β are cleared from the periphery after drainage from the brain is poorly understood. In fact, several peripheral organs and cells, such as liver, kidney, and monocytes, are thought to participate in A β catabolism and constitute potential A β clearance pathways. However, direct evidence for their roles in A β clearance is lacking. A decline in peripheral A β clearance might also impede the efflux of A β from the brain to the periphery, and thereby attenuate the central clearance of A β . In contrast, strengthening the peripheral clearance of waste alleviates A β and tau-related pathologies in the brain [6, 7], and might, therefore, represent a new therapeutic approach for neurodegenerative diseases.

Neurodegenerative diseases such as AD are traditionally regarded as disorders of the brain itself. However, growing evidence suggests that A β metabolism in the brain is dynamically correlated with A β metabolism in the

periphery [10], and pathological α -synuclein in the brain has been shown to be derived from the intestine, suggesting that the neurodegenerative diseases might be systemic disorders [9]. The discovery of the brain lymphatic system reveals a novel connection between brain and periphery, and opens a new approach to a systematic and comprehensive understanding of the pathogenesis and to the development of interventions for neurodegenerative diseases.

Acknowledgements This highlight was supported by the National Natural Science Foundation of China (91749206).

Conflict of interest The authors declare no financial or other conflicts of interests.

References

- Sun BL, Li WW, Zhu C, Jin WS, Zeng F, Liu YH, *et al.* Clinical research on Alzheimer's disease: Progress and perspectives. *Neurosci Bull* 2018, 34: 1111–1118.
- Iliff JJ, Wang M, Liao Y, Plogg BA, Peng W, Gundersen GA, *et al.* A paravascular pathway facilitates CSF flow through the

- brain parenchyma and the clearance of interstitial solutes, including amyloid beta. *Sci Transl Med* 2012, 4: 147ra111.
3. Aspelund A, Antila S, Proulx ST, Karlsen TV, Karaman S, Detmar M, *et al.* A dural lymphatic vascular system that drains brain interstitial fluid and macromolecules. *J Exp Med* 2015, 212: 991–999.
 4. Louveau A, Smirnov I, Keyes TJ, Eccles JD, Rouhani SJ, Peske JD, *et al.* Structural and functional features of central nervous system lymphatic vessels. *Nature* 2015, 523: 337–341.
 5. Ahn JH, Cho H, Kim JH, Kim SH, Ham JS, Park I, *et al.* Meningeal lymphatic vessels at the skull base drain cerebrospinal fluid. *Nature* 2019, 572: 62–66.
 6. Xiang Y, Bu XL, Liu YH, Zhu C, Shen LL, Jiao SS, *et al.* Physiological amyloid-beta clearance in the periphery and its therapeutic potential for Alzheimer's disease. *Acta Neuropathol* 2015, 130: 487–499.
 7. Wang J, Jin WS, Bu XL, Zeng F, Huang ZL, Li WW, *et al.* Physiological clearance of tau in the periphery and its therapeutic potential for tauopathies. *Acta Neuropathol* 2018, 136: 525–536.
 8. Da Mesquita S, Louveau A, Vaccari A, Smirnov I, Cornelison RC, Kingsmore KM, *et al.* Functional aspects of meningeal lymphatics in ageing and Alzheimer's disease. *Nature* 2018, 560: 185–191.
 9. Wang J, Gu BJ, Masters CL, Wang YJ. A systemic view of Alzheimer disease—insights from amyloid-beta metabolism beyond the brain. *Nat Rev Neurol* 2017, 13: 612–623.
 10. Bu XL, Xiang Y, Jin WS, Wang J, Shen LL, Huang ZL, *et al.* Blood-derived amyloid-beta protein induces Alzheimer's disease pathologies. *Mol Psychiatry* 2018, 23: 1948–1956.



RESEARCH HIGHLIGHT

Glial-neuronal Sensory Organs: Evolutionary Journey from *Caenorhabditis elegans* to Mammals

Yong Tang^{1,2,3} · Peter Illes^{1,4} · Alexei Verkhratsky^{1,5}

Received: 22 October 2019 / Accepted: 8 December 2019 / Published online: 20 January 2020
© Shanghai Institutes for Biological Sciences, CAS 2020

Recently, a paper published in *Science* reported discovery of sensory peripheral glial cells [1]. This paper demonstrated a rather unexpected property of non-myelinating Schwann cells (also known as Remak cells) dwelling in the subepidermal border of the skin [2]. These glial cells and their interactions with nociceptive nerve terminals were characterized using a variety of genetic labelling tools, transmission electron microscopy, immunocytochemistry, and electrophysiology. The morphological and functional data presented by Abdo and colleagues show that these subcutaneous glial cells form a network in the subepidermal border; moreover, these Schwann cells are intimately associated with nociceptive nerve endings to form the glial-neuronal sensory organ. These glial cells contribute to pain sensation; their optogenetic stimulation triggers electrical activity in nociceptive nerves and pain-related behaviors. Thus the new type of peripheral glia, the nociceptive Schwann cells was identified.

The discovery of a peripheral sensory glial-neuronal organ highlights an unexpected evolutionary link with primordial glia, which are associated with peripheral sensations in several invertebrates. The evolutionary history of neuroglia, supportive homeostatic and defensive neural cells, began with the emergence of central (the “brain”) and peripheral nervous systems, which accompanied the transition from Ctenophora and Cnidarians (which possess a diffuse nervous system) to more advanced life forms [3, 4]. The primordial supportive glia found in earthworms and flatworms are represented by several subtypes, which are mostly associated with peripheral nerves (neurilemmal, subneurilemmal, and periaxonal sheath-forming glia), and cells ensheathing neurons (supporting-nutritive-glia) [3, 4]. In the roundworm *Caenorhabditis elegans*, the majority of glial cells are however associated with sensory neurons. The nervous system of *C. elegans* contains 50 glial cells of ectodermal (i.e. neural) origin and 6 mesodermal supportive cells, the latter providing a link between some neurons and muscle cells [5–7]. Most of the glial cells (46 out of 50) in *C. elegans* act as an integral part of the sensory system. These 46 glial cells comprise 26 socket cells and 20 sheath cells that are associated with neuronal terminals and form specific sensory organs known as sensilla [7]. The remaining four glial cells, defined as cephalic sheath cells, serve a dual function: their anterior processes form sensilla localized in the lips of the worm, whereas their posterior processes ensheath the nerve ring (the *C. elegans* “brain”) where they contribute to the formation of the neuropil [8]. These cephalic sheath cells can be considered as the primeval ancestors of astrocytes [9].

The peripheral glia of *C. elegans* have numerous functions; they establish the location of sensilla, regulate the size and morphological appearance of sensory neuronal

✉ Yong Tang
tangyong@cducm.edu.cn

✉ Alexei Verkhratsky
Alexej.Verkhatsky@manchester.ac.uk

¹ International Collaborative Centre on Big Science Plan for Purine Signalling, Chengdu University of Traditional Chinese Medicine, Chengdu 610075, China

² Acupuncture and Tuina School, Chengdu University of TCM, Chengdu 610075, China

³ Key Laboratory of Sichuan Province for Acupuncture and Chronobiology, Chengdu 610075, China

⁴ Rudolf-Boehm-Institut für Pharmakologie und Toxikologie, Universität Leipzig, Leipzig 04107, Germany

⁵ Faculty of Biology, Medicine and Health, The University of Manchester, Manchester M13 9PT, UK

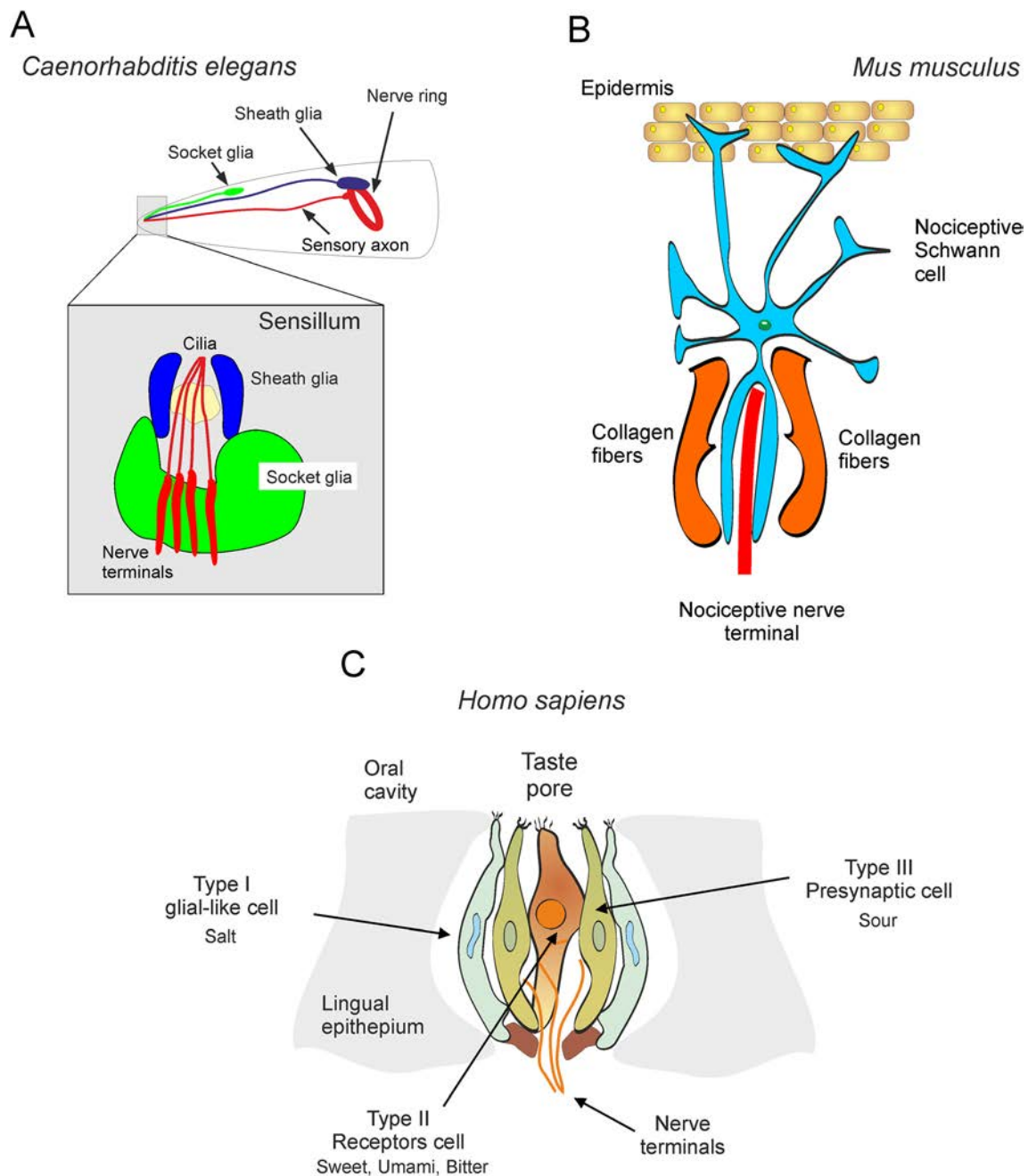


Fig. 1 Glial-neuronal sensory organs. **A** Sensilla in *C. elegans*. **B** Glial-neuronal sensory organ in the skin of mouse. **C** Glial-neuronal organisation of the taste bud in humans (redrawn from [20]).

terminals, provide for homeostatic control of the sensory organs, and (arguably) may even regulate neuronal activity. The developmental program of sensilla formation is impaired in the absence of glia (which can be selectively ablated in *C. elegans*); glia-secreted factors control sensory dendrite attachment during the migration of neurons in development, while the proper development of sensory structures requires the expression of gene sets both in neurons and in glia [8, 10]. Most unusual though was the finding that the *C. elegans* sheath and socket glia express

several types of mechanosensitive degenerin/epithelial Na^+ channel (in particular, acid-sensitive degenerin (ACD)-1 and degenerin linked to mechanosensation (DELM)-1,2 channels) [11, 12]. These channels are required for sensory function (in particular, they mediate touch sensitivity) and for several types of foraging behavior in worms [12]. Thus, from very early evolutionary stages the ancestral neuroglia were associated with the function of the sensory nervous system, and formed peripheral sensory organs.

The sensilla operate as sensory organs throughout invertebrates. In *Drosophila melanogaster* for example, taste and olfactory sensilla combine neuronal elements (2 neurons per olfactory sensillum and 2–4 per taste sensillum), and several supportive (presumably peripheral glial) cells [13, 14]. At the same time, mechanosensitive peripheral structures in *Drosophila* (trichoid sensilla, also known as bristles and cuticular campaniform sensilla) seem to be devoid of glia [15].

In mammals, peripheral glia are generally considered to be responsible for the insulation and myelination of axons (myelinating and non-myelinating Schwann cells), for covering neuro-muscular junctions (perisynaptic Schwann cells), and for maintaining homeostasis in peripheral ganglia (satellite glia). The discovery of nociceptive Schwann cells [1] prompts a fundamental extension of the repertoire of peripheral glial functions. The subcutaneous glial cells are mechanoreceptors which, upon activation, cause membrane depolarization; this depolarization is apparently conducted to nerve endings (by an as yet unknown transduction cascade) and instigate pain-associated behaviors. Thus, nociceptive Schwann cells together with nerve endings form a peripheral sensory organ, which bears a surprising semblance to sensilla in *C. elegans* (Fig. 1A, B). This evolutionary conservation of the fundamental principle behind the architecture of peripheral sensory machinery—that is, the formation of a glial-neuronal complex—is most exciting indeed.

Hitherto, the glial contribution to sensory organs in mammals has been documented only for special senses. In the retina, Muller glial cells not only provide for mechanical integrity and local homeostatic support, but also act as light-guides [16]. In the olfactory epithelium, glia-like sustentacular supporting cells insulate and support neurons, regulate ionic homeostasis, phagocytose dead cells, and secrete numerous trophic and signaling molecules [17]. The glial cells are an important part of taste-bud structure and function [18]; they are thought to sense the salty taste (Fig. 1C). From now on we shall consider the glial cell as a key element of skin sensory organs involved in nociception.

Many questions and future research directions arise from the discovery of nociceptive glia. It is of course of immense interest to reveal the mechanism through which the depolarization of nociceptive Schwann cells excites neuronal endings. It is also of importance to discern the sensory modalities (apart from mechanosensitivity) which are mediated through the glia. Another obvious fundamental question is whether the glial-neuronal sensory organs are operational in higher primates and humans, and the contributions of these organs to pain and other sensory perceptions. Could nociceptive glial cells connect not only to non-myelinated fibers but also to fast A-fibers mediating ultra-fast pain in humans?

[19]. Ultimately, we need to determine whether nociceptive peripheral glia can be a substrate for pain-related pathologies and a target for therapeutic interventions. Be all this as it may, the surprising evolutionary connection between the roundworm and mammals opens new avenues for understanding the basic principles of neuronal-glia interactions and further extends the roles played by glia in the function of the nervous system.

Acknowledgements The authors' research was supported by National Key R&D Program of China(2019YFC1709101), the Project First-Class Disciplines Development of Chengdu University of Traditional Chinese Medicine (CZYHW1901), the National Natural Science Foundation of China (81774437 and 81973969), and Science and Technology Program of Sichuan Province, China (2019YFH0108 and 2018SZ0257).

Conflict of interest The authors declare that they have no conflict of interest.

References

1. Abdo H, Calvo-Enrique L, Lopez JM, Song J, Zhang MD, Usoskin D, *et al.* Specialized cutaneous Schwann cells initiate pain sensation. *Science* 2019, 365: 695–699.
2. Cauna N. The free penicillate nerve endings of the human hairy skin. *J Anat* 1973, 115: 277–288.
3. Hartline DK. The evolutionary origins of glia. *Glia* 2011, 59: 1215–1236.
4. Verkhratsky A, Ho MS, Parpura V. Evolution of neuroglia. *Adv Exp Med Biol* 2019, 1175: 15–44.
5. Ward S, Thomson N, White JG, Brenner S. Electron microscopical reconstruction of the anterior sensory anatomy of the nematode *Caenorhabditis elegans*.? 2UU. *J Comp Neurol* 1975, 160: 313–337.
6. Stout RF, Jr., Verkhratsky A, Parpura V. *Caenorhabditis elegans* glia modulate neuronal activity and behavior. *Front Cell Neurosci* 2014, 8: 67.
7. Oikonomou G, Shaham S. The glia of *Caenorhabditis elegans*. *Glia* 2011, 59: 1253–1263.
8. Oikonomou G, Shaham S. On the morphogenesis of glial compartments in the sensory organs of *Caenorhabditis elegans*. *Worm* 2012, 1: 51–55.
9. Verkhratsky A, Nedergaard M. Physiology of Astroglia. *Physiol Rev* 2018, 98: 239–389.
10. Perens EA, Shaham S. *C. elegans* daf-6 encodes a patched-related protein required for lumen formation. *Dev Cell* 2005, 8: 893–906.
11. Wang Y, Apicella A, Jr., Lee SK, Ezcurra M, Slone RD, Goldmit M, *et al.* A glial DEG/ENaC channel functions with neuronal channel DEG-1 to mediate specific sensory functions in *C. elegans*. *EMBO J* 2008, 27: 2388–2399.
12. Han L, Wang Y, Sangaletti R, D'Urso G, Lu Y, Shaham S, *et al.* Two novel DEG/ENaC channel subunits expressed in glia are needed for nose-touch sensitivity in *Caenorhabditis elegans*. *J Neurosci* 2013, 33: 936–949.
13. Chai PC, Cruchet S, Wigger L, Benton R. Sensory neuron lineage mapping and manipulation in the *Drosophila* olfactory system. *Nat Commun* 2019, 10: 643.
14. Amrein H. Mechanism of Taste Perception in *Drosophila*. *Chemosensory Transduction*. Cambridge: Academic Press, 2016: 245–269.

15. Tuthill JC, Wilson RI. Mechanosensation and adaptive motor control in insects. *Curr Biol* 2016, 26: R1022–R1038.
16. Franze K, Grosche J, Skatchkov SN, Schinkinger S, Foja C, Schild D, *et al.* Muller cells are living optical fibers in the vertebrate retina. *Proc Natl Acad Sci U S A* 2007, 104: 8287–8292.
17. Hegg CC, Irwin M, Lucero MT. Calcium store-mediated signaling in sustentacular cells of the mouse olfactory epithelium. *Glia* 2009, 57: 634–644.
18. Gravina SA, Yep GL, Khan M. Human biology of taste. *Ann Saudi Med* 2013, 33: 217–222.
19. Nagi SS, Marshall AG, Makdani A, Jarocka E, Liljencrantz J, Ridderstrom M, *et al.* An ultrafast system for signaling mechanical pain in human skin. *Sci Adv* 2019, 5: eaaw1297.
20. Burnstock G, Verkhratsky A. *Purinergic Signalling in the Nervous System*. Heidelberg: Springer Verlag, 2012: 715.



CORRECTION

Correction to: Regional Metabolic Patterns of Abnormal Postoperative Behavioral Performance in Aged Mice Assessed by ¹H-NMR Dynamic Mapping Method

Taotao Liu^{1,2} · Zhengqian Li¹ · Jindan He¹ · Ning Yang¹ · Dengyang Han¹ · Yue Li¹ · Xuebi Tian³ · Huili Liu² · Anne Manyande⁴ · Hongbing Xiang³ · Fuqiang Xu^{2,5} · Jie Wang^{2,5,6} · Xiangyang Guo¹

Published online: 4 April 2020
© Shanghai Institutes for Biological Sciences, CAS 2020

Correction to:
Neurosci Bull 2020, 36(1):25–38
<https://doi.org/10.1007/s12264-019-00414-4>

The original version of this article unfortunately contained some mistakes.

The authors found that in this article, Figure 10C was a wrong placed figure (it was duplicated with Figure 10D), and the corrected figure was shown as follows (C).

The original article can be found online at <https://doi.org/10.1007/s12264-019-00414-4>.

✉ Jie Wang
jie.wang@wipm.ac.cn

✉ Xiangyang Guo
guoxiangyangmzk@163.com

¹ Department of Anesthesiology, Peking University Third Hospital, Beijing 100191, China

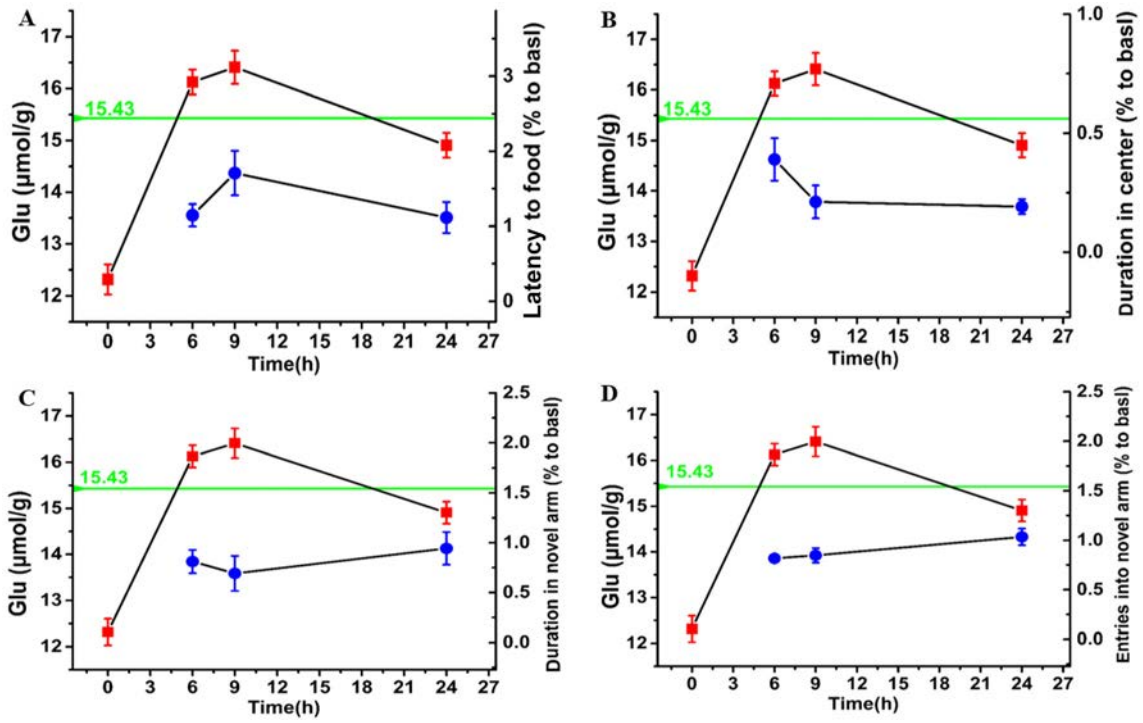
² Key Laboratory of Magnetic Resonance in Biological Systems, State Key Laboratory of Magnetic Resonance and Atomic and Molecular Physics, Wuhan Institute of Physics and Mathematics, Chinese Academy of Sciences, Wuhan 430071, China

³ Department of Anesthesiology and Pain Medicine, Tongji Hospital, Tongji Medical College, Huazhong University of Science and Technology, Wuhan 430030, China

⁴ School of Human and Social Sciences, University of West London, Middlesex TW89GA, UK

⁵ University of Chinese Academy of Sciences, Beijing 100049, China

⁶ The Second Hospital of Shijiazhuang, Shijiazhuang 050051, China



Neuroscience Bulletin Copyright Transfer Statement and Submission Form

We submit this type of article (√):

- Original Article
- Insight

- Review
- Letter to the Editor

- Research Highlight
- Method

Title of article:

Words: Figures: (Color figures:); Tables:

A signature below certifies compliance with the following statements

Copyright Transfer Statement: The copyright to this article is transferred to *Neuroscience Bulletin*, Shanghai Institutes for Biological Sciences, CAS and Springer (respective to owner if other than Shanghai Institutes for Biological Sciences, CAS and Springer and for U.S. government employees: to the extent transferable) effective if and when the article is accepted for publication. The author warrants that his/her contribution is original and that he/she has full power to make this grant. The author signs for and accepts responsibility for releasing this material on behalf of any and all co-authors. The copyright transfer covers the exclusive right and license to reproduce, publish, distribute and archive the article in all forms and media of expression now known or developed in the future, including reprints, translations, photographic reproductions, microform, electronic form (offline, online) or any other reproductions of similar nature. An author may self-archive an author-created version of his/her article on his/her own website. He/she may also deposit this version on his/her institution's and funder's (funder designated) repository at the funder's request or as a result of a legal obligation, including his/her final version, provided it is not made publicly available until after 12 months of official publication. He/she may not use the publisher's PDF version which is posted on www.springerlink.com for the purpose of self-archiving or deposit. Furthermore, the author may only post his/her version provided acknowledgement is given to the original source of publication and a link is inserted to the published article on Springer's website. The link must be accompanied by the following text: "The original publication is available at www.springerlink.com". The author is requested to use the appropriate DOI for the article. Articles disseminated *via* www.springerlink.com are indexed, abstracted and referenced by many abstracting and information services, bibliographic networks, subscription agencies, library networks, and consortia.

After submission of this agreement signed by the corresponding author, changes of authorship or in the order of the authors listed will not be accepted by *Neuroscience Bulletin*, Shanghai Institutes for Biological Sciences of Chinese Academy of Sciences and Springer.

Authorship responsibilities

I/We confirm that:

- (1) The work described has not been published before in any language or in any journal or media; that it is not under consideration for publication elsewhere; that its publication has been approved by all co-authors, if any, as well as (tacitly or explicitly) by the responsible authorities at the institution where the work was carried out.
- (2) We also give an assurance that the material will not be submitted for publication elsewhere until a decision has been made as to its acceptability for *Neuroscience Bulletin* in 2 months, then declare this statement becomes null and void.
- (3) I am/We are responsible for obtaining permission for the use of any material in the manuscript that may be under copyright to my/our employer(s) or other party(ies).
- (4) I have read the complete manuscript and accept responsibility for the content and completeness.
- (5) I have made a significant contribution to this work and am familiar with the contents.

Author (1) signed: Date: Author (2) signed: Date:

Author (3) signed: Date: Author (4) signed: Date:

Author (5) signed: Date: Author (6) signed: Date:

Author (7) signed: Date: Author (8) signed: Date:

Author (9) signed: Date: Author (10) signed: Date:

Corresponding author signed: Date:

Corresponding author address:

Tel: E-mail:

Neuroscience Bulletin

Editors-in-Chief

Shumin Duan, Zhejiang University, Hangzhou, China
Ru-Rong Ji, Duke University, Durham, USA

Consulting Editors

Yizhang Chen, Second Military Medical University, Shanghai, China
Muming Poo, Institute of Neuroscience, CAS, Shanghai, China
Larry R. Squire, University of California, San Diego, USA
Charles F. Stevens, The Salk Institute, San Diego, USA
Xiongli Yang, Fudan University, Shanghai, China

Executive Associate Editors

Iain C. Bruce, Zhejiang University, Hangzhou, China
Guangyin Xu, Institute of Neuroscience, Soochow University, Suzhou, China

Associate Editors

Zhong Chen, Zhejiang University, Hangzhou, China
Tianming Gao, South Medical University, Guangzhou, China
Shihui Han, Peking University, Beijing, China
Cheng He, Second Military Medical University, Shanghai, China
Tianzi Jiang, Institute of Automation, CAS, Beijing, China
Weidong Le, Dalian Medical University, Dalian, China
Tao Li, West China Hospital, Sichuan University, Chengdu, China
Mengsheng Qiu, Hangzhou Normal University, Hangzhou, China
Fu-Dong Shi, St. Joseph's Hospital and Medical Center, Phoenix, USA

You Wan, Peking University, Beijing, China
Jian-Zhi Wang, Huazhong University of Science and Technology, Wuhan, China
Yanjiang Wang, Daping Hospital, Third Military Medical University, Chongqing, China
Longjun Wu, Mayo Clinic, Rochester, USA
Zhi-Ying Wu, Huashan Hospital, Shanghai Medical College, Fudan University, Shanghai, China
Tianle Xu, Shanghai Jiaotong University, Shanghai, China
Dai Zhang, Peking University, Beijing, China
Hanting Zhang, West Virginia University Health Sciences Center, Morgantown, USA
Chunjiu Zhong, Fudan University, Shanghai, China

Editorial Board

Philippe Ascher, Pairs Diderot University, Paris, France
George Baillie, Institute of Cardiovascular and Medical Sciences, University of Glasgow, UK
Guo-Qiang Bi, University of Science and Technology of China, Hefei, China
Junli Cao, Xuzhou Medical College, Xuzhou, China
L. Judson Chandler, Medical University of South Carolina, USA
Jun Chen, The Fourth Military Medical University, Xi'an, China
Qing-Hui Chen, Michigan Technological University, Houghton, USA
Isaac M. Chiu, Harvard Medical School, Boston, USA

Yiru Fang, Shanghai Mental Health Center, Shanghai Jiaotong University School of Medicine, Shanghai, China
Richard S. Frackowiak, University of Lausanne, Lausanne, Switzerland
Tamás F. Freund, Institute of Experimental Medicine of the Hungarian Academy of Sciences, Budapest, Hungary
Yongjing Gao, Institute of Nautical Medicine, Nantong University, Nantong, China
Charles Gilbert, The Rockefeller University, New York, USA
Xiaosong Gu, Nantong University, Nantong, China
Junhai Han, Southeast University, Nanjing, China
Philip G. Haydon, Tufts University, Boston, USA
Joe Herbert, University of Cambridge, Cambridge, UK
Gregg E. Homanics, University of Pittsburgh, USA

- Zhi-An Hu**, Third Military Medical University, Chongqing, China
- Kazuhide Inoue**, Kyushu University, Fukuoka, Japan
- Yong-Hua Ji**, Shanghai University, Shanghai, China
- Helmut Kettenmann**, Max-Delbrück Center for Molecular Medicine, Berlin, Germany
- O.A. Krishtal**, Bogomoletz Institute of Physiology, Kiev, Ukraine
- Robert H. LaMotte**, Yale University School of Medicine, New Haven, USA
- Pierre Lavenex**, University of Fribourg, Fribourg, Switzerland
- C. Justin Lee**, Korea Institute of Science and Technology, Korea
- Juan Lerma**, Instituto de Neurociencias de Alicante, Alicante, Spain
- Bao-Ming Li**, Nanchang University, Nanchang, China
- Wolfgang Liedtke**, Duke University School of Medicine, Durham, USA
- David J. Linden**, Johns Hopkins University, Baltimore, USA
- Stuart A. Lipton**, Sanford-Burnham Medical Research Institute and University of California at San Diego, San Diego, USA
- Tong Liu**, Institute of Neuroscience, Soochow University, Suzhou, China
- Lin Lu**, Peking University Sixth Hospital, Beijing, China
- Bridget Lumb**, University of Bristol, Bristol, UK
- Benyan Luo**, Zhejiang University School of Medicine, China
- Jian-Hong Luo**, Zhejiang University School of Medicine, China
- Zhen-Ge Luo**, ShanghaiTech University, China
- Lan Ma**, Fudan University, Shanghai, China
- Qiufu Ma**, Dana-Farber Cancer Institute, Boston, USA
- Quanhong Ma**, Institute of Neuroscience, Soochow University, Suzhou, China
- Robert C. Malenka**, Stanford University, Stanford, USA
- Manuel S. Malmierca**, Universidad de Salamanca, Salamanca, Spain
- John H.R. Maunsell**, Harvard Medical School, Houston, USA
- Earl K. Miller**, Massachusetts Institute of Technology, Cambridge, USA
- Enrico Mugnaini**, Northwestern University, Feinberg School of Medicine, Chicago, USA
- Vladimir Parpura**, University of Alabama at Birmingham, Birmingham, USA
- Jos Prickaerts**, School for Mental Health and Neuroscience, Maastricht University, the Netherland
- Bruce R. Ransom**, University of Washington, Seattle, USA
- Tom E. Salt**, University College London, London, UK
- Joshua R. Sanes**, Harvard University, Boston, USA
- Michael N. Shadlen**, Columbia University, New York, USA
- Morgan Sheng**, Genentech, Inc., South San Francisco, USA
- Yousheng Shu**, Beijing Normal University, Beijing, China
- Sangram S. Sisodia**, The University of Chicago, Chicago, USA
- Peter Somogyi**, University of Oxford, Oxford, UK
- Feng-Yan Sun**, Fudan University, Shanghai, China
- Dick F. Swaab**, Netherlands Institute for Neuroscience, Amsterdam, Netherlands
- Keiji Tanaka**, RIKEN Brain Science Institute, Tokyo, Japan
- Xiaoqing Tang**, University of South China, Hengyang, China
- Yong Tang**, Chengdu University of TCM, Chengdu, China
- Makoto Tsuda**, Kyushu University, Fukuoka, Japan
- Alexej Verkhratsky**, The University of Manchester, Manchester, UK
- Steven R. Vincent**, University of British Columbia, Vancouver, Canada
- Guanghui Wang**, Soochow University, Suzhou, China
- Jian-Jun Wang**, Nanjing University, Nanjing, China
- Yun Wang**, Neuroscience Research Institute, Peking University, Beijing, China
- Xu-Chu Weng**, Hangzhou Normal University, Hangzhou, China
- William Wisden**, Imperial College London, London, UK
- Jun-Xia Xie**, Qingdao University, Qingdao, China
- Lin Xu**, Kunming Institute of Zoology, CAS, Kunming, China
- Xiao-Hong Xu**, Institute of Neuroscience, CAS, Shanghai, China
- Ying Xu**, School of Pharmacy & Pharmaceutical Sciences, University at Buffalo, The State University of New York, USA
- Yun Xu**, Nanjing Drum Tower Hospital, Nanjing, China
- Fengwei Yu**, National University of Singapore, Singapore
- Shanping Yu**, Emory University School of Medicine, Atlanta, USA
- Hong Zhang**, The Second Affiliated Hospital of Zhejiang University School of Medicine, Hangzhou, China
- Xiaohui Zhang**, Beijing Normal University, Beijing, China
- Xu Zhang**, Institute of Neuroscience, CAS, Shanghai, China
- Yong Zhang**, Peking University, Beijing, China
- Yu-Qiu Zhang**, Fudan University, Shanghai, China
- Zhi-Jun Zhang**, Zhongda Hospital, Southeast University, Nanjing, China
- Ping Zheng**, Fudan University, Shanghai, China
- Jiang-Ning Zhou**, University of Science and Technology of China, Hefei, China
- Libin Zhou**, Joint Laboratory for Brain Function and Health, Jinan University and The University of Hong Kong, Guangzhou, China
- Richard E. Zigmond**, Case Western Reserve University, Cleveland, USA
- Yimin Zou**, University of California-San Diego, USA

Neuroscience Bulletin

Copyright Information

For Authors

As soon as an article is accepted for publication, authors will be requested to assign copyright of the article (or to grant exclusive publication and dissemination rights) to the publisher (respective the owner if other than Springer Nature). This will ensure the widest possible protection and dissemination of information under copyright laws.

More information about copyright regulations for this journal is available at www.springer.com/12264

For Readers

While the advice and information in this journal is believed to be true and accurate at the date of its publication, neither the authors, the editors, nor the publisher can accept any legal responsibility for any errors or omissions that may have been made. The publisher makes no warranty, express or implied, with respect to the material contained herein.

All articles published in this journal are protected by copyright, which covers the exclusive rights to reproduce and distribute the article (e.g., as offprints), as well as all translation rights. No material published in this journal may be reproduced photographically or stored on microfilm, in electronic data bases, on video disks, etc., without first obtaining written permission from the publisher (respective the copyright owner if other than Springer Nature). The use of general descriptive names, trade names, trademarks, etc., in this publication, even if not specifically identified, does not imply that these names are not protected by the relevant laws and regulations.

Springer Nature has partnered with Copyright Clearance Center's RightsLink service to offer a variety of options for reusing Springer Nature content. For permission to reuse our content please locate the material that you wish to use on link.springer.com or on springerimages.com and click on the permissions link or go to copyright.com and enter the title of the publication that you wish to use. For assistance in placing a permission request, Copyright Clearance Center can be contacted directly via phone: +1-855-239-3415, fax: +1-978-646-8600, or e-mail: info@copyright.com

© Shanghai Institutes for Biological Sciences, CAS 2020

Journal Website

www.springer.com/12264
Electronic edition: link.springer.com/journal/12264

Subscription Information

Volume 36 (12 issues) will be published in 2020.

ISSN: 1673-7067 print
ISSN: 1995-8218 electronic

For information on subscription rates please contact Springer Nature Customer Service Center: customerservice@springernature.com

The Americas (North, South, Central America and the Caribbean)
Springer Nature Journal Fulfillment,
Harborside Plaza II,
200 Hudson Street, Jersey City,
NJ 07302, USA
Tel. 800-SPRINGER (777-4643);
212-460-1500 (outside
North America)

Outside the Americas

Springer Nature Customer Service
Center GmbH, Tiergartenstr. 15,
69121 Heidelberg, Germany
Tel.: +49-6221-345-4303

Advertisements

E-mail contact: advertising@springer.com or anzeigen@springer.com (Germany)

Disclaimer

Springer Nature publishes advertisements in this journal in reliance upon the responsibility of the advertiser to comply with all legal requirements relating to the marketing and sale of products or services advertised. Springer Nature and the editors are not responsible for claims made in the advertisements published in the journal. The appearance of advertisements in Springer Nature publications does not constitute endorsement, implied or intended, of the product advertised or the claims made for it by the advertiser.

Office of Publication

Springer Nature Singapore Pte Ltd.
152 Beach Road, #21-01/04
Gateway East, Singapore 189721,
Singapore



NEUROSCIENCE BULLETIN

Impact Factor

4.246

Q2

2018 Journal Citation Report
(Clarivate Analytics, 2019)

NEUROSCIENCE BULLETIN 神经科学通报 (Monthly)

Vol. 36 No. 5 May 15, 2020

Sponsored by: Shanghai Institutes for Biological Sciences, Chinese Academy of Sciences
Chinese Neuroscience Society
Second Military Medical University

Editors-in-Chief: Shumin Duan, Ru-Rong Ji

Edited by: Editorial Board of *Neuroscience Bulletin*

319 Yueyang Road, Building 31 B, Room 405, Shanghai 200031, China

Phone: +86-21-54922863; Fax: +86-21-54922833

E-mail: nsb@sibs.ac.cn; <http://www.neurosci.cn>

Editors: Bin Wei, Xu Jiang, Zhi-Rui Liu

Published by: Shanghai Institutes for Biological Sciences, Chinese Academy of Sciences (320 Yueyang Road, Shanghai)

Printed by: Shanghai Shengtong Times Printing Co., Ltd (A6, No. 2888, Caolang Highway, Jinshan District, Shanghai)

Overseas Distributed by: Springer Nature

Home Distributed by: Local Post Offices

ISSN 1673-7067

CN 31-1975/R

Post Office Code Number: 4-608

Permit of Ad. Number: 3100420130051

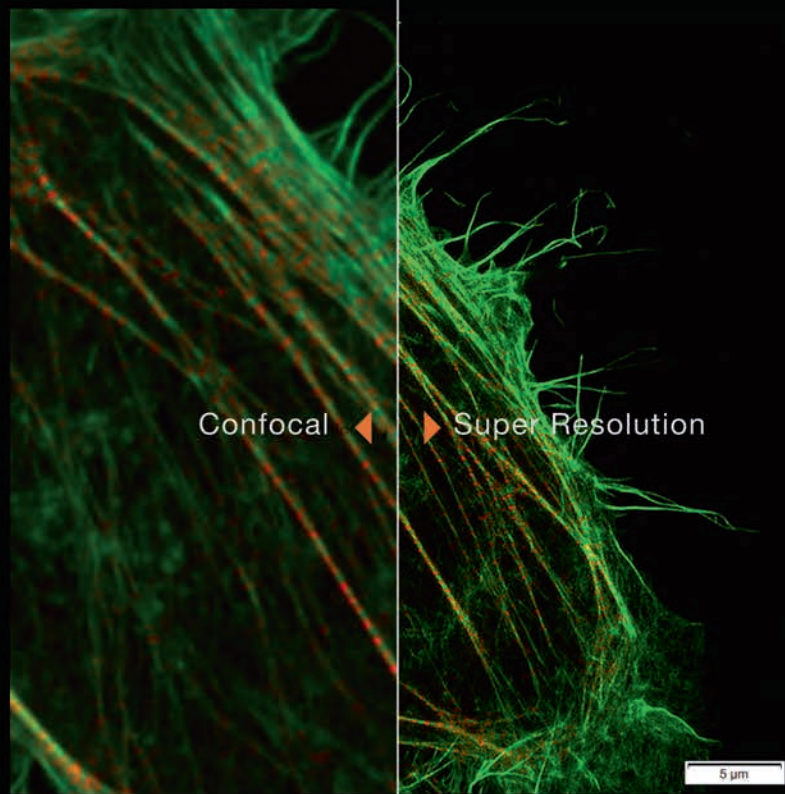
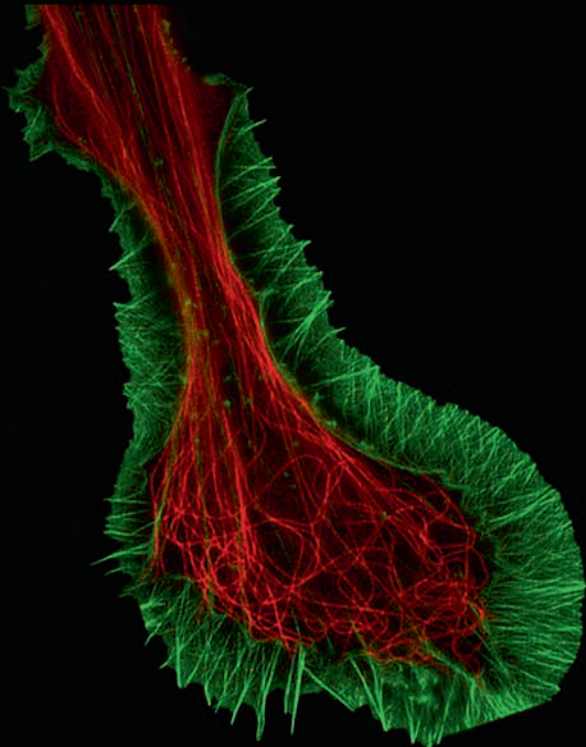
Price: ¥ 100.00

ISSN 1673-7067



兼顾分辨率和速度的

转盘共聚焦活细胞超分辨系统 **SpinSR10**



- 分辨率高达110nm的实时超分辨率成像
- 专有反卷积算法进一步提升图像质量
- 宽视野成像，速度高达 200fps
- 特色硅油物镜可以实现活细胞深层成像
- 宽场、共聚焦、超分辨率模式自由切换
- 功能强大的智能cellSens软件平台



奥林巴斯（北京）销售服务有限公司

北京朝阳区酒仙桥路10号恒通商务园B12C座2F (北京) 010-59756006
 上海市徐汇区淮海中路1010号嘉华中心11楼 (上海) 021-51582084
 广州市环市东路403号广州电子大厦16楼 (广州) 020-61227171

陕西省西安市新城区尚德路85号太平洋保险大厦8F

湖北省武汉市江岸区中山大道1628号武汉天地企业中心5号7楼701单元
 四川省成都市人民南路四段三号来福士广场T1-11楼
 辽宁省沈阳市沈河区友好街10号新地中心1号楼3501室

(西安) 029-87206108

(武汉) 027-82718838

(成都) 028-86703700

(沈阳) 024-23342084